TU Dortmund University

Dissertation
for the academic degree
Doctor rerum naturalium (Dr. rer. nat.)

Chemomechanical Simulation of Microtubule Dynamics

Matthias Schmidt

Dortmund, 2020

Submission Date: December 2, 2020
Oral Examination Date: April 8, 2021

Examination Board:
Prof. Dr. Heinrich Päs
Prof. Dr. Jan Kierfeld
PD Dr. Ute Löw
PD Dr. Alex Greilich

Acknowledgements

I want to thank Prof. Dr. Jan Kierfeld, my supervisor for this thesis, and PD Dr. Ute Löw for being the second referee. I am grateful to Dr. Carsten Nase for technical support and Dr. Carsten Lindner and Lina Heydenreich for proofreading parts of the manuscript. Lastly, I want to thank my office colleagues for discussions on- and off-topic of this thesis.

Contents

Introduction

1

1.1 Cells, Their Cytoskeleton, and Mitosis

The fundamental building blocks of life are cells, be it for simple organisms only consisting of a single cell or complex organisms like human beings that are made up of more than 10^{13} cells[1]. Cells store the information for every aspect of their life cycle in form of deoxyribonucleic acid (DNA) double helices in their nucleus. Cells are complex structures consisting of many components that are responsible for a wide range of different tasks like mitochondria in eucaryotic[2] cells producing adenosine triphosphate (ATP), an important energy source for cells. For the following discussion, however, we will drastically simplify the architecture of cells as shown in Figure 1.1, which focuses on the cytoskeleton.

In this simplified model, the cell is confined by a membrane surrounding the intracellular fluid (also called cytosol) and the nucleus with the DNA. In the cytosol, three different types of protein filaments form the cytoskeleton. The cytoskeleton fulfills a multitude of functions in cells like providing their shape and their physical robustness, facilitating their movement, and enabling intracellular transport. The protein filaments constituting the cytoskeleton are actin filaments, intermediate filaments, and the topic of this thesis, microtubules. Each type of filament is responsible for different main aspects of the cells' functioning: Actin filaments are below the membrane and are thus perfectly positioned to change the shape of the cells and to allow cells to move by protruding the part of the cell in movement direction and pulling back the part of the cell on the opposite site. The different types of intermediate filaments are responsible for the mechanical stability of the cells. Microtubules form the pathways for cargo being transported in the cell by kinesin and dynein motor proteins. Microtubules are stiff polymers with a persistence length of $L_\mathrm{p} = \mathcal{O}(1\,\mathrm{mm})$[2,3], while actin filaments ($L_\mathrm{p} = \mathcal{O}(10\,\mathrm{\mu m})$[2,4]) and intermediate filaments ($L_\mathrm{p} = \mathcal{O}(1\,\mathrm{\mu m})$[5], the actual value depends on the type of intermediate filament) are softer. The persistence length is the characteristic length over which the correlation of tangential directions along a polymer are lost (see (4.20)).

While actin filaments and intermediate filaments are not statically anchored in the cells (though actin filaments can be anchored to each other by forming bundles or networks via additional proteins, and they can also connect to microtubules), microtubules generally grow from a microtubule-organizing center (MTOC)[6,7] (see Figure 1.1), which serves as their nucleation site and anchor point. One type of such a microtubule-organizing center are centrosomes found in animals. It is important to note that while we generally associate the term "skeleton" with our own human skeleton and thus consider it a static structure, the cytoskeleton, however, is anything but static. As already mentioned, the cytoskeleton enables cells to move by reorganizing the actin filament network, but the components of the cytoskeleton, the protein

---

[1] The short introduction into cells given in this section is based on Alberts et al.[1].

[2] Eucaryotes are organisms with a distinct, membrane-enclosed nucleus in contrast to procaryotes like bacteria that do not have a membrane-enclosed nucleus.

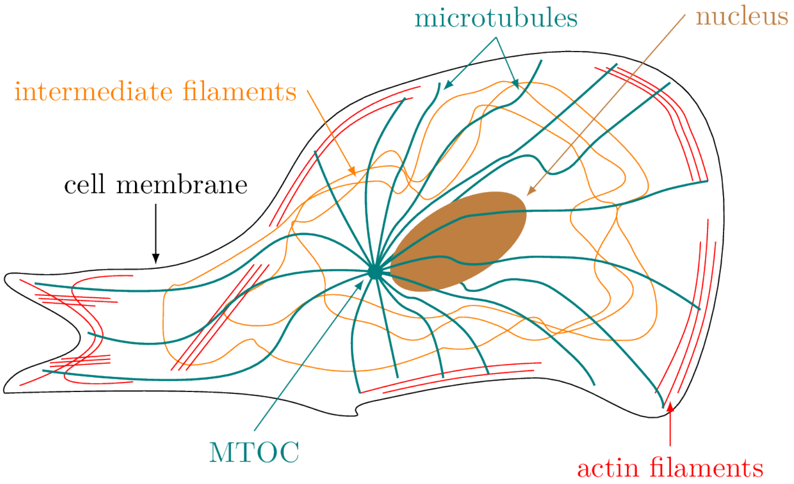

Figure 1.1: Schematic illustration of the cytoskeleton formed by microtubules, actin filaments, and intermediate filaments (based on similar images from Alberts et al.[1]).

filaments themselves, are also generally non-static, i.e., change their length by growing or shrinking.

One important step in the life cycle of cells is cell division and in the part of cell division called mitosis in which the duplicated chromosomes are separated and the two new daughter cells are formed, microtubules and actin filaments play crucial roles. Microtubules form the mitotic spindle that attaches to the duplicated chromosomes during the prometaphase and aligns the duplicated chromosomes in the center of the cell during the following metaphase. In the anaphase of mitosis, the microtubules that are attached to the chromosomes shrink and pull the chromosomes with them and thus separate them. In the following and last phase of mitosis, which is called telophase, the actin filaments start forming the contractile ring, which separates the original cell into the two daughter cells during cytokinesis, the step following mitosis. Figure 1.2 gives a graphic overview of the previously described different parts of mitosis and cytokinesis related to microtubules and actin filaments. During mitosis, in addition to the kinetochore microtubules that are attached to the duplicated chromosomes via kinetochores (thus the name “kinetochore microtubules”), there are also two other types of microtubules: interpolar microtubules and astral microtubules. Interpolar microtubules grow towards the opposite pole of the cell and the free ends of interpolar microtubules growing in opposite directions are linked by motor proteins in the center of the cell. There are two types of these motor proteins that either pull the poles together or push them apart, which helps correctly positioning the mitotic spindle in the cell. In contrast, astral microtubules can be found at the two poles of the cell near their MTOC, and they also help to ensure that the mitotic spindle is correctly positioned.

From this short introduction, it is already obvious that microtubules are an important aspect of life and thus of great interest for research. Additionally, microtubules are important parts of dendrites and axons in neurons, which are responsible for the propagation of electrical impulses. Several diseases affecting the nervous system like Alzheimer’s disease are linked to

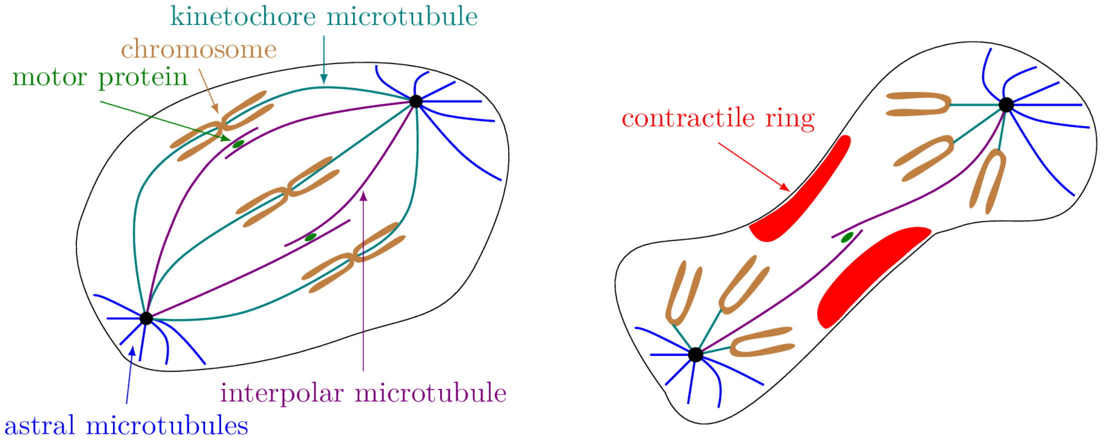

(a) Initial configuration with the chromosomes aligned in the center of the cell.

(b) Configuration after the kinetochore microtubules have pulled the chromosomes apart and the formation of the contractile ring.

Figure 1.2: Oversimplified illustration of how the kinetochore microtubules are pulling the chromosomes apart and how the actin filaments form the contractile ring separating the cells (based on similar images from Alberts et al.[1]).

microtubules[8]. Furthermore, successful "antimitotic drugs"[9] used in cancer treatment target microtubule dynamics making microtubules "the best cancer target to be identified so far"[9]. By influencing how microtubule grow and shrink and by disrupting mitosis of cancer cells, these drugs lead the cancer cells to apoptosis ("programmed cell death")[9]. Another way of how cancer influences microtubules are changes to their monomeric building blocks, for example via post-translational modifications, though this is still an active field of research[10].

We have already mentioned that during anaphase, it becomes important that the kinetochore microtubules shrink. However, it is important for all three types of microtubules that they can switch between growth and shrinkage. While in cells in general, and thus during mitosis specifically, such switching is often facilitated by additional proteins, it is an important intrinsic property of microtubules as well (see next section). Hence, not only are microtubules themselves of interest, but also their growth dynamics in particular, which is the topic of this thesis.

1.2 A Short History of Microtubules

Starting in the 1950s[11], long filaments were found in cells that were named "microtubules" in 1963[12,13] due to their tubular structure. Retrospectively, Slautterback[12] was able to identify many of the previously reported structures as microtubules. Shortly thereafter[14,15], while investigating microtubules in plant cells, it was discovered that microtubules consist of "slender filamentous subunits"[14] and that there were probably 13 of these "protofilaments"[15]. In the following years, microtubules with 8 up to 17 protofilaments[16–24] were found in different cells or *in vitro*, though not every number of protofilaments found *in vitro* experiments might also be found in actual cells[22]. It has even been observed that within the same microtubule, the number of protofilaments can change[22,25], which can be considered a defect in the microtubule lattice. Microtubules can also form doubles and triples in which microtubules share protofilaments between each other[26]. Additionally, while imaging microtubules, spiral structures and rings formed by depolymerized subunits of microtubules have been found[27–29].

Following the discovery of microtubules, research into and isolation of their subunits was under way[30], which was ultimately named "tubulin"[31]. Previously, the "axial repeat along the [proto]filaments"[32] was already measured as either 4 nm or 8 nm[26,32,33]. The discrepancy between these two lengths was explained by the subunit being a dimer[34–37] with a length of 8 nm consisting of two tubulin monomers with a length of 4 nm per monomer. Each tubulin monomer has a binding site for a guanosine nucleotide molecule[34]. In the beta-tubulin monomer, guanosine triphosphate (GTP) can hydrolyze into guanosine triphosphate (GDP), which is why it is also called the "E site" (with "E" for "exchangeable")[34,38], while in the alpha-tubulin, the "N site" (with "N" for "nonexchangeable")[34,38], the GTP molecule does not hydrolyze[34], resulting in a alpha-beta-heterodimer[35]. These hetero-dimers are arranged "head-to-tail"[34] in protofilaments, i.e., they form an alternating chain of alpha- and beta-tubulin monomers. Figure 1.3 gives a schematic overview of how individual tubulin dimers build the protofilament and how then multiple protofilaments form the microtubule.

An important breakthrough for further investigations into microtubules was the *in vitro* growth of microtubules from tubulin[39,40]. In these initial experiments and in later ones[41–43] as well, it was shown that the contents and their amounts in the buffer solution, like different amounts of specific ions, influence the microtubule dynamics. It has also been shown that there are different tubulin isotypes that influence the dynamics of the microtubules they build[44,45][4]. Together, these aspects can make comparisons between different experiments difficult and can result, for example, in different values for growth velocities.

Having the ability to grow microtubules *in vitro* lead to the discovery of their "dynamic instability" by Mitchison and Kirschner[46,47], which results in growing and shrinking microtubules being present in the same buffer at the same time. It was also found that microtubules shrink significantly faster than they grow[47–49]. Two years after the discovery of the dynamic instability of microtubules, individual microtubules could be tracked and their length recorded over time showing when a growing microtubule would switch to shrinking and vice versa[48]. Figure 1.4(b) shows schematically how a microtubule switches from growth to shrinkage, which is called

---

[3] Used with permission of Springer Nature BV, from "Structure of the $\alpha\beta$ tubulin dimer by electron crystallography" by E. Nogales, S. G. Wolf, and K. H. Downing, *Nature* **391** (6663), 1998[37]; permission conveyed through Copyright Clearance Center, Inc.

[4] In humans alone, there are eight different α-tubulin isotypes and seven different β-tubulin isotypes[10].

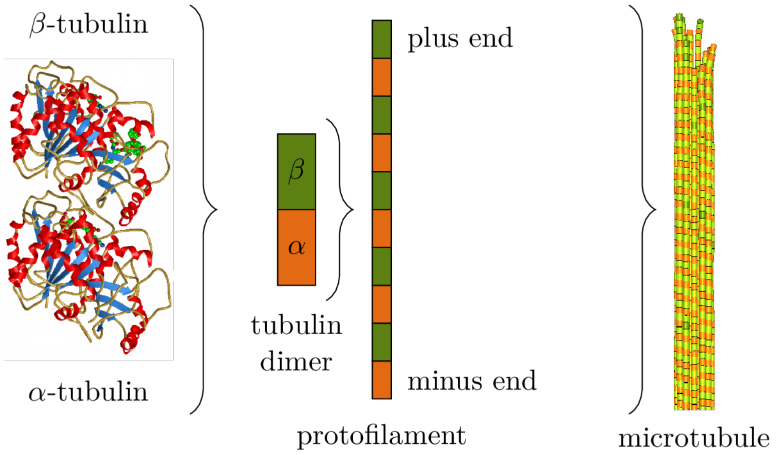

Figure 1.3: Schematic illustration of the building blocks (tubulin dimers and protofilaments) of microtubules (based on a similar image from Alberts et al.[1]). The tubulin dimer structure on the left has been taken from Nogales et al.[3]

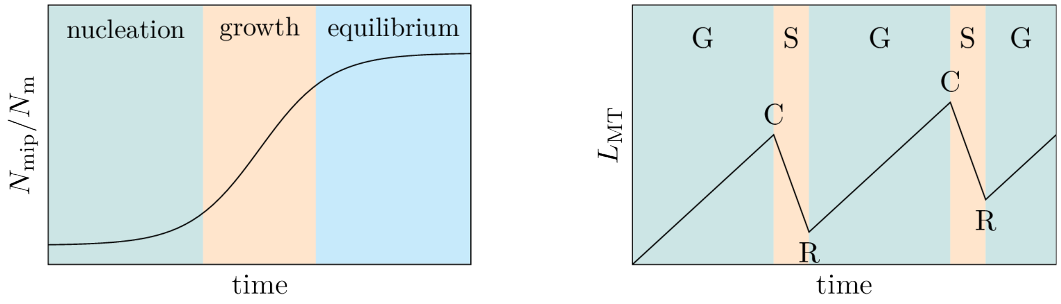

(a) Exemplary time evolution of the ratio of the number of monomers incorporated into polymers N_{mip} and the total number of monomers N_{m} for a simple type of polymers. (Based on a similar image from Alberts et al.[1].)

(b) Exemplary growth trajectory (microtubule length L_{MT} as a function of time) of a microtubule undergoing catastrophes (C) after a period of growth (G) switching to shrinkage (S) until a rescue (R) occurs.

Figure 1.4: Comparison between the growth behavior of simple types of polymers and microtubules.

a catastrophe, and then switches back to growth after a rescue. This behavior is different from a simple type of polymer growth as shown in Figure 1.4(a), which starts with a "lag phase"[1] during which monomers require some time to form a stable polymer. This lag phase is also relevant for microtubules and can generally be avoided if there is an existing seed or nucleation side from with the polymer can grow. After stable polymers have formed, they can grow (growth phase) and the number of monomers incorporated into polymers increases, which in turn results in a decrease of monomers in the surrounding buffer. After the concentration of free monomers in the buffer has reached the critical concentration c_{crit}[50,51] at which the flux of free monomers into the polymers equals the flux of monomers from the polymers back into the solution, a steady state is reached.

An explanation for these sudden switches between growth and shrinkage is given by the "GTP-cap model" in which newly polymerized GTP-tubulin dimers form a cap, which grows via the attachment of new GTP-tubulin dimers and shrinks because of the detachment of GTP-tubulin dimers and the hydrolysis of GTP to GDP resulting in a "GDP body"[27,47,52]. After the development of techniques to identify GTP-tubulin dimers in microtubules[53–56], islands of GTP-tubulin dimers inside the GDP-body were detected and proposed as one possible rescue mechanisms for microtubules[53,57].

In vitro experiments[47–49] also showed that the two ends of the free microtubules behave differently: One end, called the "plus end", grows faster and changes its growth state more often than the other end, the "minus end". Later, it was established that the beta-tubulin with the exchangeable GTP molecule is located at the plus end and the alpha-tubulin at the minus end[37,38,58]. The minus end is also the end from which microtubules grow from MTOCs. In the sense of there being two distinct ends, microtubules are referred to as "polar" filaments[59], which ultimately originates from the heterogeneity of the tubulin-dimer, i.e., alpha-tubulin monomers and beta-tubulin monomers being distinct. Free microtubules also have the ability to shrink at one end and grow at the other end[51,60,61], a phenomenon called "treadmilling", which effectively allows them to "move" in the surrounding fluid and which is a relevant process for actin filaments as well[50]. For microtubules anchored in cells at MTOCs, however, only dynamic instability is relevant because the minus end is static.

An important finding to understand how the GTP-cap stabilizes microtubules were "ram's horns" at the tip of shrinking microtubules[29]: In contrast to straight tips of growing microtubules (see Figure 1.5(a)), protofilaments were found to bent outward while the microtubule shrinks making them look like "ram's horns"[27,29,62] as shown in Figure 1.5(b). During the debate of why the lattice of the GDP-body of microtubules is unstable and why the GTP-cap stabilizes, two models emerged trying to explain the stabilizing effect of the GTP-cap: the lattice model and the allosteric model. In the lattice model[64,65], GTP- and GDP-tubulin dimers are intrinsically curved (supported by newer images of protofilament ends also being bent during growth, as shown in Figure 1.5(c)), but when GTP-tubulin dimers polymerize into the microtubule, they assume a straight conformation, which is then kept after hydrolysis due to the lattice constraints. To explain the stabilizing effect of the GTP-cap, lateral bonds between GTP-tubulin dimers are assumed to be stronger than for GDP-tubulin dimers. In the allosteric model[28,29,66,67], however, GTP-tubulin dimers are assumed to be straight regardless of whether they are part of the microtubule or whether they are unbound in the surrounding buffer solution, resulting in a naturally stable GTP-cap as there are no lattice forces acting on these tubulin dimers keeping them straight because it is already their preferred conformation. While we are using the allosteric model, as we will explain in the description of our model in chapter 2, we will come back to the lattice model in section 10.2 as part of our conclusions and outlook to highlight recent findings.

We end our short history of microtubules here as most aspects relevant for the rest of this thesis

---

[5] Used with permission of Rockefeller University Press, from "Microtubule Dynamics and Microtubule Caps: A Time-resolved Cryo-Electron Microscopy Study" by E. M. Mandelkow, E. Mandelkow, and R. A. Milligan, *J. Cell Biol.* **114** (5), 1991[29]; permission conveyed through Copyright Clearance Center, Inc.

[6] Used with permission of Rockefeller University Press, from "Microtubules grow by the addition of bent guanosine triphosphate tubulin to the tips of curved protofilaments" by J. R. McIntosh, E. O'Toole, G. Morgan, J. Austin, E. Ulyanov, F. Ataullakhanov, and N. Gudimchuk, *J. Cell Biol.* **217** (8), 2018[63]; permission conveyed through Copyright Clearance Center, Inc.

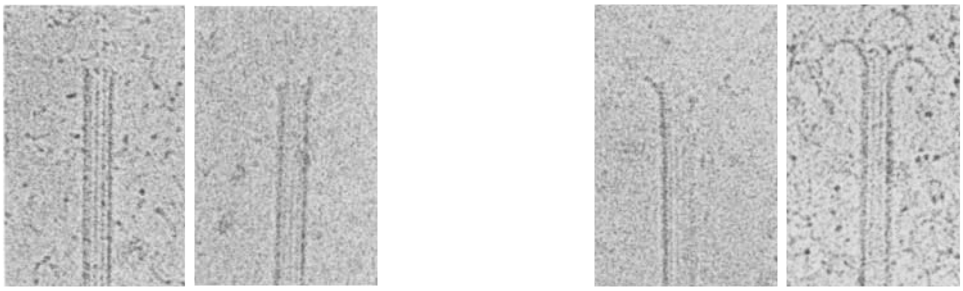

(a) Images of straight ends of growing microtubules[5].

(b) Images of bent protofilament ends of shrinking microtubules[5].

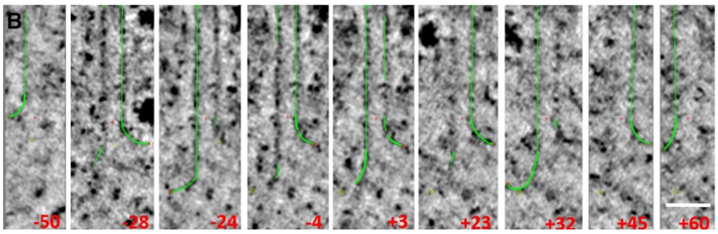

(c) Images of bent protofilament ends of a growing microtubule with green trace marks and the viewing angles (red numbers)[6].

Figure 1.5: Images of the ends of growing and shrinking microtubules.

have been introduced. Further information can be found in various review articles that have been published in the last decades[7,68–78].

(a) Continuous macroscopic one-dimensional microtubule model with growth velocity v_{gr} and shrinkage velocity v_{sh}.

(b) Discrete microscopic one-dimensional microtubule model with polymerization rate k_{on} and depolymerization rate k_{off}.

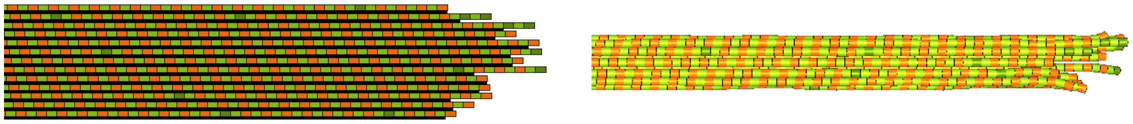

(c) Discrete microscopic two-dimensional microtubule model.

(d) Discrete microscopic three-dimensional microtubule model in which tubulin monomers are represented by cylinders.

Figure 1.6: Schematic illustration of different types of major microtubule models in different dimensions.

1.3 Microtubule Modeling

To understand the growth dynamics of microtubules, since the 1980s, theoretical and computational models have been developed on different levels of complexity, which we will review briefly in this section[79,80]. There are three main types of microtubule models corresponding to the number of dimensions used to model the microtubule. In one-dimensional models, or single protofilament models, microtubules are represented as a one-dimensional object with either a continuous length or as a sequence of one-dimensional tubulin dimers. Two-dimensional models explicitly include the multi-protofilament structure of microtubules but represent each protofilament as a one-dimensional object made up of one-dimensional tubulin dimers. Lastly, three-dimensional models represent tubulin dimers as three-dimensional objects resulting in an overall three-dimensional model. The level at which tubulin dimers are modeled can differ in three-dimensional models, however. They can either be just a dimer of two tubulin monomers that themselves have no substructure or they can be modeled at (near-)atomic resolution. Obviously, as the models get more detailed, they also require more computational power so that the three-dimensional models were the last ones to be developed. Figure 1.6 provides a graphic overview of the different types of major microtubule models in different dimensions.

1.3.1 One-Dimensional Models

Early microtubule modeling in the 1980s, in particular by Hill et al.[52,81–85], considered the microtubule as a one-dimensional sequence of GDP- and GTP-tubulin dimers with polymerization rates dependent on the nucleotide state of the terminal tubulin dimer, depolymerization rates dependent on the nucleotide state of the terminal tubulin dimer that is depolymerizing and the nucleotide tubulin dimer below it, and hydrolysis rates depending on whether the terminal tubulin dimer or an “interior”[82] tubulin dimer is being hydrolyzed. While these models were used for Monte Carlo simulations, they also allowed to calculate, for example, the probability of a growth microtubule of a certain length to depolymerize completely[84] or to compare the growth and shrinkage velocities after reducing the amount of available free GTP-tubulin dimers in experiments[52].

An important step forward was the work by Flyvbjerg et al.[86,87] in the 1990s, which incorporated different types of hydrolysis mechanisms: vectorial and random hydrolysis (which we will explain later in subsection 2.3.3). For most of their discussion, they also change from a "microscopic" view represented by the rates of individual events to a "coarse-grained" view represented by growth, shrinkage, and hydrolysis velocities with which they estimated the GTP-cap size, the catastrophe rate and more.

Despite the advances in recent years with modeling microtubules in two and three dimensions, the one-dimensional model is still used today, in particular for analytical calculations and approximations, for example for the distribution of GTP in microtubules[88–90] (also see Appendix F), to consider fluctuations in the free GTP-tubulin dimer concentration[91] or the influence of a maximum microtubule length[92], or to use master equations for the microscopic processes as a starting point[93–97] (Flyvbjerg et al.[86,87] also used a master equation in their *coarse-grained* description, similar to later research[98]). By continuously changing the free GTP-tubulin dimer concentration, hysteresis behavior was found for the average growth velocity using a one-dimensional model[99].

1.3.2 Two-Dimensional Models

The first two-dimensional model by Chen and Hill[100] is based on their previous one-dimensional modeling and considers the microtubule as a five-stranded helix. New tubulin dimers can only attach at the ends of the helices, which means that polymerization requires both a longitudinal neighbor below (i.e., in the previous helix) and a lateral neighbor on the left side (i.e., a tubulin dimer in the same helical strand). In the lateral cap model published a few years later[101–103], the same structure was used, but the polymerization of a new GTP-tubulin dimer causes the instantaneous hydrolysis of the previous GTP-tubulin dimer creating a direct coupling between polymerization and hydrolysis and a minimal cap.

An important advancement for the modeling of microtubule dynamics was to incorporate thermodynamics by VanBuren et al.[104,105] into a simple model with few parameters. They incorporated depolymerization as a thermally activated bond rupture process, which depends on the total energy of all the relevant (longitudinal and lateral) bonds that must be broken for the tubulin dimer(s) to depolymerize. The importance of the VanBuren et al. model is shown by the fact that it has been used as the basis for many other modeling efforts[106–110]. While the model by VanBuren et al. did not consider the rupture (and formation) of lateral bonds explicitly (they were automatically formed when a new tubulin dimer polymerized, and their bond energy was considered for the depolymerization rate so that longitudinal and lateral bonds ruptured at the same time during depolymerization), Margolin et al.[111–113] extended this model by explicitly considering the formation and rupture of lateral bonds as separate processes that now give rise to "cracks" between protofilaments, i.e., stretches of broken lateral bonds.

Two-dimensional models have also been used for analytical calculations and approximations for microtubules in particular or multi-stranded polymers in general[114–117].

1.3.3 Three-Dimensional Models

Following their two-dimensional model, VanBuren et al.[118] extended it to a three-dimensional model, which also incorporates mechanics like bending of tubulin dimers and longitudinal and lateral stretching[118–120]. Using a mechanical model without any polymerization and depolymerization, but with hydrolysis, the influence of different hydrolysis rules and the influence of coupling mechanics to hydrolysis, which we will also consider in this thesis, was investigated[121]. An important additional requirement for three-dimensional models with mechanics[122–124] is the need for some form of mechanical relaxation, for example via explicit energy minimization[118,122] or by explicitly simulating the thermal motion of tubulin monomers[125,126]. Instead of using explicit energy minimization, Zakharov et al.[126] use Brownian dynamics to simulate the thermal motion of tubulin dimers by which the microtubule structure relaxes and by which bonds are stretched until they are considered broken. By using such an approach, they have to use a very small time step for their Brownian dynamics simulation compared to the stochastic events like attachment and detachment of tubulin dimers, making this approach much more computationally expensive.

To investigate the mechanics of microtubules, three-dimensional models have been used in which the microtubule wall is represented as an elastic two-dimensional mesh structure[127,128]. Others have also focused on the mechanical properties of microtubules but have chosen a three-dimensional representation of the tubulin monomers instead of a mesh structure[129–131].

Starting in the 2000s, computationally expensive simulations of microtubule or microtubule parts were conducted using (near-)atom resolution based on tubulin dimer structures obtained in experiments[132,133]. One of the earliest simulation used two protofilaments with five tubulin dimers each and was able to show that longitudinal bonds between tubulin dimers are much stronger than lateral bonds[134]. Others investigated mechanical properties of tubulin monomers[135] or microtubules[136,137], for example by applying external forces on protofilaments[138] or microtubules[139]. There has also been an “intermediate” approach between a dimer-based model and a (near-)atomic representation of microtubules by modeling each tubulin monomer as multiple interacting beads to allow for (slight) form changes without having to go to the (near-)atomic resolution[140]. At the end of this thesis, in section 10.2, we will come back to some results of such models when discussing the lattice model again.

1.4 Thesis Outline

The goal of this thesis to develop, implement, and parameterize a computationally efficient three-dimensional microtubule model that combines the mechanics of the microtubule with its microscopic dynamics, i.e., the addition and removal of new tubulin dimers, the formation and rupture of lateral bonds, and the hydrolysis of GTP-tubulin dimers. In the next chapter, in chapter 2, we will describe how we model microtubules structurally and mechanically and how these two aspects are linked to the dynamics and internal changes of the simulated microtubules. This modeling builds on the author's master thesis[141]. After explaining how this model is used in a computer program to simulate microtubule growth in chapter 3, chapter 4 details the process of determining the free parameters of our model, which were introduced in chapter 2. After determining the model parameters, we show the results of full microtubule dynamics simulations with catastrophes and rescues in chapter 5 as the result of hydrolysis (with a constant rate). In chapter 6, we investigate the influence of coupling hydrolysis of GTP to GDP to the mechanics of the microtubule, and in chapter 7, we focus on selected properties of microtubules. To get an understanding for the underlying mechanisms causing catastrophes and rescues, we analyze individual microtubule trajectories in chapter 8 for both, constant hydrolysis rates and mechanical hydrolysis. Lastly, we simulate dilution experiments in chapter 9 in which the concentration of free GTP-tubulin dimer is (drastically) reduced at one point during the experiment/simulation.

Microtubule Model

2

Our microtubule model consists of three parts: the spatial microtubule structure, the energy of the microtubule that describes its mechanics, and the chemical events that can change the structure and the energy of the microtubule. In the following sections, each part will be explained, and it is highlighted how the different parts interact leading to a chemomechanical microtubule model. The static model by Müller et al.[121], which did not include polymerization and depolymerization dynamics, serves as the basis for our model.

2.1 Structural Model

The fundamental units of our structural microtubule model are tubulin monomers in form of alpha- and beta-tubulin monomers. The only difference between alpha- and beta-tubulin monomers in our model is that the GTP molecule in beta-tubulin monomers can hydrolyze to a GDP molecule. The shape of real tubulin monomers are ellipsoids with a width of 4.6 nm, a height of 4.0 nm, and a depth of 6.5 nm[58]. In our model, we represent the tubulin monomers as cylinders with radius $r_{\text{tub}} = 2\,\text{nm}$ and length $\ell_{\text{tub}} = 4\,\text{nm}$, thus we do not resolve them on an atomic or an almost atomic level[132–137,139,142–144]. The radius of the cylinders is intentionally smaller than half of the real width and depth of tubulin monomers because we will model lateral bonds between tubulin monomers in neighboring protofilaments with a finite rest length, which accounts for the difference. The next level of our structural microtubule model are tubulin dimers, which are formed by an alpha-tubulin monomer and a beta-tubulin monomer linked with an unbreakable bond. These tubulin dimers are arranged "head-to-tail", i.e., the tubulin dimers only bond at heterotypic interfaces between beta- and alpha-tubulin monomers resulting in an alternating chain of alpha- and beta-tubulin monomers (see Figure 1.3). These chains are called protofilaments. The end at which an alpha-tubulin monomer is exposed is called the "minus end", and the other end at which a beta-tubulin monomer is exposed is called the "plus end". Lastly, 13 of these protofilaments form the surface of a cylinder by arranging them parallel so that the minus ends of all protofilaments are at the same end of the microtubule, its minus end, and the plus ends of all protofilaments form the microtubule's plus end at the opposite side. As the minus end will be static during our simulations, we will be referring to the microtubules' plus end as their tip. While the protofilaments are aligned parallel, they are also positioned in a staggered way so that there is a small offset in the direction of the cylinder axis between neighboring protofilaments. These small individual offsets result in a larger offset of three tubulin monomer lengths, i.e., 12 nm, between the 13th and the first protofilament. As the offset is an odd number of tubulin monomer lengths, the lateral bonds between the 13th and the first protofilament are heterotypic, i.e., only alpha-beta lateral bonds exist in contrast to all of the other lateral interfaces at which only homotypic lateral bonds exist, i.e., only alpha-alpha and beta-beta bonds. The interface between the 13th and the first protofilament is generally refereed to as the microtubule's "seam"[145]. While there is debate[3,146–150] over whether the lateral bonds between neighboring tubulin monomers at the seam are weaker, we only include the seam as a structural component as a result of the offset and do not distinguish between lateral bonds at the seam and elsewhere. Because we use 13 protofilaments and because of the offset of three tubulin monomer lengths at the seam, this type of microtubule is referred to as a 13_3 microtubule[22]. One special property of 13_3 microtubules in contrast to other microtubule configurations like 14_3 is the absence of a skew angle of protofilaments[20–22] meaning that it is the only configurations for which the protofilaments are aligned in parallel to the cylinder axis (in absence of any protofilament bending).

Whenever we want to reference a specific tubulin monomer within the microtubule, we will use the triple (p, d, t). $p \in \{1, \ldots, 13\}$ is the index of the protofilament and $d_{\text{max}}(p)$ is the number of tubulin dimers in the protofilament. $d \in \{1, \ldots, d_{\text{max}}(p)\}$ is the index of the tubulin dimer in protofilament p, where $d = 1$ refers to the tubulin dimer at the minus end and $d = d_{\text{max}}(p)$ refers to the tubulin dimer at the plus end. Lastly, $t \in \{1, 2\}$ is the index of the specific tubulin monomer in tubulin dimer (p, d). Alpha-tubulins are indexed with $t = 1$ and beta-tubulins are indexed with $t = 2$. In the remainder of this thesis, we will also be referencing potential neighboring tubulin monomers of monomer (p, d, t): It can have two longitudinal neighbors $(p, d, t - 1)$ and $(p, d, t + 1)$ and two lateral neighbors $(p - 1, d, t)$ and $(p + 1, d, t)$. In order for this indexing to work, we additionally define

$$
\begin{aligned}
(p, d, 0) &\equiv (p, d - 1, 2), && \text{(2.1a)}\\
(p, d, 3) &\equiv (p, d + 1, 2), && \text{(2.1b)}\\
(0, d, t) &\equiv (13, d, t), && \text{(2.1c)}\\
(14, d, t) &\equiv (1, d, t). && \text{(2.1d)}
\end{aligned}
$$

When considering the lateral neighbors $(p \pm 1, d, t)$ of tubulin monomer (p, d, t), $(p \pm 1, d, t)$ should be understood *contextually* as the lateral neighbor in the previous/next protofilament. For most protofilaments this is also *literally* correct. At the seam, which is located between protofilaments $p = 13$ and $p = 1$, however, neighboring tubulin monomers differ in all three indices due to the helical shift. For example, the lateral neighbor of tubulin monomer $(13, 2, 2)$ in the first protofilament is $(1, 1, 1)$. To avoid having special cases for the seam, we simply use $(p \pm 1, d, t)$. When referencing tubulin dimers, we will omit the tubulin monomer index t and simply use (p, d).

After having explained the microtubule structure descriptively and after having established the tubulin monomer indices, we can now introduce the mathematical modeling of the microtubule structure. The basis of this modeling are vectors pointing to different points of the tubulin monomer cylinders and vectors connecting different points on the tubulin monomer cylinders with other points on the same or a different tubulin monomer cylinder. To describe the orientation of tubulin monomers, we use spherical coordinates $(\ell_{\text{tub}}, \phi, \theta)$ with the constant tubulin monomer length ℓ_{tub}, the azimuthal angle ϕ, and the polar angle θ. Whenever explicit values of angles are given in this thesis, degrees is used as their unit because we generally have an easier understanding of angles in degrees than in radian. In all calculations, however, their value in radian is used.

Each tubulin monomer is described by three vectors: the minus end vector $\boldsymbol{m}(p, d, t)$ pointing to the center of the bottom circle facing the microtubule's minus end, the plus end vector $\boldsymbol{p}(p, d, t)$ pointing to the center of the top circle facing the microtubule's plus end, and the direction vector $\boldsymbol{d}(p, d, t)$, which connects the tubulin monomer's minus end with its plus end.

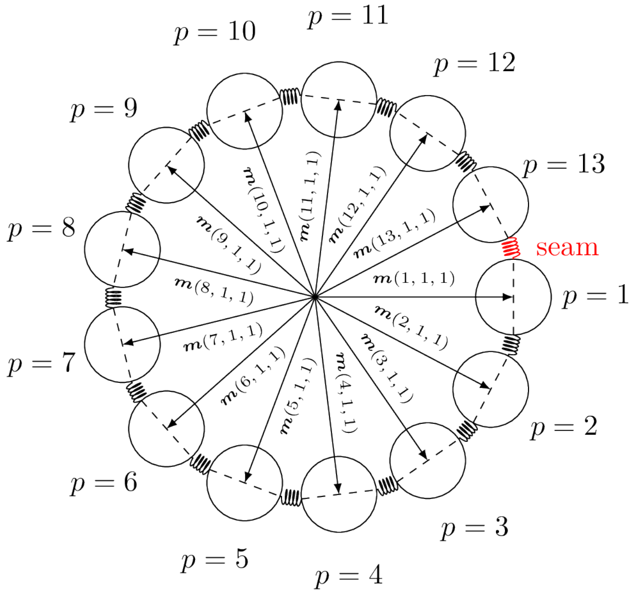

Figure 2.1: Schematic view onto the minus end of our microtubule model showing the minus end vectors $\boldsymbol{m}(p,1,1)$ of the first alpha-tubulin in each protofilament and highlighting the position of the seam.

The minus end vector of the first tubulin monomer in each protofilament is given by

$$\boldsymbol{m}(p,1,1) = \begin{pmatrix} R_{\mathrm{MT}} \cos\phi(p) \\ -R_{\mathrm{MT}} \sin\phi(p) \\ (p-1)\Delta z_{\mathrm{h}} \end{pmatrix} \tag{2.2}$$

with the average microtubule radius $R_{\mathrm{MT}} = 10.5\,\mathrm{nm}$ from the inner microtubule radius $8.5\,\mathrm{nm}$[151] and the outer microtubule radius $12.5\,\mathrm{nm}$[16,20]. (R_{MT} is the spatial average radius, while the "average radius to the dimer center of mass"[152] was determined as $11.2\,\mathrm{nm}$[152].) The minus sign in the y-component ensures the left-handed chirality of the microtubule lattice and the z-component positions the seam between protofilaments $p = 13$ and $p = 1$ (see Figure 2.1) with

$$\Delta z_{\mathrm{h}} = \frac{3}{13}\ell_{\mathrm{tub}}. \tag{2.3}$$

The azimuthal angle of all tubulin monomers in a protofilament has the same fixed value of

$$\phi(p) = 2\pi\frac{p-1}{13}. \tag{2.4}$$

Starting from these initial points, each protofilament can be regarded as a vector chain of the direction vectors

$$\boldsymbol{d}(p,d,t) = \boldsymbol{p}(p,d,t) - \boldsymbol{m}(p,d,t) = \ell_{\mathrm{tub}} \begin{pmatrix} \cos\phi(p)\sin\theta(p,d,t) \\ -\sin\phi(p)\sin\theta(p,d,t) \\ \cos\theta(p,d,t) \end{pmatrix}. \tag{2.5}$$

As $\ell_{\mathrm{tub}} = \mathrm{const}$ and $\phi(p) = \mathrm{const}$ for a given protofilament, a tubulin monomer's only degree of freedom is its polar angle $\theta(p,d,t)$, which is a crucial aspect of our microtubule modeling. As a

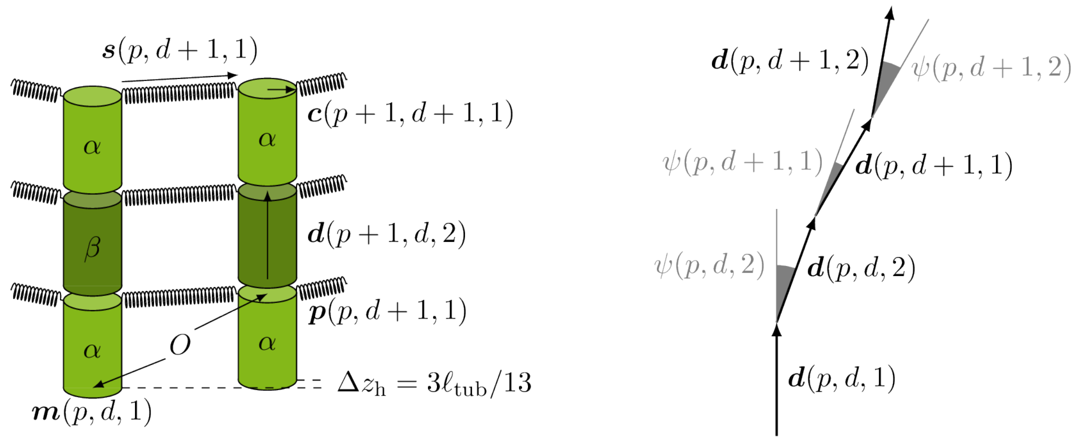

(a) Two protofilament segments with three tubulin monomers each showing the different structural vectors. (The gaps between the tubulin monomers in z-direction were only added for this illustration.)

(b) Bending angles ψ as the difference of the polar angles of successive tubulin monomers between the tubulin monomer direction vectors.

Figure 2.2: Schematic illustration of the structural vectors and bending angles.

consequence, the whole microtubule has the same number of degrees of freedom as it contains tubulin monomers.

Using (2.5), the other minus end vectors and the plus end vectors of all tubulin monomers can thus be calculated by summing the appropriate number of direction vectors:

$$\boldsymbol{m}(p, d, t) = \boldsymbol{m}(p, 1, 1) + \sum_{d'=1}^{d-1} \sum_{t'=1}^{2} \boldsymbol{d}(p, d', t') + \delta_{t,2} \boldsymbol{d}(p, d, 1), \tag{2.6}$$

$$\boldsymbol{p}(p, d, t) = \boldsymbol{m}(p, d, t) + \boldsymbol{d}(p, d, t) = \boldsymbol{m}(p, 1, 1) + \sum_{d'=1}^{d} \sum_{t'=1}^{2} \boldsymbol{d}(p, d', t') - \delta_{t,1} \boldsymbol{d}(p, d, 2). \tag{2.7}$$

Figure 2.2(a) shows a graphic illustration of the different structural vectors introduced in this section.

The length L_{proto} of protofilament p is defined as the maximum z-coordinate of all tubulin monomer in the protofilament:

$$L_{\text{proto}}(p) = \max_{d,t} \left[\boldsymbol{p}(p, d, t) \cdot \boldsymbol{e}_z \right] . \tag{2.8}$$

If the protofilament is perfectly straight, i.e., $\theta(p, d, t) = 0$ for all tubulin monomers in protofilament p (see Figure 2.3(a)), this protofilament's length is given by the z-coordinate of the plus end of the last tubulin monomer in the protofilament:

$$L_{\text{proto}}(p) = \boldsymbol{p}(p, d_{\max}(p), 2) \cdot \boldsymbol{e}_z . \tag{2.9}$$

For slightly curved protofilaments, (2.9) also holds (see Figure 2.3(b)). In contrast, for a very curved protofilament (see Figure 2.3(c)), the protofilament length will be larger than the

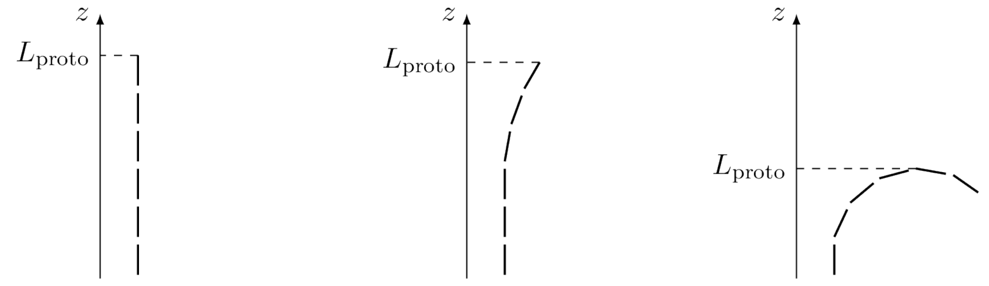

(a) Straight protofilament. **(b)** Slightly curved protofilament. **(c)** Curved protofilament.

Figure 2.3: Schematic illustration of the protofilament length (2.8) for different degrees of protofilament curvature. The gaps between the tubulin monomers are for illustration purposes only.

z-coordinate of the plus end of the last tubulin monomer in the protofilament:

$$L_{\text{proto}}(p) > \boldsymbol{p}(p, d_{\max}(p), 2) \cdot \boldsymbol{e}_z. \tag{2.10}$$

There are different experimental methods used to determine the length of a microtubule[79]: Dark field microscopy measures the microtubule length of the closed tubular part of the microtubule, thus the length of the shortest protofilament, differential-interference-contrast (DIC) microscopy measures the microtubule length as the average length of protofilaments, and optical tweezers are sensitive to the longest protofilament so that they measure the length of the longest protofilament as the microtubule length. As we will be using DIC microscopy data[49] later on, we define the length of a microtubule as the average protofilament length:

$$L_{\text{MT}} = \frac{1}{13} \sum_{p=1}^{13} L_{\text{proto}}(p). \tag{2.11}$$

Lateral bonds between neighboring tubulin monomers are modeled as elastic springs that are fixed at the edge of upper circular base of the tubulin cylinders. The connection vector from $\boldsymbol{p}(p, d, t)$ to the attachment point of the lateral bond to the next tubulin monomer $(p + 1, d, t)$ is

$$\boldsymbol{c}(p, d, t) = -r_{\text{tub}} \begin{pmatrix} \sin\phi(p) \\ \cos\phi(p) \\ 0 \end{pmatrix} \tag{2.12}$$

so that $\boldsymbol{c}(p, d, t) \perp \boldsymbol{p}(p, d, t)$ in the x-y-plane. Consequently, the connection vector from $\boldsymbol{p}(p, d, t)$ to the attachment point of the lateral bond to the previous tubulin monomer $(p - 1, d, t)$ is simply $-\boldsymbol{c}(p, d, t)$. The vectors representing the lateral bonds themselves are then given by

$$\boldsymbol{s}(p, d, t) = -\left[\boldsymbol{p}(p, d, t) + \boldsymbol{c}(p, d, t)\right] + \left[\boldsymbol{p}(p + 1, d, t) - \boldsymbol{c}(p + 1, d, t)\right]. \tag{2.13}$$

The spring vectors are defined so that $\boldsymbol{s}(p, d, t)$ points from tubulin monomer (p, d, t) to its next neighbor $(p + 1, d, t)$. The rest length s_0 of these springs can be calculated in two steps as

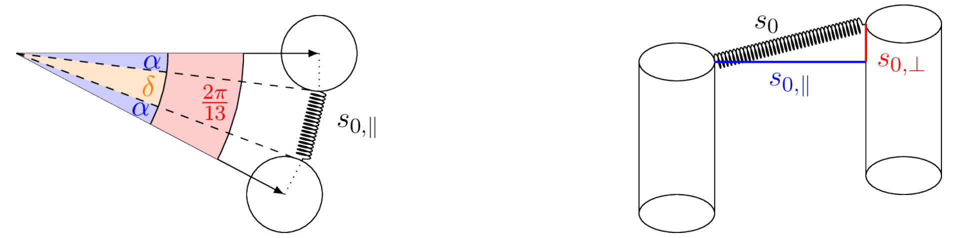

(a) Projection of a lateral spring into the x-y-plane illustrating the way to calculate $s_{0,\parallel}$.

(b) Projections of a lateral spring into the x-y-plane and onto the z-axis illustrating the way to calculate s_0.

Figure 2.4: Illustrations for the calculation of the rest length s_0 of lateral springs.

illustrated in Figure 2.4. First, we consider the projection of the spring into the x-y-plane as shown in Figure 2.4(a) and whose length is given by

$$s_{0,\parallel} = 2C \sin \frac{\delta}{2}, \tag{2.14}$$

where C is the length of the dashed lines in Figure 2.4(a) and

$$\phi = \frac{2\delta}{13} - 2\alpha. \tag{2.15}$$

The angle α (see Figure 2.4(a)) in turn can be expressed via the average microtubule radius R_{MT} and the tubulin radius r_{tub}:

$$\alpha = \arctan \frac{r_{\mathrm{tub}}}{R_{\mathrm{MT}}}. \tag{2.16}$$

From the same right triangle, it follows that

$$C = \sqrt{R_{\mathrm{MT}}^2 + r_{\mathrm{tub}}^2} \tag{2.17}$$

with which $s_{0,\parallel}$ can finally be written as[121]:

$$\begin{aligned}
s_{0,\parallel} &= 2\sqrt{R_{\mathrm{MT}}^2 + r_{\mathrm{tub}}^2} \sin\left(\frac{\pi}{13} - \arctan\frac{r_{\mathrm{tub}}}{R_{\mathrm{MT}}}\right) && (2.18)\\
&= 2\sqrt{R_{\mathrm{MT}}^2 + r_{\mathrm{tub}}^2}\frac{R_{\mathrm{MT}}}{\sqrt{R_{\mathrm{MT}}^2 + r_{\mathrm{tub}}^2}}\left(\sin\frac{\pi}{13} - \frac{r_{\mathrm{tub}}}{R_{\mathrm{MT}}}\cos\frac{\pi}{13}\right) && (2.19)\\
&= 2\sin\frac{\pi}{13}\left(R_{\mathrm{MT}} - r_{\mathrm{tub}}\cot\frac{\pi}{13}\right) && (2.20)\\
&\simeq 1.14\,\mathrm{nm}. && (2.21)
\end{aligned}$$

The projection of the spring onto the z-axis, $s_{0,\perp}$, is due to the shift between protofilaments and given by

$$s_{0,\perp} = \frac{3\ell_{\mathrm{tub}}}{13} \simeq 0.92\,\mathrm{nm}. \tag{2.22}$$

Geometric Parameter	**Symbol**	**Value**
mean microtubule radius	R_{MT}	10.5 nm
tubulin monomer radius	r_{tub}	2 nm
tubulin monomer length	ℓ_{tub}	4 nm
helical shift between protofilaments	Δz_{h}	0.92 nm
rest length of lateral springs	s_0	1.47 nm
straight equilibrium bending angle	ψ_0	0°
curved equilibrium bending angle	ψ_0	11°

Table 2.1: Geometric model parameters and their values.

Finally, the rest length of the spring is

$$s_0 = \sqrt{s_{0,\parallel}^2 + s_{0,\perp}^2} \simeq 1.47\,\mathrm{nm}. \tag{2.23}$$

Table 2.1 lists the geometric parameters introduced in this and the following section.

With the three-dimensional structure of the microtubule lattice introduced, we can now use it to define the energy of the microtubule.

2.2 Mechanical Model

There are two main contributors to the mechanical energy in our model: the stretching of lateral bonds and the bending energy of longitudinal junctions. There is also an additional repulsion energy between neighboring tubulin monomers to ensure the cylindrical shape of the microtubule. While the longitudinal intra-dimer bond between the alpha-tubulin and the beta-tubulin of the same tubulin dimer is unbreakable, the inter-dimer bond between the beta-tubulin of one tubulin dimer and the alpha-tubulin of the next tubulin dimer is breakable. As a consequence, the longitudinal inter-dimer bond is explicitly contained in our model via the longitudinal bond energy $\Delta G^{0*}_{\text{long}}$[1].

Lateral bonds are modeled as elastic springs with equilibrium energy ΔG^0_{lat} and spring constant k_{lat} so that the energy of the lateral bond connecting tubulin monomers (p, d, t) and $(p+1, d, t)$ is given by:

$$E_{\text{lat}}(p, d, t) = \Delta G^0_{\text{lat}} + \frac{1}{2} k_{\text{lat}} \left[|\boldsymbol{s}(p, d, t)| - s_0 \right]^2 . \tag{2.24}$$

If no such lateral bond exists, the implicit assumption is that $E_{\text{lat}}(p, d, t) = 0$.

Independent of the existence of a lateral bond between the two lateral neighboring tubulin monomers (p, d, t) and $(p+1, d, t)$, there is also a repulsive energy

$$E_{\text{rep}}(p, d, t) = k_{\text{rep}} \left[|\boldsymbol{p}(p, d, t) - \boldsymbol{p}(p+1, d, t)| - 2 r_{\text{tub}} \right]^{-12} \tag{2.25}$$

with the repulsion constant k_{rep}. The need for such an additional energy contribution will be detailed at the end of this section.

The last part of our mechanical model is the bending energy, which penalizes the enforced straight conformation of GDP-tubulin dimers in the microtubule lattice. To keep the model as simple as possible, the bending energy, just like the lateral spring energy, is modeled via a harmonic potential with bending constant κ:

$$E_{\text{bend}}(p, d, t) = \frac{1}{2} \kappa \left[\psi(p, d, t) - \psi_0(p, d, t) \right]^2 \equiv \frac{1}{2} \kappa \Delta\psi^2(p, d, t). \tag{2.26}$$

$\psi(p, d, t)$ is the bending angle of tubulin monomer (p, d, t) and it is the difference in the polar angle to the previous tubulin monomer $(p, d, t-1)$:

$$\psi(p, d, t) = \begin{cases} \theta(p, d, t) & \text{if } d = 1, t = 1 \\ \theta(p, d, t) - \theta(p, d, t-1) & \text{else} \end{cases} \tag{2.27}$$

so that for a tubulin monomer's bending, the tubulin-tubulin interface at its minus end is relevant (see Figure 2.2(b)). Additionally, the deviation of the bending angle from its equilibrium value

$$\Delta\psi(p, d, t) = \psi(p, d, t) - \psi_0(p, d, t) \tag{2.28}$$

---

[1] We use the same nomenclature introduced by VanBuren et al.[105] that we will come back to in the next section.

was introduced for brevity. $\psi_0(p,d,t)$ in (2.26) is the equilibrium value of the bending angle $\psi(p,d,t)$. In principle, there are different possible choices for $\psi(p,d,t)$ depending on the value of t and whether or not tubulin dimer (p,d) is hydrolyzed. Regardless of this choice, a free protofilament made up entirely by GDP-tubulin dimers must form an arc with an radius of 21 nm[67,153]. Two ways of achieving such a radius would be to set $\psi_0(p,d,2) = 22°$ and $\psi_0(p,d+1,1) = 0°$ or $\psi_0(p,d,2) = 0°$ and $\psi_0(p,d+1,1) = 22°$ if the tubulin dimer (p,d) is hydrolyzed. In the first case, there would only be intra-dimer bending, and in the second case, there would only be inter-dimer bending. Experimental data suggests, however, that there is both intra-dimer bending and inter-dimer bending[154,155]. Thus, as a consequence of tubulin dimer (p,d) being hydrolyzed, we choose a simple uniform distribution between both angles:

$$\psi_0(p,d,1) = \begin{cases} 11° & \text{if tubulin dimer } (p,d-1) \text{ is hydrolyzed} \\ 0° & \text{else} \end{cases} \tag{2.29a}$$

$$\psi_0(p,d,2) = \begin{cases} 11° & \text{if tubulin dimer } (p,d) \text{ is hydrolyzed} \\ 0° & \text{else} \end{cases} \tag{2.29b}$$

As alpha-tubulin monomers are only influenced by the hydrolysis state of the previous tubulin dimer, this choice leaves the first alpha-tubulin unaffected so that we also use $\psi_0(p,1,1) = 11°$ if tubulin dimer $(p,1)$ is hydrolyzed[2].

The total energy of a microtubule is given as the sum of all relevant energies:

$$E_{\mathrm{MT}} = \sum_{p=1}^{13} \sum_{d=1}^{d_{\max}(p)} \left(\Delta G^{0*}_{\mathrm{long}} + \sum_{t=1}^{2} \left[E_{\mathrm{lat}}(p,d,t) + E_{\mathrm{rep}}(p,d,t) + E_{\mathrm{bend}}(p,d,t) \right] \right), \tag{2.30}$$

which depends on the polar angles $\theta(p,d,t)$ of all tubulin monomers.

Our mechanical microtubule model introduces five free parameters:

1. the longitudinal bond energy $\Delta G^{0*}_{\mathrm{long}}$,
2. the lateral bond energy $\Delta G^{0}_{\mathrm{lat}}$,
3. the lateral spring constant k_{lat},
4. the lateral repulsion constant k_{rep}, and
5. the bending constant κ.

While the lateral bond energy (2.24) and the bending energy (2.26) are of significant interest as they are relevant for the lateral bond rupture process and protofilament bending, respectively, the lateral repulsion energy (2.25) was only introduced as a means to ensure a tubular structure. As a consequence, the lateral repulsion energy is of no interest when investigating the dynamics of microtubules and to avoid having k_{rep} as another free parameter in the model, it has already been previously[121] determined that setting

$$k_{\mathrm{rep}} = 10^{-6}\,\mathrm{rad}^2\,\mathrm{nm}^{-12}\kappa \tag{2.31}$$

---

[2] In hindsight, either always using $\psi_0(p,1,1) = 0°$ or $\psi_0(p,1,1) = 11°$ seems to be a more intuitive choice. In practice, however, this choice has no relevant influence as actual bending of this tubulin monomer only becomes relevant once the microtubule has already depolymerized almost completely.

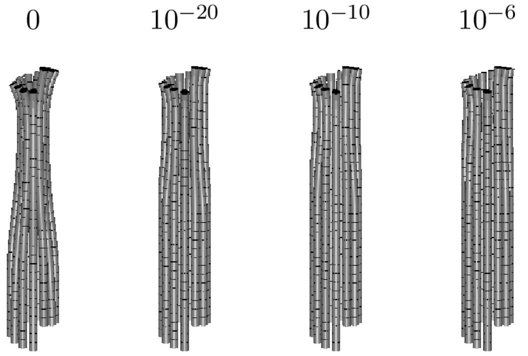

Figure 2.5: Microtubule structures for different values of k_{rep}/κ in units of $\mathrm{rad}^2\,\mathrm{nm}^{-12}$ show how the repulsion energy (2.25) is needed to avoid buckling.

results in a tubular structure while keeping k_{rep} as small as possible. The necessity of an additional repulsive energy $E_{\mathrm{rep}}(p, d, t)$ is illustrated in Figure 2.5, which shows that the protofilaments constrict and neighboring protofilaments start to overlap for $k_{\mathrm{rep}} = 0$ and that increasing k_{rep} widens the constriction until a proper tube is formed. (The VanBuren et al. model[118] did not introduce such a repulsive energy but instead enforced that their polar angles θ cannot be negative).

Due to (2.31), there are now only four free parameters left from the mechanical part of our model.

2.3 Chemical Model

During the simulation of the microtubule dynamics, different types of chemical events can occur: New GTP-tubulin dimers can attach at any protofilament (polymerization), tubulin dimers without lateral bonds can detach from any protofilament (depolymerization), lateral bonds between tubulin monomers can form or break, and the GTP molecule in tubulin dimers' beta-tubulin can hydrolyze to GDP. The polymerization and depolymerization dynamics are restricted to the microtubule's plus end, and the minus end is considered as fixed (as they are in cells at MTOCs).

2.3.1 Dimer Polymerization and Depolymerization

In general, polymerization and depolymerization reactions can be written as[156]

$$\mathrm{P}_n + \mathrm{M} \underset{k_\mathrm{off}}{\overset{k_\mathrm{on}}{\rightleftharpoons}} \mathrm{P}_{n+1}, \tag{2.32}$$

where P_n is a polymer consisting of n monomers and M is a monomer. k_on is the attachment rate of a new monomer onto the polymer, and k_off is the detachment rate of a monomer from the polymer.

The dissociation constant for a polymerization process at standard conditions, i.e., $c^0 = 1\,\mathrm{M}$, with on-rate k_on and off-rate k_off is given by[156]

$$K_\mathrm{diss} = \frac{k_\mathrm{off}}{k_\mathrm{on}} = \exp\left(\beta \Delta G^0\right), \tag{2.33}$$

where $\Delta G^0 < 0$ is the energy of the bond that is formed during polymerization and broken during depolymerization and $\beta = (k_\mathrm{B} T)^{-1}$.

In general, (2.32) is a second-order reaction for which the forward reaction rate k_on depends on the concentration of the polymers and the monomers. As the concentration of polymers is much smaller than the concentration of monomers, the concentration of polymers is assumed to be constant, and this second-order reaction simplifies to a pseudo-first order reaction. As a consequence, the attachment rate of monomers onto the polymer is only proportional to the monomer concentration:

$$k_\mathrm{on} = k_+ c, \tag{2.34}$$

where k_+ is the pseudo-first order polymerization rate. With (2.33), the detachment rate is given by

$$k_\mathrm{off} = k_+ c^0 \exp\left(\beta \Delta G^0\right). \tag{2.35}$$

During our microtubule simulation, the concentration of free GTP-tubulin dimers is $c = c_\mathrm{tub}$. This solution of individual GTP-tubulin dimers is not explicitly modeled but only represented by the concentration c_tub. It is assumed that c_tub is sufficiently large so that the decrease in c_tub due to the attachment of dimers can be neglected so that $c_\mathrm{tub} = \mathrm{const}$ during the

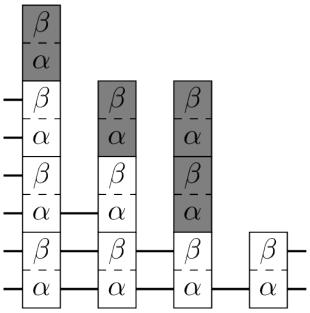

Figure 2.6: Exemplary two-dimensional representation of four protofilament plus ends of a microtubule with lateral bonds between tubulin monomers represented by black lines. Only the four tubulin dimers highlighted in gray can depolymerize because they have no lateral bonds. In the third protofilament, either only the top tubulin dimer can depolymerize by breaking its longitudinal bond to the gray tubulin dimer below it or both gray tubulin dimer can depolymerize together by breaking the longitudinal bond between the second gray tubulin dimer and the white tubulin dimer below.

simulation[3]. In contrast to a simple linear polymer, which only contains one type of bond, microtubules contain two types of bonds: longitudinal bonds between tubulin dimers in the same protofilament and lateral bonds between tubulin monomers in neighboring protofilaments. When a new tubulin dimer attaches to the tubulin dimer, we assume that only a longitudinal bond forms so that the relevant bond energy ΔG^0 for the polymerization process is the bond energy $\Delta G^{0*}_{\text{long}}$ of such a longitudinal bond. The depolymerization rate of a tubulin dimer from a protofilament is thus given by

$$k_{\text{off}} = k_+ c^0 \exp\left(\beta \Delta G^{0*}_{\text{long}}\right). \tag{2.36}$$

When a tubulin dimer attaches to the microtubule, the tubulin dimer also has to pay an entropic cost of "immobilization"[104], which was previously estimated to be between $11.8\,k_{\text{B}}T$ and $18.5\,k_{\text{B}}T$[104,157]. In reality, the value of this entropic cost depends on the surroundings of the attachment side, i.e., whether the polymerized tubulin dimer has lateral neighbors or not. However, to keep our model simple, we assume that the difference in entropic cost is negligible so that we can use the same value for all polymerization reactions. As during each polymerization reaction, a longitudinal bond is formed, the entropic cost of immobilization can be combined with the longitudinal bond energy resulting in $\Delta G^{0*}_{\text{long}}$[104].

As our model explicitly contains the formation and breakage of lateral bonds, we only allow depolymerization of laterally unbonded tubulin dimers, which also allows for the detachment of whole longitudinally connected protofilament segments as long as all of the relevant tubulin dimers are laterally unbonded (see Figure 2.6). Other models that do not consider the formation and breakage of lateral bonds explicitly[104,106–108,118,120] change the bond energy in the depolymerization rate (2.36) to the total energy of all bonds, i.e., longitudinal and lateral bonds, that need to be broken for the tubulin dimer(s) to detach.

2.3.2 Formation and Breakage of Lateral Bonds

As mentioned in section 1.2, in shrinking microtubules, protofilaments can bend outward forming "ram's horns". In order for such a process to occur, the lateral bonds between protofilaments must break illustrating why bond breakage is most likely an important process

---

[3] Walker et al.[49] use 5 µL samples with tubulin dimer concentrations of $c_{\text{tub}} = \mathcal{O}(10\,\mu\text{M})$ resulting in $\mathcal{O}(10^{13})$ tubulin dimers in the sample. A single microtubule with length $L_{\text{MT}} = 10\,\mu\text{m}$, however, only contains $\mathcal{O}(10^4)$ tubulin dimers resulting in a negligible decrease of the tubulin dimer concentration in the surrounding solution.

for catastrophes to occur. Bond formation and rupture was already previously considered in a chemical model without explicit three-dimensional mechanics[111–113]. Additionally, MD simulations of microtubules under an external force[143] showed that lateral bonds can easily reform also highlighting the need to explicitly consider the (re)formation of lateral bonds in our model.

For the formation and breakage of lateral bonds, another dissociation constant can be defined resulting in the following relation between the rate for the formation of lateral bonds k_{form} and the rate for the rupture of lateral bonds k_{rup}:

$$\frac{k_{\text{rup}}}{k_{\text{form}}} = \exp\left(\beta \Delta G^0_{\text{lat}}\right). \tag{2.37}$$

In contrast to the formation and breakage of longitudinal bonds, i.e., polymerization and depolymerization, where the bond formation rate k_{on} could be explicitly expressed as a function of the tubulin dimer concentration c_{tub}, there is no analog for lateral bonds. In general, it is possible to "split" the exponential factor in (2.37) between the formation and the breakage rate:

$$k_{\text{form}} = k_{\text{att}} \exp\left(\gamma\beta \Delta G^0_{\text{lat}}\right), \tag{2.38}$$

$$k_{\text{rup}} = k_{\text{att}} \exp\left((1-\gamma)\beta \Delta G^0_{\text{lat}}\right), \tag{2.39}$$

where k_{att} is the attempt rate to form or break a lateral bond and γ is a "load distribution factor"[158] that determines to which extent the strength of the lateral bond affects the bond formation and the bond rupture rate. To avoid introducing another parameter and to only have the bond energy dependence in the rupture process like for longitudinal bonds, we chose $\gamma = 0$:

$$k_{\text{form}} = k_{\text{att}}, \tag{2.40}$$

$$k_{\text{rup}} = k_{\text{att}} \exp\left(\beta \Delta G^0_{\text{lat}}\right). \tag{2.41}$$

Until now, we only considered lateral bonds without any external forces. In section 2.2, however, we introduced the lateral bonds as stretchable springs so that we also have to consider external forces acting on the lateral bonds. As these forces influence the bond energy, they have to be incorporated into the bond rupture rate via Bell theory[159,160]:

$$k_{\text{rup}}(p,d,t) = k_{\text{att}} \exp\left[\beta\left(\Delta G^0_{\text{lat}} + F_{\text{lat}}(p,d,t)\ell_{\text{rup}}\right)\right]. \tag{2.42}$$

F_{lat} is the force acting on the lateral bond, which is given by

$$F_{\text{lat}}(p,d,t) = \frac{\partial E_{\text{lat}}(p,d,t)}{\partial |\boldsymbol{s}(p,d,t)|} \tag{2.43}$$

for the lateral bond between tubulin monomers (p,d,t) and $(p+1,d,t)$. ℓ_{rup} is the characteristic lateral bond rupture length, which accounts for "all features of the energy landscape"[160] and which we define as the length *increase* of the lateral bonds from their rest length s_0 so that

$$\Delta G^0_{\text{lat}} + E_{\text{lat}} = 0 \qquad \Longleftrightarrow \qquad \ell_{\text{rup}} = \sqrt{\frac{-2\Delta G^0_{\text{lat}}}{k_{\text{lat}}}}. \tag{2.44}$$

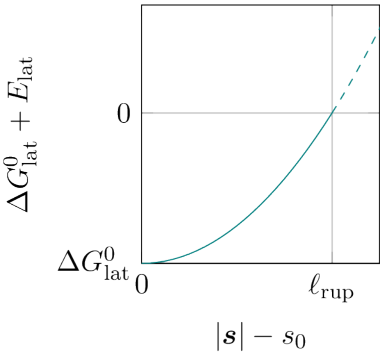

Figure 2.7: Illustration of the characteristic bond rupture length ℓ_{rup} at which the lateral spring energy E_{lat} cancels the equilibrium bond energy $\Delta G^0_{\mathrm{lat}}$.

(see Figure 2.7). If it was experimentally possible, ℓ_{rup} would be determined experimentally via the characteristic bond rupture force $(\beta\ell_{\mathrm{rup}})^{-1}$. We must highlight that the rupture rate of lateral bonds (2.42) in this form is a crucial part of the model because this is where the mechanical model represented by the lateral bond force F_{lat} and the chemical model in form of the rupture rate k_{rup} are combined making the model a chemomechanical model.

When introducing the depolymerization process in our model in subsection 2.3.1, we added no explicit dependence of the depolymerization rate (2.36) on the nucleotide state of the depolymerizing tubulin dimer or the nucleotide state of the tubulin dimer below it[112] (see discussion in section 10.2). However, as the lateral bond rupture rate (2.42) depends on the lateral bond force (2.43), there will be a different “effective” depolymerization rate for a terminal GDP-tubulin dimer with all four of its lateral bonds formed compared to a GTP-tubulin dimer in the same situation. As the GDP-tubulin dimer prefers a bent conformation and as there are no more tubulin dimers on top of it generating lattice constraints in that direction, a terminal GDP-tubulin dimer is able to bent outward resulting in stretched lateral bonds, which makes it more likely for them to rupture. In contrast, a GTP-tubulin dimer can stay in its preferred straight conformation without any external forces on it, and it itself will thus not cause any lateral bond stretching and thus generally have more stable lateral bonds. As a consequence, the overall depolymerization process of lateral bond rupture followed by the longitudinal bond rupture is on average easier for terminal GDP-tubulin dimers than for terminal GTP-tubulin dimers.

Until now, we have only discussed the rates with which lateral bonds can form and rupture. We have, however, not discussed where bonds can form and rupture. In principle, it would be possible to allow bonds to form wherever a tubulin monomer has a lateral neighbor with which it has not already formed a lateral bond and to allow any existing lateral bond to break. We have, however, already mentioned that rupture of lateral bonds at the microtubule tip allows protofilaments to bend outward and form ram’s horns. Only the existence of lateral bonds below the starting point of the bent protofilament part stops the bending. At this interface between existing and ruptured lateral bonds, the bond rupture forces will be the highest so that here, bonds would rupture predominantly creating a zipper-like mechanism for rupture. On the simulation side, having any bond potentially rupture causes a significant slowdown of the simulation for long microtubules as for each bond, the lateral spring forces must be determined to calculate the rupture rate. As a consequence, we only allow one of the lateral bonds between

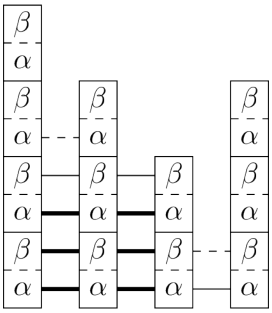

Figure 2.8: Exemplary two-dimensional representation of four protofilament plus ends of a microtubule with lateral bonds between tubulin monomers that cannot rupture represented by thick black lines, lateral bonds that can rupture represented by thin black lines, and lateral bond that can form represented by dashed lines.

two protofilaments to rupture: the bond closest to the plus end. Consequently, we also only allow the formation of a lateral bond above an existing lateral bond. These rules result in one continuous stretch of formed bonds starting at the minus end, which can be followed by a stretch where no lateral bonds exist at the plus end as illustrated in Figure 2.8. Having such a rupture rule for lateral bonds results in at most 13 bond rupture rates to be calculated (one per protofilament) instead of one rupture rate for each tubulin monomer making the required runtime for these calculations independent of the microtubule length.

2.3.3 Hydrolysis

The last chemical process included in our model is the hydrolysis of GTP-tubulin dimers into GDP-tubulin dimers. It was already found out quite early that tubulin dimers have two binding sites for GTP and that at one site the GTP is exchangeable ("E site") and at the other site, it is generally not exchangeable ("N site")[34,161–163]. Later, it was revealed that GTP at the E site hydrolyzes to GDP while microtubules grow[36,162,164,165] and that the E site is located in the beta-tubulin of the tubulin dimer[165,166]. While hydrolysis can be described as a first-order reaction[167], it was also shown that hydrolysis consists of two parts, the cleavage of the inorganic phosphate P_i followed by its release[168–171]:

$$\mathrm{GTP} \longrightarrow \mathrm{GDP} \cdot \mathrm{P}_i \longrightarrow \mathrm{GDP} + \mathrm{P}_i. \tag{2.45}$$

As in the other computational models mentioned before, we do not consider the intermediate state $\mathrm{GDP} \cdot \mathrm{P}_i$, but instead, we will only consider a simplified hydrolysis model

$$\mathrm{GTP} \longrightarrow \mathrm{GDP} + \mathrm{P}_i \tag{2.46}$$

because we want to introduce as few model parameters as possible and (2.46) only requires one rate constant while (2.45) would require two rate constants and we would also have to consider the $\mathrm{GDP} \cdot \mathrm{P}_i$-state in addition to the GTP- and the GDP-state. (Manka et al.[172] were able to investigate the $\mathrm{GDP} \cdot \mathrm{P}_i$-state, and they found structural differences, which we will discuss briefly in section 10.2.) Almost the entire energy released during the whole hydrolysis process (estimated as $4.7\,k_\mathrm{B}\,T$[173]) is believed to be stored in the microtubule lattice[173], which is then released by protofilaments bending outward during shrinkage. It has been shown that the bent protofilaments are indeed able to produce work by moving nearby beads held in laser traps[174,175] and by pulling the chromosomes apart during mitosis[176].

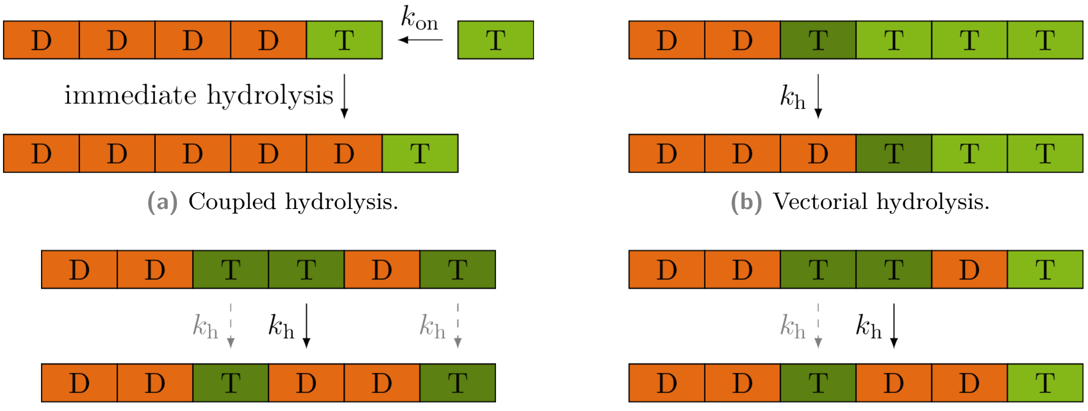

(a) Coupled hydrolysis.
(b) Vectorial hydrolysis.
(c) Random hydrolysis.
(d) Coupled random hydrolysis.

Figure 2.9: Schematic illustration of the different hydrolysis models in which only the dark tubulin dimers ("T") are allowed to hydrolyze. Actual hydrolysis events are represented by black arrows, while other possible events are represented by dashed gray arrows. (A similar figure was published by Bowne-Anderson et al.[79].)

There are different rule sets that can be applied to hydrolysis dictating which GTP-tubulin dimers are allowed to hydrolyze and which ones are not[79]. The coupled hydrolysis model (see Figure 2.9(a)) postulates that hydrolysis happens immediately after a tubulin dimer polymerizes on top of it[177] creating a maximum GTP-cap length of one tubulin dimer. In the vectorial hydrolysis model (see Figure 2.9(b)), only the GTP-tubulin dimer directly at the GDP-body/GTP-cap interface is allowed to hydrolyze resulting in a continuous GDP-body followed by a continuous GTP-cap. In the random hydrolysis model (see Figure 2.9(c)), any GTP-tubulin dimer is allowed to hydrolyze leading to a GDP-dominated body and a "porous" GTP-cap in which there are GTP-tubulin dimers and GDP-tubulin dimers. It is also possible to combine models like allowing vectorial and random hydrolysis at the same time[87] so that there are different hydrolysis rates at the GDP/GTD-interfaces and inside of GTP islands or to combine random and coupled hydrolysis (see Figure 2.9(d)) so that hydrolysis is random except for terminal GTP-tubulin dimers that cannot hydrolyze[92]. The idea that a terminal GTP-tubulin dimer cannot hydrolyze is due to experimental results that the formation of a longitudinal bond during the polymerization of a new tubulin dimer onto the terminal GTP-tubulin dimer catalyzes the hydrolysis reaction in the now second-to-last tubulin dimer[58,162]. Structural data has shown that the residue in the alpha-tubulin connecting to the "catalytic pocket"[78] of the previous beta-tubulin relevant for hydrolysis is missing in the beta-tubulin explaining why the GTP molecule in the alpha-tubulin does not hydrolyze[78,178].

In our model, hydrolysis is included as a stochastic process with constant rate k_{h} (a non-constant hydrolysis rate will be discussed in subsection 2.3.4), and we will use a slightly altered variant of the coupled random hydrolysis model: We also allow terminal GTP-tubulin dimers to hydrolyze if they ever had another tubulin dimer on top of them as illustrated in Figure 2.10. The value of k_{h} will be discussed in section 5.1.

While there is no feedback of the microtubule's mechanics on the hydrolysis rate k_{h}, hydrolysis in turn influences the mechanics as hydrolysis changes the rest bending angle ψ_0, see (2.29).

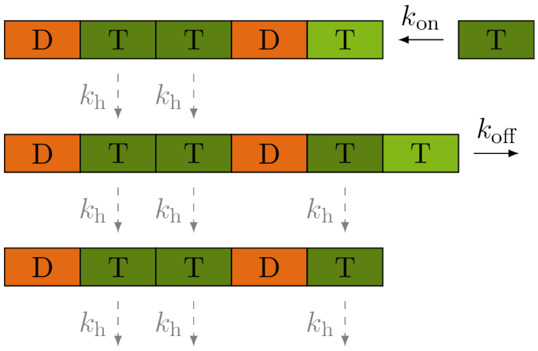

Figure 2.10: Coupled random hydrolysis model used in our simulation, where a terminal GTP-tubulin dimer can hydrolyze if it ever had another tubulin dimer on top of it. (Possible hydrolysis reactions are marked by the vertical dashed arrows with "k_{h}".)

In the next section, we will discuss an approach in which there is explicit feedback of the mechanical modeling on the hydrolysis rate resulting in a non-constant hydrolysis rate that becomes tubulin dimer-dependent.

2.3.4 Hydrolysis With Mechanical Feedback

It was already proposed previously by Müller et al.[121] to couple the hydrolysis to the mechanics of the microtubule resulting in different hydrolysis rates for different tubulin dimers. Before we discuss the coupling of hydrolysis and mechanics further, we should go back to bond rupture processes for a moment and consider a bond at different lengths: At its equilibrium length, the bond is in an energetic minimum, and if it is stretched beyond a certain length, it is energetically more favorable for the bond to rupture. In between these two extremes, there is an energy barrier that must be overcome before the bond ruptures (see Figure 2.11(a))[4]. From the perspective of the stochastic bond rupture process, the height of this energy barrier determines the rupture rate: the higher the barrier, the smaller the rupture rate. As a result, the bond length can be regarded as the "reaction coordinate" for the bond rupture process.

The idea when coupling hydrolysis and mechanics is to also apply the same general principle of activation over an energy barrier dynamics that we use in bond rupture processes to the hydrolysis reaction. In our modeling, the equilibrium value of the bending angle ψ_0 differs between GTP-tubulin dimers and GDP-tubulin dimers, see (2.29). The fact that hydrolysis of one tubulin dimer (p, d) affects the equilibrium value of two bending angles $\psi_0(p, d, 2)$ and $\psi_0(p, d+1, 1)$ will be neglected for now while we introduce the concept of the coupling mechanism. Instead, we will focus on one bending angle for now and will come back to the two angles later on.

During the hydrolysis process, the equilibrium bending angle value changes from $\psi_0 = 0°$ (GTP) to $\psi_0 = 11°$ (GDP) making it the perfect candidate for the reaction coordinate of the hydrolysis reaction. However, in contrast to the bond length in the bond rupture process, the value of ψ_0 does not change continuously but can only be $\psi_0 = 0°$ or $\psi_0 = 11°$. This case of two distinct states is equivalent to the bond rupture process in the absence of external forces (bond at

---

[4] We simplified the energy for the lateral bond in (2.24) by only considering the harmonic approximation around the energy minimum.

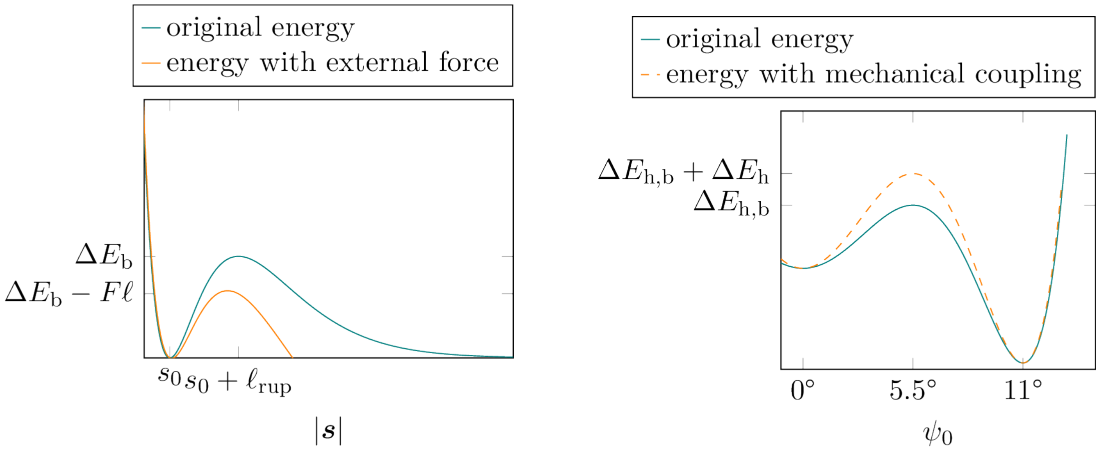

(a) Exemplary more realistic bond energy profile and altered bond energy profile due to an external force, which decreases the height of the energy barrier ΔE_b.

(b) Exemplary hydrolysis reaction energy profile and altered hydrolysis reaction energy profile due to coupling to mechanics changing the height of the energy barrier $\Delta E_\mathrm{h,b}$.

Figure 2.11: Schematic illustration of the similarity between external forces changing the height of a bond rupture energy barrier and how our coupling of the hydrolysis to the microtubule energy changes the height of the energy barrier for the hydrolysis reaction.

equilibrium length or bond is broken) so that it is only a thermally activated process. We postulate that between the straight and curved conformations at $\psi_0 = 0°$ and $\psi_0 = 11°$, there is also a rate-limiting barrier at an intermediate value of ψ_0 (see Figure 2.11(b)). Neither the position nor the height of this barrier is known, which are both irrelevant for the modeling of the hydrolysis reaction with a constant rate as they are both implicitly included in the hydrolysis rate k_h.

Going back to the bond rupture process, we have seen that an external force changes the bond rupture rate (2.42) by changing the energy landscape and decreasing the energy barrier that must be overcome (see Figure 2.11(a)). The external force, in this case, causes bonds to stretch and thus moving the bond length closer to the value at which it would rupture. As already mentioned, the reaction coordinate for hydrolysis, the rest bending angle ψ_0, cannot be changed continuously (in our model), but we can use the actual bending angle ψ in the following sense: We propose that the closer the actual bending angle ψ of a GTP-tubulin dimer is to the rest bending angle of a GDP-tubulin dimer $\psi_0 = 11°$, the easier it is for the tubulin dimer to hydrolyze. Vice versa, and we will see later on that this is actually the more relevant case, if the bending angle ψ of one tubulin dimer is further away from $\psi_0 = 11°$ (compared to the average bending angle ψ of all GTP-tubulin dimers), it will decrease the hydrolysis rate of this GTP-tubulin dimer.

As a starting point for coupling hydrolysis to the microtubule mechanics, the hydrolysis rate of tubulin dimer (p, d) can be written as

$$k_\mathrm{h}(p,d) = k_\mathrm{h}^0 \exp\left(-\beta \Delta E_\mathrm{h}(p,d)\right), \tag{2.47}$$

where k_h^0 is a constant base hydrolysis rate (which differs from the constant hydrolysis rate

k_h if hydrolysis is not coupled to mechanics, see below) and $\Delta E_\mathrm{h}(p,d)$ describes the change in the energy barrier, which the hydrolysis reaction must overcome, due to the coupling to mechanics. The goal of the following discussion is to explain how we calculate $\Delta E_\mathrm{h}(p,d)$ in our simulation. Before we can do that, however, we have to discuss the energy barrier for hydrolysis if $\Delta E_\mathrm{h}(p,d) = 0$. We have already mentioned that we have no information about the hydrolysis energy profile, except for the values of the GTP rest bending angle ($\psi_0 = 0°$) and the GDP value ($\psi_0 = 11°$). We assume that the barrier is centered between these values at $\psi_{0,\mathrm{b}} = 5.5°$ with height $\Delta E_\mathrm{h,b}$. This default height $\Delta E_\mathrm{h,b}$ of the energy barrier is already included in k_h^0 and thus does not have to be considered anymore. What we have to consider, however, is how the coupling changes the height of the energy barrier. To calculate this change in barrier height ΔE_h, we consider the microtubule energy (2.30) now as a function of the relevant rest bending angle ψ_0 with constant polar angles $\{\theta(p,d,t)\}$. As a consequence, ΔE_h is given as the energy difference of the microtubule energy for $\psi_0 = 5.5°$ (the position of the energy barrier) and $\psi_0 = 0°$ (the straight GTP conformation):

$$\Delta E_\mathrm{h} = E_\mathrm{MT}\left[\psi_0 = 5.5°\right] - E_\mathrm{MT}\left[\psi_0 = 0°\right]. \tag{2.48}$$

Now that we have established the basic principles of how we couple hydrolysis and mechanics, we have to come back to the fact that hydrolysis of tubulin dimer (p,d) changes $\psi_0(p,d,2)$ and $\psi_0(p,d+1,1)$, which changes (2.48) to

$$\begin{aligned}\Delta E_\mathrm{h}(p,d) = E_\mathrm{MT}&\left[\psi_0(p,d,2) = 5.5°, \psi_0(p,d+1,1) = 5.5°\right] \\ &- E_\mathrm{MT}\left[\psi_0(p,d,2) = 0°, \psi_0(p,d+1,1) = 0°\right].\end{aligned} \tag{2.49}$$

As the only part of the microtubule energy (2.30) that depends on ψ_0 is the bending energy (2.26), we do not have to calculate a "global" energy change as given by (2.49), but we only have to calculate a "local" bending energy change for two tubulin monomers:

$$\begin{aligned}\Delta E_\mathrm{h}(p,d) = \frac{1}{2}\kappa\Big[&(\psi(p,d,2) - 5.5°)^2 - \psi^2(p,d,2) \\ &+ (\psi(p,d+1,1) - 5.5°)^2 - \psi^2(p,d+1,1)\Big]\end{aligned} \tag{2.50}$$

$$= \frac{1}{2}\kappa\left[-11° \cdot (\psi(p,d,2) + \psi(p,d+1,1)) + 2\cdot(5.5°)^2\right]. \tag{2.51}$$

Equation (2.51) explicitly shows that, indeed, larger bending angles will result in a smaller energy barrier ΔE_h and thus a larger hydrolysis rate.

For the hydrolysis of the terminal GTP-tubulin dimer $(p, d_\mathrm{max}(p))$, (2.51) has to be adjusted because in this case, the hydrolysis reaction only affects $\psi_0(p, d_\mathrm{max}(p), 2)$ because there is no tubulin dimer on top of a terminal tubulin dimer and thus no alpha-tubulin monomer $\psi_0(p, d_\mathrm{max}(p)+1, 1)$ exists:

$$\Delta E_\mathrm{h}(p, d_\mathrm{max}(p)) = \frac{1}{2}\kappa\left[-11°\cdot\psi(p, d_\mathrm{max}(p), 2) + (5.5°)^2\right]. \tag{2.52}$$

With (2.51) and (2.52) explicitly written out, we now also see that the base hydrolysis rate k_h^0 in (2.47) is not the hydrolysis rate for perfectly straight tubulin monomers ($\psi(p,d,2) = \psi(p,d+1,1) = 0°$), because of the additional $\kappa(5.5°)^2$ term in (2.51) and $\frac{1}{2}\kappa(5.5°)^2$ term in (2.52). As these terms differ whether the relevant GTP-tubulin dimer is terminal or not and because they depend on another model parameter, the bending constant κ, they cannot simply be included in k_{h}^{0}.

Before we continue, we have to discuss the implications of having to calculate the energy barrier for the terminal GTP-tubulin dimer (2.52) separately. The underlying reason is that our model contains intra-dimer and inter-dimer bending affecting $\psi_0(p, d, 2)$ and $\psi_0(p, d + 1, 1)$, respectively, during hydrolysis. The relevant part here is the inter-dimer bending that affects $\psi_0(p, d+1, 1)$ so that every model coupling hydrolysis and mechanics like here and that includes inter-dimer bending will have to consider the terminal GTP-tubulin dimer separately. Only models with intra-dimer bending only could use the same formula for the change ΔE_{h} in the hydrolysis energy barrier. On the practical side, the hydrolysis reaction of a GTP-tubulin dimer buried in the microtubule has to overcome an energy barrier that depends on two tubulin monomers, see (2.51), while for a terminal GTP-tubulin dimer, the energy barrier only depends on one tubulin monomer, see (2.52), which results in a smaller energy barrier and thus a higher hydrolysis rate. In section 6.2, we will see that this bias for higher hydrolysis rates at the tip manifests itself in our simulation data.

Lastly, we come back to how the mechanical model and the chemical model are connected. In the previous section on the constant hydrolysis rate k_{h}, we mentioned that there is a unidirectional feedback of the hydrolysis reaction on the mechanical model by changing ψ_0. In this section, we have extended the feedback to be bidirectional as the mechanical model now also influences hydrolysis by modulating the hydrolysis rate (2.47).

To avoid having to refer to “the hydrolysis model in which the hydrolysis rate is coupled to the mechanics of the microtubule”, we will simply use “mechanical hydrolysis” in the following.

Symbol	Parameter
$\Delta G^{0*}_{\text{long}}$	longitudinal bond energy
$\Delta G^{0}_{\text{lat}}$	lateral bond energy
k_{lat}	lateral spring constant
κ	bending constant
k_{+}	pseudo-first-order polymerization rate
k_{att}	lateral bond attempt rate
k_{h}	constant hydrolysis rate
k^{0}_{h}	base hydrolysis rate for mechanical hydrolysis

Table 2.2: The seven free parameters of our model. The two hydrolysis rates only count as one parameter as only one of them is used in a specific simulation.

2.4 Summary

Table 2.2 shows all of the free parameters that were introduced in the previous sections of this chapter. In order to determine the values of all seven of them, we need the same number of values from experiments. We can already pre-empt that fixing the values of all parameters will not be possible, but we will fix as many as possible in chapter 4 (the hydrolysis rates will be discussed later in chapter 5 and chapter 6). But before we can determine these values, we have to explain how the simulation that implements the microtubule model introduced in this chapter actually works.

Microtubule Simulation

3

3.1 Gillespie Algorithm

Let us for a moment consider the phenomenological four parameter microtubule model shown in Figure 3.1 in which the microtubules only have two properties: their length $L_{\mathrm{MT}} \geq 0$ and their state, which can either be "growing" or "shrinking". The four parameters of the model are the state velocities, the growth velocity $v_{\mathrm{gr}} > 0$ and the shrinkage velocity $v_{\mathrm{sh}} < 0$, and the transition rates between the states, the catastrophe rate ω_{cat} and the rescue rate ω_{res}. One approach to simulate the microtubule growth dynamics is to discretize time into sufficiently short intervals of length Δt so that $\omega_{\mathrm{cat}}\Delta t$ is the probability for a growing microtubule to switch to shrinking within Δt and $\omega_{\mathrm{res}}\Delta t$ is the probability for a shrinking microtubule to switch to growing within Δt. If a microtubule starts in its growing state with length L_{MT}, the next step in a four parameter model simulation would be to draw a uniformly distributed random number from $[0, 1]$ and compare it with the probability of the microtubule switching its state to shrinking, $\omega_{\mathrm{cat}}\Delta t$. If the random number is smaller than the catastrophe probability, the state is switched. Otherwise, the microtubule length is increased by $v_{\mathrm{gr}}\Delta t$. The same procedure is used if the microtubule is in its shrinking state though now the probability for state switching is $\omega_{\mathrm{res}}\Delta t$, and the length increase per time interval is $v_{\mathrm{sh}}\Delta t$. Additionally, the shrinking state has a boundary condition with regard to the microtubule length as $L_{\mathrm{MT}} < 0$ is not possible so that if such a case would happen, the microtubule would automatically switch back into its growing state.

While this approach works perfectly fine and in some instance has to be used[126], for example if the microtubules are coupled to another system that also has dynamics calculated in Δt time intervals, one major drawback of the approach is the fact that due to the small catastrophe and rescue rates, in the majority of time steps, the microtubule will simply continue being in its current state. In other words: Most checks if the microtubule switches its state are effectively done for nothing but, on the other hand, have to be done to ensure that $\omega_{\mathrm{cat}}\Delta t$ and $\omega_{\mathrm{res}}\Delta t$ can be interpreted as transition probabilities. A more effective approach would be to determine the periods of time during which the microtubule stays in its current growth state and after

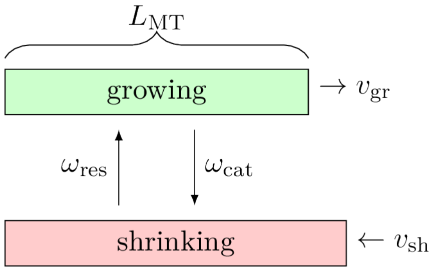

Figure 3.1: Schematic illustration of the four parameter model of microtubules in which microtubules are one-dimensional objects of a certain length L_{MT} and growth state.

which the microtubule switches its state[1]. This is were the Gillespie algorithm[179,180] comes into play.

Gillespie introduced a new method to simulate multiple chemical reactions that can occur simultaneously. In his derivation, he explicitly considered that in order to calculate the probability at time t that the next reaction will occur in the interval $[t + \Delta t, t + \Delta t + \mathrm{d}t]$ and that it will be one specific reaction of all of the possible reactions, the first step is to calculate the probability of *no* reaction occurring in the interval $[t, t + \Delta t]$. It is then the second step to calculate the probability that the relevant reaction will occur in the interval $[t + \Delta t, t + \Delta t + \mathrm{d}t]$. He presented two methods to implement its algorithm: the direct method and the first reaction method. We use the first reaction method as it is more intuitive to understand: It requires you to calculate "tentative reaction times"[179] for each possible event with rate k_i according to

$$t_i = \frac{1}{k_i} \ln \frac{1}{r} \tag{3.1}$$

were r is a uniformly distributed random number from $(0, 1)$. As the name "first reaction method" indicates, the event i with the smallest reaction time t_i is implemented, and the simulation time is advanced by t_i. While (3.1) stems from a simple exponential distribution, Gillespie emphasizes and proves as well that this approach also considers the probability that no other event happens in the meantime. Additionally, it is important to note that the tentative reaction times (3.1) must be recalculated in each iteration of the simulation because the rates change after a chemical reaction due to the changed number of molecules of each type after the previous reaction and, in our case, due to the changed configuration of the microtubule.

Before we turn to the complete simulation procedure using the Gillespie algorithm in the next section, we want to note that depending on the context, the Gillespie algorithm is also called a "rejection-free kinetic Monte Carlo method"[181]. "Rejection-free" refers to the fact that all events are successful, compared to, for example, the Metropolis algorithm where proposed events can be rejected with a certain probability, and "kinetic" highlights the goal of the method to simulate the time evolution of a system[181].

---

[1] In the four parameter model, the determined time interval for shrinking microtubules might be longer than $|L_{\mathrm{MT}}/v_{\mathrm{sh}}|$. In such cases, the rescue would happen "too late" (resulting in an unphysical negative length) and instead, the microtubule would shrink to $L_{\mathrm{MT}} = 0$ and a forced rescue would happen.

3.2 Simulation Procedure

The procedure implemented by us to simulate microtubule dynamics consists of two parts: the initialization and the event loop. The simulation initialization itself consists of two steps:

1. A microtubule with 13 protofilaments and N_{GDP} GDP-tubulin dimers followed by N_{GTP} GTP-tubulin dimers per protofilament is initialized. The $26(N_{\mathrm{GDP}} + N_{\mathrm{GTP}})$ polar angles $\{\theta(p, d, t)\}$ are initially set to $\theta(p, d, t) = 0°$.
2. To obtain the "real" initial structural configuration of the microtubule, its energy (2.30) is minimized with respect to the polar angles $\{\theta(p, d, t)\}$.

Once the simulation is initialized, it enters the event loop:

3. All of the *possible* events that were discussed in section 2.3 are determined, i.e., polymerization events for each protofilament, depolymerization events for all laterally unbonded tubulin dimers, at most one lateral bond formation and one rupture event per protofilament, and hydrolysis events for all GTP-tubulin dimers that are allowed to hydrolyze. Based on each event's rate k_i, its tentative reaction time t_i is calculated via (3.1), and the event with the shortest reaction time t_i, as described in section 3.1, is executed. Lastly, the simulation time t_{sim} is advanced by t_i.
4. As the executed event has changed the microtubule's configuration and thus its energy, its equilibrium configuration has also changed and needs to be restored. We assume that all of the conformational changes due to the executed event, like tubulin monomers bending due to a broken lateral bond, happen much faster than the chemical microtubule dynamics[118]. As a consequence, we minimize the microtubule's energy immediately after the shortest event is executed resulting in an instantaneous relaxation of the microtubule lattice. Explicitly simulating this relaxation process is computationally very expensive and will be discussed in section 3.3.
5. If the simulation time t_{sim} has exceeded the maximum simulation time t_{max} set for the simulation, the simulation ends. A second possibility for the simulation to end gracefully[2] is if any protofilament only contains one tubulin dimer, i.e., if the microtubule has shrunken almost completely. The reason to end on only one tubulin dimer in any protofilament instead of zero tubulin dimers is a practical one to extract the shrinkage velocity v_{sh} from simulations where the microtubule is only shrinking: In such simulations, the microtubule length L_{MT} decreases linearly with the simulation time t_{sim} so that the shrinkage velocity v_{sh} can be determined via a linear fit from the $(t_{\mathrm{sim}}, L_{\mathrm{MT}})$ data points automatically without any manual interference. In some instances, however, it can take the last GDP-tubulin dimer of a protofilament longer to depolymerize because there is no additional GDP-tubulin dimer below it, which would exert an additional bending moment. Consequently, the lateral bonds of the terminal tubulin dimer are stretched less resulting in smaller forces on the lateral bond making it less likely to rupture. As we are interested in the overall dynamics of microtubules, not specifically nucleation[182] or processes at the nucleation site from which the microtubule grows, we can simply regard this terminal

---

[2] in contrast to simulations running on clusters on which they can also be terminated by the scheduler if they have exceeded their allocated maximum runtime

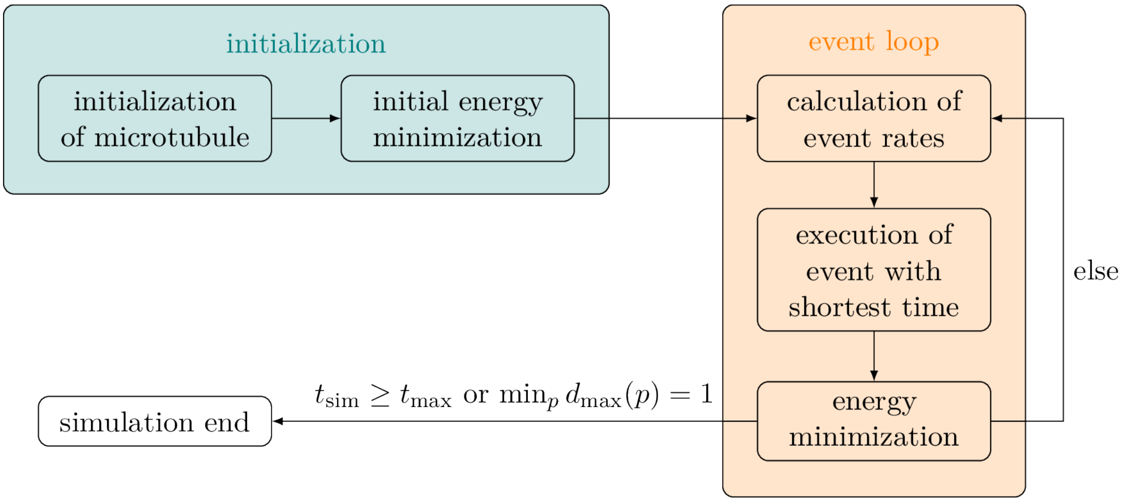

Figure 3.2: Flow chart of the different major steps of the simulation procedure.

layer as a seed on which the dynamic part of the microtubule grows. (Having a seed is an actual technique used in some experiments[56,57] and also in simulations[120].)

Figure 3.2 illustrates these steps in a flow chart. The distinction between the initial energy minimization and the energy minimization in the event loop will become clear in section 3.3. Some further details on the actual implementation of the simulation in C++ are presented in Appendix A.

As energy minimization is a crucial part of the simulation, we will discuss it in more detail in the following section.

3.3 Energy Minimization

We use the GNU Scientific Library (GSL)[183] for minimization, which provides the following minimization algorithms that use the gradient of the relevant function[3]:

1. `steepest_descent` implements the steepest descent algorithm, which “follows the downhill gradient of the function at each step”[183].
2. `conjugate_fr` implements the Fletcher–Reeves version of the conjugate gradient algorithm, which chooses its direction vectors more intelligently than the steepest descent algorithm resulting in better performance.
3. `conjugate_pr` implements the Polak–Ribiere version of the conjugate gradient algorithm and differs from the Fletcher–Reeves version by a different value of an internal parameter.
4. `bfgs` implements the Broyden–Fletcher–Goldfarb–Shanno (BFGS) algorithm, a quasi-Newton algorithm that calculates approximations of the second derivative using the gradient.
5. `bfgs2` is an improved implementation of the BFGS algorithm with better performance.

All methods expect a C++ function that returns the function value for a given set of coordinates, in our case the microtubule energy (2.30), and a C++ function that returns the gradient for a given set of coordinates, which we have implemented analytically (see Appendix B for the analytical calculation of the gradient). Figure 3.3 compares the performance of the different algorithms by minimizing the microtubule energy (2.30) of an initial GDP-only microtubule. The results clearly show that the improved version of the BFGS algorithm, `bfgs2`, performs the best, thus it is used in our simulation[4].

One major concern with the energy minimization part of our simulation is its runtime as the simulations generally spend more than 90 % of their runtime with energy minimization (see section 6.4). If we consider a microtubule in which each protofilament consists of N_{GDP} GDP-tubulin dimers and N_{GTP} GTP-tubulin dimers, then there are $26(N_{\text{GDP}} + N_{\text{GTP}})$ minimization parameters the minimization algorithm has to use. As a consequence, as the microtubule grows, the number of minimization parameters increases as well, which in turn slows down the minimization. This slowdown of the simulation makes realistic microtubule simulations with long growth phases interrupted by catastrophes and rescues unrealistic (without each simulation requiring a prohibitive amount of runtime). In order to simulate long microtubules without runtime penalties, we have to evaluate strategies to restrict the energy minimization to not (significantly) slow down for longer microtubules. In contrast to a full minimization of all minimization parameters, a restricted minimization will lead to a worse result. The goal is to find an approach that balances the required runtime for minimizations with the quality of the minimization result. At this point, we can now go back to the difference between the initial energy minimization and the energy minimization in the event loop (see Figure 3.2). To ensure a proper initial microtubule configuration, the initial energy minimization will always

---

[3] in contrast to another class of minimization algorithms that only needs the function used for minimization

[4] We use the recommended[183] tolerance parameter value for the line search of 0.1, a maximum gradient norm of 0.1, and a maximum number of iterations per minimization of 100 000.

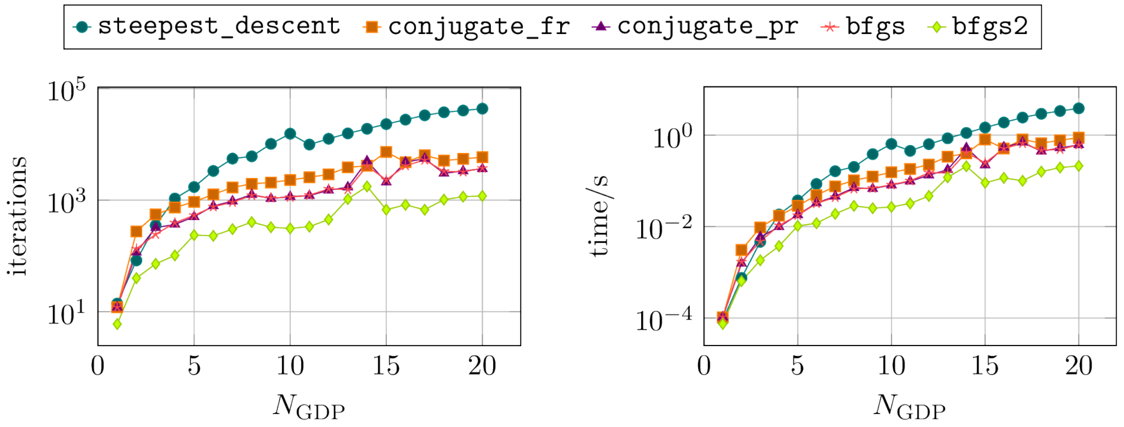

(a) Comparison by the number of minimization iterations.

(b) Comparison by the runtime.

Figure 3.3: Comparison of the different minimization algorithms to minimize the initial microtubule as a function of the number of the GDP-tubulin dimers N_{GDP} per protofilament (with $N_{\mathrm{GTP}} = 0$). The simulations were run on one core of an Intel Xeon E5-1620 v3 CPU and the program was compiled with g++ in version 8.2.0 using `-O3`, `-ffast-math`, and `-march=native`.

be unrestricted[5]; the restrictions discussed next only apply to the energy minimization in the event loop.

There are two possible types of restrictions we considered and evaluated:

1. restricting the number of iterations per minimization,
2. restricting the number of minimization parameters.

The first approach effectively results in many incomplete minimizations that would normally require further iterations. This approach, however, only solves one of the two reasons for slowdown of the minimizations for longer microtubules: the increased number of minimization iterations. The second reason for the slowdown is having to consider the whole microtubule when calculating the energy and gradient in each minimization step. This problem is not solved by the first approach, and because of the combination of a restricted number of available minimization iterations for an increasing number of parameters, the quality of the minimization might also suffer. In contrast, the second approach solves both of these issues: By only considering a subset of the minimization parameters, only a part of the microtubule has to be considered, which avoids iterations over the whole microtubule lattice, which in turn then also restricts the number of minimization iterations necessary to minimize the microtubule energy with respect to this subset of parameters. Already from this short qualitative discussion, the second approach is better than the first one.

We have, however, still to define how we restrict the number of minimization parameters in the second approach. The subset of considered tubulin dimers can be restricted to a certain

---

[5] In reality, even for “unrestricted” minimization, there is an upper limit for the number of iterations per minimization to avoid situations in which the minimization algorithm would get stuck unexpectedly and iterate indefinitely.

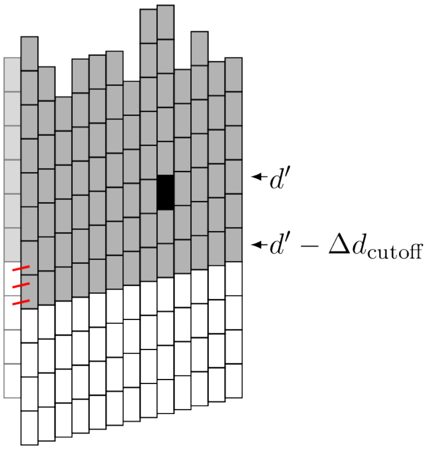

Figure 3.4: Schematic illustration of the minimization cutoff layer distance $\Delta d_{\mathrm{cutoff}}$. If an executed event affects the black tubulin dimer in layer d' and we use $\Delta d_{\mathrm{cutoff}} = 2$, then all polar angles of the gray (and black) tubulin dimers are considered for energy minimization. The first protofilament shown is the periodic image of the last protofilament (thus the added transparency). The three red lines highlight the lateral heterotypic interfaces of tubulin monomers at the seam between tubulin monomers whose polar angles are considered for minimization and tubulin monomers whose polar angles are ignored during minimization.

part of the microtubule tip at its plus end because this is the part of the microtubule where it changes its configuration due to chemical events, while its GDP-body is static. The only question remaining is how deep from the microtubule tip we have to go. While polymerization and depolymerization events happen at the very tip of protofilaments, the formation and rupture of lateral bonds can also happen a bit deeper in the microtubule lattice, while the hydrolysis of GTP-tubulin dimers can happen as deep in the microtubule lattice as there are GTP-tubulin dimers to hydrolyze. As a consequence, the subset must depend on the tubulin dimer (p', d') that was affected by the previous event. As the microtubule tip is the dynamic part for which we have to ensure a proper configuration to calculate correct event rates, we have to consider all tubulin dimers with $d \geq d'$. Additionally, configuration changes due to events can also propagate deeper into the microtubule lattice so that an additional number of $\Delta d_{\mathrm{cutoff}}$ layers below the d-th layer have to be considered as well. In summary, when using the second approach and an event happens in layer d', all polar angles of the tubulin dimers with $d \geq \min(0, d' - \Delta d_{\mathrm{cutoff}})$ are used as minimization parameters. Figure 3.4 illustrates the way in which $\Delta d_{\mathrm{cutoff}}$ cuts off tubulin dimers in longitudinal direction from the minimization. Figure 3.4, however, also shows that there are three lateral tubulin monomer interfaces at the seams at which a cutoff happens. At the seam, tubulin monomers from different layers interact laterally so that due to the helical structure, a longitudinal-only cutoff is not possible, but there has to be a lateral cutoff at the seam as well.

To assess the quality of both restriction types, we have to select an observable by which we grade the restriction, and we have to select quantities for both restriction types that we adjust to a suitable value. For the restriction of the number of iterations per minimization, the relevant quantity is the maximum number of iterations per minimization N_{iter}, and for the restriction of the number of minimization parameters, it is the layer cutoff length $\Delta d_{\mathrm{cutoff}}$. In both cases, the chosen value should be as small as possible to maximize the decrease in the required minimization time. An easily measurable observable to judge the minimization quality on is the shrinkage velocity v_{sh} of microtubules. Details on shrinkage simulations will be given in section 4.2. For now, we only have to know that the microtubules considered here should be shrinking with velocity $v_{\mathrm{sh}} = -27\,\mu\mathrm{m}\,\mathrm{min}^{-1}$[49]. Figure 3.5 shows the shrinkage velocity v_{sh} for certain sets of simulation parameters (whose origin will be explained later in chapter 4). Even though we have already argued conceptually why the second approach is better than the first

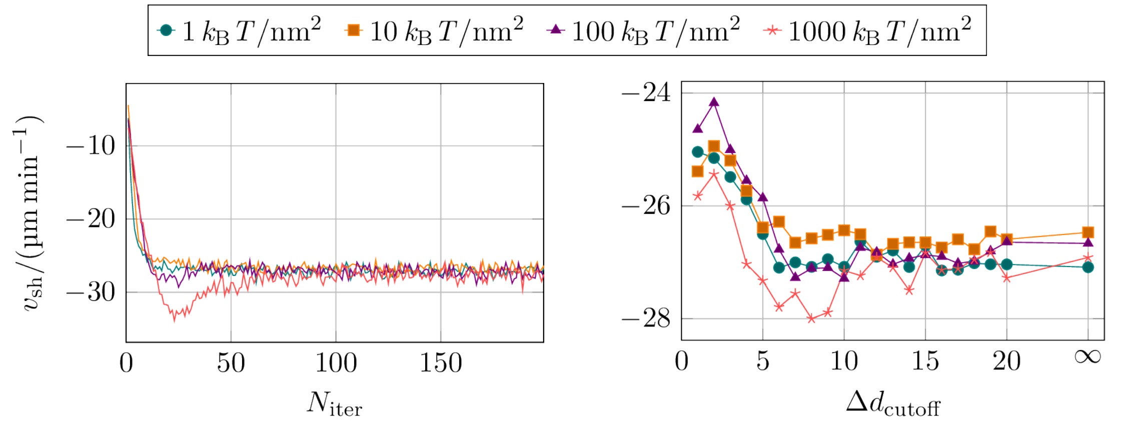

(a) Shrinkage velocity v_{sh} as a function of the maximum number of minimization iterations N_{iter}.

(b) Shrinkage velocity v_{sh} as a function of the layer cutoff distance Δd_{cutoff}. $\Delta d_{\text{cutoff}} = \infty$ means that no cutoff was used.

Figure 3.5: Comparison of the two minimization restriction approaches by running 20 shrinkage simulations with $k_+ = 4\,\text{s}^{-1}\,\text{µM}^{-1}$, $\Delta G^{0*}_{\text{long}} = -9.3\,k_B\,T$, $N_{\text{GDP}} = 20$, $N_{\text{GTP}} = 0$ and four different values of k_{lat}.

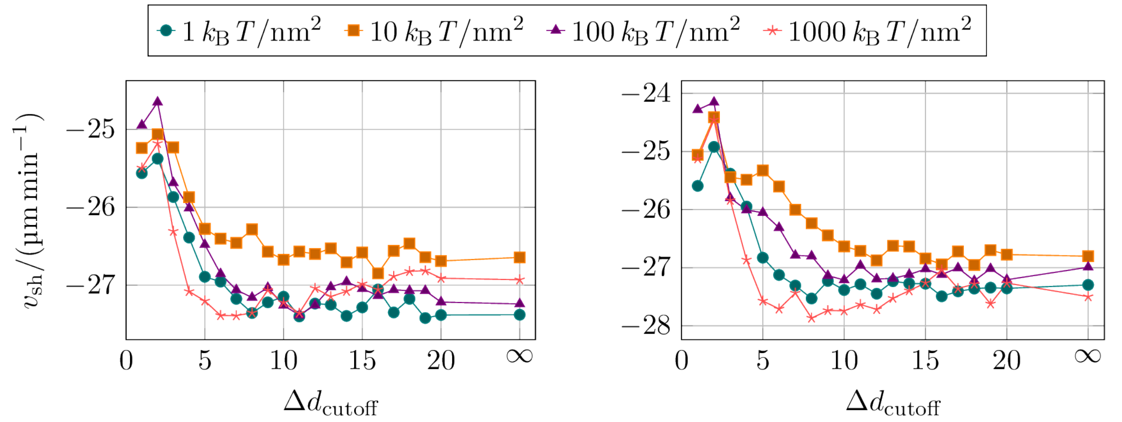

(a) $k_+ = 2\,\text{s}^{-1}\,\text{µM}^{-1}$, $\Delta G^{0*}_{\text{long}} = -9.7\,k_B\,T$, $N_{\text{GDP}} = 20$

(b) $k_+ = 4\,\text{s}^{-1}\,\text{µM}^{-1}$, $\Delta G^{0*}_{\text{long}} = -9.3\,k_B\,T$, $N_{\text{GDP}} = 50$

Figure 3.6: Shrinkage velocity v_{sh} as a function of the layer cutoff distance Δd_{cutoff} for additional parameter values (in both cases: $N_{\text{GTP}} = 0$) and four different values of k_{lat}.

one, we have also shown results for the first approach in Figure 3.5(a). The interesting results for the second minimization restriction approach are shown in Figure 3.5(b). These results indicate that $\Delta d_{\text{cutoff}} = 10$ is an appropriate choice, which is also confirmed by simulations using different simulation parameter values (see Figure 3.6). Except for the determination of some of the model parameters with shrinking microtubules in section 4.2 for which we used unrestricted minimization, $\Delta d_{\text{cutoff}} = 10$ will be used in the remainder of this thesis.

Lastly, we want to compare our approach to two other minimization approaches. During the energy minimization employed by VanBuren et al.[118], individual tubulin dimers are randomly chosen, and then, for each tubulin dimer a local energy minimization is performed during which all of the other tubulin dimers are static. It is important to note that they also restrict the values of their minimization parameters so that their polar angles cannot be negative and thus forbid tubulin dimers bending inward (a phenomenon, as we will see later on, that is not only allowed in our model but one that also happens). This approach does not guarantee that every tubulin dimer is considered during minimization, but according to VanBuren et al., the microtubule energy was minimized at least once for, on average, 95 % of all tubulin dimers and, again on average, the microtubule energy was minimized using each tubulin dimers three times. As a consequence of this approach, there is no clear way to compare our approach to minimization to theirs. Additionally, their mechanical model also contains longitudinal springs, which change how the microtubule lattice reacts to individual tubulin dimers bending outward. In their model, one tubulin dimer bending outward causes the next longitudinal spring to stretch and keep the remaining tubulin dimers in the same protofilament up to the plus end in place. This local effect of bending outward enables the usage of a local minimization approach. In our model, however, there are no such longitudinal springs (which would come with yet another free model parameter in form of second spring constant) so that one tubulin dimer bending outward results in the protofilament segment above it to also bend outward causing many lateral springs to be stretched. As a consequence, we cannot implement a local minimization for comparison as we have "non-local interactions" in our model. However, the following qualitative argument can be made: Minimizing the microtubule energy for each tubulin dimer separately is the same as minimizing a multidimensional function with fixed unit vectors as the minimization directions for each minimization step. Such an approach is generally inferior[184] to selecting the minimizing direction dynamically based on the current position in the energy landscape like, for example, the conjugate gradient method does.

In contrast, Zakharov et al.[126] use a different approach: They solve Langevin equations for the first 300 tubulin dimers at the plus end and thus also incorporate stochastic thermal motion of individual tubulin monomers. This approach, however, requires a discretization of the time as discussed in the beginning of section 3.1. First, they have a time step of $2 \cdot 10^{-10}\,\mathrm{s}$ for solving the Langevin equations, and second, they have a time step of $10^{-3}\,\mathrm{s}$ for the events in their simulation. As a consequence, they have to calculate $\mathcal{O}(10^7)$ dynamics steps for each event step resulting in a runtime of more than a day for 1 s of microtubule dynamics despite using a parallel implementation of their simulation that is run on a supercomputer, illustrating the computational cost associated with this approach. Comparing our approach to their approach is easier than for VanBuren et al. If we neglect the thermal fluctuations included in the Langevin equations, during one of their $2 \cdot 10^{-10}\,\mathrm{s}$ steps, they are basically taking one step of a gradient descent method resulting in $\mathcal{O}(10^7)$ gradient descent steps between events. Phrased differently, during one of their "minimization steps", time advances by $2 \cdot 10^{-10}\,\mathrm{s}$. While in our simulation, minimization happens instantaneously after an event is executed, we can use the time difference between an event and the next event and the number of required minimization iterations to calculate a similar quantity to their time step of $2 \cdot 10^{-10}\,\mathrm{s}$. In our simulations, the value of this minimization time step depends on different factors like the values of the model parameters and the type of the simulation (i.e., whether only growth or shrinkage is considered of whether full simulations with catastrophes and rescues are considered). When only considering shrinking microtubules (see section 4.2), minimization time steps take $\mathcal{O}(10^{-5}\,\mathrm{s})$ for polymerization events,

$\mathcal{O}(10^{-4}\,\mathrm{s})$ for depolymerization events, and $\mathcal{O}(10^{-7}\,\mathrm{s})$ for lateral bond events. (Additional values for one example of a full simulation can be found in Figure 6.16(a).) This comparison shows that significantly less minimization iterations are needed in our simulations compared to number the dynamics steps between the event steps in the simulations by Zakharov et al. As a result, our simulations running on a single CPU core only require a few hours (depending on the parameter values, sometimes even less than an hour) for simulating 1 min of microtubule dynamics, which is much more efficient. It should not be neglected, of course, that our simulations do not contain thermal motion of the tubulin monomers at the microtubule tip as the simulations by Zakharov et al. do. They use this thermal motion as a basis for when bonds are considered ruptured, i.e., when bonds exceeded their rupture length, in contrast to our approach of explicitly modeling rupture events.

In summary, we consider our approach of restricted minimization to be a fair balance between properly minimizing the dynamic part of microtubule and having a computationally efficient method that enables us to simulate long microtubules.

Determination of Model Parameters

4

In Table 2.2, we have listed the free parameters of our model of which we have to determine the values. Determining the values of all seven parameters simultaneously is prohibitive because of the large parameter space that would have to be analyzed. Instead, we use a "divide and conquer" approach[104,118] with which one subset of parameters is determined first and a second subset next. In this chapter, we will not consider hydrolysis, thus $k_\mathrm{h} = 0\,\mathrm{s}^{-1}$. We will come back to hydrolysis with a constant rate in chapter 5 and to mechanical hydrolysis in chapter 6.

To determine the values of our parameters, we need experimental results that we can compare observables of our simulation to. Walker et al.[49] did an extensive investigation into the growth behavior of microtubules at different concentrations of free GTP-tubulin dimers c_tub. They found that the growth velocity v_gr of microtubules scales linearly with c_tub

$$v_\mathrm{gr}(c_\mathrm{tub}) = (0.33 \pm 0.01)\,\frac{\mathrm{\mu m}}{\mathrm{min}\,\mathrm{\mu M}} c_\mathrm{tub} - (1.59 \pm 0.50)\,\frac{\mathrm{\mu m}}{\mathrm{min}} \tag{4.1}$$

and that the shrinkage velocity v_sh is independent of c_tub

$$v_\mathrm{sh} = (-27 \pm 1)\,\frac{\mathrm{\mu m}}{\mathrm{min}} \tag{4.2}$$

for $c_\mathrm{tub} \in [7.7\,\mathrm{\mu M}, 15.5\,\mathrm{\mu M}]$. Based on this data, we will first focus on growing microtubules in section 4.1 and then turn to shrinking microtubules in section 4.2.

From the experimental results showing bending protofilaments forming ram's horns, we know that mechanics plays a more important role for shrinking microtubules than for growing microtubules as mechanical stresses are relieved during shrinkage when the protofilaments are able to bend outward. To determine our model parameters, we take this finding to the extreme and assume that for growing microtubules, mechanics does not play any role, so that we can simply set $k_\mathrm{lat} = 0\,k_\mathrm{B}T/\mathrm{nm}^2$ and $\kappa = 0\,k_\mathrm{B}T/\mathrm{rad}^2$, i.e., ignore two of the model parameters so that only four model parameters remain: k_+, $\Delta G^{0*}_\mathrm{long}$, $\Delta G^{0}_\mathrm{lat}$, and k_att. Such "microtubules without mechanics" must then only consist of GTP-tubulin dimers so that for the initial microtubule $N_\mathrm{GDP} = 0$. As hydrolysis is ignored for now, $N_\mathrm{GDP} = 0$ stays during the whole simulation.

Like VanBuren et al.[104,118], we will not treat k_+ as yet another truly free model parameter but instead, we will also only consider $k_+ = 2\,\mathrm{s}^{-1}\,\mathrm{\mu M}^{-1}$ and $k_+ = 4\,\mathrm{s}^{-1}\,\mathrm{\mu M}^{-1}$, leaving three parameters left for each value of k_+. (These values were previously used by VanBuren et al.[104,118], which are similar to values from other publications[49,171], and $k_+ = 2\,\mathrm{s}^{-1}\,\mathrm{\mu M}^{-1}$ was previously estimated for "generic protein-protein-association" using Brownian dynamics computer simulations[185].) From the growth velocity data (4.1), we can fix two of these remaining parameters because we know the expected slope and intercept of the $v_\mathrm{gr}(c_\mathrm{tub})$. In section 4.1, we will find the lateral bond energy $\Delta G^{0}_\mathrm{lat}$ and the lateral bond attempt rate k_att as a function of $\Delta G^{0*}_\mathrm{long}$.

After the "growth parameters" have been determined, we can then turn to the "shrinkage parameters", i.e., the two parameters that are relevant for our mechanical model: the lateral spring constant k_{lat} and the bending constant κ. Here, we are only interested in shrinking microtubule to reproduce the shrinkage velocity (4.2). As the shrinkage velocity does not depend on c_{tub}, the experimental data only yields one value with which we will only be able to fix the value of κ if we specify a value of k_{lat} (it would, of course, also work vice versa, i.e., getting a value of k_{lat} for a given κ, but we have chosen the former procedure). The extreme case of shrinking microtubules are microtubules without any GTP-tubulin dimers forming a stabilizing cap in the beginning, i.e., $N_{\mathrm{GTP}} = 0$. In contrast to the growth simulations for which $N_{\mathrm{GDP}} = 0$ stayed the same, here, $N_{\mathrm{GTP}} = 0$ only holds at the beginning of the simulation as new GTP-tubulin dimers are able to polymerize onto the microtubule.

Figure 4.1 provides an overview of how we determined the model parameters as described in the two following sections.

4.1 Growing GTP-Microtubules and Growth Parameter Values

As already mentioned before, for the growing microtubules, we ignore mechanics completely, thus set $k_{\mathrm{lat}} = 0\,k_{\mathrm{B}}T/\mathrm{nm}^2$ and $\kappa = 0\,k_{\mathrm{B}}T/\mathrm{rad}^2$ and use GTP-only microtubules. As a consequence, we do not have to use energy minimization for these simulations making them much faster. For $k_+ = 2\,\mathrm{s}^{-1}\,\mathrm{\mu M}^{-1}$ and $k_+ = 4\,\mathrm{s}^{-1}\,\mathrm{\mu M}^{-1}$, we scanned the parameter space $(\Delta G^{0*}_{\mathrm{long}}, \Delta G^{0}_{\mathrm{lat}}, k_{\mathrm{att}})$ to find parameter values that reproduce the experimentally measured growth velocity (4.1). After an initial coarse-grained scan of the parameters space, we used a fine-grained scan with at least $\Delta\Delta G^{0*}_{\mathrm{long}} = 0.2\,k_{\mathrm{B}}T$ for the final parameters values. As Walker et al.[49] measured the growth velocities for $c_{\mathrm{tub}} \in [7.7\,\mathrm{\mu M}, 15.5\,\mathrm{\mu M}]$, we used $c_{\mathrm{tub}} \in \{7\,\mathrm{\mu M}, 8\,\mathrm{\mu M}, \dots, 16\,\mathrm{\mu M}\}$. For each $(k_+, \Delta G^{0*}_{\mathrm{long}}, \Delta G^{0}_{\mathrm{lat}}, k_{\mathrm{att}}, c_{\mathrm{tub}})$ parameter set, 100 simulations were run during the fine-grained scan.

The relevant observable during these simulations is the microtubule length L_{MT}, see (2.11), as a function of the simulation time t_{sim} from which the growth velocity v_{gr} can be calculated. The next step is then to calculate the growth velocity dependence on the free GTP-tubulin dimer concentration c_{tub} for each set of $(k_+, \Delta G^{0*}_{\mathrm{long}}, \Delta G^{0}_{\mathrm{lat}}, k_{\mathrm{att}})$ values and compare the results of the linear fits with the experimental data (4.1). As the experimental linear $v_{\mathrm{gr}}(c_{\mathrm{tub}})$ relation contains two values in form of the slope and intercept value, we can fix the value of $\Delta G^{0}_{\mathrm{lat}}$ and k_{att} for a given set of $(k_+, \Delta G^{0*}_{\mathrm{long}})$ values. These results are shown in Figure 4.2: For a specific set of $(k_+, \Delta G^{0*}_{\mathrm{long}})$ values, the value of the lateral bond energy $\Delta G^{0}_{\mathrm{lat}}$ can be extracted from Figure 4.2(a) and the matching value k_{att} from Figure 4.2(b). The first observation is that the lateral bond energy $\Delta G^{0}_{\mathrm{lat}}$ differs only slightly between the two values of k_+, we considered. The second observation is regarding the lateral bond attempt rate k_{att} and is twofold: k_{att} is always smaller for the larger value of k_+, and in contrast to $\Delta G^{0}_{\mathrm{lat}}(\Delta G^{0*}_{\mathrm{long}})$, $k_{\mathrm{att}}(\Delta G^{0*}_{\mathrm{long}})$ is not monotonic but after decreasing for stronger longitudinal bonds starts to increase again for very strong longitudinal bonds.

The general finding shown in Figure 4.2(a) that weakening longitudinal bonds requires strengthening the lateral bonds is expected because tubulin dimers must have the same overall “stability” in the microtubule lattice so that the microtubules grow with the same velocity. If the longitudinal bonds are weaker, this stability is decreased, which then has to be compensated

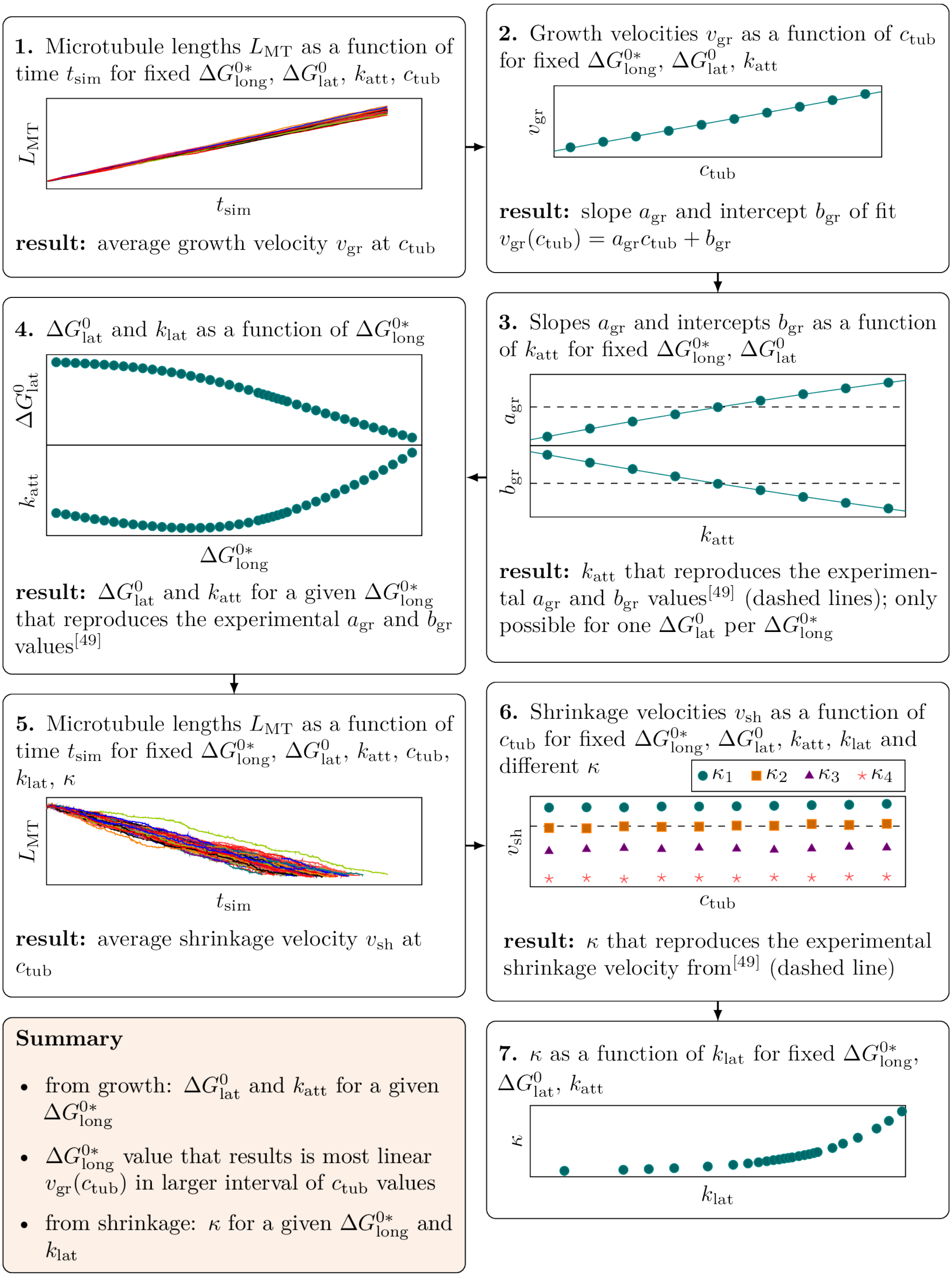

1. Microtubule lengths L_{MT} as a function of time t_{sim} for fixed $\Delta G^{0*}_{\mathrm{long}}$, $\Delta G^{0}_{\mathrm{lat}}$, k_{att}, c_{tub}

result: average growth velocity v_{gr} at c_{tub}

2. Growth velocities v_{gr} as a function of c_{tub} for fixed $\Delta G^{0*}_{\mathrm{long}}$, $\Delta G^{0}_{\mathrm{lat}}$, k_{att}

result: slope a_{gr} and intercept b_{gr} of fit $v_{\mathrm{gr}}(c_{\mathrm{tub}}) = a_{\mathrm{gr}}c_{\mathrm{tub}} + b_{\mathrm{gr}}$

3. Slopes a_{gr} and intercepts b_{gr} as a function of k_{att} for fixed $\Delta G^{0*}_{\mathrm{long}}$, $\Delta G^{0}_{\mathrm{lat}}$

result: k_{att} that reproduces the experimental a_{gr} and b_{gr} values[49] (dashed lines); only possible for one $\Delta G^{0}_{\mathrm{lat}}$ per $\Delta G^{0*}_{\mathrm{long}}$

4. $\Delta G^{0}_{\mathrm{lat}}$ and k_{lat} as a function of $\Delta G^{0*}_{\mathrm{long}}$

result: $\Delta G^{0}_{\mathrm{lat}}$ and k_{att} for a given $\Delta G^{0*}_{\mathrm{long}}$ that reproduces the experimental a_{gr} and b_{gr} values[49]

5. Microtubule lengths L_{MT} as a function of time t_{sim} for fixed $\Delta G^{0*}_{\mathrm{long}}$, $\Delta G^{0}_{\mathrm{lat}}$, k_{att}, c_{tub}, k_{lat}, κ

result: average shrinkage velocity v_{sh} at c_{tub}

6. Shrinkage velocities v_{sh} as a function of c_{tub} for fixed $\Delta G^{0*}_{\mathrm{long}}$, $\Delta G^{0}_{\mathrm{lat}}$, k_{att}, k_{lat} and different κ

result: κ that reproduces the experimental shrinkage velocity from[49] (dashed line)

7. κ as a function of k_{lat} for fixed $\Delta G^{0*}_{\mathrm{long}}$, $\Delta G^{0}_{\mathrm{lat}}$, k_{att}

Summary

- from growth: $\Delta G^{0}_{\mathrm{lat}}$ and k_{att} for a given $\Delta G^{0*}_{\mathrm{long}}$
- $\Delta G^{0*}_{\mathrm{long}}$ value that results is most linear $v_{\mathrm{gr}}(c_{\mathrm{tub}})$ in larger interval of c_{tub} values
- from shrinkage: κ for a given $\Delta G^{0*}_{\mathrm{long}}$ and k_{lat}

Figure 4.1: Schematic illustration of the procedure used to determine the values of our model parameters for a fixed value of k_{+} showing how many individual simulations (see **1.** and **5.**) ultimately result in one data point (see **4.** and **7.**).

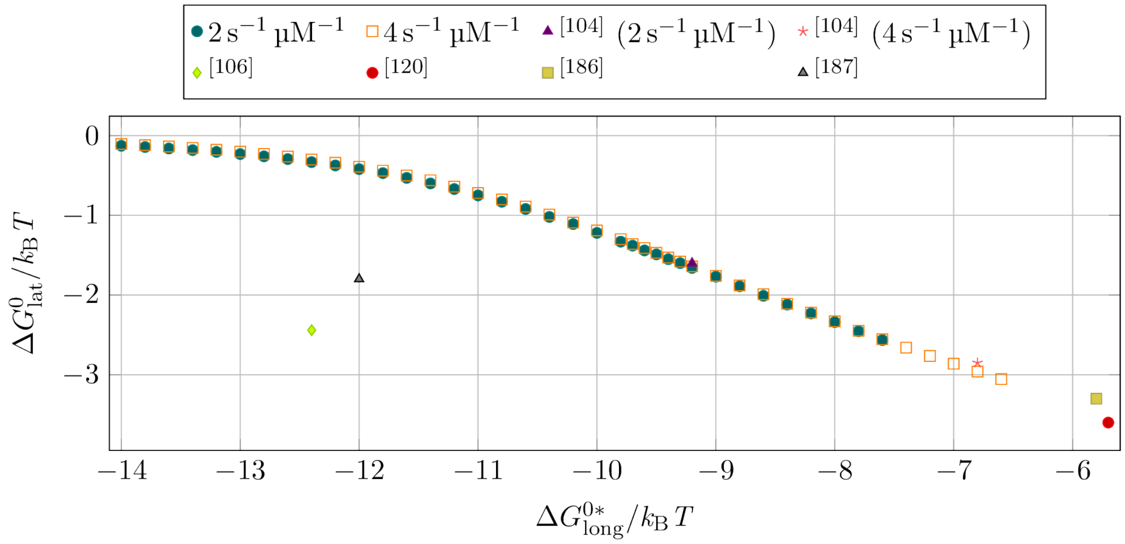

(a) Our lateral bond energy $\Delta G^0_{\mathrm{lat}}$ as a function of the longitudinal bond energy $\Delta G^{0*}_{\mathrm{long}}$ and additional parameter values from other publications. (A direct comparison of the values from other publications to our values in not always directly possible due to different mechanical models. Additionally, their values were converted to account for two lateral bonds per tubulin dimer in our model.)

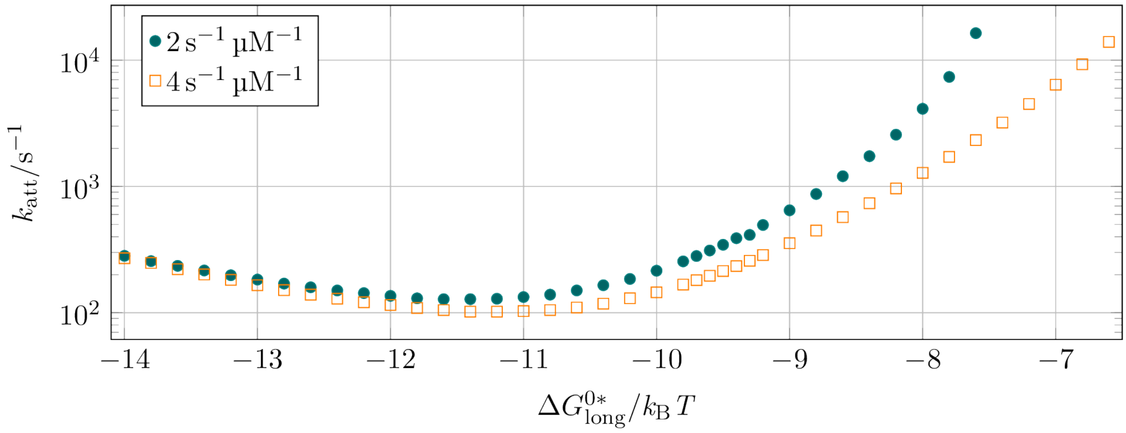

(b) Lateral bond attempt rate k_{att} as a function of the longitudinal bond energy $\Delta G^{0*}_{\mathrm{long}}$.

Figure 4.2: Results for our growth model parameters for two pseudo-first order polymerization rates k_+. The numerical values can be found in Table C.1.

by stronger lateral bonds. Additionally, our results in Figure 4.2(a) are consistent with data from other publications[104,120,186] but deviate from other data[106,187]. The molecular dynamics (MD) nano-indentation results (i.e., not from the growth dynamics of the microtubules) by Kononova et al.[143] differ significantly from all of these bond energies by having much stronger longitudinal and lateral bonds, about $-25.1\,k_B T$ and $-11.6\,k_B T$ respectively, and are thus not shown in Figure 4.2(a). Manka et al.[172], however, get a longitudinal bond energy of $\Delta G^{0*}_{\mathrm{long}} \simeq -9.1\,k_B T$ for GMPCPP, which is a slowly hydrolyzable GTP analogue, from their lattice contact analysis, which is close to our final values in Table 4.1.

The finding that k_{att} decreases if k_+ is increased can be understood qualitatively as follows: From the polymerization rate (2.36) and the depolymerization rate (2.35), we can define an effective polymerization rate as

$$k_{\mathrm{on}}^{\mathrm{eff}} = k_{\mathrm{on}} - k_{\mathrm{off}} = k_+ \left[c_{\mathrm{tub}} - c^0 \exp\left(\beta \Delta G_{\mathrm{long}}^{0*}\right)\right]. \tag{4.3}$$

Due to the lateral bonds that need to rupture before a tubulin dimer can depolymerize, there is no strict relation between $k_{\mathrm{on}}^{\mathrm{eff}}$ and the growth velocity v_{gr}, but qualitatively we know that increasing $k_{\mathrm{on}}^{\mathrm{eff}}$ will also increase v_{gr} so that an increase in k_+ will increase v_{gr} as well.

From the lateral bond formation rate (2.40) and the lateral bond rupture rate (2.41), we can also define an effective lateral bond formation rate as

$$k_{\mathrm{form}}^{\mathrm{eff}} = k_{\mathrm{form}} - k_{\mathrm{rup}} = k_{\mathrm{att}} \left[1 - \exp\left(\Delta G_{\mathrm{lat}}^{0}\right)\right]. \tag{4.4}$$

From (4.4) it follows, that increasing k_{att} increases $k_{\mathrm{form}}^{\mathrm{eff}}$ as well. An increase in the effective lateral bond formation rate $k_{\mathrm{form}}^{\mathrm{eff}}$ results in a quicker stabilization of newly polymerized tubulin dimers, which in turn decreases the depolymerization probability and thus increases the growth velocity v_{gr}.

Now, we have a qualitative understanding what happens if the values of k_+ and k_{att} are changed separately and all other parameter values are kept constant: increasing them also increases the growth velocity v_{gr}. If, however, it is the goal to keep v_{gr} constant, an increase in k_+ must be compensated for by a decrease in k_{att} (and vice versa), as shown in Figure 4.2(b).

While the previous argument with the effective rates (4.3) and (4.4) gives an intuitive understanding of the relation between k_+ and k_{att}, it should be noted that while $k_{\mathrm{form}}^{\mathrm{eff}} > 0$ is always fulfilled because $\Delta G_{\mathrm{lat}}^{0} < 0$, $k_{\mathrm{on}}^{\mathrm{eff}} > 0$ only holds for strong longitudinal bonds. For weaker longitudinal bonds, $k_{\mathrm{on}}^{\mathrm{eff}} < 0$ is possible, which again highlights the need for a large (effective) lateral bond formation rate to prevent tubulin dimers from depolymerizing again.

From now on, we will generally only give the value of $\Delta G_{\mathrm{long}}^{0*}$ and the values of $\Delta G_{\mathrm{lat}}^{0}$ and k_{att} are the ones shown in Figure 4.2 and explicitly listed in Table C.1.

For $k_+ = 4\,\mathrm{s}^{-1}\,\mu\mathrm{M}^{-1}$, Figure 4.3(a) shows the microtubule growth velocity v_{gr} as a function of $c_{\mathrm{tub}} \in \{7\,\mu\mathrm{M}, 8\,\mu\mathrm{M}, \dots, 16\,\mu\mathrm{M}\}$. While all of the shown data sets of the different values of $\Delta G_{\mathrm{long}}^{0*}$ follow the expected result quite well (as they should because reproducing (4.1) was the criterion used to determine the growth parameter values), not all of the sets are as linear as the other sets. This non-linear dependence becomes very pronounced when the interval of c_{tub} values is extended to $c_{\mathrm{tub}} \in \{1\,\mu\mathrm{M}, \dots, 50\,\mu\mathrm{M}\}$, as shown in Figure 4.3(b). As the longitudinal bond strength gets weaker, the $v_{\mathrm{gr}}(c_{\mathrm{tub}})$ relations change from concave to convex. In-between the concave and convex relations, we find one $\Delta G_{\mathrm{long}}^{0*}$ that results in the most linear $v_{\mathrm{gr}}(c_{\mathrm{tub}})$ relation for both of our k_+ values. These two parameter sets are listed in Table 4.1 and highlighted in the parameter value tables in Appendix C. To determine these parameter sets, only those values of c_{tub} above the critical concentration c_{crit} were considered as we are only interested in growing microtubules for now. The critical free GTP-tubulin dimer concentration c_{crit} is the concentration at which microtubules do not grow, i.e., $v_{\mathrm{gr}} = 0$. Figure 4.4 shows that for $c_{\mathrm{tub}} > c_{\mathrm{crit}}$, our simulated growth velocities match the expected dependence measured by Walker et al.[49] very well, even over the larger interval of values of

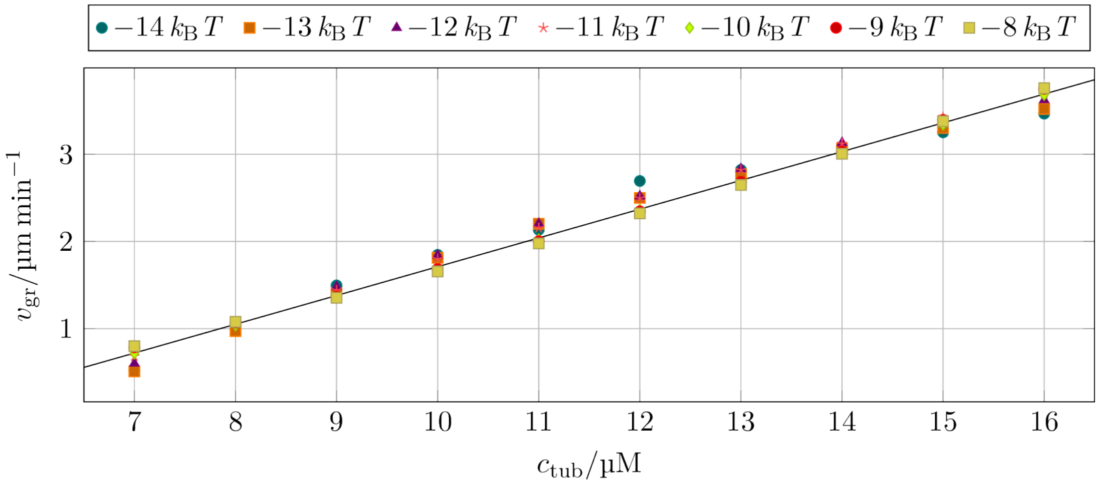

(a) Growth velocity v_{gr} for almost the same c_{tub} interval as used by Walker et al.[49].

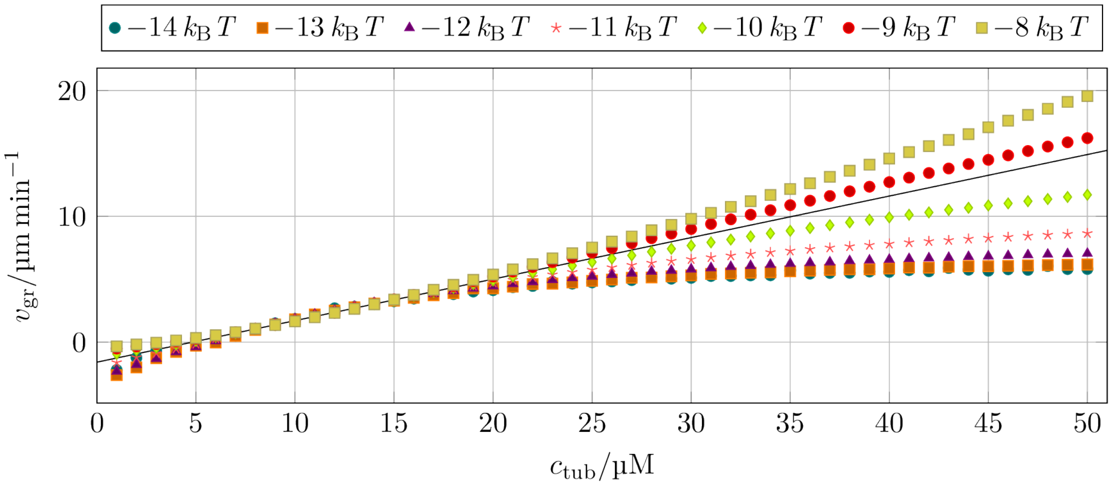

(b) Growth velocity v_{gr} for an extended interval of c_{tub} values.

Figure 4.3: Microtubule growth velocity v_{gr} as a function of the free GTP-tubulin dimer concentration c_{tub} for $k_+ = 4\,\text{s}^{-1}\,\mu\text{M}^{-1}$ and different values of $\Delta G^{0*}_{\text{long}}$. The black lines are the expected dependence from Walker et al.[49].

$k_+/\mu\text{M}^{-1}\,\text{s}^{-1}$	$\Delta G^{0*}_{\text{long}}/k_\text{B}\,T$	$\Delta G^{0}_{\text{lat}}/k_\text{B}\,T$	$k_{\text{att}}/\text{s}^{-1}$
2	−9.7	−1.38	281
4	−9.3	−1.58	258

Table 4.1: Values of the "growth parameters" $\Delta G^{0*}_{\text{long}}$, $\Delta G^{0}_{\text{lat}}$, and k_{att} for the two considered values of k_+.

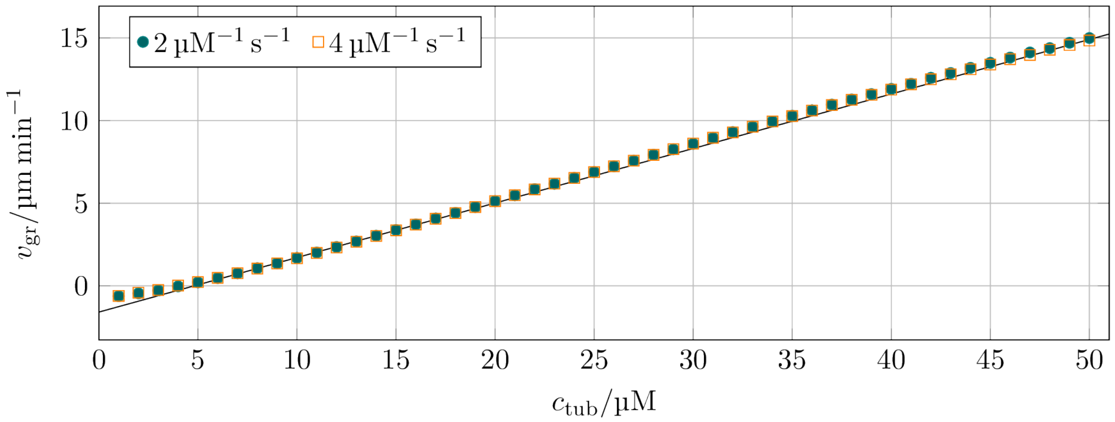

Figure 4.4: Microtubule growth velocity v_{gr} as a function of the free GTP-tubulin dimer concentration c_{tub} for the our two best parameter sets given in Table 4.1. The black line is the expected dependence from Walker et al.[49].

c_{tub}. Our choice to select the parameter set with the most linear $v_{\mathrm{gr}}(c_{\mathrm{tub}})$ relation is also based on measurements of this relation by other researchers[47,52,188–193], all of which find a linear relation, even over larger intervals of c_{tub} values[47,189,192,193] than Walker et al.[49]. Nevertheless, finding a non-linear $v_{\mathrm{gr}}(c_{\mathrm{tub}})$ relation is not surprising as just because individual protofilaments grow linearly with c_{tub} (see (4.3)), the same does not have to apply to the microtubule because it is not just a collection of uncorrelated dynamic protofilaments. Instead, because of the lateral interactions between the protofilaments, non-linear growth with c_{tub} is the result, as already shown previously for multi-stranded polymers[114]. Piette et al.[106] used a two-dimensional microtubule model based on the model by VanBuren et al.[104], and they also found a non-linear relation.

Now that we have determined the values of the growth parameters $\Delta G^{0*}_{\mathrm{long}}$, $\Delta G^{0}_{\mathrm{lat}}$, and k_{att}, we can use these values to determine the values of the “shrinkage parameters” k_{lat} and κ.

4.2 Shrinking GDP-Microtubules and Shrinkage Parameter Values

To determine the values of the shrinkage parameters k_{lat} and κ, we consider microtubules with initially $N_{\mathrm{GTP}} = 0$ and $N_{\mathrm{GDP}} = 20$, i.e., microtubules without a stabilizing GTP-cap, which, if the values of k_{lat} and κ are chosen appropriately, should shrink completely. For all of the growth parameter sets shown in Figure 4.2, we chose the same set of values of k_{lat} and then adjusted κ so that the shrinkage velocity matches the experimentally measured value (4.2). For each parameter set, 20 simulations were run and the average shrinkage velocity v_{sh} was calculated. As we have two free parameters, k_{lat} and κ, and only one experimental value, v_{sh}, we will only be able to determine κ as a function of k_{lat}.

The results of these simulations are shown for some of the considered $\Delta G^{0*}_{\mathrm{long}}$ values in Figure 4.5. Just like for the growth parameters, in the following, we will generally only give the value of k_{lat} and the matching value of κ is the value shown in Figure 4.5 and listed in Table C.2 or Table C.3.

For a given value of $\Delta G^{0*}_{\mathrm{long}}$, the values follow a square root function

$$\kappa(k_{\mathrm{lat}}) = a_{\mathrm{sh}} \sqrt{k_{\mathrm{lat}}} + b_{\mathrm{sh}}. \tag{4.5}$$

To understand this relation, we have to remember that lateral spring stretching and bending only affects the microtubule dynamics via the lateral bond rupture rate (2.42) by modulating the rate with a force-dependent exponential factor:

$$k_{\mathrm{rup}} \sim \exp\left(\beta F_{\mathrm{lat}} \ell_{\mathrm{rup}}\right). \tag{4.6}$$

To get the same shrinkage velocity for different sets of $(k_{\mathrm{lat}}, \kappa)$ values, the rupture rate must be the same, i.e.,

$$F_{\mathrm{lat}} \ell_{\mathrm{rup}} = \mathrm{const} \tag{4.7}$$

$$\iff \qquad F_{\mathrm{lat}} \sim \frac{1}{\ell_{\mathrm{rup}}} \overset{(2.44)}{\sim} \sqrt{k_{\mathrm{lat}}}. \tag{4.8}$$

The origin of the force F_{lat} acting on the lateral bonds is the stretching of these bonds because of the bending of tubulin monomers. The lateral bonds are stretching to decrease the bending force

$$F_{\mathrm{bend}} = \frac{\partial E_{\mathrm{bend}}}{\partial \theta} = \kappa \Delta \psi. \tag{4.9}$$

Consequently, in equilibrium, the lateral spring force F_{lat} and the bending force F_{bend} balance each other out so that

$$F_{\mathrm{lat}} \sim F_{\mathrm{bend}} \sim \kappa \tag{4.10}$$

resulting in

$$\kappa \sim \sqrt{k_{\mathrm{lat}}}, \tag{4.11}$$

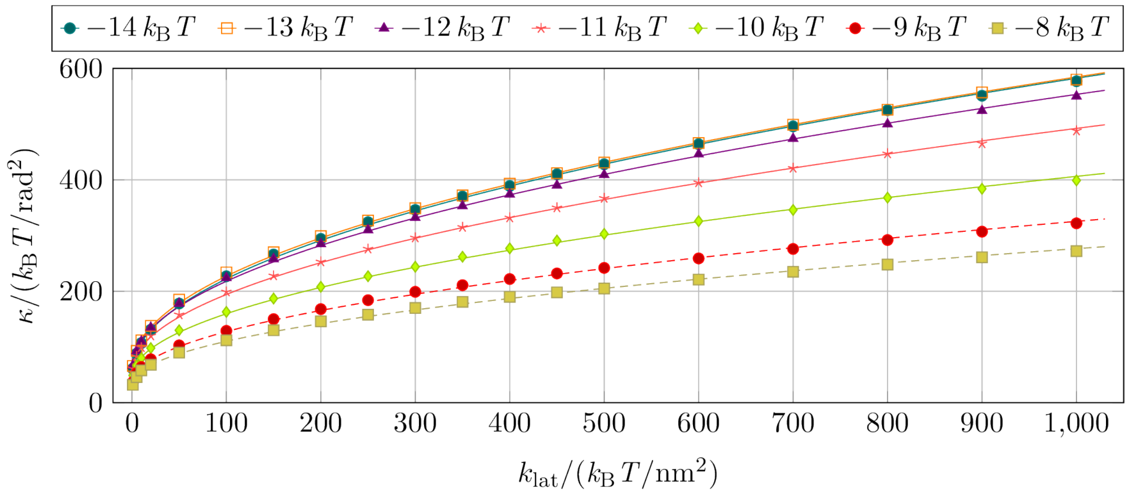

(a) $k_+ = 2\,\mathrm{s}^{-1}\,\mu\mathrm{M}^{-1}$ (Data values can be found in Table C.2.)

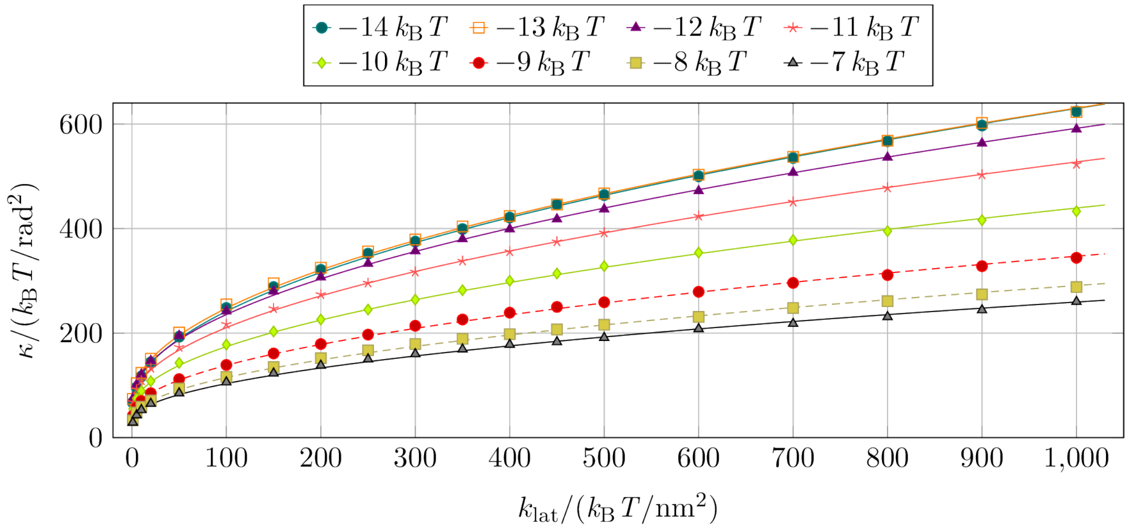

(b) $k_+ = 4\,\mathrm{s}^{-1}\,\mu\mathrm{M}^{-1}$ (Data values can be found in Table C.3.)

Figure 4.5: Bending constant κ as a function of the lateral spring constant k_lat reproducing the shrinkage velocity (4.2) by Walker et al.[49] for our two values of k_+ and different values of $\Delta G^{0*}_\mathrm{long}$. The lines are the square root functions (4.5), which can be used to describe the $\kappa(k_\mathrm{lat})$ relation.

which matches the fit function (4.5) used for our data.

To verify (4.8), we measured the lateral bond rupture force F_rup during the rupture events[1]. Figure 4.6(a) and Figure 4.6(b) show that the data indeed follows square root functions

$$F_\mathrm{rup}(k_\mathrm{lat}) = a_\mathrm{rup}\sqrt{k_\mathrm{lat}} + b_\mathrm{rup} \tag{4.12}$$

---

[1] To be clear, $F_\mathrm{lat}(p,d,t)$ is the force acting on the lateral bond connecting tubulin monomers (p,d,t) and $(p+1,d,t)$, while $F_\mathrm{rup}(p,d,t)$ is the value of $F_\mathrm{lat}(p,d,t)$ during an actual bond rupture.

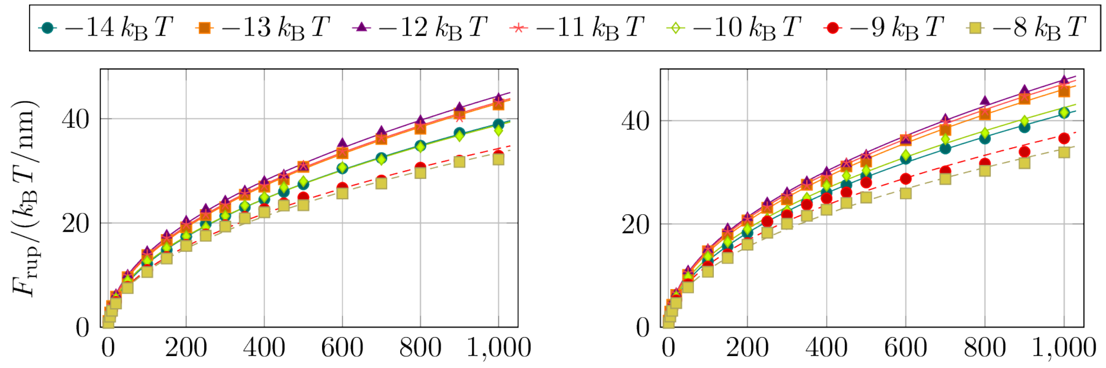

(a) Lateral bond rupture force for $k_+ = 2\,\mathrm{s}^{-1}\,\mu\mathrm{M}^{-1}$.

(b) Lateral bond rupture force for $k_+ = 4\,\mathrm{s}^{-1}\,\mu\mathrm{M}^{-1}$.

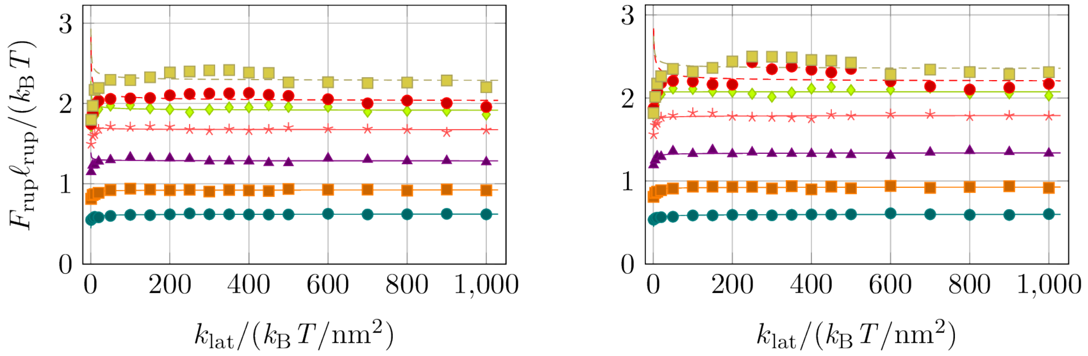

(c) Lateral bond rupture energy for $k_+ = 2\,\mathrm{s}^{-1}\,\mu\mathrm{M}^{-1}$.

(d) Lateral bond rupture energy for $k_+ = 4\,\mathrm{s}^{-1}\,\mu\mathrm{M}^{-1}$.

Figure 4.6: Lateral bond rupture force F_{rup} and lateral bond rupture energy $F_{\mathrm{rup}}\ell_{\mathrm{rup}}$ as a function of the lateral spring constant k_{lat} for our two values of k_+, different values of $\Delta G^{0*}_{\mathrm{long}}$, and $c_{\mathrm{tub}} = 10\,\mu\mathrm{M}$.

as predicted by (4.8). The values of these fit parameters can be found in Table C.4. From these results, we can already deduce that (4.7) is not strictly fulfilled. Instead, it should follow

$$F_{\mathrm{rup}}(k_{\mathrm{lat}})\ell_{\mathrm{rup}}(k_{\mathrm{lat}}) = \frac{c_{\mathrm{rup}}}{\sqrt{k_{\mathrm{lat}}}} + d_{\mathrm{rup}} \tag{4.13}$$

with

$$c_{\mathrm{rup}} = b_{\mathrm{rup}}\sqrt{-2\Delta G^0_{\mathrm{lat}}}, \tag{4.14}$$

$$d_{\mathrm{rup}} = a_{\mathrm{rup}}\sqrt{-2\Delta G^0_{\mathrm{lat}}}. \tag{4.15}$$

Figure 4.6(c) and Figure 4.6(d) show that except for small values of k_{lat}, the data points follow (4.13). The fact that some of the functions shown in Figure 4.6(c) and Figure 4.6(d) are monotonically decreasing instead of monotonically increasing like the data is due to the fit constant b_{rup} in (4.12) being negative resulting in a negative factor c_{rup} before the inverse root

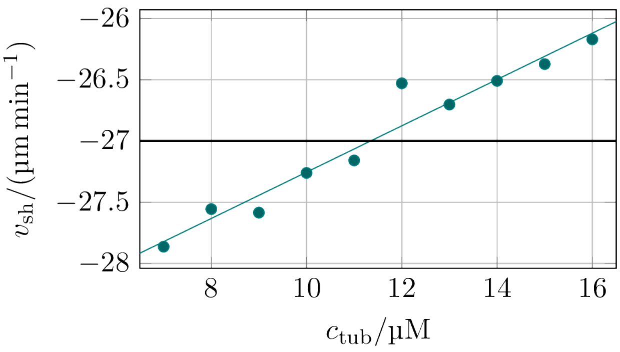

Figure 4.7: The shrinkage velocity v_sh shows a linear dependence on the free GTP-tubulin dimer concentration c_tub. 100 simulations for each c_tub value were run with $k_+ = 4\,\mathrm{s^{-1}\,\mu M^{-1}}$, $\Delta G^{0*}_\mathrm{long} = -9.3\,k_\mathrm{B}T$, and $k_\mathrm{lat} = 1\,k_\mathrm{B}T/\mathrm{nm}^2$.

function in (4.13)[2]. Apart from the deviations at small values of k_lat, overall, $(F_\mathrm{rup}\ell_\mathrm{rup})(k_\mathrm{lat})$ is mostly constant, as expected.

Lastly, we have to go back to the beginning of this section and to how we determined the values of the shrinkage parameters: We compared the shrinkage velocity v_sh at different free GTP-tubulin dimer concentrations c_tub with the experimental value from Walker et al. in (4.2). As the experimentally measured v_sh does not depend on c_tub, we also used

$$v_\mathrm{sh}(c_\mathrm{tub}) = \mathrm{const} \tag{4.16}$$

to determine v_sh for a given set of parameter values. In reality, however, we find that the microtubules in our simulations shrink slower if c_tub is increased instead of (4.16) as shown in Figure 4.7. Compared to the dependence of the growth velocity v_gr on c_tub, see (4.1), the slope in Figure 4.7 is only $0.19\,\mathrm{\mu m\,min^{-1}\,\mu M^{-1}}$, i.e., about half of the slope for growth. To confirm that this dependence is directly due to the greater number of tubulin dimers polymerizing onto the microtubule if c_tub is increased, we calculated the average number of polymerization events $\langle N_\mathrm{poly}\rangle$, depolymerization events $\langle N_\mathrm{depoly}\rangle$, lateral bond formation events $\langle N_\mathrm{form}\rangle$, and lateral bond rupture events $\langle N_\mathrm{rup}\rangle$. The data in Figure 4.8(a) shows that, expectedly, the average number of polymerization events $\langle N_\mathrm{poly}\rangle$ increases linearly with the shrinkage velocity v_sh and thus also increases linearly with c_tub. The additional plots in Figure 4.8 show that the average number of all relevant events increases linearly with v_sh so that increasing c_tub does not simply result in newly attached GTP-tubulin dimers simply depolymerizing again. Instead, as seen by the increase in the average number of lateral bond formation and rupture events in Figure 4.8(c) and Figure 4.8(d), these new GTP-tubulin dimers can also be stabilized laterally requiring additional time for these lateral bonds to rupture again before depolymerization and thus making the shrinkage process slower.

Lastly, we have to compare our values for the mechanical parameters k_lat and κ with other publications. Before doing so, however, we have to mention two aspects: First, as shown in Figure 4.5, we were not able to determine one set of such parameters due to the limited amount of data but only κ as a function of k_lat. Second, a direct comparison with other values is not always possible due to different modeling or different ways of obtaining the mechanical parameter values. In general, values $k_\mathrm{lat} \ll 1000\,k_\mathrm{B}T/\mathrm{nm}^2$ and $\kappa \ll 1000\,k_\mathrm{B}T/\mathrm{nm}^2$ are found[118,175,194],

---

[2] If c_rup and d_rup in (4.13) were treated as fit parameters instead of using (4.14) and (4.15), the monotonicity of the fit function would match the monotonicity of the data, of course.

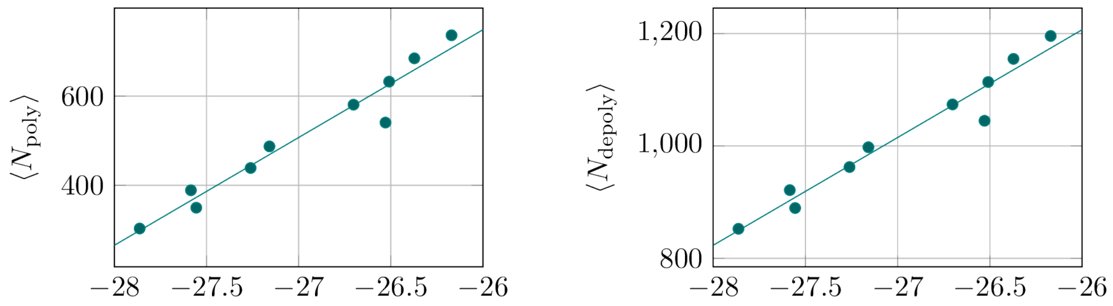

(a) Polymerization.

(b) Depolymerization.

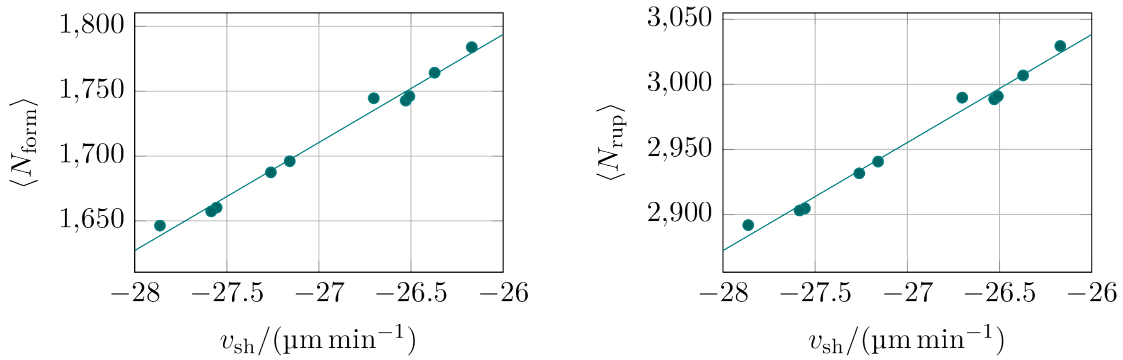

(c) Lateral bond formation.

(d) Lateral bond rupture.

Figure 4.8: Average number of different simulation events as a function of the shrinkage velocity v_{sh} using the same simulation data as in Figure 4.7.

though there are also some publications getting larger values[142,143]. The bending constant κ can be calculated[121] from the fluctuations of MD simulation data[195] resulting in a relatively small value of $\kappa \simeq 50\,k_{\mathrm{B}}T/\mathrm{rad}^2$.

The persistence length L_{p} of a flexible polymer relates to its bending rigidity K_{b} via[196]

$$L_{\mathrm{p}} = \frac{K_{\mathrm{b}}}{k_{\mathrm{B}}T} \tag{4.17}$$

from which the harmonic bending energy follows as[196]:

$$E_{\mathrm{bend}} = \frac{1}{2}\frac{K_{\mathrm{b}}}{\ell_{\mathrm{tub}}}\psi^2, \tag{4.18}$$

where we already have replaced the general segment length of the polymer bonds with the tubulin monomer length ℓ_{tub}. Comparing (4.18) to our bending energy (2.26) results in a relation between our bending constant κ and the persistence length:

$$\kappa = \frac{L_{\mathrm{p}}}{\ell_{\mathrm{tub}}}k_{\mathrm{B}}T. \tag{4.19}$$

MD simulations of individual protofilaments[143] yield a persistence length for protofilaments of $L_{\mathrm{p}} \simeq 6\,\mu\mathrm{m}$ resulting in a much larger value of $\kappa \simeq 1500\,k_{\mathrm{B}}T/\mathrm{rad}^2$ via (4.19).

Alternatively, the persistence length can also be calculated from the exponential decay of a polymer's orientation correlation function[196]

$$\langle \hat{\boldsymbol{t}}(s) \cdot \hat{\boldsymbol{t}}(0) \rangle = \exp\left(-\frac{s}{L_\mathrm{p}}\right), \tag{4.20}$$

where $\hat{\boldsymbol{t}}(s)$ is the unit tangent vector along the polymer at the polymer contour position s. By measuring the angles of bent protofilament ends, McIntosh et al.[63] were able to calculate the persistence length of protofilaments as $L_\mathrm{p} \simeq 0.2\,\mathrm{\mu m}$ resulting in a much smaller value again of $\kappa \simeq 50\,k_\mathrm{B}T/\mathrm{rad}^2$. (They also briefly discuss microtubule simulations for which they use $\kappa = 58\,k_\mathrm{B}T/\mathrm{rad}^2$.)

While this data shows that our values in Figure 4.5 are generally compatible with other results, we are still not able to definitively determine one set of k_lat and κ parameter values. However, to avoid having to do all of the following analyses with all parameters values (which would lead to an unmanageable number of simulations to run), we focus on one set of parameters shown in Table 4.2 with a value of $\kappa = 149\,k_\mathrm{B}T/\mathrm{rad}^2$ that is closer to the smaller values mentioned before and close to previously used values[118]. In the appendices to the following chapters, we will, however, also present results for some other parameters values of the mechanical parameters k_lat and κ, which do not differ qualitatively from the results presented in the main text.

Model Parameter	**Symbol**	**Standard Set of Values**
longitudinal bond energy	$\Delta G^{0*}_{\mathrm{long}}$	$-9.3\,k_{\mathrm{B}}T$
lateral bond energy	$\Delta G^{0}_{\mathrm{lat}}$	$-1.58\,k_{\mathrm{B}}T$
lateral spring constant	k_{lat}	$100\,k_{\mathrm{B}}T/\mathrm{nm}^2$
bending constant	κ	$149\,k_{\mathrm{B}}T/\mathrm{rad}^2$
pseudo-first-order polymerization rate	k_+	$4\,\mathrm{\mu M}^{-1}\,\mathrm{s}^{-1}$
lateral bond formation attempt rate	k_{att}	$258\,\mathrm{s}^{-1}$
constant hydrolysis rate	k_{h}	$0.1\,\mathrm{s}^{-1}$ to $0.5\,\mathrm{s}^{-1}$
base hydrolysis rate	k^0_{h}	$1\,\mathrm{s}^{-1}$ to $5\,\mathrm{s}^{-1}$

Table 4.2: List of the seven free parameter of our chemomechanical microtubule model and the standard set of their values we will generally be using for the rest of this thesis. (The two hydrolysis rates are counted only as one free parameter because either a constant hydrolysis rate is used or mechanical hydrolysis.)

4.3 Summary

In this chapter, we have seen that we were able, for a given value of the pseudo-first-order polymerization rate k_+, to determine the longitudinal bond energy $\Delta G^{0*}_{\mathrm{long}}$, the lateral bond energy $\Delta G^{0}_{\mathrm{lat}}$, and the lateral bond formation attempt rate k_{att} to match the growth data from Walker et al.[49] Only using their experimental value for the microtubules' shrinkage velocity, we were only able to determine bending constant κ as a function of lateral spring constant k_{lat} still leaving k_{lat} as a free parameter of the model. The influence of a constant hydrolysis rate k_{h} will be discussed in chapter 5 by running "full" simulations with catastrophes and rescues and in chapter 9 via dilution experiments. In chapter 6, we will consider mechanical hydrolysis.

Unless explicitly stated otherwise, we will use the set of parameters values given in Table 4.2.

Microtubule Dynamics

5

After having determined the growth parameters $\Delta G^{0*}_{\mathrm{long}}$, $\Delta G^{0}_{\mathrm{lat}}$, and k_{att} and the shrinkage parameters k_{lat} and κ separately in growth-only and shrinkage-only simulations in chapter 4, we will now bring growing and shrinking microtubules "together" by enabling hydrolysis. Hydrolysis will trigger catastrophes during which microtubules switch from growth to shrinkage. From shrinkage, microtubules are then able to switch back to growth via rescues (or depolymerize completely). Enabling hydrolysis adds another free parameter of model, the hydrolysis rate k_{h}, that we have to consider.

In this chapter, we will focus on the simpler hydrolysis model with a constant hydrolysis rate. In chapter 6, we will consider mechanical hydrolysis.

5.1 Hydrolysis Rate Value and Catastrophe Rate

Direct measurements of the hydrolysis rate in microtubules has not been possible yet. Experiments trying to gain insight into the hydrolysis mechanism generally rely on measuring the concentration of inorganic phosphate P_i in the solution over time[167,171,197,198]. To interpret this data, however, assumptions have to be made on how to translate this data into a hydrolysis rate (or into the individual rates of a multi-step hydrolysis process). In particular, it is relevant whether a vectorial model or a random model is used to match the experimental data because in a vectorial model, the maximum number of GTP-tubulin dimers that can hydrolyze equals the number of protofilaments while in a random model, (almost) all GTP-tubulin dimers can hydrolyze.

Melki et al. found that "the time course of tubulin polymerization [...] and of P_i release [...] demonstrates that P_i release occurs with a delay of 2 s following the onset of assembly"[171]. This finding has been used[99,126] to deduce a random hydrolysis rate of $k_{\mathrm{h}} = 0.5\,\mathrm{s}^{-1}$, which is of the same order as k_{h} values used in other publications, see Table 5.1. It must be emphasized, that several of the k_{h} values in Table 5.1 are extracted from simulations and chosen so that the simulated microtubule dynamics fulfill certain, publication-specific criteria. Except for the relatively high value of $k_{\mathrm{h}} = 0.95\,\mathrm{s}^{-1}$ from VanBuren et al.[104,118], the hydrolysis rates generally fall into the range of $0.1\,\mathrm{s}^{-1}$ to $0.5\,\mathrm{s}^{-1}$, which is the range we will choose our hydrolysis rates from in the following discussion.

As hydrolysis is the reason for the disappearance of the GTP-cap, hydrolysis and catastrophes are closely coupled. The catastrophe rate ω_{cat} indicates how often a catastrophe occurs. The inverse of ω_{cat}, $t_{\mathrm{cat}} = \omega_{\mathrm{cat}}^{-1}$, is the time a microtubule grows until it, on average, undergoes a catastrophe. Measurements of the catastrophe rate ω_{cat} as a function of the free GTP-tubulin dimer concentration c_{tub} have shown that ω_{cat} decreases as c_{tub} increases[49,189,190,199]. This dependence can understood quantitatively by considering the stabilizing GTP-cap: the GTP-cap length increases with c_{tub} (which we will discuss in more detail in section 7.2), and a longer GTP-cap make catastrophes more unlikely. Measurements of the catastrophe rate

k_h/s^{-1}	**Origin**	**Source**
0.95	simulations	[104,118]
0.3	simulations	[106]
0.20/0.25	simulations	[111]
0.20/0.25/0.7	simulations	[112]
0.20/0.25	simulations	[94,95]
0.26	estimate from microtubule lifetimes[49]	[79]
0.2–0.5	simulations	[120]
0.5	based on Melki et al.[171]	[99,126]
0.11/9	based on Gardner et al.[199]	[126]
0.14	simulations	[109]

Table 5.1: Overview of random hydrolysis rates used by or gotten from simulations by other publications.

ω_{cat} at individual concentrations c_{tub} in other experiments[48,192,200–205] are of the same order and generally $\omega_{\mathrm{cat}} < 1\,\mathrm{min}^{-1}$. For example, the fit to the catastrophe rate data of Walker et al.[49] predict a catastrophe rate of $\omega_{\mathrm{cat}} = 0.33\,\mathrm{min}^{-1}$ at $c_{\mathrm{tub}} = 7\,\mu\mathrm{M}$ and $\omega_{\mathrm{cat}} = 0.05\,\mathrm{min}^{-1}$ at $c_{\mathrm{tub}} = 16\,\mu\mathrm{M}$. These small catastrophe rates highlight the need for computationally fast simulations, which allow simulating minutes of microtubule dynamics at acceptable runtimes to observe catastrophes at such rates. To circumvent having to simulate several minutes of microtubule dynamics, Zakharov et al.[126] used much higher hydrolysis rates between $3\,\mathrm{s}^{-1}$ to $11\,\mathrm{s}^{-1}$ resulting in a much higher catastrophe rate ω_{cat}. As they found a linear $\omega_{\mathrm{cat}}(k_h)$ dependence, they calculated $k_h = 0.11\,\mathrm{s}^{-1}$ to match the catastrophe rate found by Gardner et al.[199] When they were not specifically investigating catastrophes, however, Zakharov et al. used $k_h = 0.5\,\mathrm{s}^{-1}$. For catastrophe-specific investigations, they used $k_h = 9\,\mathrm{s}^{-1}$ and then they normalized their data “by ‘slowing down’ the modeling time by a factor of 82 (ratio of the accelerated to experimental hydrolysis rate constants) prior to plotting”[126]. In the next section in which microtubule growth trajectories generated by our simulation are shown for different hydrolysis rates, we will see that we are not able to do the same as already for hydrolysis rates much smaller than $k_h = 9\,\mathrm{s}^{-1}$, the microtubules simply shrink without any growth phase. The reason why Zakharov et al. are able to use such a procedure and we are unable to do so is unknown, but it could potentially be due to the different models used.

5.2 Microtubules Undergo Catastrophes and Rescues

Based on the hydrolysis rate range mentioned in the previous section, we ran 20 simulations for each parameter set with $N_{\mathrm{GDP}} = 20$ and $N_{\mathrm{GTP}} = 10$ and the results in Figure 5.1 show the ability of our program to simulate several minutes of microtubule dynamics so that the microtubules are able to undergo catastrophes and rescues. To get an idea of the performance of the simulation, Figure 5.2(c) shows the ratio of average run time t_{run} and the simulated time t_{sim} of the simulations shown in Figure 5.1. Even though the individual simulations ran on different processor architectures with different performances, the results in Figure 5.2(c) give a good indication that the simulations require at most 600 times the runtime t_{run} for a given maximum final simulation time t_{sim} (and for hydrolysis rates $k_{\mathrm{h}} \geq 0.2\,\mathrm{s}^{-1}$, the simulations require at most 200 times the runtime t_{run} for a given maximum final simulation time t_{sim}).

In section D.1, there are additional microtubule trajectories like in Figure 5.1 but for different values of the lateral spring constant k_{lat} (and in Figure D.2 also for a longer initial GTP-cap). The additional runtime data shown in Figure 5.2 for these additional k_{lat} values show that increasing k_{lat} (and thus increasing κ as well, see Figure 4.5) also slows down the simulation due to the need for more iterations per energy minimization.

Before we determine the catastrophe and rescue rates from the simulations shown in Figure 5.1 in section 5.4, we first focus on the influence of the hydrolysis rate value on the growth velocity of the simulated microtubules.

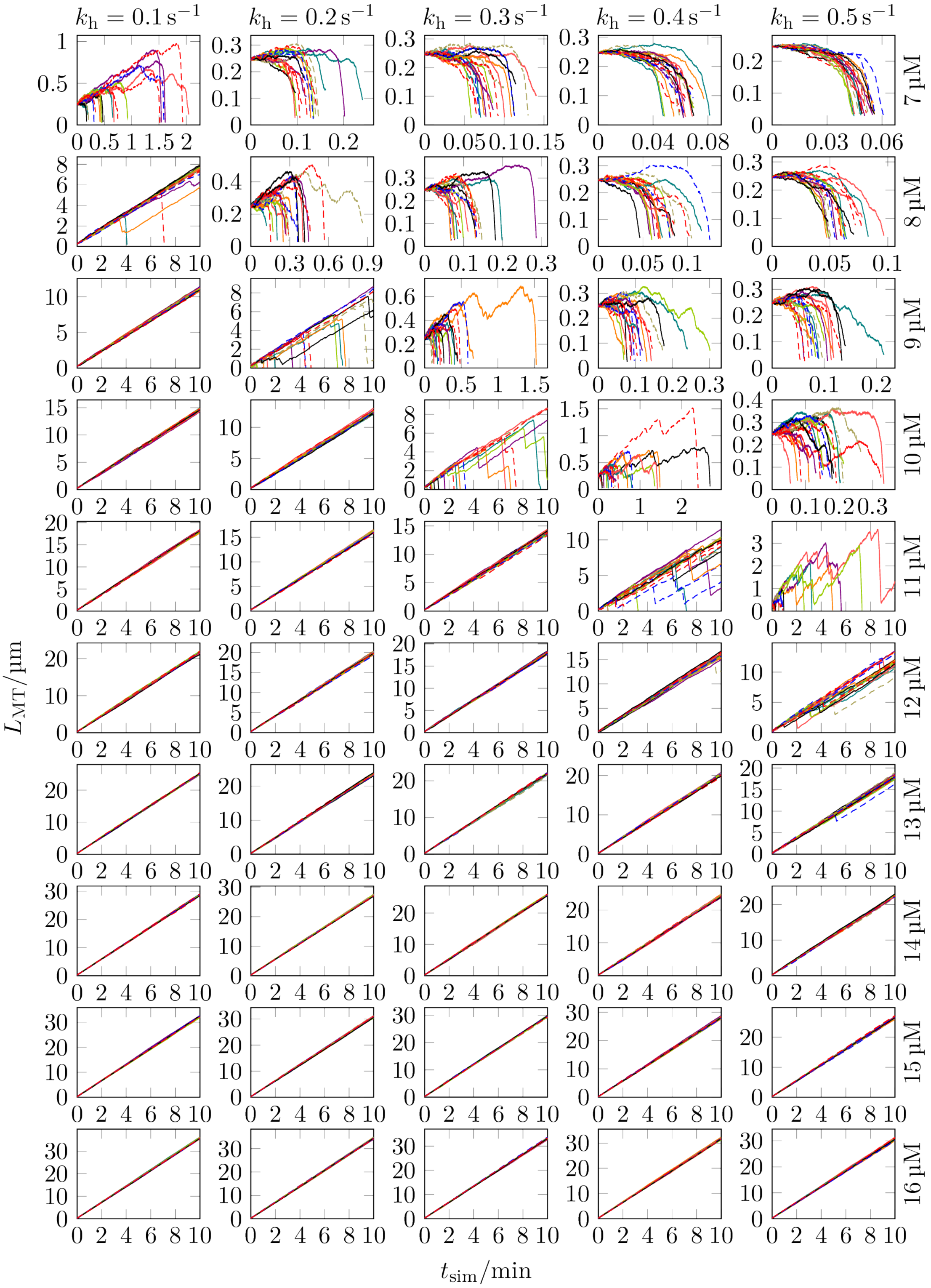

Figure 5.1: Microtubule growth trajectories of 20 different simulations for each of the considered values of the free GTP-tubulin dimer concentration c_{tub} and the hydrolysis rate k_h.

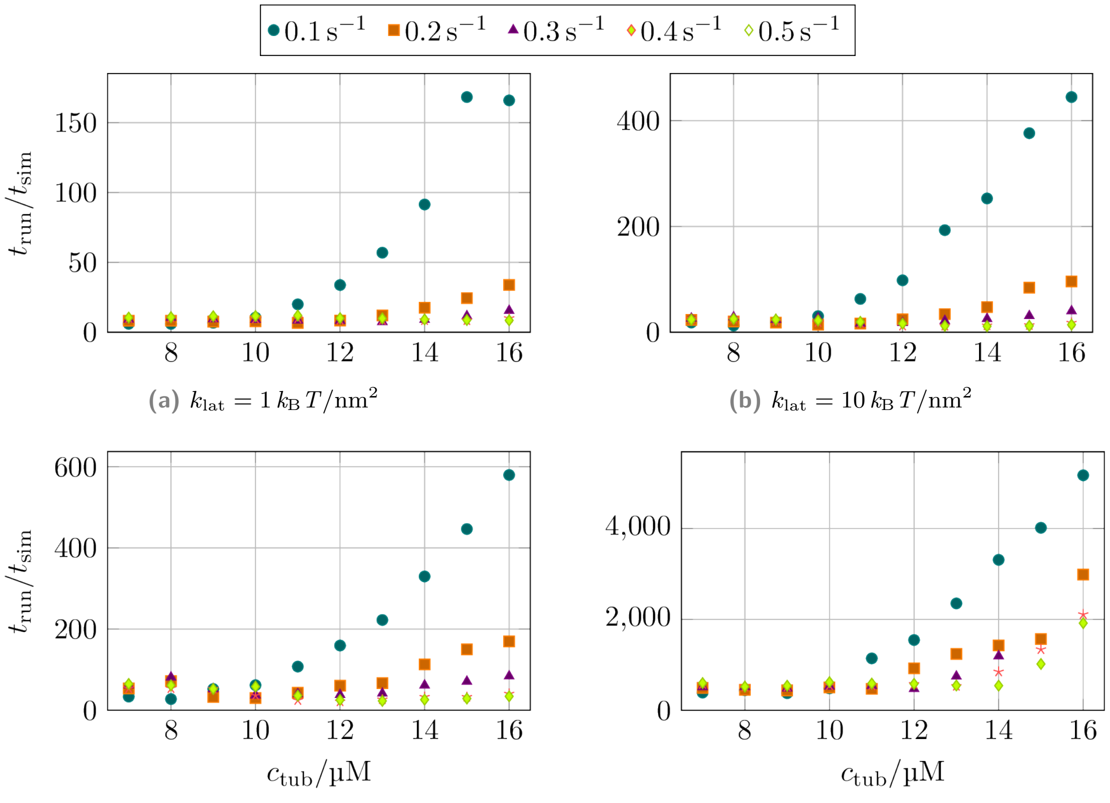

(a) $k_{\text{lat}} = 1\, k_{\text{B}}\, T/\text{nm}^2$

(b) $k_{\text{lat}} = 10\, k_{\text{B}}\, T/\text{nm}^2$

(c) $k_{\text{lat}} = 100\, k_{\text{B}}\, T/\text{nm}^2$

(d) $k_{\text{lat}} = 20\,000\, k_{\text{B}}\, T/\text{nm}^2$

Figure 5.2: The ratio of the average run time t_{run} and the simulated time t_{sim} of the simulations shown in Figure D.1, Figure D.3, and Figure D.4 for different lateral spring constants k_{lat} and hydrolysis rates k_{h} increases with the free GTP-tubulin dimer concentration c_{tub} and with k_{lat}. A higher value of c_{tub} results in a higher the rate of polymerization k_{on}, i.e., more events in the same amount of time, and a higher value of k_{lat} also results in a higher ratio because of more iterations per minimization.

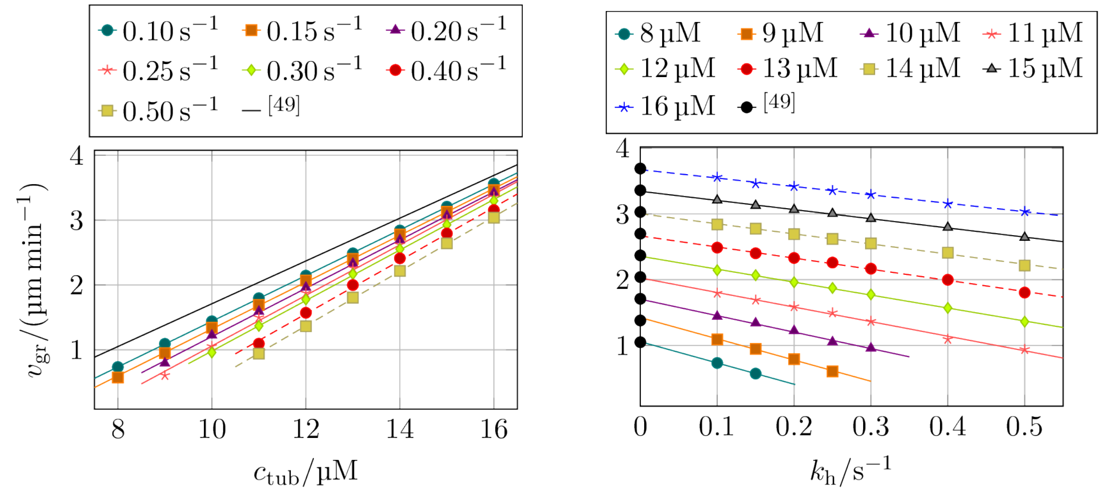

(a) Microtubule growth velocity v_{gr} as a function of the free GTP-tubulin dimer concentration c_{tub} for different hydrolysis rates k_h.

(b) Microtubule growth velocity v_{gr} as a function of the hydrolysis rates k_h for different free GTP-tubulin dimer concentrations c_{tub}.

Figure 5.3: Increasing the hydrolysis rates k_h results in a linear decrease of the microtubule growth velocity v_{gr} but also still results in a linear $v_{gr}(c_{tub})$ relation like the experimental data by Walker et al.[49]

5.3 Influence of the Hydrolysis Rates on the Growth Velocity

When we determined the growth parameters that reproduce the experimentally measured growth velocities (4.1), we did so without hydrolysis in section 4.1 to avoid having to search for parameter values in a much larger parameter space. Now with hydrolysis enabled, an interesting question is to check the validity of the divide-and-conquer approach by determining the growth velocity v_{gr} for different hydrolysis rates and comparing the results to (4.1). Taking a closer look at the final length of the microtubules shown in the last row of Figure 5.1 already shows that increasing the hydrolysis rate does have an effect on the growth velocity by decreasing it.

Figure 5.3(a) shows that while $v_{gr}(c_{tub})$ is still linear, it no longer matches the experimental data by Walker et al.[49], which were used to determine the values of the growth parameters. The higher the hydrolysis rates, the greater is the deviation of the growth velocity v_{gr} from the experimental data. If the data in Figure 5.3(a) is plotted as a function of the hydrolysis rate instead of the free GTP-tubulin dimer concentration c_{tub}, as was done in Figure 5.3(b), it is evident that there is a linear relation between v_{gr} and k_h. Figure 5.3(b) also shows that the decrease in the growth velocity while increasing the hydrolysis rate is entirely due to the presence of hydrolysis as the experimental data are on the fit lines at $k_h = 0$. (As the experimental data by Walker et al.[49] is based on real microtubules, they, of course, also account for the presence of hydrolysis at a certain rate $k_h > 0$. We, however, used their growth velocity relation (4.1) with $k_h = 0$ to determine the growth parameters so that the expected result *is* to

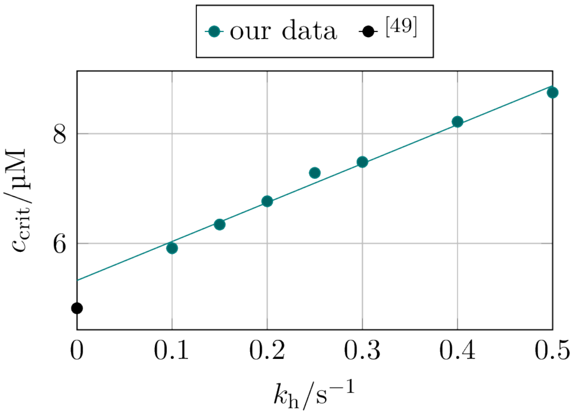

Figure 5.4: The critical GTP-tubulin dimer concentration c_{crit} calculated from the growth velocity as a function of the free GTP-tubulin dimer concentration c_{tub} in Figure 5.3(a) increases for greater hydrolysis rates k_{h}.

find the experimental data on the fit lines at $k_{\mathrm{h}} = 0$.)

From the data in Figure 5.3(a), the critical GTP-tubulin dimer concentration c_{crit} for each hydrolysis rate k_{h} can be calculated. Figure 5.4 shows that there is a linear relation between c_{crit} and k_{h} and that the linear fit only has small deviation from the experimental value $c_{\mathrm{crit}} = 4.8\,\mu\mathrm{M}$ by Walker et al.[49] This increase of c_{crit} with k_{h} has already been seen in Figure 5.1, where most microtubules can grow the full ten minutes of simulation time already at $c_{\mathrm{tub}} = 8\,\mu\mathrm{M}$ for $k_{\mathrm{h}} = 0.1\,\mathrm{s}^{-1}$, while for $k_{\mathrm{h}} = 0.5\,\mathrm{s}^{-1}$, such prolonged growth is only possible starting at $c_{\mathrm{tub}} = 12\,\mu\mathrm{M}$.

The decrease of the growth velocity v_{gr} for increasing hydrolysis rates k_{h} as shown in Figure 5.3(b) is due to the higher probability of terminal tubulin dimers being hydrolyzed. As such tubulin dimers prefer to be bent, they stretch the lateral springs to their neighbors, which increases the rate of bond rupture making it ultimately more likely for them to depolymerize. (Even though in our model, a newly polymerized GTP-tubulin directly at the tip of a protofilament is not allowed to hydrolyze as explained in subsection 2.3.3, it enables the previous GTP-tubulin dimer to hydrolyze. If after the hydrolysis event, the terminal GTP-tubulin depolymerizes, there is now a GDP-tubulin dimer at the protofilament tip.) If a terminal tubulin dimer of a protofilament is hydrolyzed, the cap length of this protofilament is $N_{\mathrm{cap}} = 0$. Thus, it makes sense to analyze the cap length N_{cap} as a function of the hydrolysis rate k_{h}. The cap length N_{cap} is the number of consecutive GTP-tubulin dimers at the plus end of a protofilament or, depending on the context, the average number of consecutive GTP-tubulin dimers per protofilament at the plus end of the microtubule. As expected, the cap length N_{cap} decreases if the hydrolysis rate k_{h} is increased, see Figure 5.5(a). Additionally, the cap length increases for higher free GTP-tubulin dimer concentrations c_{tub} as a higher c_{tub} means that there a more GTP-tubulin dimers polymerizing onto the microtubules.

The data in Figure 5.5 are averages over the whole course of multiple simulations, which also results in an average over different growth states. In the shrinking state, the GTP-cap is significantly shorter than in the growing state so that the cap lengths in Figure 5.5(a) can be regarded as lower limits for the cap length in the growing state. Similarly, the probability for a terminal GDP-tubulin dimer is higher in the shrinkage state than in the growth state, so that the probabilities in Figure 5.5(b) are upper limits for the probability for a terminal GDP-tubulin

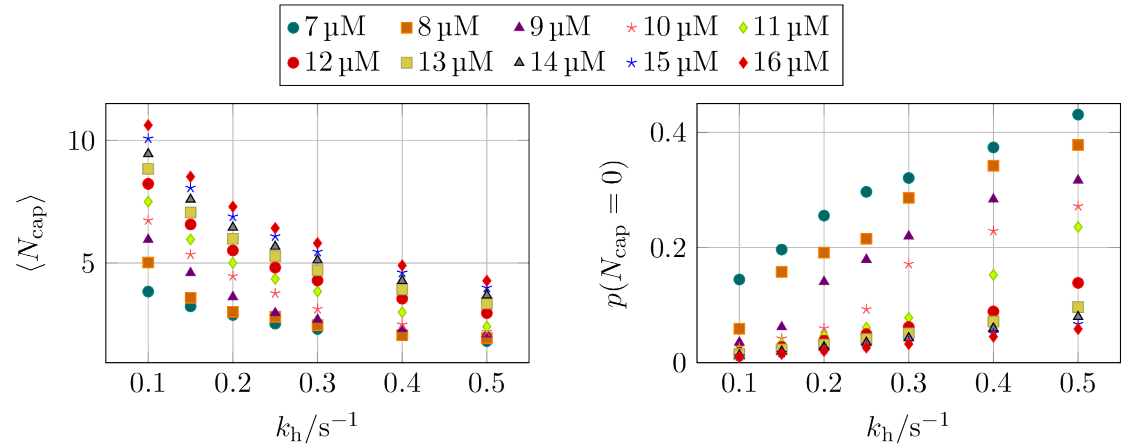

(a) The average GTP-cap length N_{cap} decreases with increasing hydrolysis rates k_{h} and increases for higher free GTP-tubulin dimer concentrations c_{tub}.

(b) The probability of the terminal tubulin dimer being hydrolyzed, i.e., the probability of there being no cap, $p(N_{\mathrm{cap}} = 0)$, increases with the hydrolysis rate k_{h} and decreases for higher free GTP-tubulin dimer concentrations c_{tub}.

Figure 5.5: Influence of the hydrolysis rate on the microtubule tip for different concentrations c_{tub}.

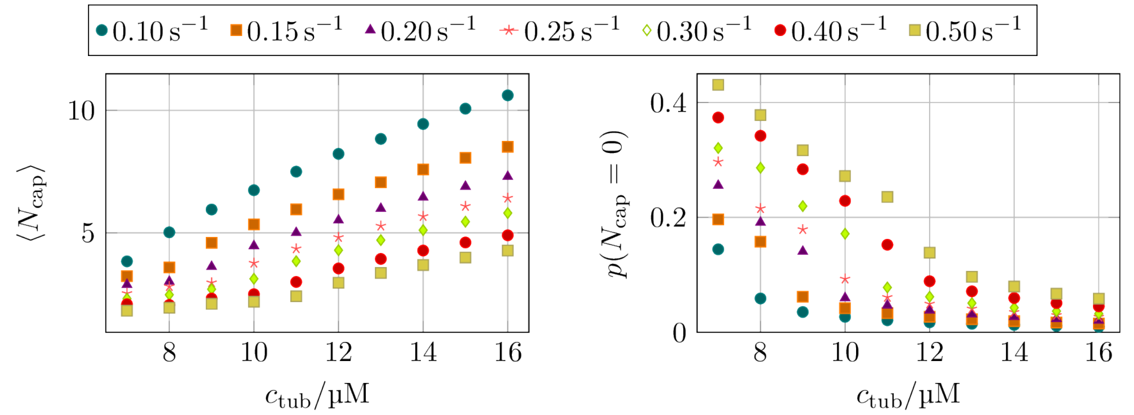

(a) The average GTP-cap length $\langle N_{\mathrm{cap}} \rangle$ increases with higher free GTP-tubulin dimer concentrations c_{tub}.

(b) The probability of the terminal tubulin dimer being hydrolyzed, $p(N_{\mathrm{cap}} = 0)$, decreases for higher free GTP-tubulin dimer concentrations c_{tub}.

Figure 5.6: The same data as in Figure 5.5 but now as a function of the free GTP-tubulin dimer concentration c_{tub}.

dimer in the growing state. To get a better understanding that this averaging affects the results, it is sufficient to plot the data in Figure 5.5 not as a function of the hydrolysis rate k_{h} but as a function of the free GTP-tubulin dimer concentration c_{tub} as shown in Figure 5.6. For c_{tub} below or near the critical concentration c_{crit} shown in Figure 5.4, N_{cap} only increases weakly with c_{tub}. For $c_{\mathrm{tub}} > c_{\mathrm{crit}}$, the slope increases. In the simulations with $c_{\mathrm{tub}} < c_{\mathrm{crit}}$, a $N_{\mathrm{cap}} > 0$

value is due to the initial GTP-cap at the start of the simulation that is hydrolyzed before and during the shrinkage of the microtubule. The same effect is visible for the probability of the terminal tubulin dimer being hydrolyzed in Figure 5.6(b) as a discontinuity in the data near $c_{\mathrm{tub}} = c_{\mathrm{crit}}$. As the goal of this microtubule tip analysis only was to explain how the hydrolysis rate k_{h} influences the growth velocity v_{gr} as shown in Figure 5.3, this level of analysis is sufficient, even though the data is averaged over difference growth phases.

In section 7.2, we will come back to the GTP-cap and show that the dependence of $\langle N_{\mathrm{cap}} \rangle$ on k_{h} as shown in Figure 5.5(a) and on c_{tub} as shown in Figure 5.6(a) is expected.

5.4 Catastrophe and Rescue Rates

In Figure 5.1, we have shown many microtubule trajectories. To calculate catastrophe rates ω_{cat} and rescue rates ω_{res}, we have to identify catastrophes and rescues in these trajectories and determine the previous time interval during which the microtubule was growing or shrinking, respectively. Identifying them by hand is too cumbersome for a large number of simulations and can also result in biased decisions of whether catastrophe followed by a rescue is identified or whether it is just a short length fluctuation. Instead, we deployed a simple algorithm presented in subsection 5.4.1 to classify catastrophes and rescue and then calculate the catastrophe rates ω_{cat} and rescue rates ω_{res} based on this classification. Recently, a more sophisticated program based on machine learning[206,207] was introduced for the same classification, which will result in better classifications and thus better results than we do here but has also required much more time to develop than our simple algorithm.

5.4.1 Algorithm for Catastrophe and Rescue Identification

The simulations produce lists of simulation time and microtubule length tuples $\{(L_{\mathrm{MT},i}, t_{\mathrm{sim},i})\}$. The first part of the following algorithm to calculate catastrophe and rescue rates is to determine the times $\{\tau_{\mathrm{cat},j}\}$ and $\{\tau_{\mathrm{resc},j}\}$ at which catastrophes and rescues happen, respectively. The second part is then to calculate the periods of time the microtubule grows $\Delta t_{\mathrm{gr},k}$ and the periods of time the microtubule shrinks $\Delta t_{\mathrm{sh},k}$ from which the catastrophe and rescue rate can be calculated via[87]

$$\omega_{\mathrm{cat}} = \left(\frac{1}{N_{\mathrm{cat}}} \sum_{k=1}^{N_{\mathrm{cat}}} \Delta t_{\mathrm{gr},k} \right)^{-1}, \tag{5.1}$$

$$\omega_{\mathrm{res}} = \left(\frac{1}{N_{\mathrm{resc}}} \sum_{k=1}^{N_{\mathrm{resc}}} \Delta t_{\mathrm{sh},k} \right)^{-1}, \tag{5.2}$$

respectively. N_{cat} is the number of catastrophes and N_{resc} is the number of rescues. In the following description, we will use two different length increments, $\Delta\ell_1 = 50\,\mathrm{nm}$ and $\Delta\ell_2 = 300\,\mathrm{nm}$ for which we have explicitly chosen $\Delta\ell_1 < \Delta\ell_2$ for reasons that will become clear during the discussion of the algorithm.

The algorithm starts with the first data tuple with $i = 0$ and then iterates over all data tuples $\{(L_{\mathrm{MT},i}, t_{\mathrm{sim},i})\}$. Additionally, $i_0 = 0$ is set, which denotes the previous cutoff point. In the beginning, no cutoffs have been made, thus $i_0 \coloneqq 0$ is used. i continues to be increased until the microtubule has grown or shrunk by $\Delta\ell_1$ since the last cutoff, i.e., until $L_{\mathrm{MT},i} - L_{\mathrm{MT},i_0} \geq \Delta\ell_1$ or $L_{\mathrm{MT},i} - L_{\mathrm{MT},i_0} \leq -\Delta\ell_1$. In the first case, $L_{\mathrm{MT},i} - L_{\mathrm{MT},i_0} \geq \Delta\ell_1$, the microtubule has grown sufficiently so that the interval $[i_0, i]$ is marked as a growth interval. In the second case, $L_{\mathrm{MT},i} - L_{\mathrm{MT},i_0} \leq -\Delta\ell_1$, the interval $[i_0, i]$ is marked as a shrinkage interval. By setting $i_0 \coloneqq i$, we "cut off" this interval and start a new one. It should be noted that this classification "absorbs" plateaus, i.e., periods in which the microtubule stays roughly constant, into the surrounding interval. If the $(n-1)$-th interval is classified as a growth interval and the n-th interval is classified as a shrinkage interval, the n-th interval is bookmarked as potentially containing a catastrophe. Vice versa, if the $(n-1)$-th interval is classified as a shrinkage interval and the n-th interval is classified as a growth interval, the n-th interval is bookmarked as potentially containing a rescue. A consequence of this approach is that, like in reality, potential catastrophes and rescues are always alternating.

Before we continue explaining how we proceed with this preliminary classification, we want to clarify two minor aspects:

1. In the previous two examples of classifying the n-th interval to potentially containing a catastrophe or a rescue, we intentionally chose the n-th interval and neither the $(n-1)$-th interval nor combining both intervals and then bookmarking this merged interval. For the $(n-1)$-th interval to be marked as a growth interval, the length difference between the last two data tuples in this interval must have been positive for the length difference between the first and last data tuples in this interval to exceed the threshold length difference $\Delta\ell_1$. In the general case, the microtubule will continue growing at the beginning of the n-th interval and then shrink until the threshold length difference $-\Delta\ell_1$ is met. In this case, the switch between growth and shrinkage happens in this n-th interval and the classification is correct. In the extreme edge case of the microtubule starting to shrink between the first two data tuples in the n-th interval, the catastrophe happens directly at the *common* border between the two intervals so that marking the n-th interval is also correct.

2. The last data tuples $\{(L_{\mathrm{MT},i}, t_{\mathrm{sim},i})\}$ will generally not be included in any interval because the length change of the microtubule will not be sufficient for either classification resulting in unclassified data. There are, however, two reasons why this leftover data is no problem: Firstly, if the remaining data would be classified as the opposite growth type as the previous interval, there would not be enough “surrounding” data to validate whether a catastrophe or rescue really occurred or whether it was just a local fluctuation. Secondly, the fine-grained analysis of the preliminary classification, which we will describe next, will also take this leftover data into consideration so that the lack of classification of these last data tuples will have no effect on the analysis of the previous intervals.

The result of this first part is a list of intervals $\{[c_{1,m}, c_{2,m}]\}$ with potential catastrophes and a list of intervals $\{[r_{1,m}, r_{2,m}]\}$ with potential rescues. We initially mentioned that $\Delta\ell_1 < \Delta\ell_2$ so that these initial preliminary classifications using $\Delta\ell_1$ are done more greedily (i.e., small fluctuations can already lead to a classification as a potential catastrophe or rescue) so that we can filter them in the second part with a higher threshold for the relevant length differences.

In the second part of the algorithm, first, we iterate over all catastrophe intervals $\{[c_{1,m}, c_{2,m}]\}$ and then per catastrophe interval iterate over all indices within the interval $k \in [c_{1,m}, c_{2,m}]$. For k, we now determine an interval $[k_-, k_+]$ around k so that the microtubule grows by $\Delta\ell_2$ in the subinterval $[k_-, k]$ and shrinks by $\Delta\ell_2$ in the following subinterval $[k, k_+]$, i.e., $L_{\mathrm{MT},k} - L_{\mathrm{MT},k_-} \geq \Delta\ell_2$ and $L_{\mathrm{MT},k_+} - L_{\mathrm{MT},k} \leq -\Delta\ell_2$. To avoid going back and forth too far, for example to $k_- = 0$, which would, on the one hand, worsen the classifications, and on the other hand massively increase the runtime of the analysis script, we use a threshold criterion for the time differences $|t_{k_\pm} - t_k|$. If $t_k - t_{k_-} > \Delta t_{\max}$, we skip the current k as there was no sufficient growth before k required for a catastrophe event, i.e., the microtubule did not grow by $\Delta\ell_2$ within the previous $\Delta t_{\max} = 50\,\mathrm{s}$. To keep the target interval $[k_-, k_+]$ as small as possible, we select the largest value of k_- fulfilling $L_{\mathrm{MT},k} - L_{\mathrm{MT},k_-} \geq \Delta\ell_2$. Once k_- is

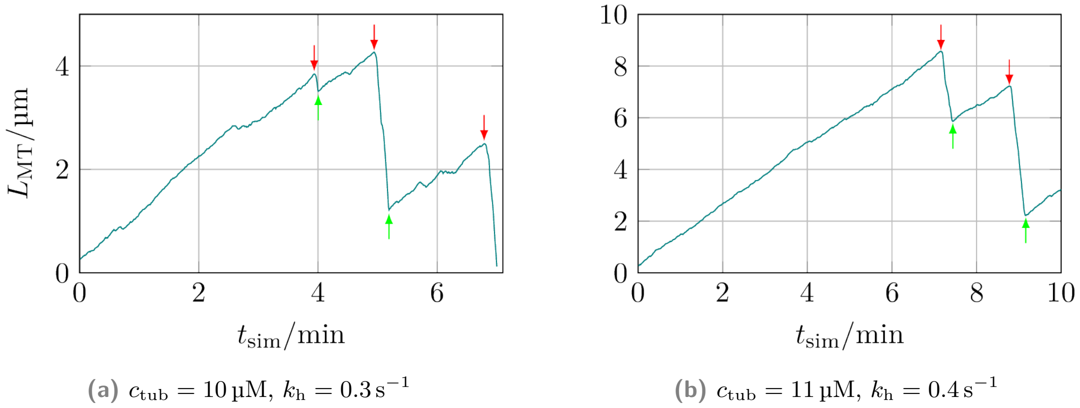

(a) $c_{\text{tub}} = 10\,\mu\text{M}$, $k_{\text{h}} = 0.3\,\text{s}^{-1}$ **(b)** $c_{\text{tub}} = 11\,\mu\text{M}$, $k_{\text{h}} = 0.4\,\text{s}^{-1}$

Figure 5.7: Two exemplary microtubule trajectories in which catastrophes and rescues determined by the algorithm are marked by red arrows pointing down and green arrows pointing up, respectively.

determined, the same approach is used for k_+ so that the microtubule's length must change by $L_{\text{MT},k_+} - L_{\text{MT},k} \leq -\Delta\ell_2$. We also use $t_{k_+} - t_k \leq \Delta t_{\text{max}}$ to avoid considering too much of the following data again. If no k_+ can be found, k is skipped. Otherwise, we use the smallest value of k_+ to also keep the second interval $[k, k_+]$ as small as possible. After having checked all $k \in [c_{1,m}, c_{2,m}]$, we select the value of k as the point where the catastrophe happened if both k_- and k_+ values could be determined for k and for which $t_{k_+} - t_{k_-}$ is the smallest. If no $k \in [c_{1,m}, c_{2,m}]$ could be determined fulfilling these criteria, no catastrophe happened in this interval. As rescues follow catastrophes, we can also discard the rescue interval following this catastrophe interval from consideration. After going through all catastrophe intervals $\{[c_{1,m}, c_{2,m}]\}$ as described previously, we repeat the same procedure for the rescue intervals $\{[r_{1,m}, r_{2,m}]\}$ except that the microtubule must have been shrinking before and be growing after the considered $k \in [r_{1,m}, r_{2,m}]$.

As a result of this algorithm, we get a list of indices at which catastrophes occurred and a list of indices at which rescues occurred. Figure 5.7 shows two examples of microtubule trajectories and marks the times determined by the algorithm at which the microtubules underwent catastrophes and rescues with arrows. Having identified catastrophes and rescues, we can calculate the growth times Δt_{gr} and shrinkage times Δt_{sh} used in (5.1) and (5.2) to determine the catastrophe rate ω_{cat} and rescue rate ω_{res}.

5.4.2 Catastrophe and Rescue Rate Values

Table 5.2 contains the catastrophe rates ω_{cat} and rescue rates ω_{res} calculated from the simulations previously shown in Figure 5.1. In Figure 5.8, we have plotted these values and the experimental results by Walker et al.[49] for comparison. While the values of both rates that we were able to measure are of the same order as the experimental values and generally follow the same trend (ω_{cat} decreasing and ω_{res} increasing with c_{tub}), we are unable to reproduce the same overall dependence of the rates on the free GTP-tubulin dimer concentration c_{tub}. The same also holds true for other mechanical parameters as shown in section D.2.

k_{h} c_{tub}	$0.1\,\mathrm{s}^{-1}$	$0.2\,\mathrm{s}^{-1}$	$0.3\,\mathrm{s}^{-1}$	$0.4\,\mathrm{s}^{-1}$	$0.5\,\mathrm{s}^{-1}$
7 µM	$(0.70\,\mathrm{min}^{-1})$	—	—	—	—
8 µM	$0.02\,\mathrm{min}^{-1}$	—	—	—	—
9 µM	~ 0	$0.15\,\mathrm{min}^{-1}$	—	—	—
10 µM	~ 0	~ 0	$0.24\,\mathrm{min}^{-1}$	$0.89\,\mathrm{min}^{-1}$	—
11 µM	~ 0	~ 0	~ 0	$0.14\,\mathrm{min}^{-1}$	$0.67\,\mathrm{min}^{-1}$
12 µM	~ 0	~ 0	~ 0	~ 0	$0.11\,\mathrm{min}^{-1}$
13 µM	~ 0	~ 0	~ 0	~ 0	$(0.01\,\mathrm{min}^{-1})$
14 µM	~ 0	~ 0	~ 0	~ 0	~ 0
15 µM	~ 0	~ 0	~ 0	~ 0	~ 0
16 µM	~ 0	~ 0	~ 0	~ 0	~ 0

(a) Catastrophe rates ω_{cat} for different free GTP-tubulin dimer concentrations c_{tub} and different hydrolysis rates k_{h}. For parameter combinations with "—" as catastrophe rate, no proper growth phase was observed, so no catastrophe rates could be calculated. "~ 0" is used to denote cases in which microtubules grew during the whole simulation without any catastrophe resulting in catastrophe rates close to zero (at least $\omega_{\mathrm{cat}} \ll 0.01\,\mathrm{min}^{-1}$). For values in parentheses, only one or two catastrophe happened.

k_{h} c_{tub}	$0.1\,\mathrm{s}^{-1}$	$0.2\,\mathrm{s}^{-1}$	$0.3\,\mathrm{s}^{-1}$	$0.4\,\mathrm{s}^{-1}$	$0.5\,\mathrm{s}^{-1}$
7 µM	$(1.06\,\mathrm{min}^{-1})$	—	—	—	—
8 µM	$1.31\,\mathrm{min}^{-1}$	—	—	—	—
9 µM	—	$0.79\,\mathrm{min}^{-1}$	—	—	—
10 µM	—	—	$1.48\,\mathrm{min}^{-1}$	$(0.76\,\mathrm{min}^{-1})$	—
11 µM	—	—	—	$2.98\,\mathrm{min}^{-1}$	$1.76\,\mathrm{min}^{-1}$
12 µM	—	—	—	$(4.32\,\mathrm{min}^{-1})$	$6.88\,\mathrm{min}^{-1}$
13 µM	—	—	—	—	$(7.45\,\mathrm{min}^{-1})$
14 µM	—	—	—	—	—
15 µM	—	—	—	—	—
16 µM	—	—	—	—	—

(b) Rescue rates ω_{res} for different free GTP-tubulin dimer concentrations c_{tub} and different hydrolysis rates k_{h}. For parameter combinations with "—" as rescue rate, no rescues were observed and for values in parentheses only one or two rescues happened.

Table 5.2: Catastrophe rates ω_{cat} and rescue rates ω_{res} for different free GTP-tubulin dimer concentrations c_{tub} and different hydrolysis rates k_{h}.

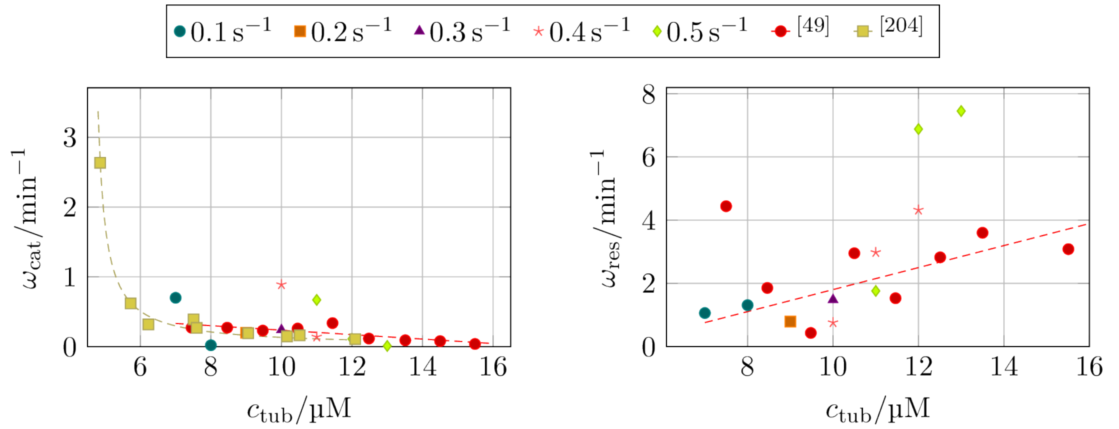

(a) Catastrophe rate ω_{cat} as a function of the free GTP-tubulin dimer concentration c_{tub}.

(b) Rescue rate ω_{res} as a function of the free GTP-tubulin dimer concentration c_{tub}.

Figure 5.8: Comparison between our values for the catastrophe and rescue rates from Table 5.2 and the values measured by Walker et al.[49] and Janson et al.[204]

The catastrophe rates from the data of Janson et al.[204], which is also shown in Figure 5.8, however, imply that the relation between the catastrophe rate ω_{cat} and the free GTP-tubulin dimer concentration c_{tub} is not linear like in Walker et al.[49] but instead follows[208]

$$\omega_{\mathrm{cat}}(c_{\mathrm{tub}}) = \frac{1}{a_{\mathrm{Jan}} c_{\mathrm{tub}} + b_{\mathrm{Jan}}}, \tag{5.3}$$

where a_{Jan} and b_{Jan} are fit parameters. The corresponding curve in Figure 5.8(a) shows that such a relation and the underlying data by Janson et al.[204] do have a steeper dependence of c_{tub} on ω_{cat} like in our data, but the decline in ω_{cat} with increasing values of c_{tub} happens for a smaller value of c_{tub} than in our data.

In summary, the reason why the dependence on c_{tub} for both rates is too steep in our models compared to experimental results[49,199] cannot be explained at the moment but could hint at an underlying problem in the model. Regardless of these discrepancies, it is important to highlight the ability of our simulation program to generate $\omega_{\mathrm{cat}}(c_{\mathrm{tub}})$ and $\omega_{\mathrm{res}}(c_{\mathrm{tub}})$ data in the first place.

Mechanical Hydrolysis

6

In subsection 2.3.4, we have explained how we couple the mechanics of the microtubule to the hydrolysis rate of individual GTP-tubulin dimers via (2.47). In this chapter, we focus on our standard set of parameters with $k_{\mathrm{lat}} = 100\,k_{\mathrm{B}}T/\mathrm{nm}^2$ (see Table 4.2), but in Appendix E, we present additional data for $k_{\mathrm{lat}} = 10\,k_{\mathrm{B}}T/\mathrm{nm}^2$.

6.1 Actual Hydrolysis Rates and Comparison to Constant Hydrolysis Rate

The major difference between the model with a constant hydrolysis rate and a non-constant hydrolysis rate depending on the mechanics is the very fact that in the second case, there is a distribution of rates at which hydrolysis events occur. For the following discussion, we want to remind ourselves that there is a difference between the rates of proposed events and the rates of the events that are actually implemented (see third step of the simulation procedure in section 3.2). Here, the rates of *actually executed hydrolysis events* are relevant from which we calculate the average hydrolysis rate, i.e., we average over multiple simulations with the same parameters and also over the whole microtubule as we do not consider the position of the GTP-tubulin dimer that is hydrolyzed in the microtubule lattice for now. In section 6.2, however, we will investigate how the hydrolysis rate depends on the position of the hydrolyzed GTP-tubulin dimer.

First, we consider how this average hydrolysis rate $\langle k_{\mathrm{h}} \rangle$ depends on the base hydrolysis rate k_{h}^0 that we introduced in (2.47). We find $\langle k_{\mathrm{h}} \rangle (k_{\mathrm{h}}^0)$ to be a linear function of k_{h}^0 for smaller free GTP-tubulin dimer concentrations c_{tub}, as shown in Figure 6.1(a). For larger values of c_{tub}, $\langle k_{\mathrm{h}} \rangle (k_{\mathrm{h}}^0)$ is still linear for larger values of k_{h}^0 but increases slower for smaller values of k_{h}^0.

In Figure 6.1(b), we see that $\langle k_{\mathrm{h}} \rangle (c_{\mathrm{tub}})$ starts at a constant value and then decreases. The initial constant value is a manifestation again of parameter combinations for which the initial microtubule does not grow (i.e., c_{tub} is below the individual critical concentration c_{crit}) so that hydrolysis events only happen in the same initial GTP-cap for all of these c_{tub} values resulting in the same value of $\langle k_{\mathrm{h}} \rangle$.

To compare simulations with a constant hydrolysis rate k_{h} to simulations with mechanical hydrolysis, we selected one pair of constant hydrolysis rate k_{h} and base hydrolysis rate k_{h}^0 so that the average actual hydrolysis rate is close to the constant hydrolysis rate $\langle k_{\mathrm{h}} \rangle \simeq k_{\mathrm{h}}$ for growing microtubules. Figure 6.2 shows that $k_{\mathrm{h}}^0 = 1.5\,\mathrm{s}^{-1}$ results in an average hydrolysis rate $\langle k_{\mathrm{h}} \rangle \simeq 0.25\,\mathrm{s}^{-1}$ for growing microtubules at sufficiently high c_{tub} values. While the average rates are comparable, the length of the porous GTP-cap N_{pcap} reveals that when mechanical hydrolysis is used, N_{pcap} is much larger compared to a comparable constant hydrolysis rate, as shown in Figure 6.3(a). In contrast to the GTP-cap length N_{cap} that considers the continuous stretch of GTP-tubulin dimers at the end of a protofilament, the porous GTP-cap length N_{pcap} measures the distance from the plus end to the last GTP-tubulin dimer in a protofilament

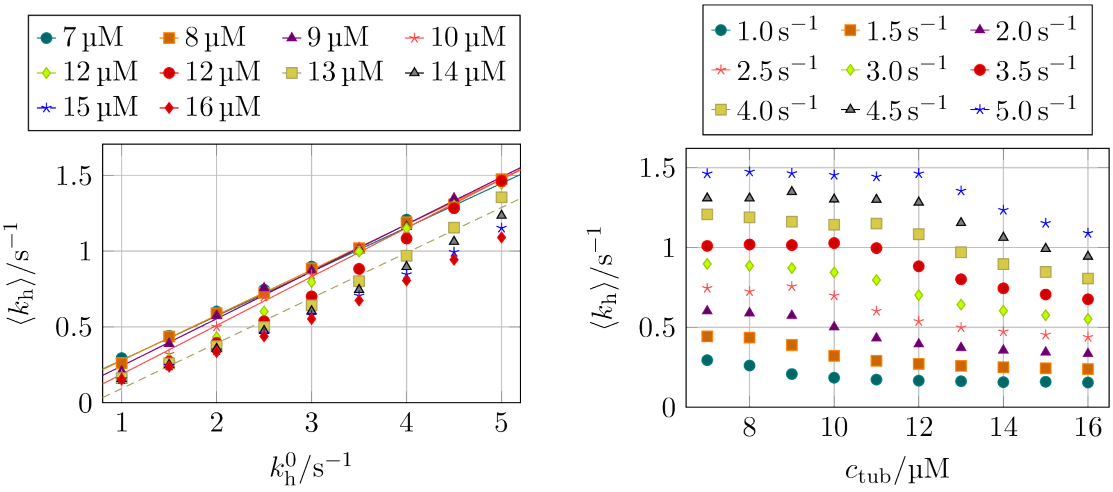

(a) Average hydrolysis rate $\langle k_h \rangle$ as a function of the base hydrolysis rate k_h^0 for different free GTP-tubulin dimer concentrations c_{tub}.

(b) Average hydrolysis rate $\langle k_h \rangle$ as a function of the free GTP-tubulin dimer concentration c_{tub} for different base hydrolysis rates k_h^0.

Figure 6.1: Average hydrolysis rate $\langle k_h \rangle$ calculated from the hydrolysis events executed in the relevant simulations.

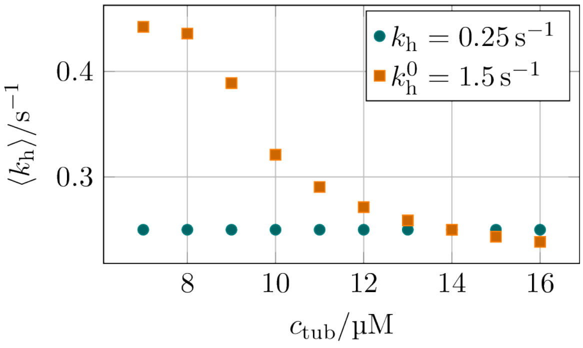

Figure 6.2: Comparison of the average hydrolysis rate $\langle k_h \rangle$ as a function of the free GTP-tubulin dimer concentration c_{tub} for a constant hydrolysis rate $k_h = 0.25\,\mathrm{s}^{-1}$ and mechanical hydrolysis with a base hydrolysis rate $k_h^0 = 1.5\,\mathrm{s}^{-1}$.

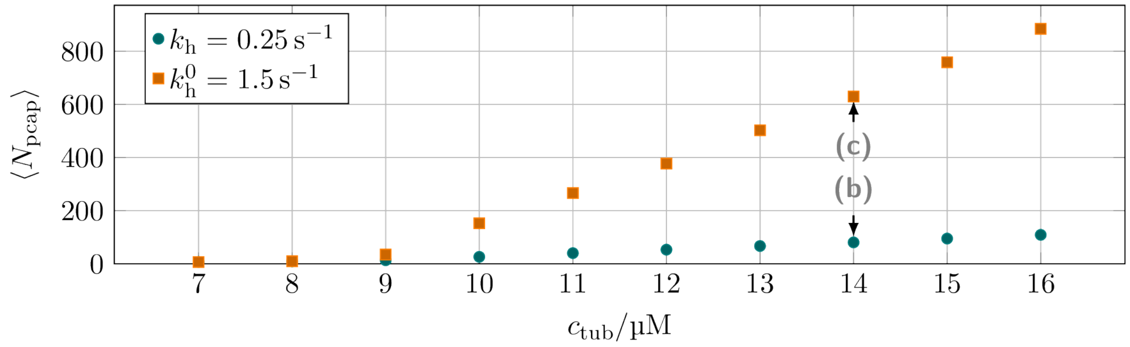

(a) Comparison of the average porous GTP-cap length $\langle N_\mathrm{pcap} \rangle$ between a constant hydrolysis rate of $k_\mathrm{h} = 0.25\,\mathrm{s}^{-1}$ and mechanical hydrolysis with a base hydrolysis rate $k_\mathrm{h} = 1.5\,\mathrm{s}^{-1}$.

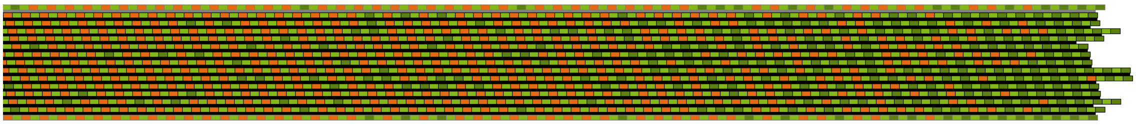

(b) Example configuration of a simulation with a constant hydrolysis rate $k_\mathrm{h} = 0.25\,\mathrm{s}^{-1}$. (The top and bottom protofilament are the period image of the last and first protofilament, respectively.)

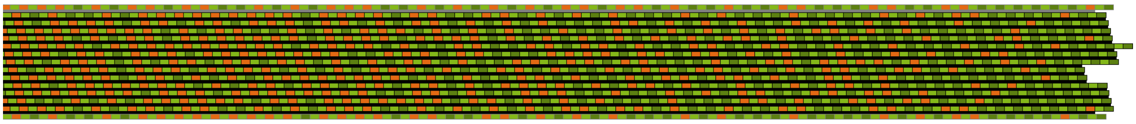

(c) Example configuration of a simulation with a base hydrolysis rate $k_\mathrm{h} = 1.5\,\mathrm{s}^{-1}$. (The top and bottom protofilament are the period image of the last and first protofilament, respectively.)

Figure 6.3: Comparison of the porous GTP-cap between a constant hydrolysis rate and mechanical hydrolysis.

in units of tubulin dimers. If the only GTP-tubulin dimers in a protofilament happen to be directly at its plus end, $N_\mathrm{pcap} = N_\mathrm{cap}$. Figure 6.3(b) and Figure 6.3(c) are two exemplary configuration snapshots that show how for mechanical hydrolysis, more GTP-tubulin dimers can be found further away from the microtubule tip. A more detailed discussion of the porous GTP-cap length N_pcap can be found in section 7.3.

In addition to the average hydrolysis rates in Figure 6.1, we also analyzed the distribution of hydrolysis rates k_h for different base hydrolysis rates k_h^0 and different free GTP-tubulin dimer concentrations c_tub. Before continuing with this discussion, however, we will first investigate the influence of the distance of the hydrolyzed tubulin dimer from the protofilament tip (which we will refer to as “layer-dependence” for brevity) on the average hydrolysis rate because this discussion will lay the foundation for understanding the distribution of actual hydrolysis rates.

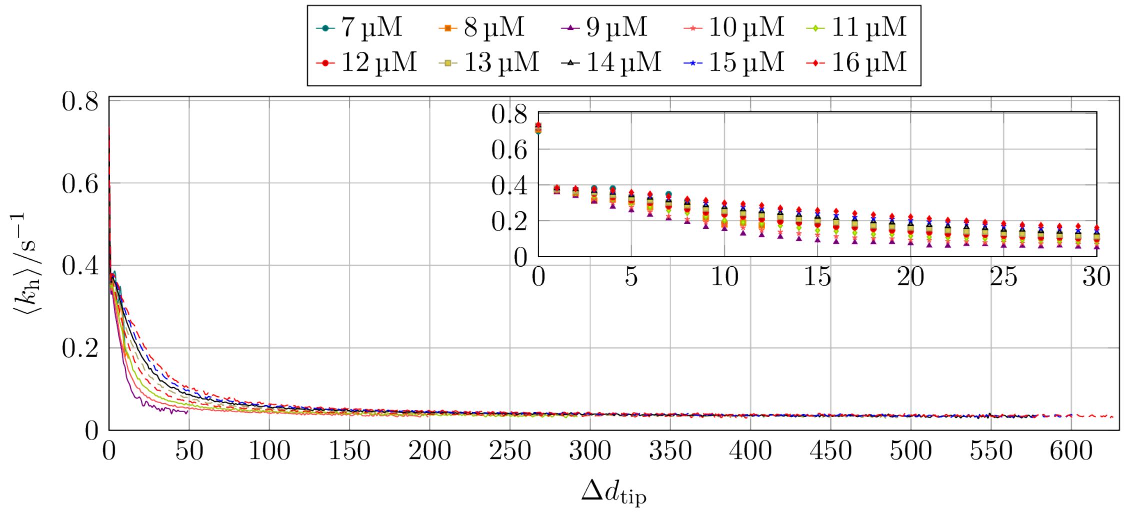

Figure 6.4: Average hydrolysis rate $\langle k_\mathrm{h}\rangle$ as a function of the distance Δd_tip of the hydrolyzed tubulin dimer from the tip of its protofilament for $k_\mathrm{h}^0 = 1.5\,\mathrm{s}^{-1}$.

6.2 Layer-Dependence of Average Hydrolysis Rate

Previously[121], coupling mechanics and hydrolysis was already considered in a simplified model and even though a random hydrolysis rule was used, the coupling caused hydrolysis to occur layer by layer.

To account for different lengths of individual protofilaments, we will consider the distance of a tubulin dimer (p, d) from the tip of the protofilament it is in:

$$\Delta d_\mathrm{tip} = d_\mathrm{max}(p) - d. \tag{6.1}$$

In Figure 6.4, we see that the average hydrolysis rate $\langle k_\mathrm{h}\rangle$ is higher at the plus end of the microtubule. In subsection 2.3.4, we had already discussed that due to our choice of where tubulin dimers are able to bend (both intra- and inter-dimer bending is possible), we will have a higher hydrolysis rate at the very end of the protofilament, $\Delta d_\mathrm{tip} = 0$, which is highlighted in the inset in Figure 6.4. However, for $\Delta d_\mathrm{tip} > 0$ but still close to the tip, the hydrolysis rate is still higher than for GTP-tubulin dimers buried deep into the microtubule lattice ($\Delta d_\mathrm{tip} \gg 0$).

We have modeled the coupling between hydrolysis and mechanics in (2.51) and (2.52) so that a larger bending angle ψ results in a higher hydrolysis rate. Compared to a straight GTP-tubulin dimer with $\psi = 0°$, hydrolysis of a GTP-tubulin dimer with $\psi > 0°$ is more likely and less likely if $\psi < 0°$. From (2.51), (2.52), and the average hydrolysis rate data in Figure 6.4, it is possible to calculate the average bending angles $\langle\tilde{\psi}\rangle$:

$$\langle\tilde{\psi}(\Delta d_\mathrm{tip})\rangle = \frac{1}{11°}\left[\frac{1+\delta_{\Delta d_\mathrm{tip},0}}{\kappa}\ln\left(\frac{\langle k_\mathrm{h}\rangle(\Delta d_\mathrm{tip})}{k_\mathrm{h}^0}\right) + (5.5°)^2\right], \tag{6.2}$$

which are shown in Figure 6.5. While the intent of the coupling between hydrolysis and

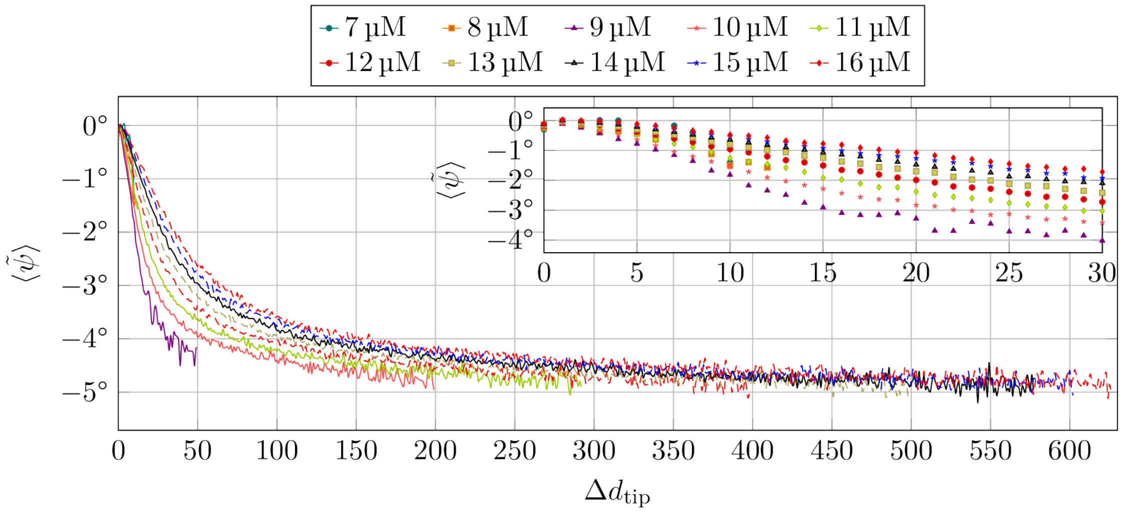

Figure 6.5: Average bending angle $\langle\tilde{\psi}\rangle$ calculated via (6.2) from the average hydrolysis rate $\langle k_{\mathrm{h}}\rangle$ shown in Figure 6.4.

mechanics was to *ease* hydrolysis of GTP-tubulin dimers that are already bent outward, we find that in reality, the GTP-tubulin dimers tend to bent inward instead of outward resulting in a *penalty* for the hydrolysis of these tubulin dimers compared to straight GTP-tubulin dimers. To understand why it is energetically preferable for GTP-tubulin dimers to bend inward (in the GDP-body of the microtubule), we generated a GDP-only microtubule and then artificially changed the beta-nucleotide of certain tubulin dimers back to GTP and investigated the effect of these changes on the bending angles ψ. In Figure 6.6, we first changed the nucleotide of five GTP-tubulin dimers in the same layer. In Figure 6.6(b), after changing the first nucleotide, the two tubulin monomers, whose bending angles are affected by the relevant nucleotide, bend inward to allow the tubulin monomers below and above these two tubulin monomers to bent outward resulting in an overall energy decrease. If we average the bending angles of the inward-bending tubulin monomers in the last configuration in Figure 6.6(f), we find a similar bending angle as the asymptotic value in Figure 6.5.

Additionally, we also changed the nucleotide of five GTP-tubulin dimers in the same protofilament as shown in Figure 6.7. The interesting finding here is that as the length of the GTP-island in the protofilament grows, the monomers in the center become straighter, ultimately resulting in the following succession of bending angles in the last configuration in Figure 6.7(f): straight GDP-tubulin monomers[1] due to the lattice constraints, GDP-tubulin monomers bending outward at the interface of the GDP/GTP-region, GTP-tubulin monomers bending inward to compensate for the previous GDP-tubulin monomers bending outward, straight GTP-tubulin monomers, GTP-tubulin monomers bending inward to compensate for the following GDP-tubulin monomers bending outward, which are then followed by straight GDP-tubulin monomers. Finally, at the plus end tip of the protofilament, there are again GDP-tubulin monomers bending outward due to the reduced lattice constraints at the tip. Having straight GTP-tubulin dimers

---

[1] We use the shortcut "GTP/GDP-tubulin monomer" here to refer to tubulin monomers whose rest configuration is either straight (GTP) or bent (GDP).

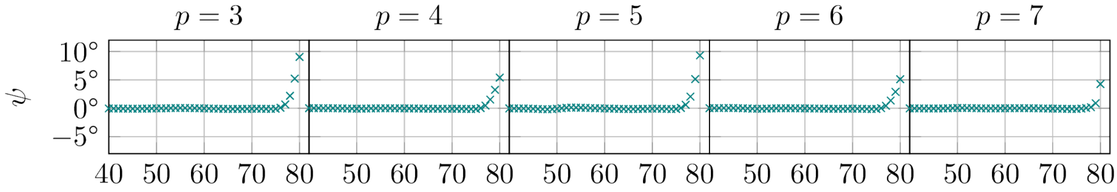

(a) Bending angles of initial configuration.

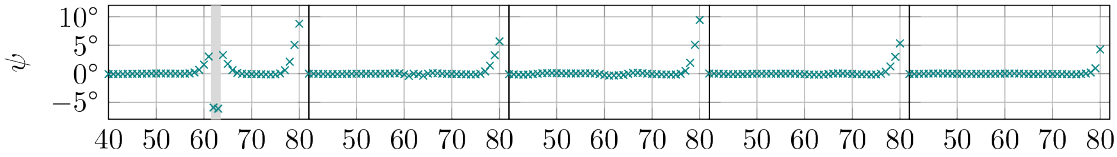

(b) Bending angles after changing the beta-nucleotide of tubulin dimer $(3, 31)$ from GDP to GTP.

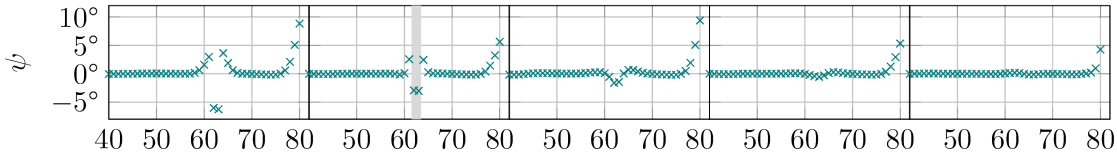

(c) Bending angles after changing the beta-nucleotide of tubulin dimer $(4, 31)$ from GDP to GTP.

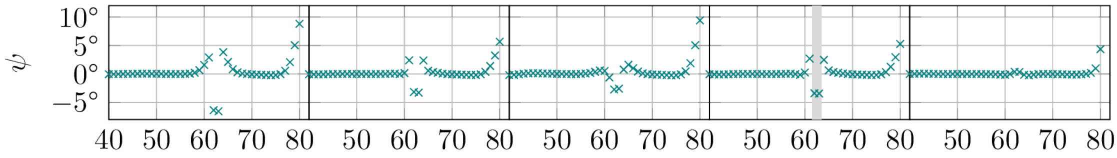

(d) Bending angles after changing the beta-nucleotide of tubulin dimer $(6, 31)$ from GDP to GTP.

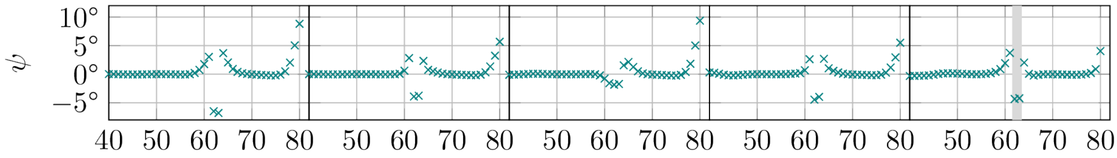

(e) Bending angles after changing the beta-nucleotide of tubulin dimer $(7, 31)$ from GDP to GTP.

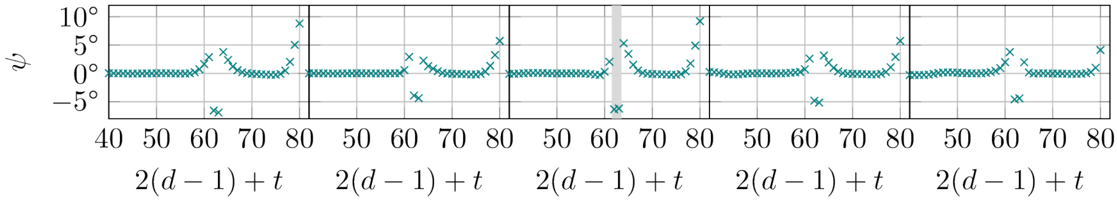

(f) Bending angles after changing the beta-nucleotide of tubulin dimer $(5, 31)$ from GDP to GTP.

Figure 6.6: Bending angles $\psi(p, d, t)$ as a function of the tubulin monomer in five protofilaments of a microtubule with initially $N_{\mathrm{GDP}} = 40$ and $N_{\mathrm{GTP}} = 0$ and subsequent artificial changes of certain beta-nucleotides from GDP to GTP. The highlighted tubulin monomers are the ones bending inward as a result of the previous change of the beta-nucleotide from GDP to GTP.

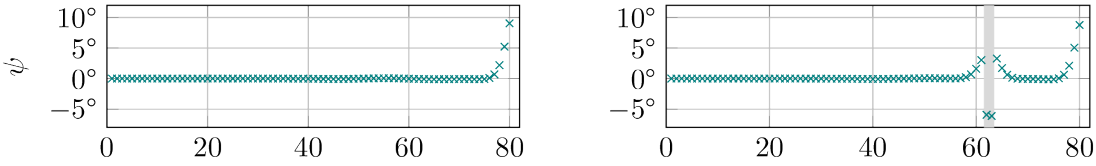

(a) Bending angles of initial configuration.

(b) Bending angles after changing the beta-nucleotide of tubulin dimer $(3,31)$ from GDP to GTP.

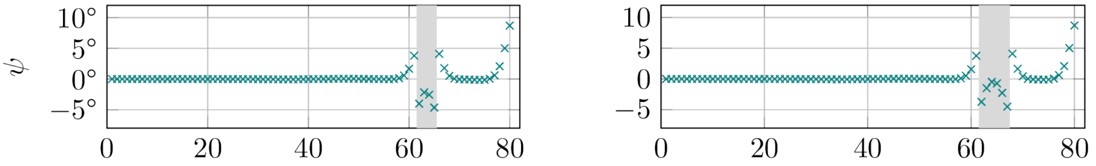

(c) Bending angles after changing the beta-nucleotide of tubulin dimer $(3,32)$ from GDP to GTP.

(d) Bending angles after changing the beta-nucleotide of tubulin dimer $(3,33)$ from GDP to GTP.

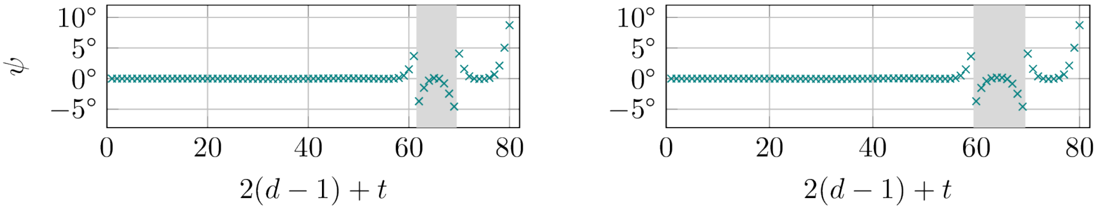

(e) Bending angles after changing the beta-nucleotide of tubulin dimer $(3,34)$ from GDP to GTP.

(f) Bending angles after changing the beta-nucleotide of tubulin dimer $(3,30)$ from GDP to GTP.

Figure 6.7: Bending angles $\psi(p,d,t)$ as a function of the tubulin monomer in protofilament $p=3$ of a microtubule with initially $N_{\text{GDP}}=40$ and $N_{\text{GTP}}=0$ and subsequent artificial changes of certain beta-nucleotides from GDP to GTP. The highlighted tubulin monomers are the ones bending inward as a result of all the changes of the beta-nucleotide from GDP to GTP.

in the interior of the GTP-island compared to the GTP-dimers bending outward at the edges of the GTP-island, results in a higher hydrolysis rate in the interior of the GTP-island, which can be interpreted as an “anti-vectorial” hydrolysis mechanism (compared to the normal vectorial hydrolysis mechanism in which such a GTP-island would be hydrolyzed from its edges, see Figure 2.9(b)).

It must be noted that these findings regarding the bending angles of GTP-tubulin monomers in the GDP-body of the microtubule are independent of whether hydrolysis is coupled to mechanics or not. The conclusion regarding the influence of these negative bending angles on the hydrolysis rate, of course, only applies to mechanical hydrolysis.

In section 6.1, we have seen that for mechanical hydrolysis, the porous GTP-cap length N_{pcap} is much longer for growing microtubules (see Figure 6.3(a)). Hence, it makes sense to analyze the probability of finding GTP-tubulin dimers as a function of the distance from the tip.

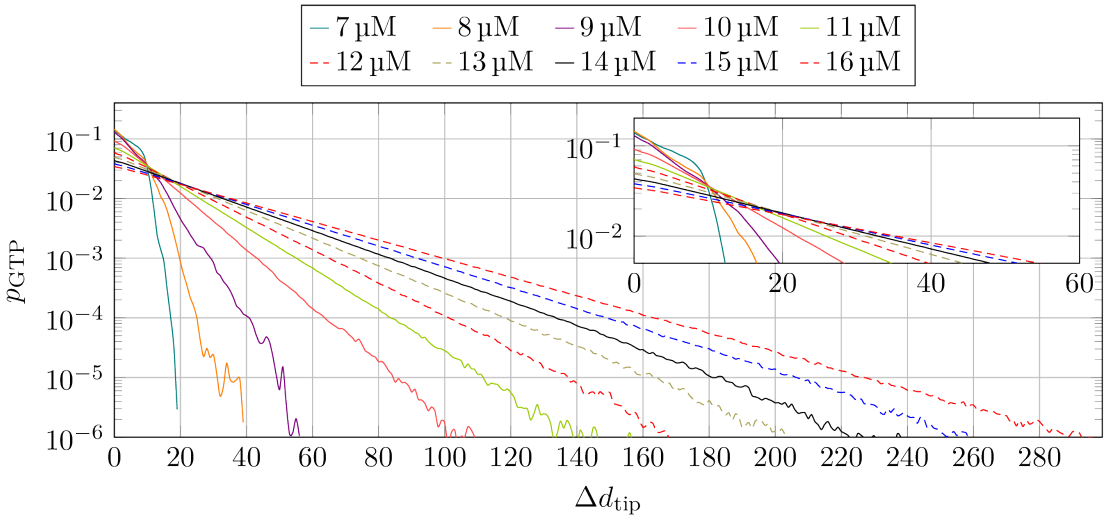

(a) Constant hydrolysis rate $k_{\mathrm{h}} = 0.25\,\mathrm{s}^{-1}$.

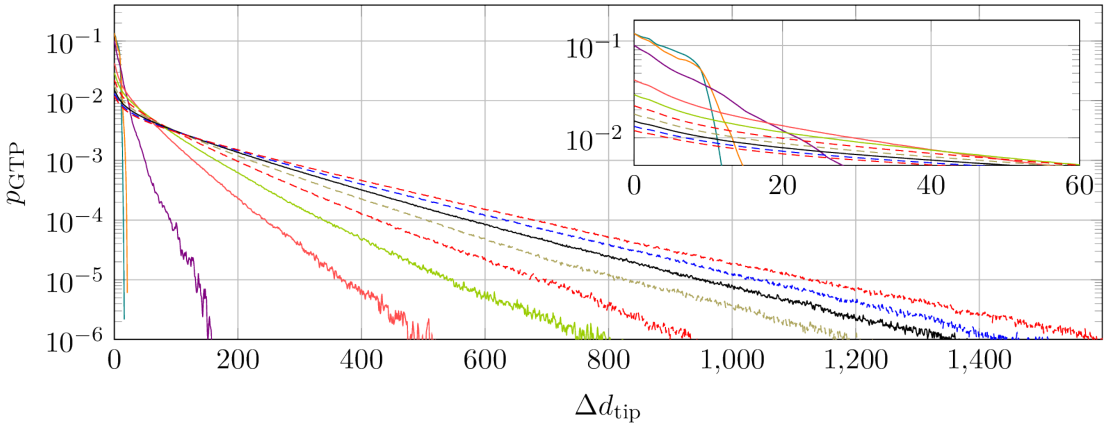

(b) Base hydrolysis rate $k_{\mathrm{h}}^{0} = 1.5\,\mathrm{s}^{-1}$.

Figure 6.8: Probability p_{GTP} to find a GTP-tubulin dimer at the distance Δd_{tip} from the tip of its protofilament for a constant hydrolysis rate and for mechanical hydrolysis.

From the higher value of N_{pcap} for mechanical hydolysis mentioned before in section 6.1, we already know that this probability distribution will have a longer tail for mechanical hydrolysis than for a constant hydrolysis, which is confirmed by our data shown in Figure 6.8. For a constant hydrolysis rate, the GTP probability distribution shown in Figure 6.8(a) is exponential, which is consistent with *in vivo* experiments[209]. In Appendix F, we show analytically with a simple one-dimensional model with a polymerization rate k_{on}, depolymerization rate k_{off}, and hydrolysis rate k_{h} for all GTP-tubulin dimers that our p_{GTP} data for a constant hydrolysis rate can be reproduced with such a simple model. While there is a direct mapping from our three-dimensional model to the one-dimensional model for the polymerization rate k_{on} and the hydrolysis rate k_{h} (if we ignore whether or not a newly polymerized GTP-tubulin dimer can be hydrolyzed or not), there is no such direct mapping for the depolymerization rate k_{off}. In our three-dimensional model, we, of course, also have a depolymerization rate k_{off}, see (2.36), the actual depolymerization *process*, however, is an interplay between depolymerization and lateral bond dynamics, which are not part of the one-dimensional model. As a consequence, the depolymerization rate obtained via fitting from the one-dimensional model can be viewed as an "effective" depolymerization rate $k_{\mathrm{off}}^{\mathrm{eff}}$ that represents the actual depolymerization process and the lateral bond dynamics of our three-dimensional model.

For mechanical hydrolysis, we find that $p_{\mathrm{GTP}}(\Delta d_{\mathrm{tip}})$ is only exponential in its tail, see Figure 6.8(b). Additionally, this tail is much longer and reaches deeper into the GDP-body of the microtubule compared to a constant hydrolysis rate. These results are consistent with the decrease of the hydrolysis rate in the GDP-body of the microtubule shown in Figure 6.4. The fact that the distribution is no longer exponential is not surprising as the hydrolysis rate is not constant. The data, for the average hydrolysis $\langle k_{\mathrm{h}} \rangle$ shown in Figure 6.4, however, demonstrates that in the GDP-body, i.e., in the tail of the distribution shown in Figure 6.8(b), $\langle k_{\mathrm{h}} \rangle$ is almost constant resulting in an exponential GTP-tubulin dimer distribution in that region.

In Appendix F, we show that the following differential equation for p_{GTP} can be derived from the balance of the polymerization, depolymerization, and hydrolysis of GTP-tubulin dimers in the stationary case, see (F.45):

$$\frac{\mathrm{d}p_{\mathrm{GTP}}}{\mathrm{d}\Delta d_{\mathrm{tip}}} = -\frac{\langle k_{\mathrm{h}} \rangle (\Delta d_{\mathrm{tip}})}{k_{\mathrm{on}} - k_{\mathrm{off}}^{\mathrm{eff}}} p_{\mathrm{GTP}}(\Delta d_{\mathrm{tip}}). \tag{6.3}$$

Equation (6.3) explains why there is a much larger decrease of p_{GTP} directly at the tip for mechanical hydrolysis compared to a constant hydrolysis because there is a significant drop in the average hydrolysis rate $\langle k_{\mathrm{h}} \rangle$ from $\Delta d_{\mathrm{tip}} = 0$ to $\Delta d_{\mathrm{tip}} = 1$, see the inset in Figure 6.4. Equation (6.3) also explicitly shows what we have already discussed before: For large Δd_{tip}, $\langle k_{\mathrm{h}}(\Delta d_{\mathrm{tip}}) \rangle$ reaches a constant value so that (6.3) can be solved explicitly yielding an exponential distribution. For all values of $\langle k_{\mathrm{h}}(\Delta d_{\mathrm{tip}}) \rangle$, however, (6.3) cannot be solved analytically to compare it to our data. Instead, we can solve (6.3) for $k_{\mathrm{off}}^{\mathrm{eff}}$:

$$k_{\mathrm{off}}^{\mathrm{eff}}(\Delta d_{\mathrm{tip}}) = k_{\mathrm{on}} + \left(\frac{\mathrm{d}p_{\mathrm{GTP}}}{\mathrm{d}\Delta d_{\mathrm{tip}}} \right)^{-1} \langle k_{\mathrm{h}} \rangle (\Delta d_{\mathrm{tip}})\, p_{\mathrm{GTP}}(\Delta d_{\mathrm{tip}}). \tag{6.4}$$

We have added a Δd_{tip}-dependence on the left-hand side of (6.4) because the right-hand side also depends on Δd_{tip}. Additionally, $k_{\mathrm{off}}^{\mathrm{eff}}(\Delta d_{\mathrm{tip}})$ is not the depolymerization rate of tubulin dimers with a distance of Δd_{tip} from the tip, but the depolymerization rate in the one-dimensional model of the terminal tubulin dimer calculated with the data of the tubulin dimer with a distance of Δd_{tip} from the tip. If our simulation results can be understood qualitatively via the one-dimensional model, we expect, however, $k_{\mathrm{off}}^{\mathrm{eff}}$ to be independent of Δd_{tip}. For $\langle k_{\mathrm{h}} \rangle (\Delta d_{\mathrm{tip}})$ and $p_{\mathrm{GTP}}(\Delta d_{\mathrm{tip}})$, we can use the data shown in Figure 6.4 and Figure 6.8(b), respectively, and the derivative in (6.4) can be calculated from our $p_{\mathrm{GTP}}(\Delta d_{\mathrm{tip}})$ data using a central difference quotient (and a forward and backward difference quotient for the first and last data point, respectively). The results of these calculations for the data from Figure 6.4 and Figure 6.8 and, as a comparison, also for the data with a constant hydrolysis rate are shown in Figure 6.9. Despite the significant peaks visible for both data sets for all values of c_{tub} due to numerical issues, and, in particular for larger values of Δd_{tip}, due to an insufficient amount of data, it is clear that the $k_{\mathrm{off}}^{\mathrm{eff}} \approx \mathrm{const}$ in both cases holds, which validates our data.

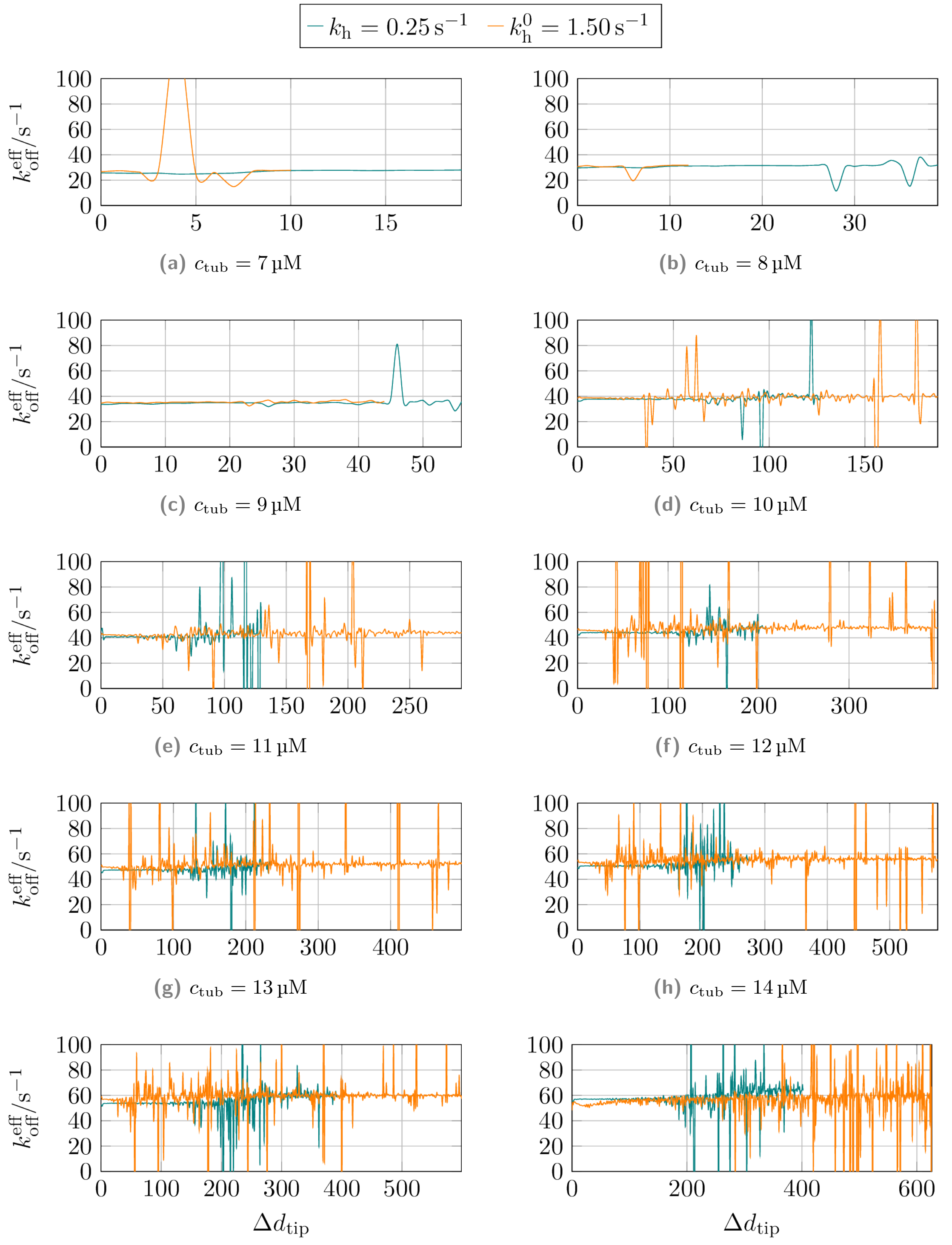

Figure 6.9: Effective depolymerization rate k_{off}^{eff} calculated via (6.4) for a constant hydrolysis rate $k_{off} = 0.25\,s^{-1}$ and a base hydrolysis rate $k_h^0 = 1.5\,s^{-1}$ and different free GTP-tubulin dimer concentrations c_{tub}. (k_{off}^{eff} values outside of $[0\,s^{-1}, 100\,s^{-1}]$ were cut off.)

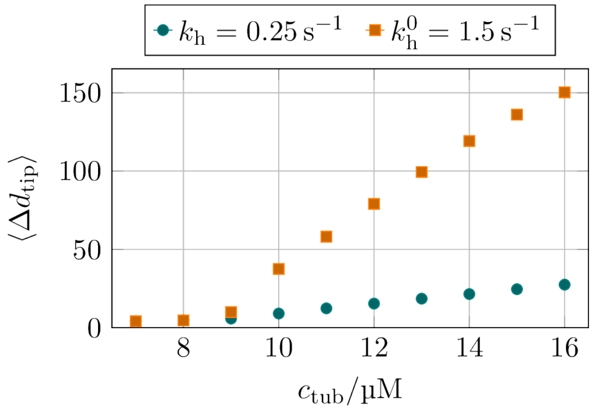

Figure 6.10: Average distance of GTP-tubulin dimers from the microtubule tip calculated from the data shown in Figure 6.8 for a constant hydrolysis rate and mechanical hydrolysis via (6.5).

The GTP-tubulin dimer probability results for mechanical hydrolysis shown in Figure 6.8(b) can also be used to explain the increase in the porous GTP-cap length shown in Figure 6.3(a) in a simple way by considering the average distance of GTP-tubulin dimers from the tip:

$$\langle \Delta d_\mathrm{tip} \rangle = \sum_{i=0}^{\infty} i\, p_\mathrm{GTP}(i). \tag{6.5}$$

Using the data in Figure 6.8, $\langle \Delta d_\mathrm{tip} \rangle$ was calculated and the results in Figure 6.10 show that, unsurprisingly, $\langle \Delta d_\mathrm{tip} \rangle$ is much larger for mechanical hydrolysis. While $\langle \Delta d_\mathrm{tip} \rangle$ is only the average distance from the tip, the porous GTP-cap length N_pcap is the maximum distance so that $\langle \Delta d_\mathrm{tip} \rangle \leq N_\mathrm{pcap}$, which causes N_pcap to also increase as $\langle \Delta d_\mathrm{tip} \rangle$ increases.

Comparing the probability p_GTP directly at the tip, we find there to be a relative increase of GDP-tubulin dimers for mechanical hydrolysis compared to a constant hydrolysis rate, see insets in Figure 6.8. As GDP-tubulin dimers at the microtubule tip destabilize the microtubule, mechanical hydrolysis might cause an increase in the catastrophe rate compared to a constant hydrolysis rate (see section 5.4) and potentially a flatter concentration dependence of the catastrophe rate. To investigate whether this hypothesis is true, we simulated microtubule growth trajectories like we did for constant hydrolysis rates as shown in Figure 5.1, which we will consider in the next section. Before continuing with that topic however, we have to finish the discussion we started in the previous section about the distribution of the actual hydrolysis rates.

Using the raw simulation data from which the average hydrolysis rates in Figure 6.1(a) were calculated, we generated histograms of the distribution of the rates of individual hydrolysis events for different base hydrolysis rates k_h^0 and free GTP-tubulin dimer concentrations c_tub shown in Figure 6.11. Most probability densities in Figure 6.11 show three clear distinct peaks for all base hydrolysis rates k_h^0. The k_h values of the peaks are greater, the greater the base hydrolysis rate k_h^0 is. To eliminate the influence of k_h^0, we replotted the data in Figure 6.11 as a function of $k_\mathrm{h}/k_\mathrm{h}^0$ in Figure 6.12. By eliminating k_h^0, we can clearly see that the second and third peak is present at the same value of $k_\mathrm{h}/k_\mathrm{h}^0$ regardless of the actual value of k_h^0 and c_tub. The position of the first peak is not as clearly defined as for the other peaks, which was already visible in the separate data for the different k_h^0 values, as seen, for example, in

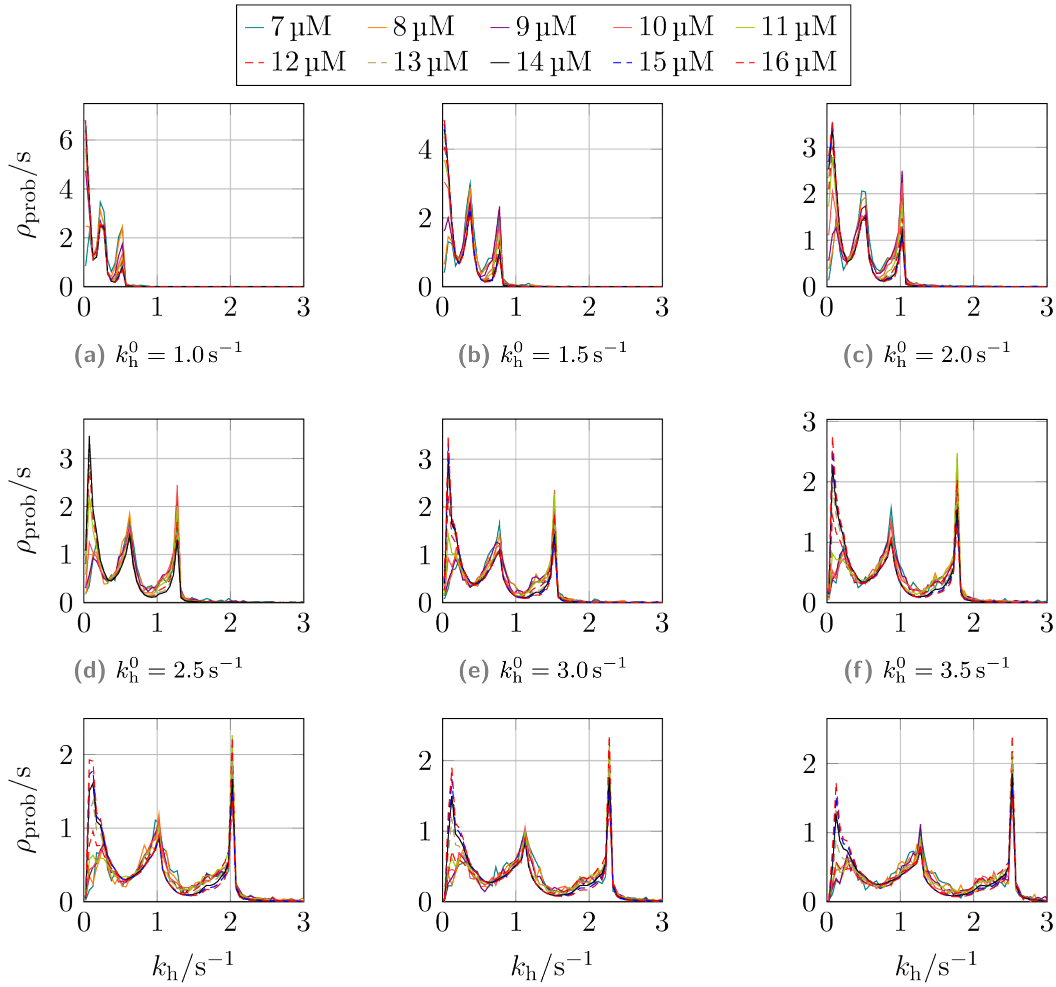

(a) $k_{\text{h}}^0 = 1.0\,\text{s}^{-1}$ (b) $k_{\text{h}}^0 = 1.5\,\text{s}^{-1}$ (c) $k_{\text{h}}^0 = 2.0\,\text{s}^{-1}$

(d) $k_{\text{h}}^0 = 2.5\,\text{s}^{-1}$ (e) $k_{\text{h}}^0 = 3.0\,\text{s}^{-1}$ (f) $k_{\text{h}}^0 = 3.5\,\text{s}^{-1}$

(g) $k_{\text{h}}^0 = 4.0\,\text{s}^{-1}$ (h) $k_{\text{h}}^0 = 4.5\,\text{s}^{-1}$ (i) $k_{\text{h}}^0 = 5.0\,\text{s}^{-1}$

Figure 6.11: Probability density ρ_{prob} of the actual hydrolysis rates k_{h} for different base hydrolysis rates k_{h}^0 and free GTP-tubulin dimer concentrations c_{tub}. ρ_{prob} was generated as a histogram with a histogram bar width of $\Delta k_{\text{h}} = 0.05\,\text{s}^{-1}$. The cutoff $k_{\text{h}}^0 = 3\,\text{s}^{-1}$ for the plots has been chosen as beyond $k_{\text{h}}^0 = 3\,\text{s}^{-1}$, ρ_{prob} is negligible.

Figure 6.11(i). The “sub-peak” in the first peak that is at larger values of k_{h} appears for small free GTP-tubulin dimer concentrations c_{tub}, while the sub-peak at smaller values of k_{h} appears for larger free GTP-tubulin dimer concentrations c_{tub}. To explain this substructure, we again calculated the average bending angles from these rates via

$$\tilde{\psi}(k_{\text{h}}) = \frac{1}{11^\circ}\left[\frac{1}{\kappa}\ln\left(\frac{k_{\text{h}}}{k_{\text{h}}^0}\right) + (5.5^\circ)^2\right], \tag{6.6}$$

which is (6.2) without the special consideration of GTP-tubulin dimers directly at the tip being hydrolyzed as we averaged over all tubulin dimers. The probability for the calculated angles is shown in Figure 6.12(b). The second peak in Figure 6.12(b) is due to straight GTP-tubulin

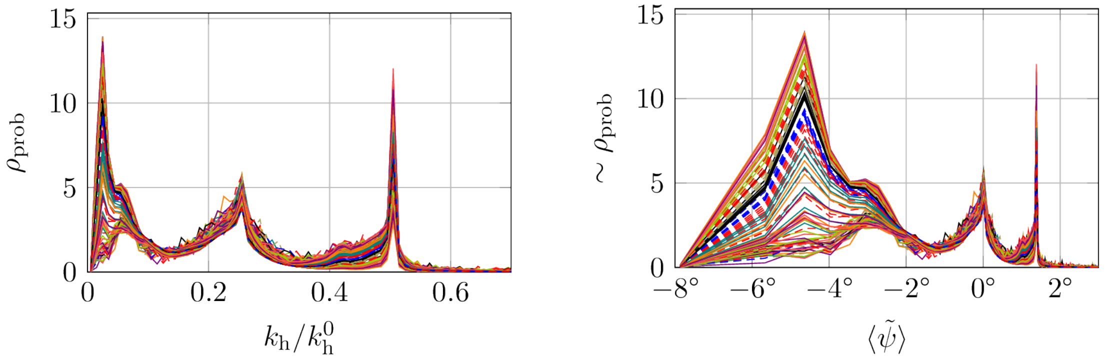

(a) Probability density ρ_{prob} of the actual hydrolysis rates k_{h} normalized by the base hydrolysis rate k_{h}^0 for different base hydrolysis rates k_{h}^0 and free GTP-tubulin dimer concentrations c_{tub}. ρ_{prob} was generated as a histogram with a histogram bar width of $\Delta(k_{\text{h}}/k_{\text{h}}^0) = 0.01$.

(b) Relative occurrence probability of the average bending angle $\langle\tilde{\psi}\rangle$ calculated via (6.6) using the k_{h} values from the left plot for the average bending angles on the x-axis, while keeping the y-data the same (and thus not making it probability *density* anymore).

Figure 6.12: Further analysis of the hydrolysis rate distribution and the resulting bending angle distribution using the data in Figure 6.11. The cutoffs on the x-axis for the plots have been chosen so that beyond it, ρ_{prob} is negligible. Due to the large amount of indistinguishable individual lines in the plots, no legend is given.

dimers being hydrolyzed, and the third peak is due to GTP-tubulin dimers that are bending outward. Straight GTP-tubulin dimers are mostly likely found in the GTP-cap or in any longer GTP-island (see Figure 6.7(f)) and, as discussed before, GTP-tubulin dimers bending inward is due to neighboring GDP-tubulin dimers (see Figure 6.7). The only open question now is the origin of the sharp peak of positive bending angles around $\langle\tilde{\psi}\rangle \simeq 1.4°$ in Figure 6.12(b) as there is generally no reason for GTP-tubulin monomers to bend outward (see Figure 6.6 and Figure 6.7[2]). As mentioned when introducing (6.6), the bending angles in Figure 6.12(b) are calculated without the knowledge of where an hydrolysis event occurred so that GTP-tubulin dimers at the tip were not considered separately as in (6.2). If we take the $k_{\text{h}}/k_{\text{h}}^0 \simeq 0.5$ peak from Figure 6.12(a) and calculate the bending angle for a terminal GTP-tubulin dimer with it, we get $\langle\tilde{\psi}\rangle \simeq 0°$, showing that this peak is due to the hydrolysis of straight terminal GTP-tubulin dimers that our average over all hydrolysis events does not properly consider.

In the next section, we will discuss microtubule trajectories and in Figure 6.13, we will see that for small values of c_{tub}, where there is only the left sub-peak of the first peak in Figure 6.12(a), the initial microtubules shrink immediately so that the case of GTP-tubulin dimers deeply embedded into the GDP-body of the microtubule does not happen as the only GTP-tubulin dimers relevant for this scenario are the ones from the initial GTP-cap, which is being hydrolyzed while the microtubule shrinks. Such deeply embedded GTP-tubulin dimers only exist for growing microtubules, which requires larger values of c_{tub}.

---

[2] Although it is not explicitly mentioned, GTP-tubulin dimers bending inward also applies at the microtubule tip if it allows neighboring GDP-tubulin dimers to bend outward. If no such neighboring GDP-tubulin dimers exist, GTP-tubulin dimers at the microtubule tip are straight.

6.3 Microtubule Trajectories and Individual Catastrophes and Rescues

Like in Figure 5.1 for a constant hydrolysis rate, we also logged the microtubule lengths of the simulations with mechanical hydrolysis we analyzed in the previous sections, which are shown in Figure 6.13. In the previous section, we speculated that due to more GDP-tubulin dimers being at the microtubule tip, we might find a flatter dependence of the catastrophe rate ω_{cat} on the free GTP-tubulin dimer concentration c_{tub}. In reality, however, we again find that between values of c_{tub} at which microtubules only shrink and values of c_{tub} at which microtubules grow for the whole duration of the simulation, there is only one intermediate concentration at which we can observe catastrophes and rescues. The catastrophe rate ω_{cat} still having such a steep dependence on the free GTP-tubulin dimer concentration c_{tub} despite a different hydrolysis mechanism hints at a different problem with our modeling. Table 6.1(a) and Figure 6.14(a) show the values of the catastrophe and rescue rates determined the same way as for a constant hydrolysis rate in section 5.4 based on the simulations shown in Figure 6.13. Figure 6.14 shows the data from Table 6.1(a) and Table 6.1(b) and compares it to the rates from Walker et al.[49] and Janson et al.[204]

Lastly, in section 5.3, we have seen that the growth velocity decreases if the constant hydrolysis rate k_{h} is increased. We repeated the same analysis for mechanical hydrolysis and find the same quantitative behavior as shown in Figure 6.15. Overall, however, the growth velocities v_{gr} are smaller as the linear fit in Figure 6.15(b) does not reach the value from Walker et al.[49] as it did in Figure 5.3(b) for constant hydrolysis rates k_{h}. These smaller values of v_{gr} can be explained by the decreased probability of finding a stabilizing GTP-tubulin dimer directly at the tips of protofilaments as discussed previously in section 6.2.

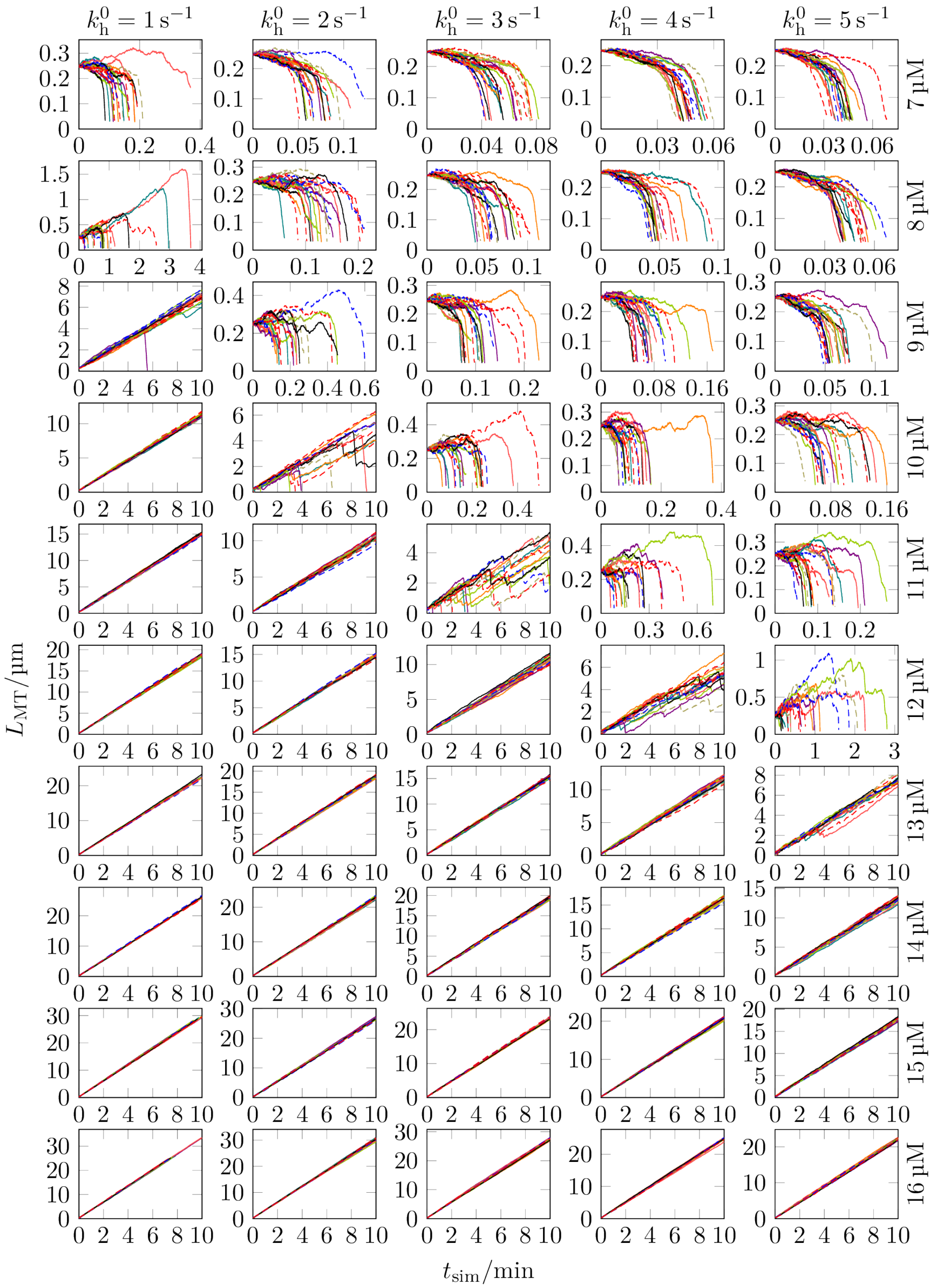

Figure 6.13: Microtubule growth trajectories of 20 different simulations for each of the considered values of the free GTP-tubulin dimer concentration c_tub and the base hydrolysis rate k_h^0.

k_h^0 c_tub	$1\,\mathrm{s}^{-1}$	$2\,\mathrm{s}^{-1}$	$3\,\mathrm{s}^{-1}$	$4\,\mathrm{s}^{-1}$	$5\,\mathrm{s}^{-1}$
7 µM	—	—	—	—	—
8 µM	$0.25\,\mathrm{min}^{-1}$	—	—	—	—
9 µM	$(0.01\,\mathrm{min}^{-1})$	—	—	—	—
10 µM	~ 0	$0.11\,\mathrm{min}^{-1}$	—	—	—
11 µM	~ 0	~ 0	$0.21\,\mathrm{min}^{-1}$	—	—
12 µM	~ 0	~ 0	~ 0	$0.16\,\mathrm{min}^{-1}$	$0.24\,\mathrm{min}^{-1}$
13 µM	~ 0	~ 0	~ 0	~ 0	$0.05\,\mathrm{min}^{-1}$
14 µM	~ 0	~ 0	~ 0	~ 0	~ 0
15 µM	~ 0	~ 0	~ 0	~ 0	~ 0
16 µM	~ 0	~ 0	~ 0	~ 0	~ 0

(a) Catastrophe rates ω_cat for different free GTP-tubulin dimer concentrations c_tub and different hydrolysis rates k_h. For parameter combinations with "—" as catastrophe rate, no proper growth phase was observed, so no catastrophe rates could be calculated. "~ 0" is used to denote cases in which microtubules grew during the whole simulation without any catastrophe resulting in catastrophe rates close to zero (at least $\omega_\mathrm{cat} \ll 0.01\,\mathrm{min}^{-1}$). For values in parentheses, only one or two catastrophe happened.

k_h^0 c_tub	$1\,\mathrm{s}^{-1}$	$2\,\mathrm{s}^{-1}$	$3\,\mathrm{s}^{-1}$	$4\,\mathrm{s}^{-1}$	$5\,\mathrm{s}^{-1}$
7 µM	—	—	—	—	—
8 µM	—	—	—	—	—
9 µM	$(1.22\,\mathrm{min}^{-1})$	—	—	—	—
10 µM	—	$2.11\,\mathrm{min}^{-1}$	—	—	—
11 µM	—	—	$1.73\,\mathrm{min}^{-1}$	—	—
12 µM	—	—	—	$3.61\,\mathrm{min}^{-1}$	—
13 µM	—	—	—	—	$4.67\,\mathrm{min}^{-1}$
14 µM	—	—	—	—	—
15 µM	—	—	—	—	—
16 µM	—	—	—	—	—

(b) Rescue rates ω_res for different free GTP-tubulin dimer concentrations c_tub and different hydrolysis rates k_h. For parameter combinations with "—" as rescue rate, no rescues were observed and for values in parentheses only one or two rescues happened.

Table 6.1: Catastrophe rates ω_cat and rescue rates ω_res for different free GTP-tubulin dimer concentrations c_tub and different base hydrolysis rates k_h^0.

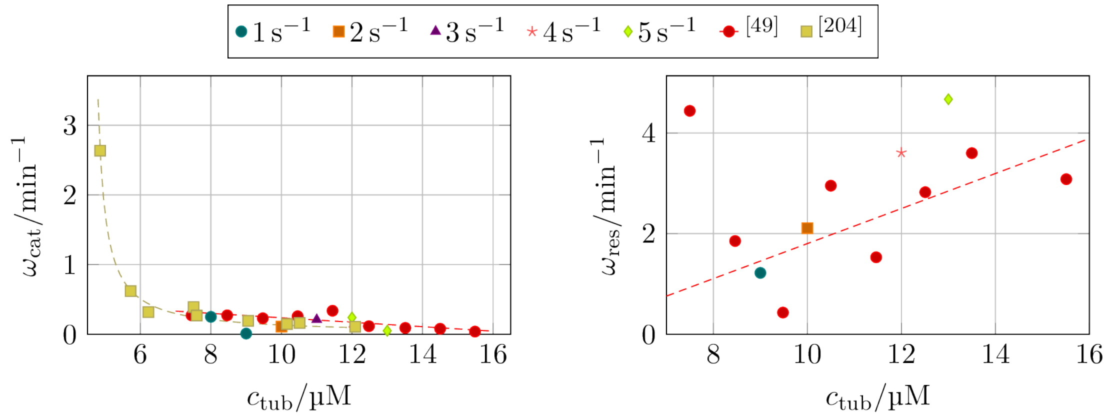

(a) Catastrophe rate ω_{cat} as a function of the free GTP-tubulin dimer concentration c_{tub}.

(b) Rescue rate ω_{res} as a function of the free GTP-tubulin dimer concentration c_{tub}.

Figure 6.14: Comparison between our values for the catastrophe and rescue rates from Table 6.1(a) and Table 6.1(b) and the values measured by Walker et al.[49] and Janson et al.[204]

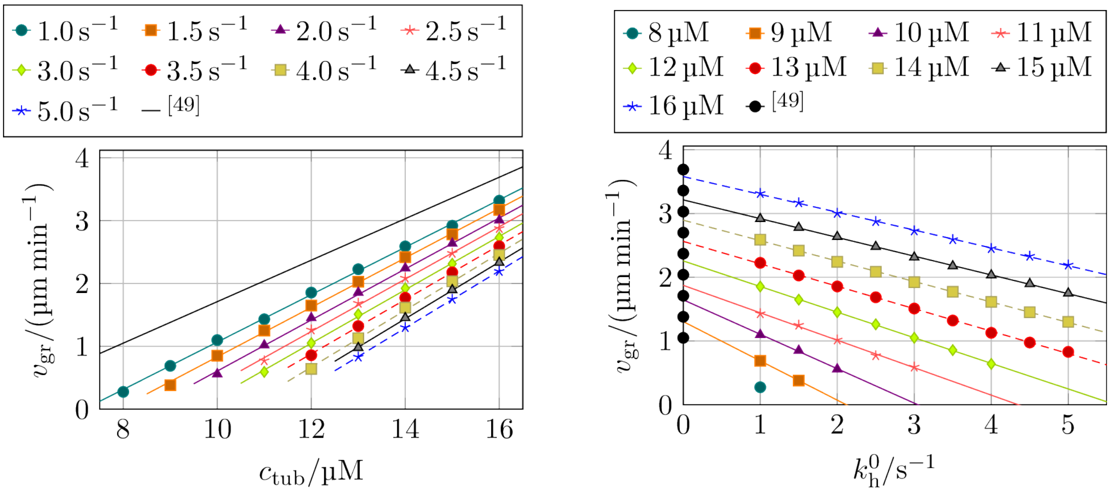

(a) Microtubule growth velocity v_{gr} as a function of the free GTP-tubulin dimer concentration c_{tub} for different base hydrolysis rates k_{h}^0.

(b) Microtubule growth velocity v_{gr} as a function of the base hydrolysis rates k_{h}^0 for different free GTP-tubulin dimer concentrations c_{tub}.

Figure 6.15: Increasing the hydrolysis rates k_{h} results in a linear decrease of the microtubule growth velocity v_{gr} but also still results in a linear $v_{\text{gr}}(c_{\text{tub}})$ relation like the experimental data by Walker et al.[49]

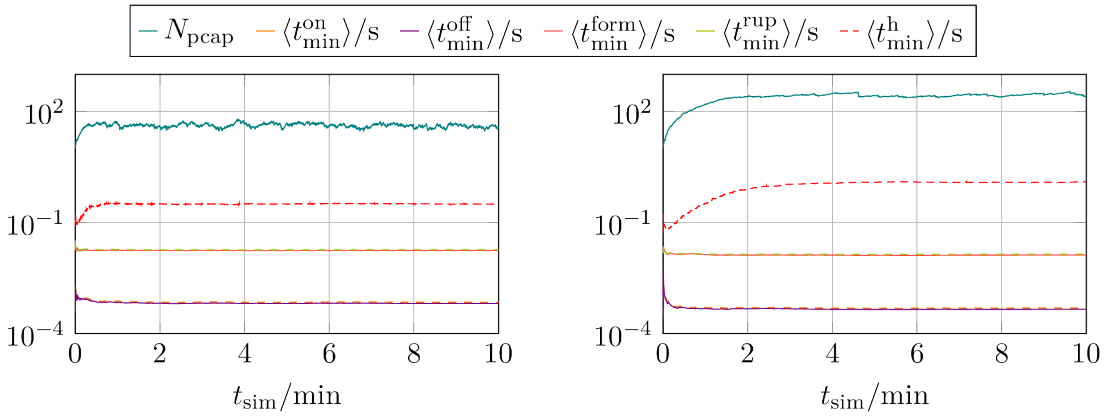

(a) Simulation with $k_\text{h} = 0.25\,\text{s}^{-1}$ run on a single core of an Intel Xeon E5-2650 (Sandy Bridge) processor (originally released in the first quarter of 2012 with a base frequency of 2.0 GHz[210]).

(b) Simulation with $k_\text{h}^0 = 1.5\,\text{s}^{-1}$ run on a single core of an Intel Xeon E5-2630 v3 (Haswell) processor (originally released in the third quarter of 2014 with a base frequency of 2.4 GHz[211]).

Figure 6.16: Comparison of the porous GTP-cap length N_pcap and the cumulative running averages $\langle t_\text{min}^i\rangle$ of the minimization times after an event of type i with possible events being polymerization (i = on), depolymerization (i = off), lateral bond formation (i = form), lateral bond rupture (i = rup), and hydrolysis (i = rup). Both simulations were run with $c_\text{tub} = 11\,\mu\text{M}$.

6.4 Impact on Computational Speed

In subsection 2.3.4, we have discussed that calculating the mechanical hydrolysis rate only requires calculating a local energy difference for each relevant GTP-tubulin dimer. For a constant hydrolysis rate, no rate must be calculated making it faster to calculate the tentative reaction times for such hydrolysis events. While running the simulations and comparing runtimes between a constant hydrolysis rate and mechanical hydrolysis, it became clear, however, that the increase in runtime for mechanical hydrolysis simulations could not solely be due to this change. Instead, we found that minimizations required more time. To understand this effect, we measured the runtimes of the minimizations after each event execution and calculated the running average for each possible event type as a function of the simulation t_sim. The results in Figure 6.16 show that the minimization times after polymerization, depolymerization, lateral bond formation, and lateral bond rupture events are similar between a constant hydrolysis rate and mechanical hydrolysis. In both cases, we also see that the running average of the minimization time after hydrolysis events takes some time until it reaches it steady-state value. This value is, however, four times higher for mechanical hydrolysis than for a constant hydrolysis rate.

To explain this increase in minimization time, we have also plotted the porous GTP-cap length N_pcap in Figure 6.16, and we see that for both simulations, the porous GTP-cap length N_pcap and the average minimization time after hydrolysis events $\langle t_\text{min}^\text{h}\rangle$ reach their steady-state value around the same time, though N_pcap is about six times longer for the mechanical hydrolysis simulation than the simulation with a constant hydrolysis rate. This increase in the porous GTP-cap length means that during minimizations, up to six times more layers need to be considered if a GTP-tubulin dimer located far from the microtubule plus end is hydrolyzed. This significant increase in the number of tubulin dimers that are used for minimization results in a slowdown of the minimization.

Lastly, we want to mention that both simulations spend about 98 % of their runtime with minimizations, further showing that the differences in calculating the hydrolysis rates are negligible. If we split up that total minimization time between the different event types, however, the simulation with a constant hydrolysis rate, whose data is shown in Figure 6.16(a), uses about 30 % of its minimization time for minimizations after hydrolysis events. The simulation with mechanical hydrolysis, whose data is shown in Figure 6.16(b), on the other hand, uses about 66 % of its minimization time for minimizations after hydrolysis events. At the same time, the percentage of hydrolysis events from all events was only about 0.1 percentage points higher for mechanical hydrolysis. Additionally, such large deviations can also not be explained by different processors on which individual simulations run, in particular as the example for mechanical hydrolysis in Figure 6.16(b) ran on a newer and faster processor compared to the simulation with a constant hydrolysis rate in Figure 6.16(a).

Microtubule Properties

7

Before we focus on and analyze individual microtubule growth trajectories in chapter 8, we first consider different properties related to the distribution of GTP-tubulin dimers in the simulated microtubules and the structure of their tips.

7.1 GTP-Islands

Due to the random hydrolysis rule that we implemented, there can be multiple segments of GTP-tubulin dimers within each protofilament, not just one terminal segment in form of the GTP-cap. Such "GTP-islands"[53,57,88,89] are not just a feature introduced by this random hydrolysis rule, but they have been observed in experiments[53,57] as well. The length of a GTP-island L_{isl} is defined as the number of GTP-tubulin dimers in the island so that the minimum length is 1 and the maximum length is the number of tubulin dimers in the protofilament. In addition to the GTP-island length L_{isl}, we will also consider the number of GTP-islands per protofilament N_{isl}. Figure 7.1 shows the probability distributions of L_{isl} and N_{isl} for different free GTP-tubulin dimer concentrations c_{tub} and different hydrolysis rates k_{h}.

Antal et al.[88,89] used a one-dimensional microtubule model and calculated the probability of GTP-islands having the length L_{isl} in the case of unrestricted growth and fast polymerization as:

$$p(L_{\text{isl}}) = \frac{4}{L_{\text{isl}}(L_{\text{isl}}+1)(L_{\text{isl}}+2)}. \tag{7.1}$$

Our simulation data in the left column of Figure 7.1 matches their one-dimensional simulations results, even in the form of the deviations from (7.1) by first increasing a bit above (7.1) before being lower for larger values of L_{isl}. They explain this deviation as a finite-size effect of the system, which is also supported by our data as the deviation in the tail of the distribution starts later for larger values of c_{tub} for which the simulated microtubules are longer. In our case, there is another factor causing deviations for some parameter combinations as the values of c_{tub} and k_{h} influence whether the microtubule can be considered growing (almost) unrestrictedly. For small values of c_{tub} and/or large values of k_{h}, there is not even a proper growth phase, as previously shown in Figure 5.1. The small peak around $L_{\text{isl}} = 10$, which becomes more pronounced the smaller c_{tub} and the larger k_{h} is, is a direct result of the initial GTP-cap length of $N_{\text{GTP}} = 10$.

From (7.1), the predicted average length of a GTP-island can be calculated as

$$\langle L_{\text{isl}} \rangle = \sum_{L_{\text{isl}}=1}^{\infty} L_{\text{isl}}\, p(L_{\text{isl}}) = 2, \tag{7.2}$$

which our simulations reach quite closely in the relevant case of fast growing microtubules as shown in Figure 7.2(a). Deviations from (7.2) in Figure 7.2 are artifacts because for the relevant

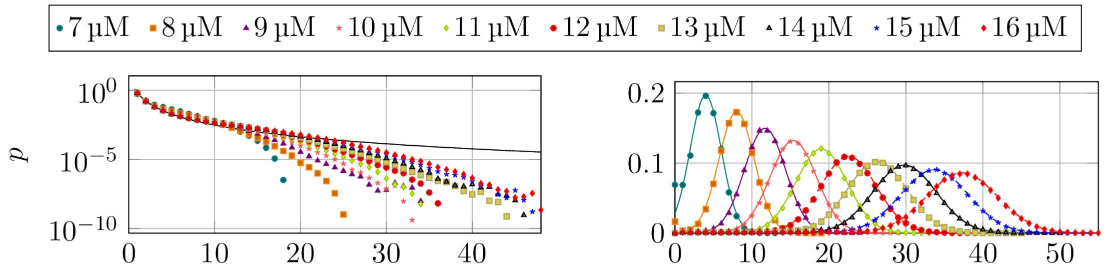

(a) $k_{\mathrm{h}} = 0.1\,\mathrm{s}^{-1}$ **(b)** $k_{\mathrm{h}} = 0.1\,\mathrm{s}^{-1}$.

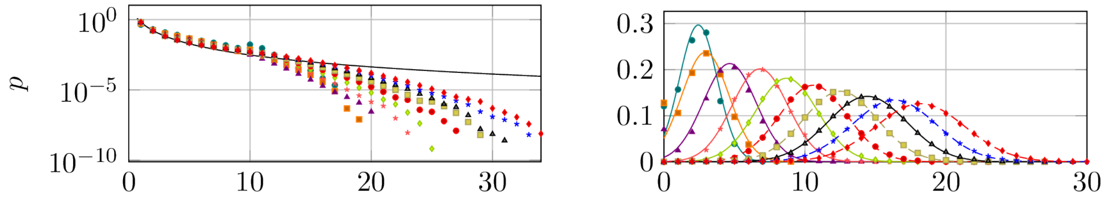

(c) $k_{\mathrm{h}} = 0.2\,\mathrm{s}^{-1}$ **(d)** $k_{\mathrm{h}} = 0.2\,\mathrm{s}^{-1}$

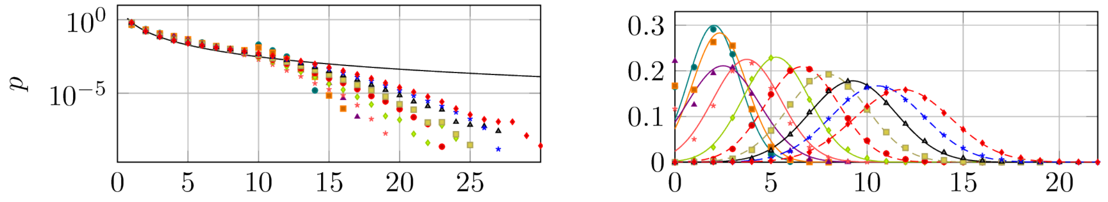

(e) $k_{\mathrm{h}} = 0.3\,\mathrm{s}^{-1}$ **(f)** $k_{\mathrm{h}} = 0.3\,\mathrm{s}^{-1}$

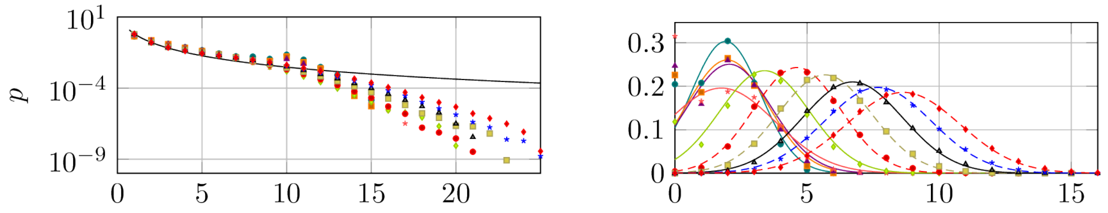

(g) $k_{\mathrm{h}} = 0.4\,\mathrm{s}^{-1}$ **(h)** $k_{\mathrm{h}} = 0.4\,\mathrm{s}^{-1}$

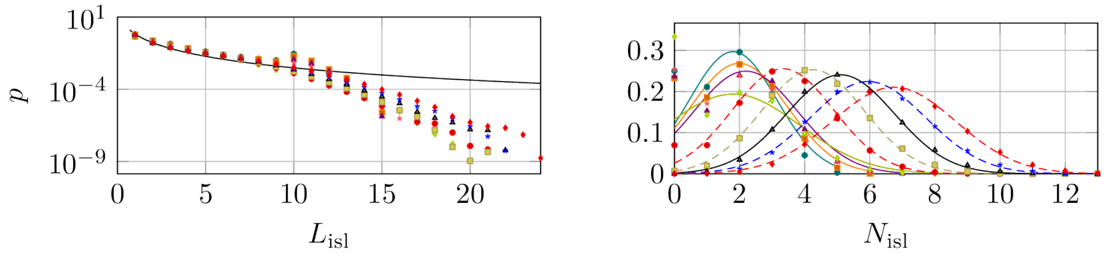

(i) $k_{\mathrm{h}} = 0.5\,\mathrm{s}^{-1}$ **(j)** $k_{\mathrm{h}} = 0.5\,\mathrm{s}^{-1}$

Figure 7.1: Distribution of the GTP-islands lengths L_{isl} (left column, with black lines showing (7.1)) and the number of GTP-islands per protofilament N_{isl} (right column, with fits via (7.4)) for different free GTP-tubulin dimer concentrations c_{tub} and different constant hydrolysis rates k_{h}.

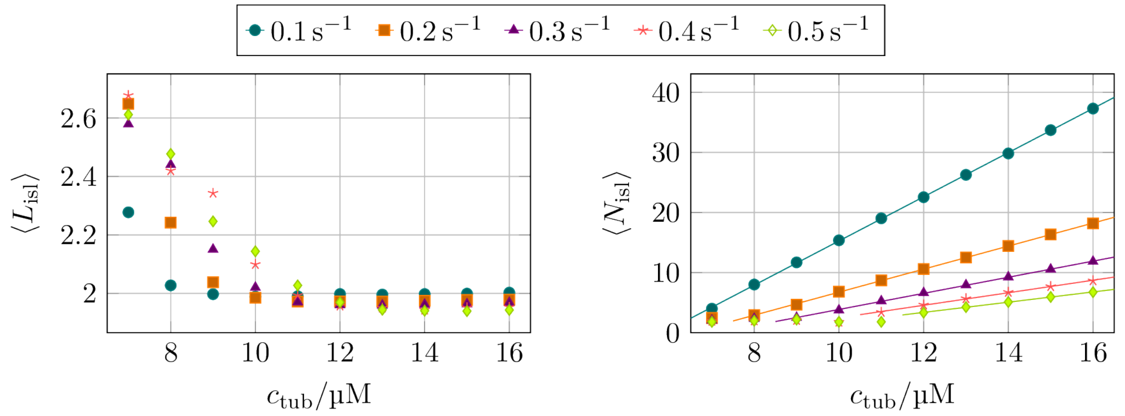

(a) Average length of GTP-islands $\langle L_{\text{isl}} \rangle$ as a function of c_{tub}.

(b) Average number of GTP-islands per protofilament $\langle N_{\text{isl}} \rangle$ as a function of c_{tub}.

Figure 7.2: The average length of GTP-islands $\langle L_{\text{isl}} \rangle$ and the average number of GTP-islands per protofilament $\langle N_{\text{isl}} \rangle$ as a function of the free GTP-tubulin dimer concentration c_{tub} for different hydrolysis rates k_{h} from the data in Figure 7.1.

parameter sets, microtubules are not growing so that (7.2) does not apply and the presence of GTP-islands is only due to the initial GTP-cap. On first sight, it might be surprising that (7.2) does not depend on the free GTP-tubulin dimer concentration c_{tub} as a larger c_{tub} value also implies a larger number of GTP-tubulin dimers N_{GTP}. As the hydrolysis current, however, increases with N_{GTP} as well, see (F.53), the average GTP-island length stays the same. In the following discussion of the number of GTP-islands, we will see that increasing c_{tub} does increase the number of GTP-islands so that

$$\langle L_{\text{isl}} \rangle = \left\langle \frac{N_{\text{GTP}}}{N_{\text{isl}}} \right\rangle \simeq \frac{\langle N_{\text{GTP}} \rangle}{\langle N_{\text{isl}} \rangle} \simeq 2 \tag{7.3}$$

for $c_{\text{tub}} > c_{\text{crit}}$. Figure 7.3 shows that N_{GTP} also increases linearly with c_{tub}, just like $\langle N_{\text{isl}} \rangle$ (see Figure 7.2(b)).

The right column of Figure 7.1 shows that the number of GTP-islands per protofilament follows a normal distribution

$$\rho_{\text{prob}}(N_{\text{isl}}) = \frac{1}{\sqrt{2\pi}\,\sigma} \exp\left[-\frac{1}{2} \left(\frac{N_{\text{isl}} - \langle N_{\text{isl}} \rangle}{\sigma} \right)^2 \right]. \tag{7.4}$$

For smaller values of c_{tub} at which the microtubules do not grow, the values for $N_{\text{isl}} = 0$ and sometimes $N_{\text{isl}} = 1$ are increased compared to a normal distribution due to domination of shrinkage when using these parameters. In such cases, we ignored these N_{isl} values when fitting the normal distribution (7.4).

The average number of GTP-islands per protofilament $\langle N_{\text{isl}} \rangle$ obtained from fitting (7.4) to the data in Figure 7.1 increases linearly with the free GTP-tubulin dimer concentration c_{tub} from $c_{\text{tub}} > c_{\text{crit}}$, i.e., when the microtubules are able to grow, as shown in Figure 7.2(b). This

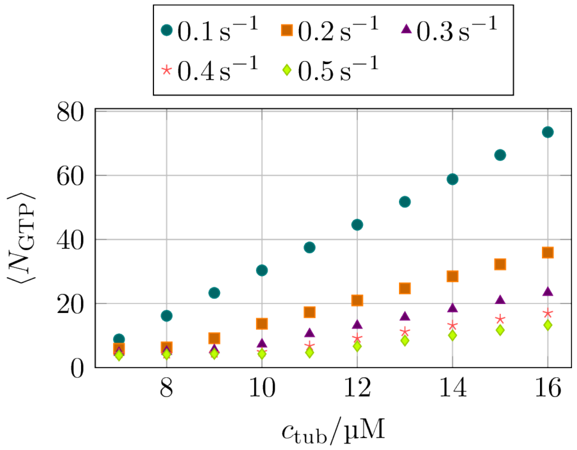

Figure 7.3: Average number of GTP-tubulin dimers per protofilament $\langle N_{\mathrm{GTP}} \rangle$ as a function of c_{tub}.

increase in $\langle N_{\mathrm{isl}} \rangle$ for larger c_{tub} is a direct consequence of the greater number of GTP-tubulin dimers in the microtubule when c_{tub} is increased and k_{h} is kept the same.

We repeated the same analysis for mechanical hydrolysis and found the number of GTP-islands N_{isl} to still follow a Gaussian distribution as shown in the right column of Figure 7.4. The distribution of the GTP-island lengths L_{isl}, however, does not generally match (7.1) anymore due to the non-constant hydrolysis rate in the simulations while a constant hydrolysis was used to calculate (7.1). Compared to the GTP-island lengths when using a constant hydrolysis shown in Figure 7.1, the GTP-islands with mechanical hydrolysis are shorter. The GTP-islands being shorter is already visible in Figure 7.4 but becomes even more evident when comparing the average GTP-island length in Figure 7.5(a) with Figure 7.2(a). We observe the same small peak around $L_{\mathrm{isl}} = 10$ as for constant hydrolysis rates, though the peak is more pronounced for mechanical hydrolysis due to the overall smaller island lengths. The reason for shorter GTP-islands was already mentioned in section 6.2: the tendency of GTP-islands being hydrolyzed from the interior, which we called an “anti-vectorial hydrolysis mechanism”, making it more likely that a GTP-island is split in half than the island shrinking by one GTP-tubulin dimer from its borders. As a consequence of this anti-vectorial hydrolysis mechanism, longer GTP-islands are suppressed. Additionally, Figure 7.5(a) shows that for growing microtubules, the average GTP-islands length becomes $\langle L_{\mathrm{isl}} \rangle \simeq 1$. The persistence of such remaining individual GTP-tubulin dimers in the GDP-body was implicitly already foreshadowed in Figure 6.6(b), where we showed the bending angles of tubulin monomers in a protofilament in which all but one tubulin dimers were hydrolyzed. The effect of an individual GTP-tubulin dimer was that this tubulin dimer bends inward resulting in a decrease of the hydrolysis rate making such individual GTP-tubulin dimers more unlikely to hydrolyze. As a consequence of smaller GTP-islands, there are now more GTP-islands, see Figure 7.5(b), than for a constant hydrolysis rate (see Figure 7.2(b)).

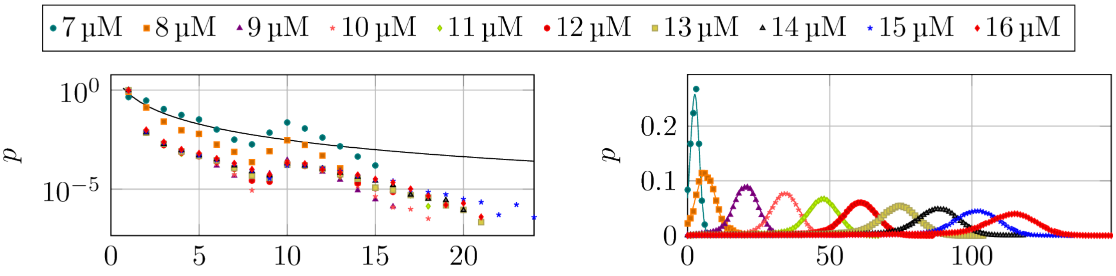

(a) $k_\mathrm{h}^0 = 1\,\mathrm{s}^{-1}$ (b) $k_\mathrm{h}^0 = 1\,\mathrm{s}^{-1}$

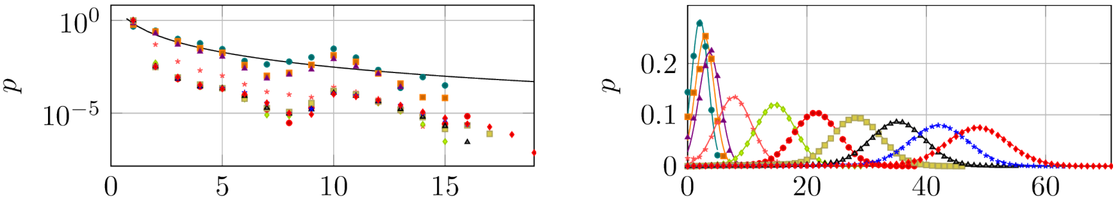

(c) $k_\mathrm{h}^0 = 2\,\mathrm{s}^{-1}$ (d) $k_\mathrm{h}^0 = 2\,\mathrm{s}^{-1}$

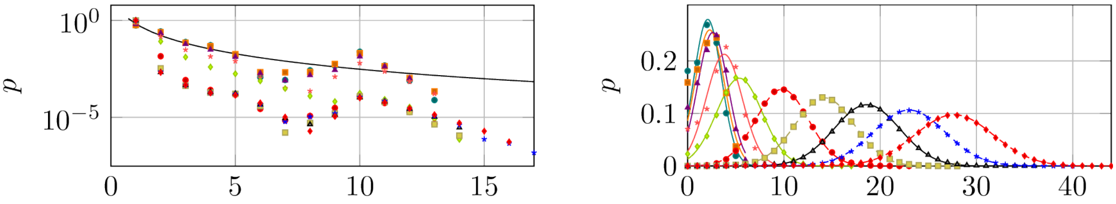

(e) $k_\mathrm{h}^0 = 3\,\mathrm{s}^{-1}$ (f) $k_\mathrm{h}^0 = 3\,\mathrm{s}^{-1}$

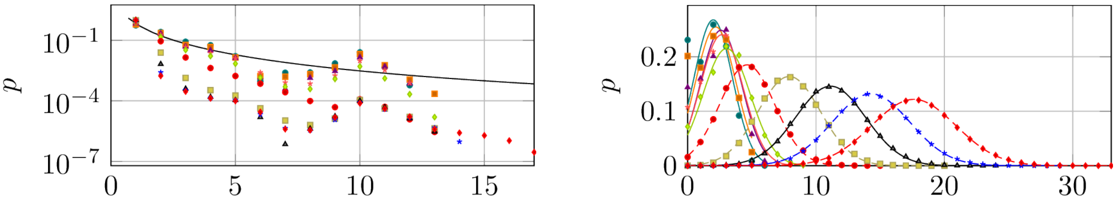

(g) $k_\mathrm{h}^0 = 4\,\mathrm{s}^{-1}$ (h) $k_\mathrm{h}^0 = 4\,\mathrm{s}^{-1}$

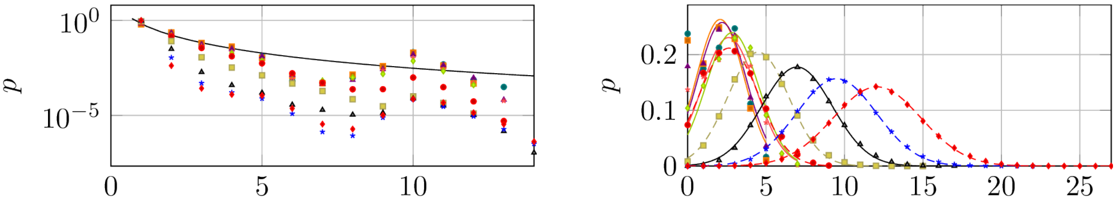

(i) $k_\mathrm{h}^0 = 5\,\mathrm{s}^{-1}$ (j) $k_\mathrm{h}^0 = 5\,\mathrm{s}^{-1}$

Figure 7.4: Distribution of the GTP-islands lengths L_isl (left column, with black lines showing (7.1)) and the number of GTP-islands per protofilament N_isl (right column, with fits via (7.4)) for different free GTP-tubulin dimer concentrations c_tub and different base hydrolysis rates k_h^0.

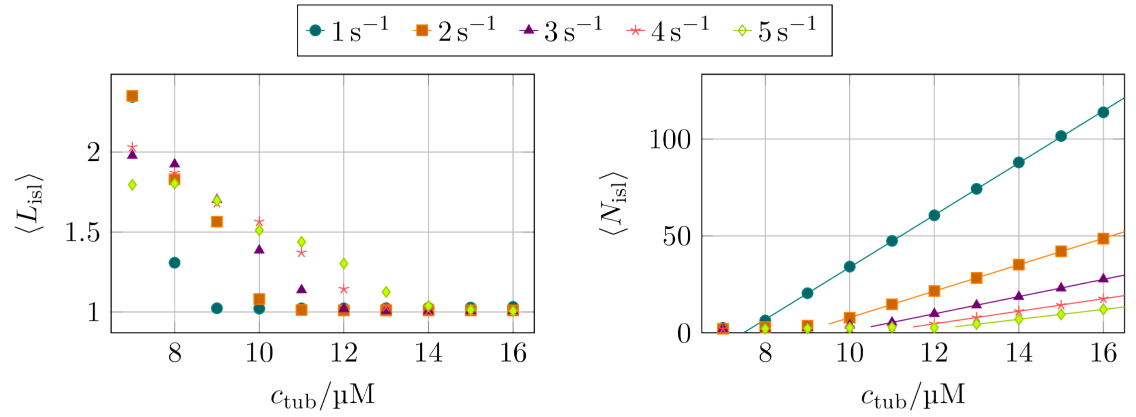

(a) Average length of GTP-islands $\langle L_{\mathrm{isl}} \rangle$ as a function of c_{tub}.

(b) Average number of GTP-islands per protofilament $\langle N_{\mathrm{isl}} \rangle$ as a function of c_{tub}.

Figure 7.5: The average length of GTP-islands $\langle L_{\mathrm{isl}} \rangle$ and the average number of GTP-islands per protofilament $\langle N_{\mathrm{isl}} \rangle$ as a function of the free GTP-tubulin dimer concentration c_{tub} for different base hydrolysis rates k_{h}^{0} from the data in Figure 7.4.

7.2 GTP-Cap Length

In section 5.3, we have already considered the GTP-cap length when discussing the influence of the hydrolysis rate k_h on the growth velocity v_gr. In this section, we will now show that the previously mentioned dependence of the average GTP-cap length $\langle N_\mathrm{cap} \rangle$ on k_h and on c_tub is expected.

While discussing a one-dimensional actin filament model, which is equivalent to a one-dimensional microtubule model for the discussion in this section, Li et al.[212] found the following probability distribution for ATP-caps (in our case: GTP-caps) of length N_cap for fast growth[1] using a master equation approach similar to Antal et al.[88,89]:

$$p(N_\mathrm{cap}) \simeq \frac{N_\mathrm{cap} k_\mathrm{h}}{k_\mathrm{gr}} \exp\left(-\frac{k_\mathrm{h} N_\mathrm{cap}^2}{2k_\mathrm{gr}} \right), \tag{7.5}$$

where k_gr (in units of s^{-1}) is the growth rate, which relates to the growth velocity v_gr (given in units of $\mathrm{\mu m\, min^{-1}}$) via

$$k_\mathrm{gr} = \frac{125 v_\mathrm{gr}}{60} \frac{\mathrm{min}}{\mathrm{\mu m\, s}}. \tag{7.6}$$

From (7.5), the average GTP-cap length follows as[212]

$$\langle N_\mathrm{cap} \rangle \simeq \sqrt{\frac{\pi k_\mathrm{gr}}{2k_\mathrm{h}}}. \tag{7.7}$$

The upper row of Figure 7.6 shows the distribution of the GTP-cap lengths for constant hydrolysis rates and the expected distributions according to (7.5) with the growth rates k_gr calculated from the growth velocities $v_\mathrm{gr}(c_\mathrm{tub})$ in Figure 5.3. We find relatively good agreement between the prediction (7.5) of the one-dimensional and the data of our three-dimensional model for higher values of c_tub. As expected, however, the deviations between prediction and data grow as c_tub decreases and/or k_h increases as in both cases, the assumption of fast growth becomes less valid until the microtubules do not even grow anymore. Additional deviations arise for smaller GTP-cap lengths due to newly polymerized GTP-tubulin dimers not being able to hydrolyze directly as explained in subsection 2.3.3 making smaller GTP-caps more likely. In Figure G.1, we show that by using the general form of (7.5) and adding a “shift parameter” ($N_\mathrm{cap} \to N_\mathrm{cap} + b$), the data can be reproduced better by such fit functions. We also find that for $c_\mathrm{tub} > c_\mathrm{crit}$, the average GTP-cap length $\langle N_\mathrm{cap} \rangle$ shown in Figure 7.7(a) matches the expectation (7.7).

The GTP-cap length distribution for mechanical hydrolysis is shown in the lower row of Figure 7.6. For mechanical hydrolysis, (7.5) does not fit anymore due to the increased probability for cap-less protofilaments or GTP-caps only consisting of a single tubulin dimer. This finding is consistent with the results in section 6.2, where we found a higher probability for GTP-tubulin dimers at the tip being hydrolyzed.

---

[1] Li et al.[212] considered different ATP-hydrolysis rates depending on the neighbor of the relevant monomer via the parameter ρ_c. If there is no influence of the neighbor’s hydrolysis state, as it is the case for us when using a constant hydrolysis rate k_h, $\rho_\mathrm{c} = 1$.

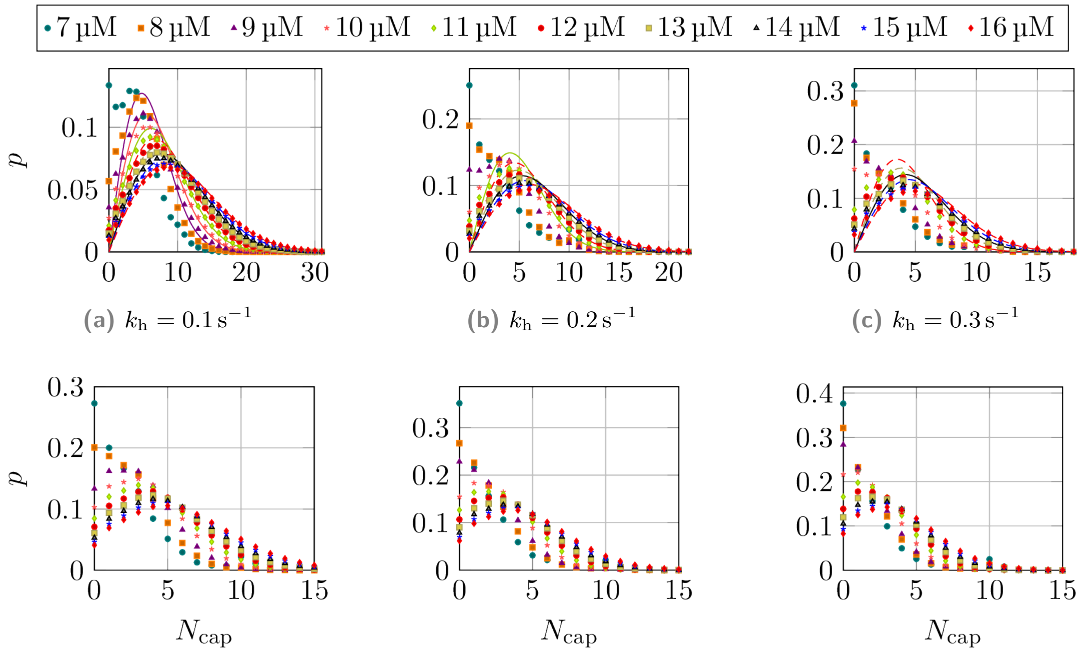

(a) $k_{\mathrm{h}} = 0.1\,\mathrm{s}^{-1}$ (b) $k_{\mathrm{h}} = 0.2\,\mathrm{s}^{-1}$ (c) $k_{\mathrm{h}} = 0.3\,\mathrm{s}^{-1}$

(d) $k_{\mathrm{h}}^{0} = 1.0\,\mathrm{s}^{-1}$ (e) $k_{\mathrm{h}}^{0} = 1.5\,\mathrm{s}^{-1}$ (f) $k_{\mathrm{h}}^{0} = 2.0\,\mathrm{s}^{-1}$

Figure 7.6: The GTP-cap length distribution $p(N_{\mathrm{cap}})$ for different constant hydrolysis rates k_{h} (upper row) and different base hydrolysis rates k_{h}^{0} (lower row) and different free GTP-tubulin dimer concentrations c_{tub}. The lines are the expected results according to (7.5).

In Figure 6.15(a), we have shown the growth velocity as a function of the free GTP-tubulin dimer distribution $v_{\mathrm{gr}}(c_{\mathrm{tub}})$. In contrast to a constant hydrolysis rate k_{h}, there is no clear fixed hydrolysis rate we can use in (7.5) and (7.7), in particular because we have seen in Figure 6.15(b) that $\langle k_{\mathrm{h}} \rangle$ depends on c_{tub}. For the average GTP-cap length data in Figure 7.7(b) for mechanical hydrolysis, however, there is still a square root-like dependence on c_{tub} if we ignore the data points with $c_{\mathrm{tub}} < c_{\mathrm{crit}}$. By using k_{h} as a fit parameter and using the known $v_{\mathrm{gr}}(c_{\mathrm{tub}})$ relation to calculate the growth rate k_{gr}, (7.7) still fits the data, as shown in Figure 7.7(b). As already mentioned, $\langle k_{\mathrm{h}} \rangle$ is not independent of c_{tub}, but if, nevertheless, we average the rates of actual hydrolysis events over c_{tub} and compare them to the fitted values used for the lines in Figure 7.7(b), we find there to be only a systematic shift manifested in different y-intercepts of the fit lines but almost identical slopes that only deviate about 3 % from each other.

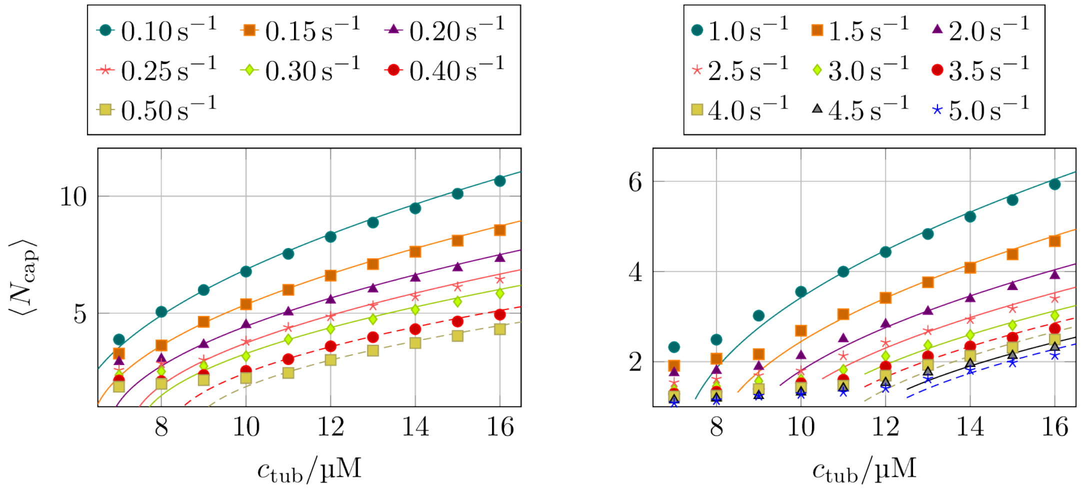

(a) Constant hydrolysis rate with expected results via (7.7) as lines.

(b) Mechanical hydrolysis with fits using k_{h} in (7.7) as a fit parameter.

Figure 7.7: Average GTP-cap length $\langle N_{\mathrm{cap}} \rangle$ as a function of the free GTP-tubulin dimer concentration c_{tub} for different constant hydrolysis rates k_{h} and different base hydrolysis rates k_{h}^{0} (mechanical hydrolysis).

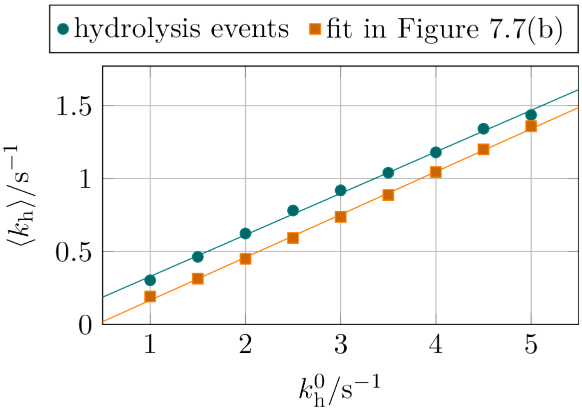

Figure 7.8: Comparison of the average hydrolysis rate $\langle k_{\mathrm{h}} \rangle$ as a function of the base hydrolysis rate k_{h}^{0} obtained from averaging the rates of actually executed hydrolysis events and from the fits shown in Figure 7.7(b).

7.3 Porous GTP-Cap Length and GTP-Tubulin Dimer Distribution

The porous GTP-cap length N_{pcap} gives an indication of the extent that GTP-tubulin dimers remain unhydrolyzed in the GDP-dominated body of a microtubule. If $N_{\mathrm{pcap}} \simeq N_{\mathrm{cap}}$, the GTP-tubulin dimers are concentrated at the microtubule plus end, while for $N_{\mathrm{pcap}} \gg N_{\mathrm{cap}}$, there are GTP-tubulin dimers far from the GTP-cap and thus also far from the microtubule plus end.

In Figure 6.8(a), we have seen that, at least for $c_{\mathrm{tub}} > c_{\mathrm{crit}}$, the probability to find a GTP-tubulin dimer at a certain distance from the tip follows an exponential distribution for a constant hydrolysis rate and to follow at least an exponential distribution in the body of the microtubule for mechanical hydrolysis (see Figure 6.8(b)). If we consider a protofilament with GTP-tubulin dimers at positions $\{\Delta d_{\mathrm{tip}}^{\mathrm{GTP}}(i)\}$, then the length of the porous GTP-cap is, by definition,

$$N_{\mathrm{pcap}} = \max_i \Delta d_{\mathrm{tip}}^{\mathrm{GTP}}(i) + 1, \tag{7.8}$$

i.e., the porous GTP-cap length is the extreme value of the GTP-tubulin dimer positions (plus one, which is due to $\Delta d_{\mathrm{tip}}^{\mathrm{GTP}} = 0$ referencing the terminal tubulin dimer, which would result in $N_{\mathrm{pcap}} = 1$ if it was the only GTP-tubulin dimer in the protofilament). Hence, the distribution of the porous GTP-cap lengths is a so-called extreme value distribution. As the Δd_{tip} values are distributed exponentially, the expectation is that N_{pcap} follows an extreme value distribution of type 1, also called the Gumbel distribution[213,214]:

$$g(x) = \frac{1}{\sigma} \exp\left[-\frac{x-\mu}{\sigma} - \exp\left(-\frac{x-\mu}{\sigma}\right)\right] \tag{7.9}$$

with $\sigma > 0$. In contrast to the Gaussian distribution in which μ denotes the expected value of the distribution, the expected value of the Gumbel distribution (7.9) is

$$\langle x \rangle = \mu + \gamma\sigma \tag{7.10}$$

with the Euler–Mascheroni constant $\gamma \simeq 0.57722$.[213,214]

If N random number are drawn from an exponential distribution

$$p(x) = \lambda \exp(-\lambda x) \tag{7.11}$$

then the parameters of the Gumbel distribution (7.9) are[213,214]

$$\sigma = \frac{1}{\lambda}, \tag{7.12}$$

$$\mu = \frac{1}{\lambda} \ln N \tag{7.13}$$

changing (7.9) to:

$$g(x) = \lambda N \exp\left[-\lambda x - N \exp(-\lambda x)\right]. \tag{7.14}$$

It must be noted that the Gumbel distribution is not an exact result but only the asymptotic distribution. The exact extreme value distribution can be calculated as follows[215]: For a given probability density function $p(x)$, the probability to draw a random number from $p(x)$ to be less than or equal to X is given by the associated cumulative distribution function

$$\mathrm{Prob}(x \leq X) = q(X) = \int_{-\infty}^{X} \mathrm{d}x p(x) \tag{7.15}$$

so that

$$p(x) = \frac{\mathrm{d}q}{\mathrm{d}x} \, . \tag{7.16}$$

The probability that N numbers x_i from $p(x)$ are less than or equal to X is then given by

$$\mathrm{Prob}(\forall x_i \leq X) = \big[\mathrm{Prob}(x_i \leq X)\big]^N = \big[q(X)\big]^N \equiv Q(X). \tag{7.17}$$

The matching probability density function follows from (7.16) as

$$P(x) = \frac{\mathrm{d}Q}{\mathrm{d}x} = N \left[q(x)\right]^{N-1} \frac{\mathrm{d}q}{\mathrm{d}x} = N p(x) \left[q(x)\right]^{N-1} . \tag{7.18}$$

The cumulative distribution function of the exponential function (7.11) is

$$q(x) = 1 - \exp\left(-\lambda x\right) \tag{7.19}$$

so that $P(x)$ for the exponential distribution is

$$\begin{align} P(x) &= N\lambda \exp\left(-\lambda x\right) \left[1 - \exp\left(-\lambda x\right)\right]^{N-1} \tag{7.20} \\ &= N\lambda \exp\Big(-\lambda x + (N-1) \ln\left[1 - \exp\left(-\lambda x\right)\right]\Big) . \tag{7.21} \end{align}$$

For large N so that $N \simeq N - 1$ and for small values λx so that the logarithm in (7.21) can be replaced by the first term of its Taylor expansion, (7.21) becomes

$$P(x) \simeq N\lambda \exp\left[-\lambda x - N \exp\left(-\lambda x\right)\right] , \tag{7.22}$$

which is exactly the Gumbel distribution (7.14).

For illustration purposes, we calculated 100 000 maxima of distinct sets of N exponentially distributed numbers for different values of N and λ and compared the distribution of these maxima with the Gumbel distribution (7.14). The generated data and the matching Gumbel distributions are shown in Figure 7.9. The data in Figure 7.9 shows that the Gumbel distribution (7.14) fits the data very well except for $N = 10$ for which there are small deviations at smaller values of x.

We now have to identify the observable/parameter in our model that matches the λ parameter from which the exponentially distributed numbers are drawn and the other observable/parameter in our model that matches the number of exponentially distributed numbers N that are drawn. From (7.8), we see that the positions of the GTP-tubulin dimers in a protofilament are the relevant quantities. As there are N_{GTP} GTP-tubulin dimers in a protofilament, we can identify

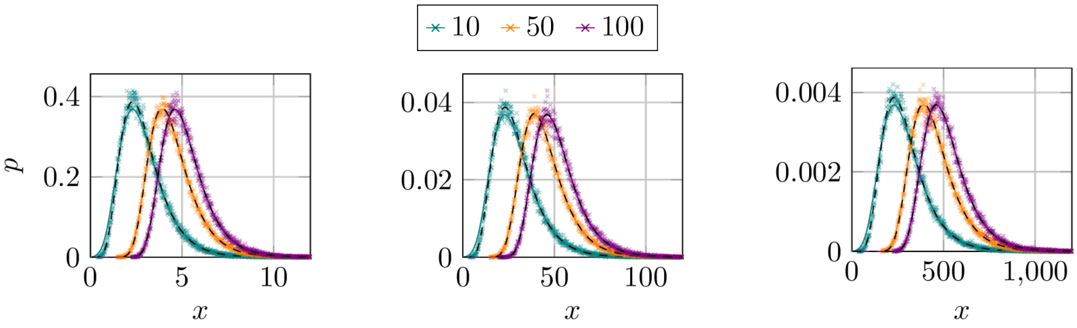

(a) $\lambda = 1$ **(b)** $\lambda = 0.1$ **(c)** $\lambda = 0.01$

Figure 7.9: Comparison of the distribution of the 100 000 maximum values from sets of exponentially distributed random numbers and the corresponding Gumbel distribution (7.14) and the exact distribution (7.21) (black dashed lines) with different numbers N of generated random numbers per set and different values of λ.

$N = N_{\text{GTP}}$. At the beginning of the section, we have already mentioned that the GTP-tubulin dimer positions are distributed exponentially, i.e.,

$$p_{\text{GTP}}(\Delta d_{\text{tip}}) = \lambda \exp\left(-\lambda \Delta d_{\text{tip}}\right) \tag{7.23}$$

so that we now also know the origin of λ. In the context of how mechanical hydrolysis influence the distribution of GTP-tubulin dimers, we have already shown the distribution of $p_{\text{GTP}}(\Delta d_{\text{tip}})$ for one value k_{h} in Figure 6.8(a). The remaining distributions can be found in Figure G.2 and the associated values of λ in Table G.1. We have to emphasize again here that the exponential distribution is only expected for growing microtubules so that for parameter sets for which $c_{\text{tub}} < c_{\text{crit}}$, i.e., for which microtubules do not grow, a non-exponential distribution is expected.

As we already have identified $N = N_{\text{GTP}}$, we have to group all of the porous GTP-cap lengths by the current number of GTP-tubulin dimers in the relevant protofilament as N_{GTP} changes over time. Otherwise, we get the distribution of porous GTP-cap lengths averaged over all N_{GTP} values. Additionally, in the case of growing microtubules, it will take some time before both, the porous GTP-cap length N_{pcap} and the number of GTP-tubulin dimers N_{GTP}, will reach a steady-state value (or, to be more precise, fluctuate around a steady-state value), as shown in Figure 7.10. Considering the pre-steady-state values would result in an increased probability for smaller N_{pcap} values. As a consequence for the following analysis of the porous GTP-cap length distribution, we ignore the first data sets until N_{pcap} reaches its steady-state value.

7.3.1 Constant Hydrolysis Rate

Figure 7.11 shows the distribution of the porous GTP-cap length N_{GTP} for some parameter sets. For each parameter set of k_{h} and c_{tub}, three values of N_{GTP} were chosen so that the smallest and largest value is shown for which sufficient data exists. While all data sets have the form of

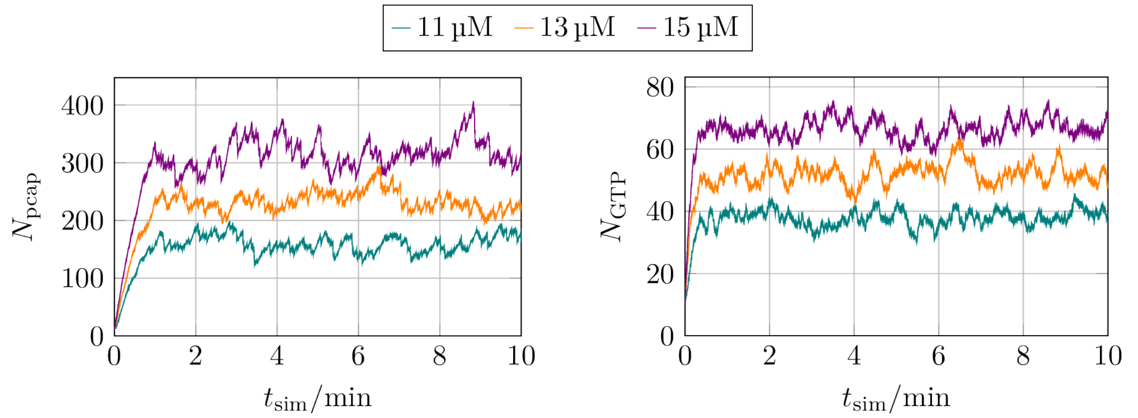

(a) Porous GTP-cap length N_pcap as a function of time t_sim.

(b) Number of GTP-tubulin dimers per protofilament N_GTP as a function of time t_sim.

Figure 7.10: The porous GTP-cap length N_pcap and the number of GTP-tubulin dimers per protofilament N_GTP take some time until they fluctuate around a steady-state value. The shown data is for three exemplary simulations with $k_\mathrm{h} = 0.1\,\mathrm{s}^{-1}$ and different values of c_tub.

Gumbel distributions and the deviations between the Gumbel distribution (7.14) and the exact distribution (7.21) are relatively small (compare the solid colored lines and the dashed black lines in Figure 7.11), the expected distributions only sometimes match the actual data.

To investigate the origin of these deviations, we first considered correlations. For the examples in Figure 7.9, we have determined the maximum of 100 000 *independent* sets of exponentially distributed numbers. For our microtubules, the individual GTP-tubulin dimer distributions of the simulation are inherently *not* independent of each other as the GTP-tubulin dimer distribution at iteration i directly follows from the GTP-tubulin dimer distribution at iteration $i - 1$. (In the actual simulation, we only logged observables every 20 iterations to keep the file sizes smaller, but after 20 iterations, the GTP-tubulin dimer distribution generally does not change drastically.) To avoid any other potential underlying influence affecting our microtubule data, we return to drawing random number from an exponential distribution directly like we did for Figure 7.9. Now, however, after the first set of N random numbers is draw, a random subset of M of these numbers is kept and only $N - M$ new random numbers are drawn. Using the same number parameters as in Figure 7.9 and choosing different rations M/N, the data in Figure 7.12 shows that increasing M “worsens” the data in the sense that there are greater fluctuations around the expected Gumbel distributions, but there is no shift of the peak of the distributions. These results indicate that correlations are not responsible for the deviations in Figure 7.11 between the data and the expected distributions.

Another possible explanation for the deviations could lie in the expected distributions themselves. While the value of $N = N_\mathrm{GTP}$ is fixed, we determined the value of λ from the exponential decay of the GTP-tubulin dimer distribution as shown in Figure G.2. Instead of using the $p_\mathrm{GTP}(\Delta d_\mathrm{tip})$ data, determining λ by fitting (7.23) and then using this value of λ as the parameter value for the expected extreme value distribution, we can also use the $\{(\Delta d_\mathrm{tip}, p_\mathrm{GTP})\}$ data as a discrete probability distribution. We can draw random numbers from this discrete probability

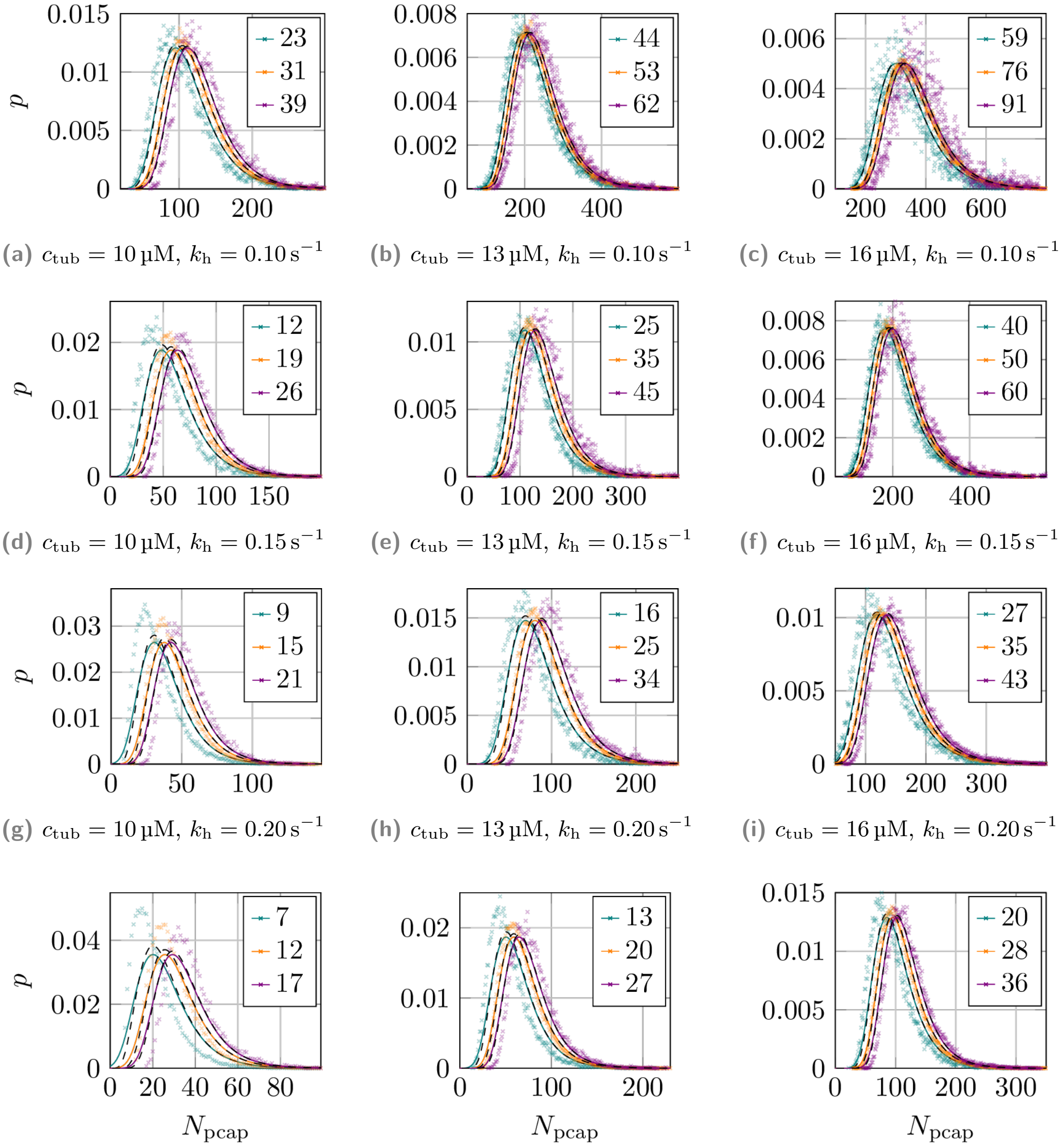

(a) $c_{\text{tub}} = 10\,\mu\text{M}$, $k_{\text{h}} = 0.10\,\text{s}^{-1}$ (b) $c_{\text{tub}} = 13\,\mu\text{M}$, $k_{\text{h}} = 0.10\,\text{s}^{-1}$ (c) $c_{\text{tub}} = 16\,\mu\text{M}$, $k_{\text{h}} = 0.10\,\text{s}^{-1}$

(d) $c_{\text{tub}} = 10\,\mu\text{M}$, $k_{\text{h}} = 0.15\,\text{s}^{-1}$ (e) $c_{\text{tub}} = 13\,\mu\text{M}$, $k_{\text{h}} = 0.15\,\text{s}^{-1}$ (f) $c_{\text{tub}} = 16\,\mu\text{M}$, $k_{\text{h}} = 0.15\,\text{s}^{-1}$

(g) $c_{\text{tub}} = 10\,\mu\text{M}$, $k_{\text{h}} = 0.20\,\text{s}^{-1}$ (h) $c_{\text{tub}} = 13\,\mu\text{M}$, $k_{\text{h}} = 0.20\,\text{s}^{-1}$ (i) $c_{\text{tub}} = 16\,\mu\text{M}$, $k_{\text{h}} = 0.20\,\text{s}^{-1}$

(j) $c_{\text{tub}} = 10\,\mu\text{M}$, $k_{\text{h}} = 0.25\,\text{s}^{-1}$ (k) $c_{\text{tub}} = 13\,\mu\text{M}$, $k_{\text{h}} = 0.25\,\text{s}^{-1}$ (l) $c_{\text{tub}} = 16\,\mu\text{M}$, $k_{\text{h}} = 0.25\,\text{s}^{-1}$

Figure 7.11: Distribution of the porous GTP-cap lengths N_{pcap} for different free GTP-tubulin dimer concentrations c_{tub}, hydrolysis rates k_{h}, and numbers of GTP-tubulin dimers per protofilaments N_{GTP}, the expected Gumbel distributions (7.14), and the exact distribution (7.21) (black dashed lines).

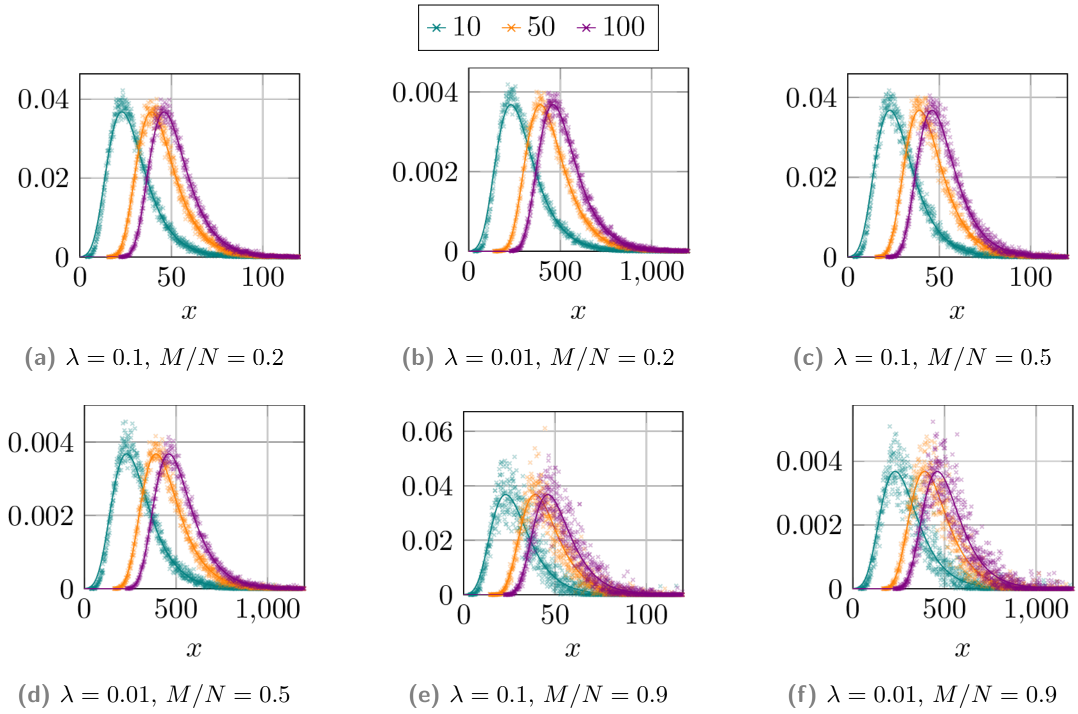

Figure 7.12: Comparison of the distribution of the 100 000 maximum values from sets of exponentially distributed random numbers and the corresponding Gumbel distribution (7.14) with different numbers N of generated random numbers per set, different numbers M of randomly kept numbers between sets, and different values of λ.

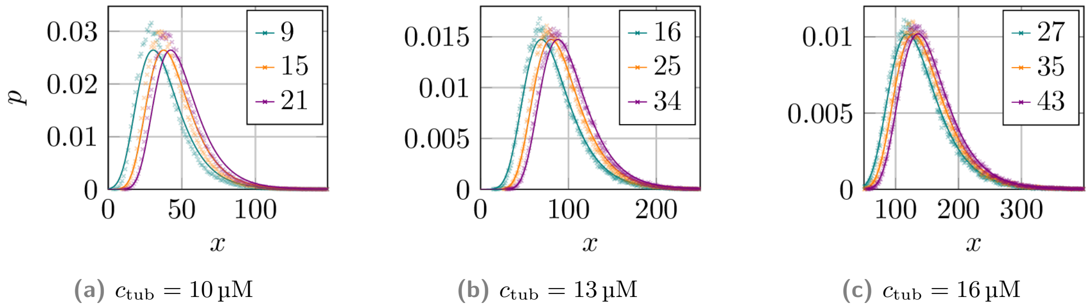

Figure 7.13: Comparison of the distribution of the 100 000 maximum values from sets of random numbers distributed according the to measured GTP-tubulin dimer distribution in Figure G.2(c) for $k_{\text{h}} = 0.20\,\text{s}^{-1}$ and the corresponding Gumbel distribution (7.14) with λ from Table G.1, i.e., from the exponential fits to $p_{\text{GTP}}(\Delta d_{\text{tip}})$.

distribution instead of the fitted exponential distribution and then compare the distribution of the maxima of sets of such random numbers with the expected Gumbel distribution. The data in Figure 7.13 shows some discrepancies between the data and the expected Gumbel distribution, in particular for $c_{\text{tub}} = 10\,\mu\text{M}$ in Figure 7.13(a). They are, however, not as pronounced as our

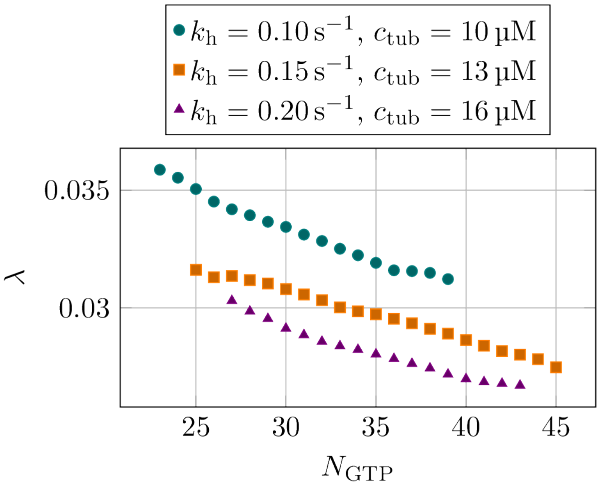

Figure 7.14: λ as a function of the number of GTP-tubulin dimers N_{GTP} in a protofilament by fitting some of the porous GTP-cap distributions in Figure 7.11 with Gumbel distributions (7.14) and using λ as the only fit parameter.

microtubule data in Figure 7.11 and thus also not explaining the deviations.

While our data for the porous GTP-cap length distributions shown in Figure 7.11 does not match the expected Gumbel distributions, the overall shape of the data still resembles Gumbel distributions. We use this fact to now *fit* Gumbel distributions to the data using λ as a fit parameter. If the data actually matched the expected Gumbel distribution, we expect λ to be independent of N_{GTP}. The data in Figure 7.14 confirms the deviations between data and expected distribution in Figure 7.11 because $\lambda(N_{GTP}) \neq \text{const}$. As the value of λ in the Gumbel distribution (7.14) has the same value as in the exponential distribution of the GTP-tubulin dimers $p_{GTP}(\Delta d_{tip})$, this finding implies that the overall exponential decays of $p_{GTP}(\Delta d_{tip})$ shown in Figure G.2 are the result of averaging individual distinct distributions $p_{GTP}(\Delta d_{tip}, N_{GTP})$ with different values of $\lambda(N_{GTP})$.

To check whether this hypothesis is actually true, we determined the distributions of GTP-tubulin dimers separately for the different numbers of GTP-tubulin dimers per protofilament N_{GTP}, i.e., $p_{GTP}(\Delta d_{tip}, N_{GTP})$. For some of the parameter combinations whose porous GTP-cap length distributions $p(N_{pcap})$ are shown in Figure 7.11, Figure 7.15 compares the individual distributions $p_{GTP}(\Delta d_{tip}, N_{GTP})$ with the distribution of GTP-tubulin dimers averaged over N_{GTP}. The first observation is the distinctness of the data for different values of N_{GTP}. Fitting each $p_{GTP}(\Delta d_{tip}, N_{GTP})$ with an exponential distribution would result in different values of λ then, underpinning our previous hypothesis. Secondly, the data in Figure 7.15 then also explains why there is the best agreement between data and expected Gumbel distribution for the intermediate values of N_{GTP} per plot shown in Figure 7.11: For these values of N_{GTP}, the average distribution $p_{GTP}(\Delta d_{tip})$ and the distribution $p_{GTP}(\Delta d_{tip}, N_{GTP})$ are quite close. Lastly, however, we only find the intermediate values of N_{GTP} to follow exponential distributions, while the two other curves deviate, in particular for small values of Δd_{tip}.

To check whether these differences in GTP-tubulin dimer distributions for different values of N_{GTP} explain the deviations in Figure 7.11, we again draw sets of random numbers from the discrete distributions[2] shown in Figure 7.15 and determine their maxima. Then, we fit Gumbel

---

[2] As shown in Figure 7.14, the $p_{GTP}(\Delta d_{tip}, N_{GTP})$ distributions are quite close to exponential distributions in

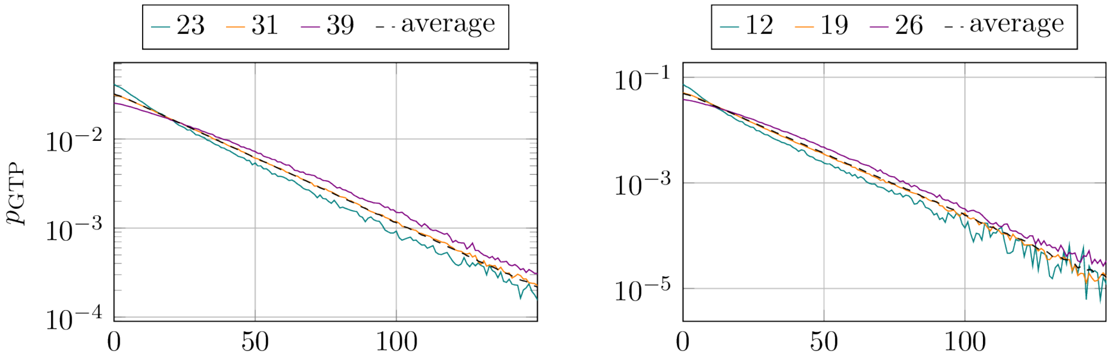

(a) $k_{\mathrm{h}} = 0.10\,\mathrm{s}^{-1}$, $c_{\mathrm{tub}} = 10\,\mu\mathrm{M}$ **(b)** $k_{\mathrm{h}} = 0.15\,\mathrm{s}^{-1}$, $c_{\mathrm{tub}} = 10\,\mu\mathrm{M}$

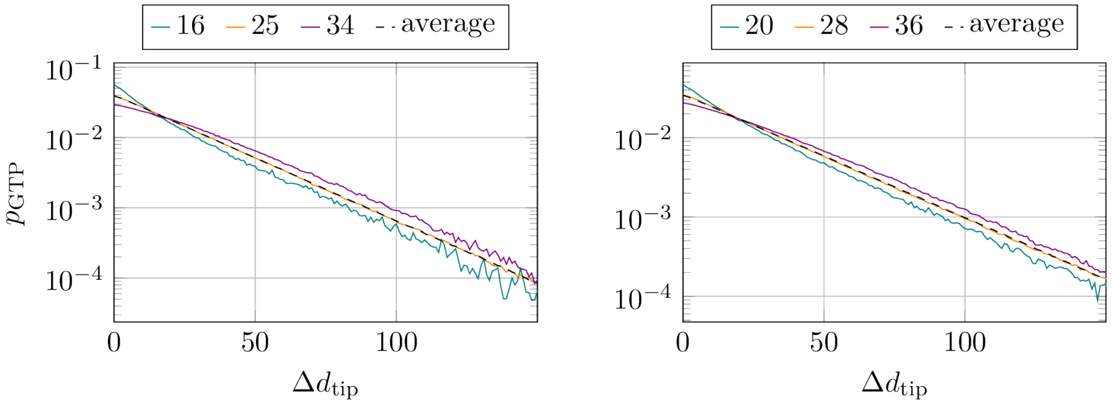

(c) $k_{\mathrm{h}} = 0.20\,\mathrm{s}^{-1}$, $c_{\mathrm{tub}} = 13\,\mu\mathrm{M}$ **(d)** $k_{\mathrm{h}} = 0.25\,\mathrm{s}^{-1}$, $c_{\mathrm{tub}} = 16\,\mu\mathrm{M}$

Figure 7.15: Probability p_{GTP} to find a GTP-tubulin dimer at the distance Δd_{tip} from the tip of its protofilament for different hydrolysis rates k_{h}, free GTP-tubulin dimer concentrations c_{tub}, and different numbers of GTP-tubulin dimers in the protofilament N_{GTP}. The "average" data refers to the data shown in Figure G.2, where the data was not split up by the value of N_{GTP}, i.e., these results were implicitly averaged over N_{GTP}. (To highlight the differences between the different values of N_{GTP}, the Δd_{tip}-axis was cut off compared to Figure G.2.)

distributions to the distribution data of these maxima using λ as a fit parameter and compare these values of λ with the ones we get from fitting the porous GTP-cap distribution data (see Figure 7.14). Figure 7.16 shows that the values of λ obtained by these two approaches match, thus finally explaining the deviations in Figure 7.11.

Having found the reason for the deviations in Figure 7.11 in the dependence of the GTP-tubulin dimer distribution $p_{\mathrm{GTP}}(\Delta d_{\mathrm{tip}})$ on the number of GTP-tubulin dimers in the protofilament N_{GTP}, as shown in Figure 7.15, we have to turn to this finding now. While we have previously compared our porous GTP-cap length data to determining the maximum of sets of exponentially distributed random numbers, this comparison can be misleading. The porous GTP-cap, i.e.,

---

their tail but deviate for small values of Δd_{tip} from exponential distributions so that first fitting an exponential distribution to the data and then drawing random numbers from these fitted distributions would cause additional deviations.

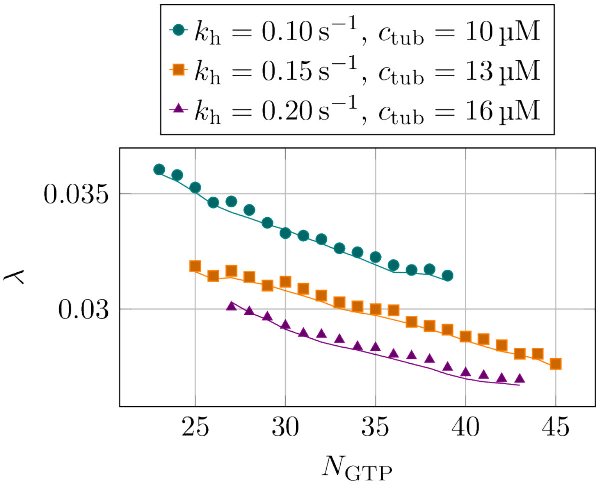

Figure 7.16: Comparison of the values of λ by fitting Gumbel distributions to the distribution of 100 000 maxima of sets of random numbers drawn from the discrete GTP-tubulin dimer distributions $p_{\mathrm{GTP}}(\Delta d_{\mathrm{tip}}, N_{\mathrm{GTP}})$ (data points) with the values of λ when fitting Gumbel distributions to the distribution of porous GTP-cap lengths $p(N_{\mathrm{pcap}}, N_{\mathrm{GTP}})$ like in Figure 7.14 (lines).

the distribution of GTP-tubulin dimers in a protofilament, is not the result of randomly placing GTP-tubulin dimers in a protofilament according to an exponential distribution. Instead, it is the result of the interplay between the polymerization of new GTP-tubulin dimers and the hydrolysis of GTP-tubulin dimers to GDP-tubulin dimers[3]. As a consequence, fluctuations can occur where there are more GTP-tubulin dimers at the tip, for example in the form of a longer GTP-cap, or where there are less GTP-tubulin dimers at the tip. The probability of there being more GTP-tubulin dimers at the tip than on average is, of course, higher if there is a greater number GTP-tubulin dimers present in a protofilament. In practice, it is easy to illustrate these two cases starting from a “perfect” protofilament whose N_{GTP} GTP-tubulin dimer follow an exponential distribution without deviations. In a situation where randomly multiple new GTP-tubulin dimers attach to the protofilament without any existing GTP-tubulin dimers hydrolyzing, the GTP-tubulin dimers are no longer distributed exponentially, but there is a bias for more GTP-tubulin dimers at the tip. In this situation, there are now more than N_{GTP} GTP-tubulin dimers present in the protofilament. The inverse scenario is the bias for less GTP-tubulin dimers at the tip, for example if randomly multiple GTP-tubulin dimers at the tip of the protofilament detach. In this scenario, however, there is still a bias for the terminal tubulin dimer to be a GTP-tubulin dimer because of *new* GTP-tubulin dimers not being hydrolyzable (see subsection 2.3.3). For this case, there are now less than N_{GTP} GTP-tubulin dimers in the protofilament. To check if this link between the number of GTP-tubulin dimers at the tip and the total number of GTP-tubulin dimers in the protofilament explains the data shown in Figure 7.15, we artificially generated GTP-tubulin dimer positions. The starting point is an exponential distribution to which we either add a bias for the last tubulin dimers in the protofilament to be GTP-tubulin dimers or by using a steeper exponential distribution for a shorter GTP-cap in a subset of samples[4]. Figure 7.17 shows that these two cases do indeed

---

[3] Only mentioning these two processes is a simplification for the discussion here. In reality, the depolymerization of GTP-tubulin dimers, which could be combined with their polymerization into a “net polymerization process”, and the depolymerization of GDP-tubulin dimers are also relevant, of course.

[4] For the data with a bias for long GTP-caps, we enforced that the last 10 tubulin dimers to be GTP-tubulin dimers in 2/3 of the configurations generated. To generate a bias for shorted GTP-caps, we used an exponential distribution with $\lambda = 0.09$ in 2/5 of the cases instead of the default unbiased $\lambda = 0.03$. All of these values were chosen arbitrarily to generate a similar plot to Figure 7.15.

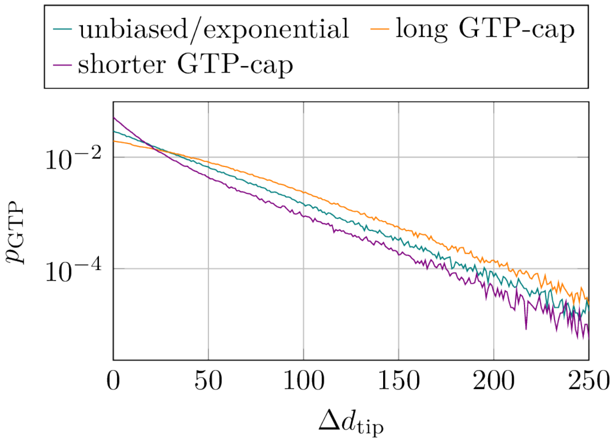

Figure 7.17: Comparison between an unbiased/perfectly exponential GTP-tubulin dimer distribution, a GTP-tubulin dimer distribution favoring longer caps, and a GTP-tubulin dimer distribution favoring shorter caps.

result in similar non-exponential distributions as in Figure 7.15.

In Figure 7.18, we present the overall porous GTP-cap length distributions $p(N_{\mathrm{pcap}})$ not split up by the number of GTP-tubulin dimers N_{GTP}. These distributions are still Gumbel distributions with N_{GTP} close to the average number of GTP-tubulin dimers in a protofilament and λ close to the average λ when fitting the overall GTP-tubulin dimers distributions, as shown in Figure 7.19.

Lastly, before turning to the porous GTP-cap lengths when mechanical hydrolysis is used, we consider the average porous GTP-cap length $\langle N_{\mathrm{pcap}} \rangle$ at different free GTP-tubulin dimer concentrations and for different hydrolysis rates k_{h}, as shown in Figure 7.20. In Figure 7.20(a), we find $\langle N_{\mathrm{pcap}} \rangle(k_{\mathrm{h}})$ to decrease exponentially with k_{h} and Figure 7.20(b) shows that $\langle N_{\mathrm{pcap}} \rangle(c_{\mathrm{tub}})$ increases linearly with c_{tub} for $c_{\mathrm{tub}} > c_{\mathrm{crit}}$. From (7.10), (7.12), and (7.13) the average porous GTP-cap length follows as:

$$\langle N_{\mathrm{pcap}} \rangle \simeq \frac{1}{\langle \lambda \rangle} \left(\ln \langle N_{\mathrm{GTP}} \rangle + \gamma \right) . \tag{7.24}$$

Using the data from Figure 7.20, we can compare $\langle N_{\mathrm{pcap}} \rangle$ calculated via (7.24) and calculated with the actual simulation data in Figure 7.20. Figure 7.21 shows good agreement between the data calculated via (7.24) and directly measured in the simulation showing that the dependencies in Figure 7.20 are expected.

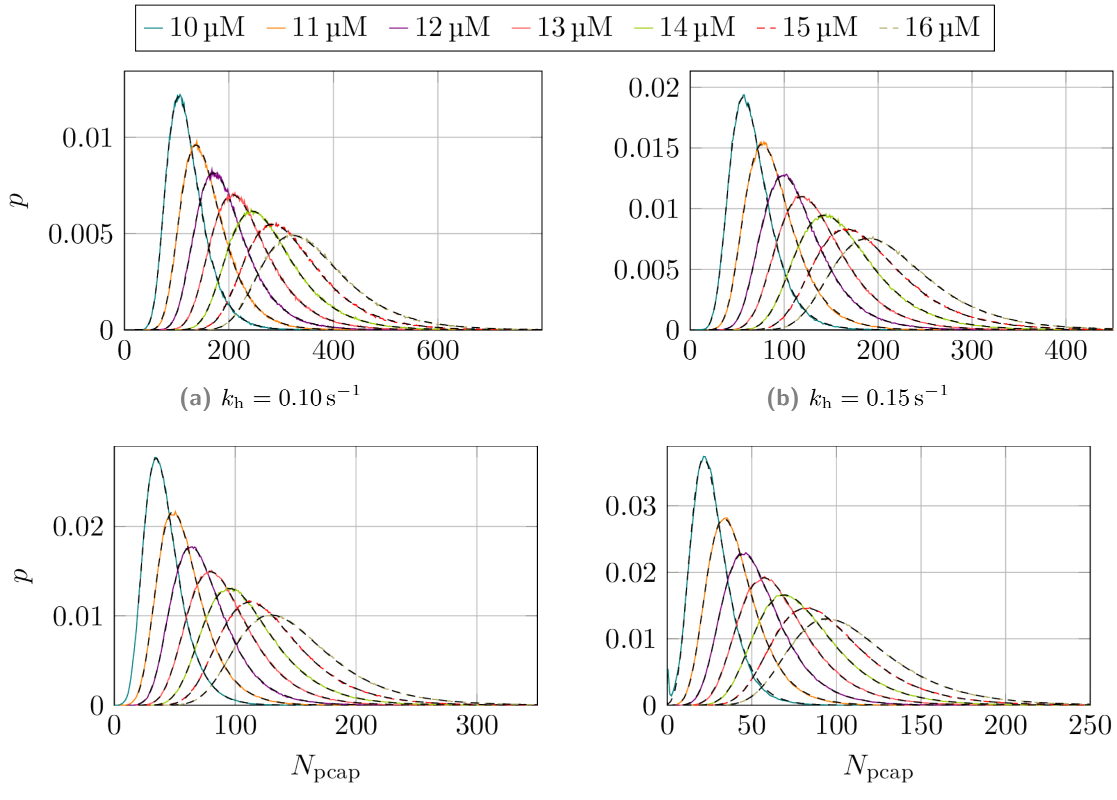

(a) $k_\text{h} = 0.10\,\text{s}^{-1}$ **(b)** $k_\text{h} = 0.15\,\text{s}^{-1}$

(c) $k_\text{h} = 0.20\,\text{s}^{-1}$ **(d)** $k_\text{h} = 0.25\,\text{s}^{-1}$

Figure 7.18: Distribution of the porous GTP-cap lengths N_pcap for different free GTP-tubulin dimer concentrations c_tub and hydrolysis rates k_h averaged over the number of GTP-tubulin dimers per protofilaments N_GTP and fitted Gumbel distributions using λ and N_GTP as fit parameters (black dashed lines).

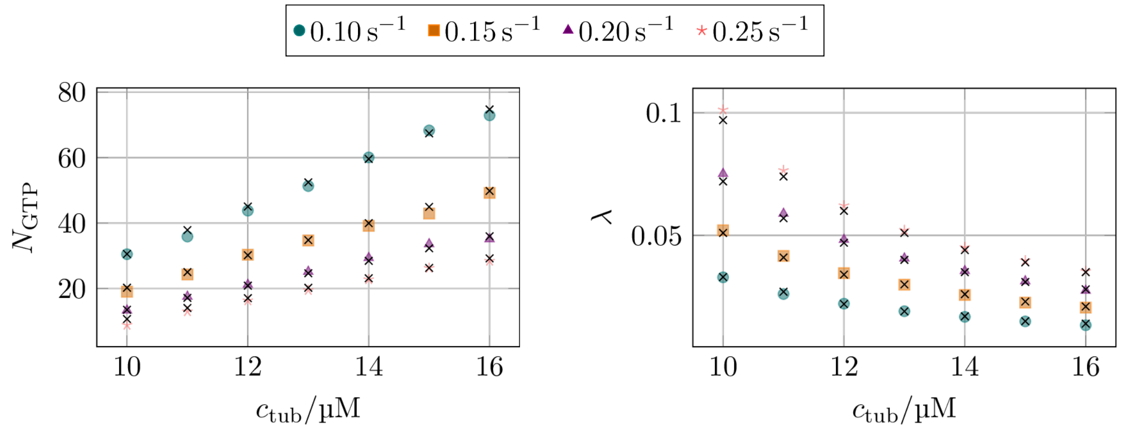

(a) Number of GTP-tubulin dimers per protofilament.

(b) Exponential decay parameter of GTP-tubulin dimer distribution.

Figure 7.19: Comparison of the values of the two parameters N_{GTP} and λ of the Gumbel distributions shown in Figure 7.18 and the average values obtained from the GTP-island data ($\langle N_{\mathrm{GTP}}\rangle \simeq \langle N_{\mathrm{isl}}\rangle\langle L_{\mathrm{isl}}\rangle$) and the exponential GTP-tubulin dimer distribution fits (black marks, see Table G.1).

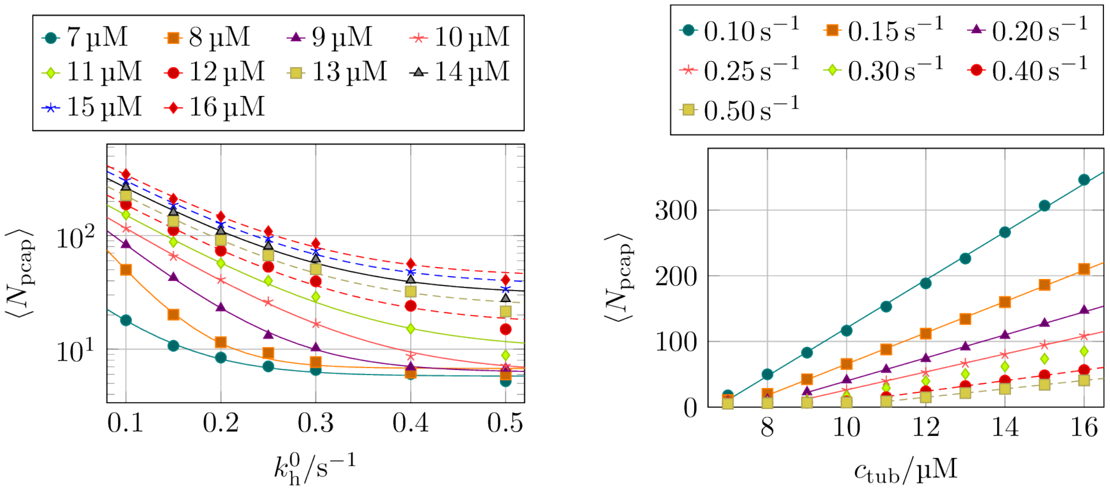

(a) Average porous GTP-cap length $\langle N_{\mathrm{pcap}}\rangle$ as a function of the hydrolysis rate k_{h}.

(b) Average porous GTP-cap length $\langle N_{\mathrm{pcap}}\rangle$ as a function of the free GTP-tubulin dimer concentrations c_{tub}.

Figure 7.20: The average porous GTP-cap length $\langle N_{\mathrm{pcap}}\rangle$ decreases with an increasing hydrolysis rate k_{h} and increases with increasing free GTP-tubulin dimer concentrations c_{tub}.

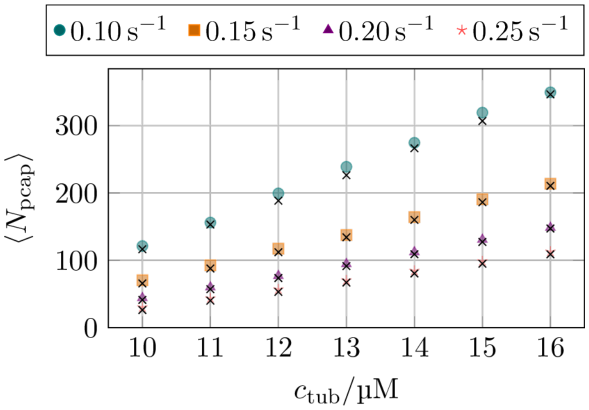

Figure 7.21: Comparison between the average porous GTP-cap length $\langle N_{\mathrm{pcap}} \rangle$ as a function of the free GTP-tubulin dimer concentration c_{tub} calculated via (7.24) using the data from Figure 7.20 and the $\langle N_{\mathrm{pcap}} \rangle$ values directly measured in the simulations (black marks, see Figure 7.20(b)).

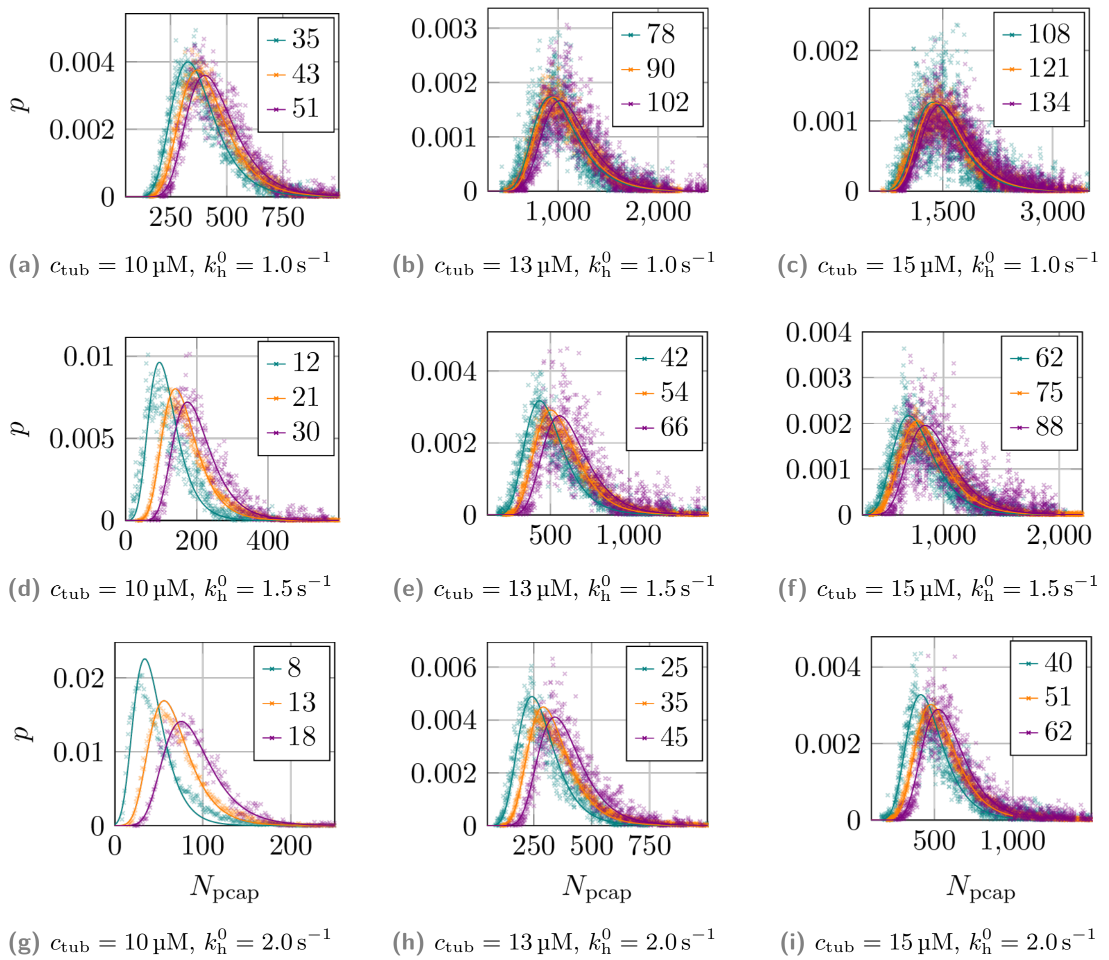

(a) $c_{\text{tub}} = 10\,\mu\text{M}$, $k_{\text{h}}^{0} = 1.0\,\text{s}^{-1}$ (b) $c_{\text{tub}} = 13\,\mu\text{M}$, $k_{\text{h}}^{0} = 1.0\,\text{s}^{-1}$ (c) $c_{\text{tub}} = 15\,\mu\text{M}$, $k_{\text{h}}^{0} = 1.0\,\text{s}^{-1}$

(d) $c_{\text{tub}} = 10\,\mu\text{M}$, $k_{\text{h}}^{0} = 1.5\,\text{s}^{-1}$ (e) $c_{\text{tub}} = 13\,\mu\text{M}$, $k_{\text{h}}^{0} = 1.5\,\text{s}^{-1}$ (f) $c_{\text{tub}} = 15\,\mu\text{M}$, $k_{\text{h}}^{0} = 1.5\,\text{s}^{-1}$

(g) $c_{\text{tub}} = 10\,\mu\text{M}$, $k_{\text{h}}^{0} = 2.0\,\text{s}^{-1}$ (h) $c_{\text{tub}} = 13\,\mu\text{M}$, $k_{\text{h}}^{0} = 2.0\,\text{s}^{-1}$ (i) $c_{\text{tub}} = 15\,\mu\text{M}$, $k_{\text{h}}^{0} = 2.0\,\text{s}^{-1}$

Figure 7.22: Distribution of the porous GTP-cap lengths N_{pcap} for different free GTP-tubulin dimer concentrations c_{tub}, base hydrolysis rates k_{h}^{0}, and numbers of GTP-tubulin dimers per protofilaments N_{GTP} and fitted Gumbel distributions (7.14) using λ as a fit parameter.

7.3.2 Mechanical Hydrolysis

With the knowledge gained from the previous section, where we only considered a constant hydrolysis rate, we now start with the distribution of the porous GTP-cap length $p(N_{\text{pcap}})$ and fit Gumbel distributions using λ as the fit parameter. The data in Figure 7.22 shows again that for mechanical hydrolysis, porous GTP-cap lengths become much longer. For the most part, in particular for higher values of c_{tub}, the Gumbel distribution fits match the data quite well, even tough the data becomes noisier the higher c_{tub} is. It is important to note, however, that for mechanical hydrolysis, deviations from the Gumbel distribution are expected as there is no longer an exponential distribution of GTP-tubulin dimers even if the number of GTP-tubulin dimers in the protofilament is not considered, as previously shown in Figure 6.8(b).

Figure 7.23 shows the GTP-tubulin dimer distribution for some of the parameter combinations from Figure 7.22. Here, we also explicitly see the non-exponential distribution if the distributions

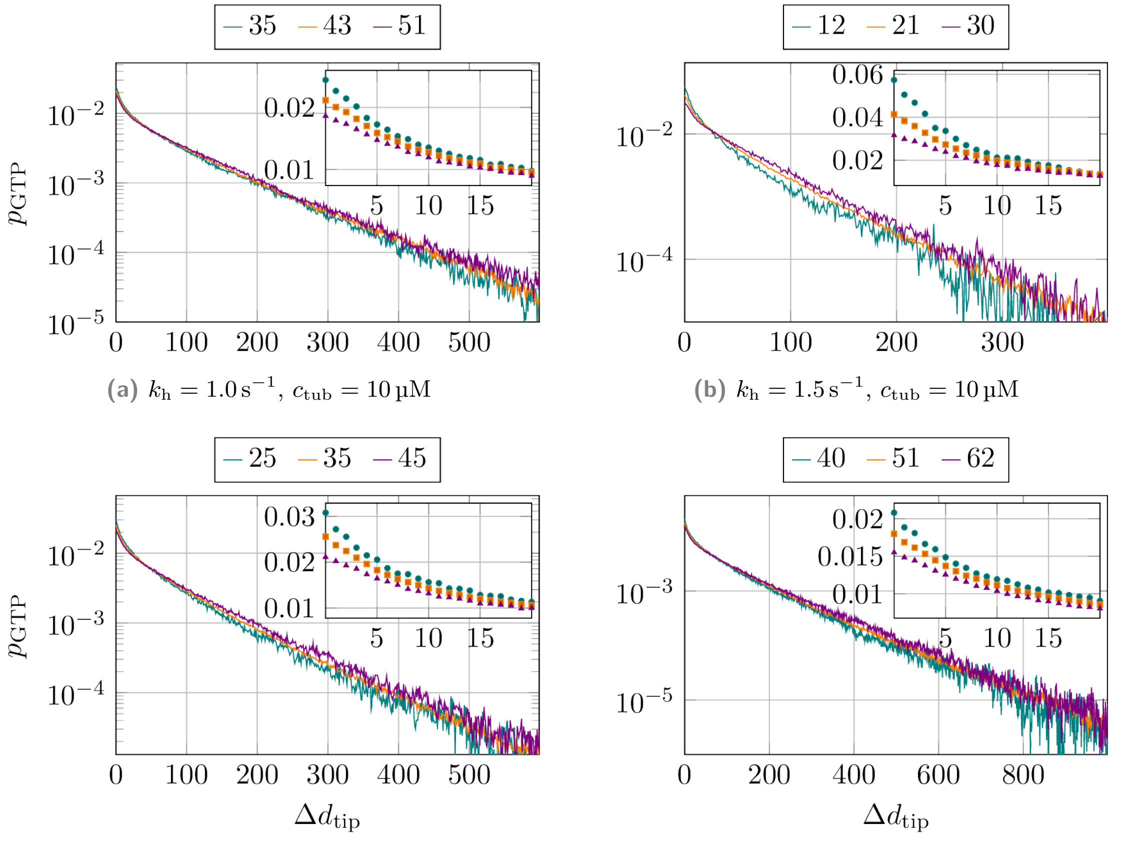

(a) $k_{\mathrm{h}} = 1.0\,\mathrm{s}^{-1}$, $c_{\mathrm{tub}} = 10\,\mu\mathrm{M}$ **(b)** $k_{\mathrm{h}} = 1.5\,\mathrm{s}^{-1}$, $c_{\mathrm{tub}} = 10\,\mu\mathrm{M}$

(c) $k_{\mathrm{h}} = 2.0\,\mathrm{s}^{-1}$, $c_{\mathrm{tub}} = 13\,\mu\mathrm{M}$ **(d)** $k_{\mathrm{h}} = 2.0\,\mathrm{s}^{-1}$, $c_{\mathrm{tub}} = 15\,\mu\mathrm{M}$

Figure 7.23: Probability p_{GTP} to find a GTP-tubulin dimer at the distance Δd_{tip} from the tip of its protofilament for different base hydrolysis rates k_{h}^{0}, free GTP-tubulin dimer concentrations c_{tub}, and different numbers of GTP-tubulin dimers in the protofilament N_{GTP}.

are split up by the number of GTP-tubulin dimers N_{GTP} in the protofilament. Just like for constant hydrolysis rates in Figure 7.15, we again find the same splitting of the data at the microtubule tip, as highlighted by the insets in Figure 7.23. For completeness, Figure 7.24 shows the porous GTP-cap length distributions not separated by N_{GTP} and we generally find good agreement with Gumbel distributions again.

Lastly, Figure 7.25 shows the average porous GTP-cap length $\langle N_{\mathrm{pcap}} \rangle$ for different free GTP-tubulin dimer concentrations c_{tub} and different base hydrolysis rates k_{h}^{0}. Figure 7.25(a) shows that for sufficiently large free GTP-tubulin dimer concentrations c_{tub}, the porous GTP-cap length follows an exponential decrease with an increasing base hydrolysis rate k_{h}^{0}. The fact that this exponential relation only exists for large c_{tub} and in some other instances only for a subset of smaller k_{h}^{0} values was explained by the results in section 6.3, as only in these cases the microtubules are able to grow. Above the same threshold, the porous GTP-cap length increases linearly with c_{tub}, as shown in Figure 7.25(b). These quantitative dependencies are similar to the ones for constant hydrolysis rates, as previously shown in Figure 7.21.

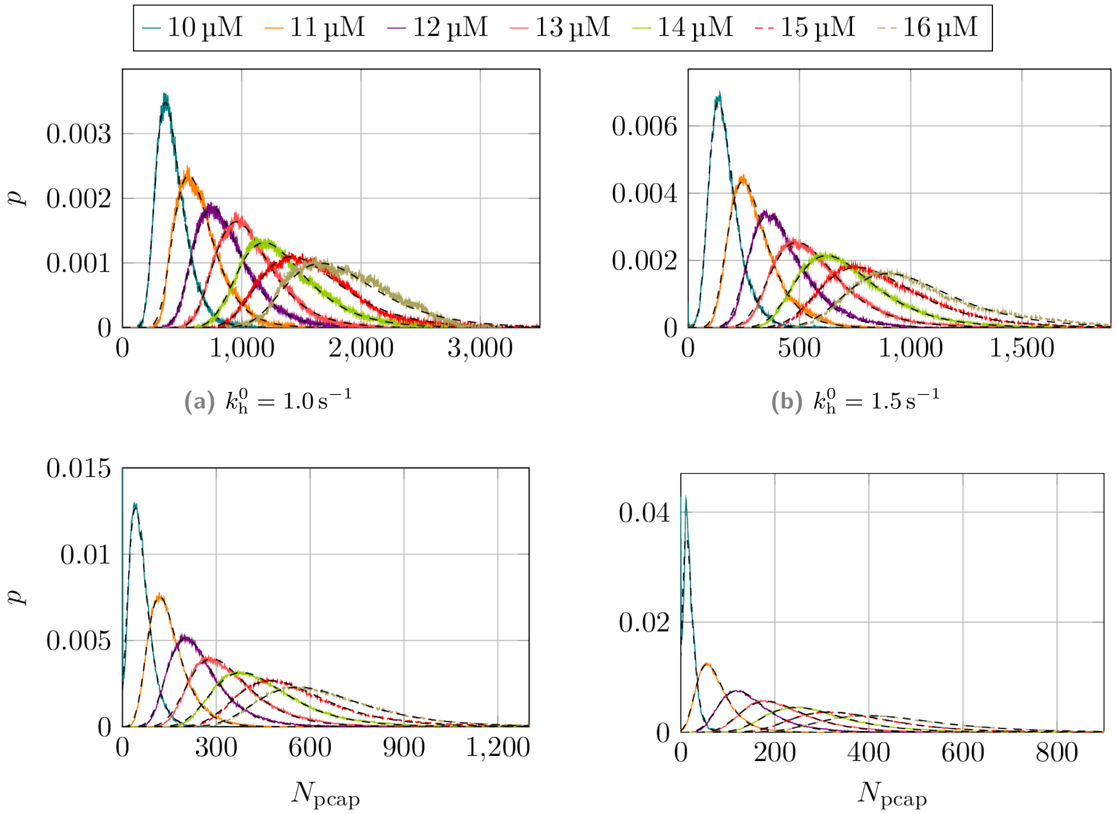

(a) $k_\text{h}^0 = 1.0\,\text{s}^{-1}$

(b) $k_\text{h}^0 = 1.5\,\text{s}^{-1}$

(c) $k_\text{h}^0 = 2.0\,\text{s}^{-1}$

(d) $k_\text{h}^0 = 2.5\,\text{s}^{-1}$

Figure 7.24: Distribution of the porous GTP-cap lengths N_pcap for different free GTP-tubulin dimer concentrations c_tub and base hydrolysis rates k_h^0 averaged over the number of GTP-tubulin dimers per protofilaments N_GTP and fitted Gumbel distributions using λ and N_GTP as fit parameters (black dashed lines).

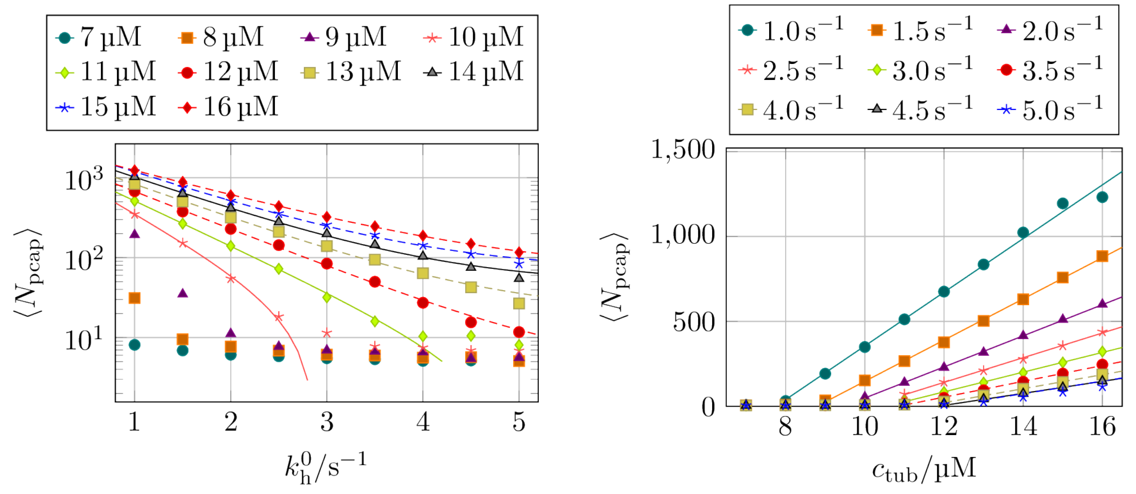

(a) Average porous GTP-cap length $\langle N_{\mathrm{pcap}} \rangle$ as a function of the hydrolysis base rate k_{h}^0.

(b) Average porous GTP-cap length $\langle N_{\mathrm{pcap}} \rangle$ as a function of the free GTP-tubulin dimer concentrations c_{tub}.

Figure 7.25: The average porous GTP-cap length $\langle N_{\mathrm{pcap}} \rangle$ decreases with an increasing base hydrolysis rate k_{h}^0 and increases with increasing free GTP-tubulin dimer concentrations c_{tub}.

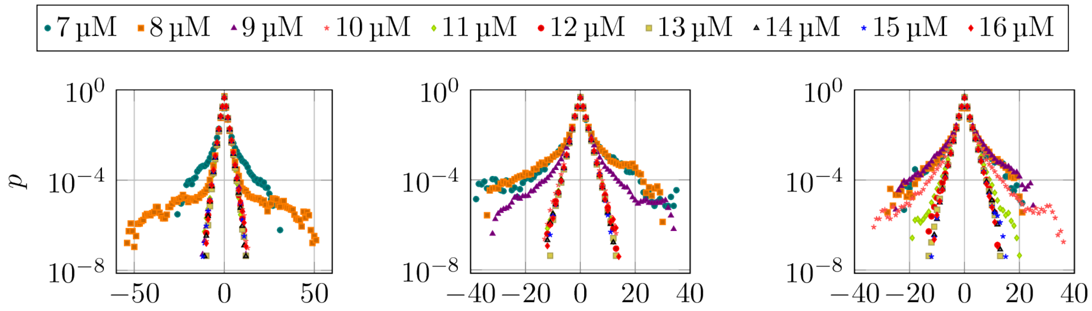

(a) $k_\mathrm{h} = 0.1\,\mathrm{s}^{-1}$ **(b)** $k_\mathrm{h} = 0.2\,\mathrm{s}^{-1}$ **(c)** $k_\mathrm{h} = 0.3\,\mathrm{s}^{-1}$

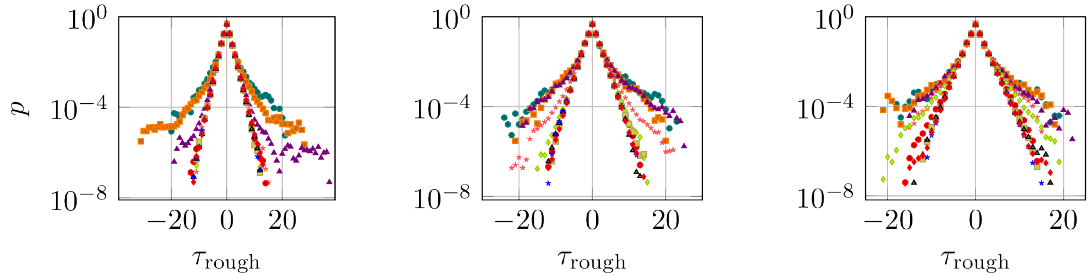

(d) $k_\mathrm{h}^0 = 1.0\,\mathrm{s}^{-1}$ **(e)** $k_\mathrm{h}^0 = 2.0\,\mathrm{s}^{-1}$ **(f)** $k_\mathrm{h}^0 = 3.0\,\mathrm{s}^{-1}$

Figure 7.26: The tip roughness distribution $p(\tau_\mathrm{rough})$ for different constant hydrolysis rates k_h (upper row) and different base hydrolysis rates k_h^0 (lower row) and different free GTP-tubulin dimer concentrations c_tub.

7.4 Tip Roughness

To analyze the structure of the microtubule tip, we consider the tip roughness τ_rough, which we define as the difference in the number of tubulin dimers in neighboring protofilaments:

$$\tau_\mathrm{rough}(p) = d_\mathrm{max}(p) - d_\mathrm{max}(p+1). \tag{7.25}$$

The first aspect to note with regard to the tip roughness (7.25) is that the average tip roughness $\langle\tau_\mathrm{rough}\rangle$ is meaningless as it is $\langle\tau_\mathrm{rough}\rangle = 0$ by definition. This property of τ_rough also manifests itself in the symmetrical distribution of τ_rough values, as shown in Figure 7.26. The distributions in Figure 7.26 can be split into two groups: narrow distributions with small minimum and maximum values of τ_rough that are less likely to be found and broader distributions. The values of c_tub resulting in broader distributions coincide with the concentrations that are below the critical concentration c_crit, i.e., shrinking microtubules, as seen in Figure 5.1 and Figure 6.13. This finding indicates a correlation between a higher tip roughness and catastrophes or shrinkage and we will come back to this point in chapter 8.

As mentioned before, $\langle\tau_\mathrm{rough}\rangle = 0$ by definition. Instead of the average value of τ_rough itself, we can consider the average value of $|\tau_\mathrm{rough}|$, as shown in Figure 7.27. Here we see that on average, the number of tubulin dimers in neighboring protofilaments is almost the same and that there are only small differences. $\langle|\tau_\mathrm{rough}|\rangle$ also shows again that the tip is rougher for

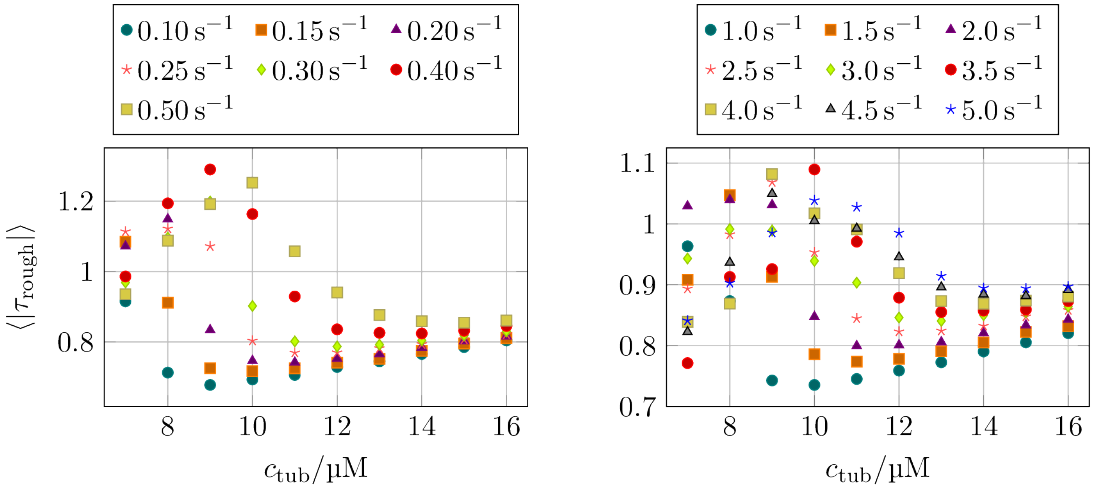

(a) Constant hydrolysis rates.

(b) Mechanical hydrolysis.

Figure 7.27: Average of the absolute tip roughness values $\langle|\tau_{\text{rough}}|\rangle$ as a function of the free GTP-tubulin dimer concentration for different hydrolysis rates k_{h}, different base hydrolysis rates k_{h}^0, and different free GTP-tubulin dimer concentrations c_{tub}.

shrinking microtubules ($c_{\text{tub}} < c_{\text{crit}}$) than for growing microtubules ($c_{\text{tub}} > c_{\text{crit}}$)[5]. For growing microtubules, we find $\langle|\tau_{\text{rough}}|\rangle$ to increase slowly with c_{tub}. This increase is expected as a higher c_{tub} value results in a higher polymerization rate while the depolymerization rate stays the same. As a consequence, the probability of finding tubulin dimers without lateral neighbors increases. Having more "tapered" ends for higher free GTP-tubulin dimer concentrations is also seen in experiments[108,120]. With regard to constant hydrolysis rates and mechanical hydrolysis, there are only minimal differences like a slightly higher $\langle|\tau_{\text{rough}}|\rangle$ value for growing microtubules when using mechanical hydrolysis, as shown in Figure 7.27.

---

[5] The maximum of $\langle|\tau_{\text{rough}}|\rangle$ being at $c_{\text{tub}} \simeq c_{\text{crit}}$ (see Figure 5.4) could be similar to the greater length fluctuations in actin filaments around their critical concentration[216–218]. While c_{crit} is defined as the concentration at which microtubules do not grow, in practice however, filaments are only not growing *on average* by alternating between periods of growth and shrinkage resulting in no length change overall. Having such frequent switches between growth and shrinkage then also explains greater length fluctuations, which in turn could result in a rougher tip structure. In chapter 8, we will see that $\langle|\tau_{\text{rough}}|\rangle$ can increase during catastrophes and rescues.

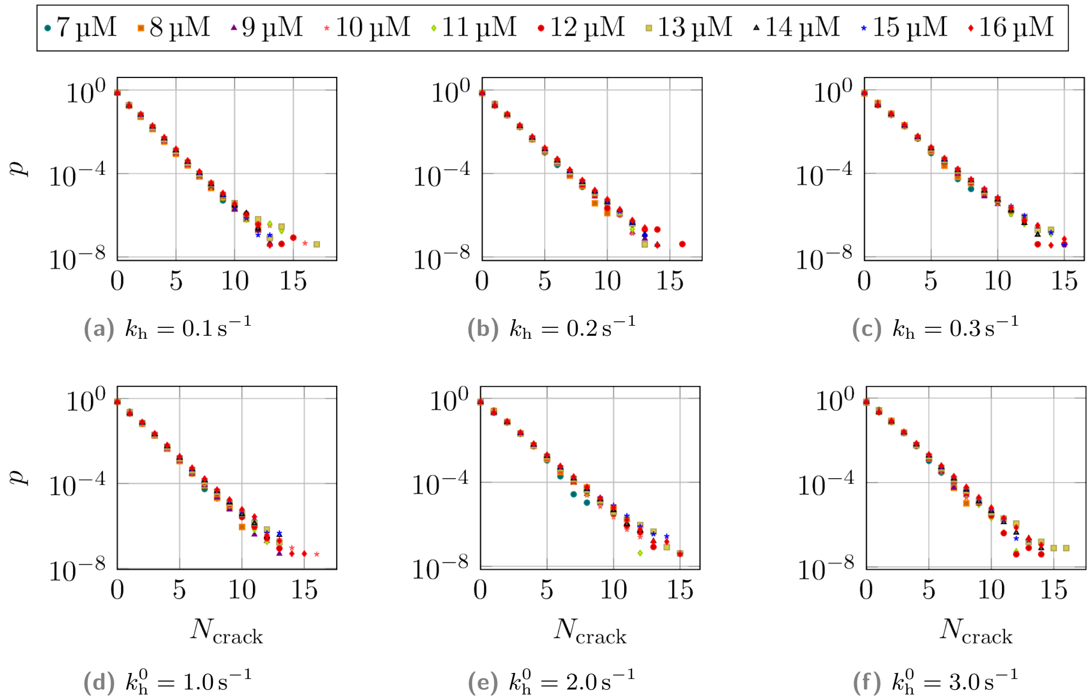

(a) $k_\text{h} = 0.1\,\text{s}^{-1}$
(b) $k_\text{h} = 0.2\,\text{s}^{-1}$
(c) $k_\text{h} = 0.3\,\text{s}^{-1}$

(d) $k_\text{h}^0 = 1.0\,\text{s}^{-1}$
(e) $k_\text{h}^0 = 2.0\,\text{s}^{-1}$
(f) $k_\text{h}^0 = 3.0\,\text{s}^{-1}$

Figure 7.28: The crack length distribution $p(N_\text{crack})$ for different constant hydrolysis rates k_h (upper row) and different base hydrolysis rates k_h^0 (lower row) and different free GTP-tubulin dimer concentrations c_tub.

7.5 Crack Length

In subsection 2.3.2, we have explained the formation and rupture of lateral bonds. As there is only one continuous stretch of lateral bonds between two protofilaments starting from the minus end, there can exist a "crack" at the plus end, where additional lateral bonds could exist. We describe this crack via its length N_crack, which we define as the number of laterally neighboring tubulin *monomers* that do not have a connecting lateral bond. If neighboring protofilaments contain different numbers of tubulin dimers, the protruding tip of the longer protofilament does not count for the crack length as the tubulin dimers in this protruding tip lack neighbors with which they could form lateral bonds. In Figure 7.28, we find the probability of a crack with length N_crack to be decreasing exponentially with the crack length and to be mostly independent of the free GTP-tubulin dimer concentration c_tub, the hydrolysis mechanism, and the hydrolysis rate k_h or k_h^0.

From the distributions in Figure 7.28 (and additional distributions not explicitly shown), we calculated the average crack lengths $\langle N_\text{crack}\rangle$ as shown in Figure 7.29. We see "large" cracks for small values of the free GTP-tubulin dimer concentration below the critical concentration, $c_\text{tub} < c_\text{crit}$, and an increase in the average crack length $\langle N_\text{crack}\rangle$ with c_tub for $c_\text{tub} > c_\text{crit}$. This increase with c_tub has the same underlying reason as the increase in tip roughness shown in Figure 7.27. The higher c_tub, the higher is the probability of two tubulin dimers polymerizing next to each other and not forming a lateral bond because the polymerization rate k_on increases

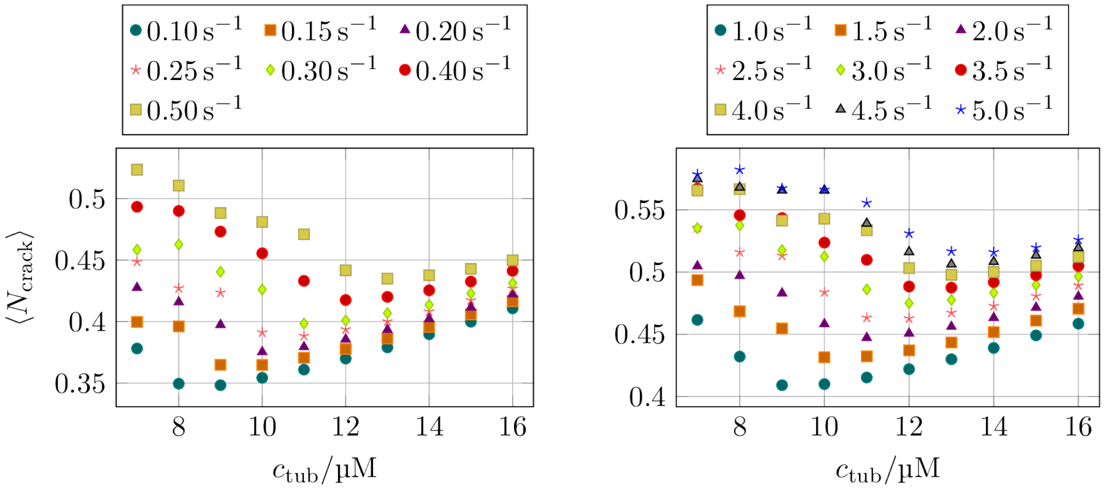

(a) Constant hydrolysis rates.

(b) Mechanical hydrolysis.

Figure 7.29: Average crack length $\langle N_{\mathrm{crack}} \rangle$ as a function of the free GTP-tubulin dimer concentration for different hydrolysis rates k_{h}, different base hydrolysis rates k_{h}^{0}, and different free GTP-tubulin dimer concentrations c_{tub}.

with c_{tub}, while the lateral bond formation rate k_{form} stays the same. Overall, however, we only find about every second terminal lateral bond not to be formed resulting in overall small cracks. Compared to other simulations[113], where average crack lengths of $\langle N_{\mathrm{crack}} \rangle \simeq 4$ are found[6], and from the existence of bent protofilaments for growing and shrinking microtubules[63], which imply that there are no lateral bonds between them, our crack lengths appear to be too small.

---

[6] Li et al.[113] used the same basic crack length definition but count tubulin *dimer* lengths, which we converted here to tubulin *monomer* lengths.

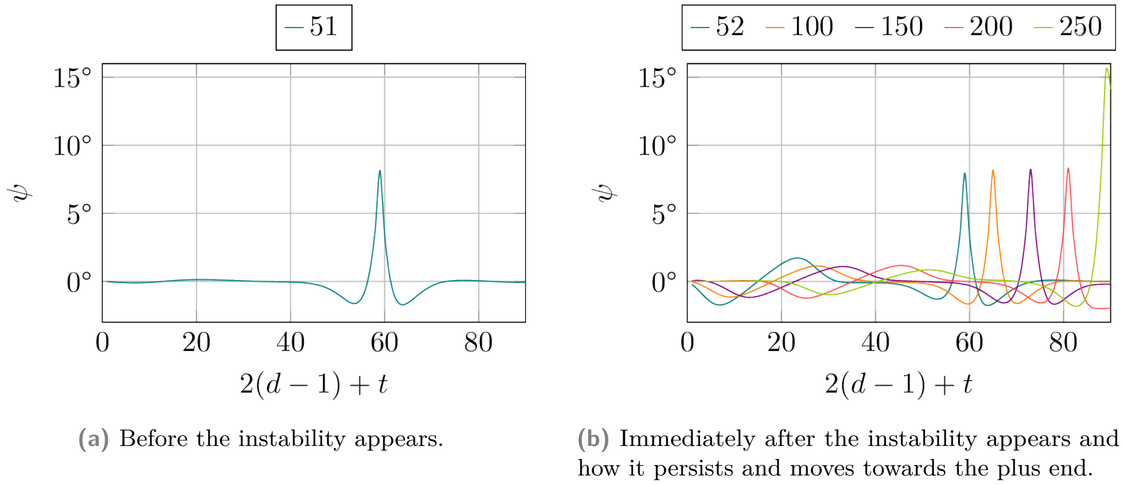

(a) Before the instability appears.

(b) Immediately after the instability appears and how it persists and moves towards the plus end.

Figure 7.30: Bending angle ψ as a function of the tubulin monomer for protofilament $p = 12$ in an artificial simulation with $N_{\text{GDP}} = 25$, $N_{\text{GTP}} = 20$, and $k_{\text{lat}} = 1\,k_{\text{B}}T/\text{nm}^2$ in which the GTP-cap is hydrolyzed systematically starting with tubulin dimer $(1, 21)$ and ending with tubulin dimer $(13, 45)$. The legend entries indicate the relevant configuration numbers (equivalent to the number of tubulin dimers that have already been hydrolyzed during the simulation). In configuration 51, tubulin dimer $(12, 28)$ was just hydrolyzed and in configuration 52, tubulin dimer $(13, 28)$ was just hydrolyzed.

7.6 Structural Instability of Microtubule Lattice

While investigating how hydrolysis affects the bending angles of neighboring tubulin dimers, we prepared microtubules with a continuous cap and then systematically hydrolyzed the cap layer by layer manually from the lowest layer to the last layer. To minimize these configurations, we used unrestricted minimization, i.e., we considered all polar angles during minimization. Figure 7.30(a) shows the bending angles of one protofilament after 51 hydrolysis events were executed. The peak shown here is a manifestation of the interface between the GDP-body and the GTP-cap that was already discussed in more detail in section 6.2.

As more and more of the original GTP-cap is hydrolyzed, the interface between the GDP-body and the GTP-cap will move to the plus end of the microtubule as the GTP-cap shrinks. This shift of the peak can be seen in Figure 7.30(b) (and the increase in the bending angle for configuration 250 is a manifestation of the reduced lattice constraints at the microtubule tip allowing tubulin monomers to bend further outward). The actual topic of this section, however, are the additional non-vanishing bending angle values in the GDP-body, i.e., for $2(d-1)+t$ values smaller than the value of the peak. This “instability” emerges suddenly, as the first configuration shown in Figure 7.30(b), is configuration 52, i.e., just one configuration after the configuration shown in Figure 7.30(a) where no instability is visible. We note that the instability in Figure 7.30(b) looks like one period of a wave that moves with the peak further to the tip as more and more tubulin dimers are hydrolyzed and whose amplitude also diminishes.

As such deviations in the bending angle are an inherently mechanical phenomenon, we used different values of the spring constant k_{lat} (and matching bending constants κ, see Appendix C)

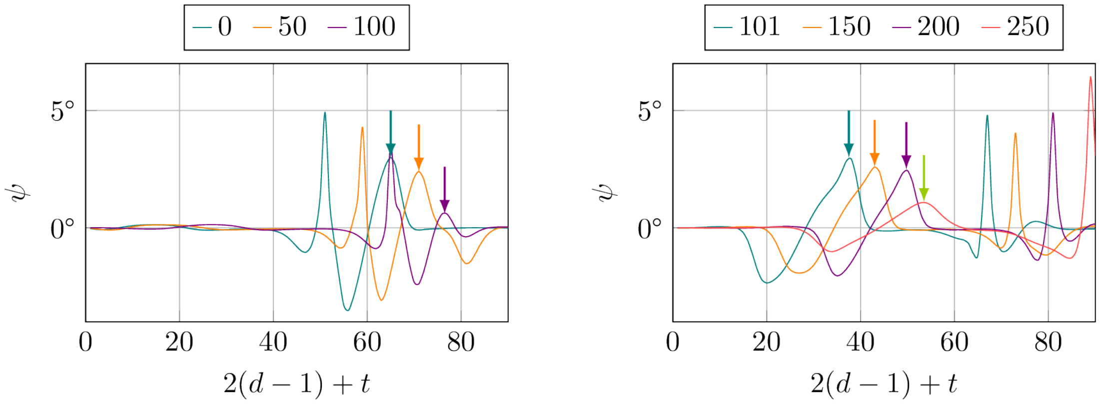

(a) Instability in front of the GDP/GTP-interface.

(b) Instability behind the GDP/GTP-interface.

Figure 7.31: Bending angle ψ as a function of the tubulin monomer for protofilament $p = 10$ in an artificial simulation with $N_{\mathrm{GDP}} = 25$, $N_{\mathrm{GTP}} = 20$, and $k_{\mathrm{lat}} = 100\,k_{\mathrm{B}}T/\mathrm{nm}^2$ in which the GTP-cap is hydrolyzed systematically starting with tubulin dimer $(1, 21)$ and ending with tubulin dimer $(13, 45)$. Between configuration 100 and configuration 101, the instability (marked by arrows) moves from in front of the GDP/GTP-interface to behind the GDP/GTP-interface.

to check whether this is a persistent phenomenon. Figure 7.31 shows the bending angles for another protofilament for $k_{\mathrm{lat}} = 100\,k_{\mathrm{B}}T/\mathrm{nm}^2$ instead of $k_{\mathrm{lat}} = 1\,k_{\mathrm{B}}T/\mathrm{nm}^2$. Here, we see that the instability already exists in the original configuration but now within the GTP-cap (see arrows in Figure 7.31(a)) and that the instability behaves as before. As the expected peak moves closer to the microtubule tip, the instability also moves closer to the tip and its amplitude decreases. At one point, however, in Figure 7.31 between configurations 100 and 101, the instability is “reflected” back from the GTP-cap to the GDP-body (see arrows in Figure 7.31(b)) where it now also continues moving towards the tip with a decreasing amplitude.

We mentioned in the beginning of this section that we used unrestricted minimization for the simulations in Figure 7.30 and Figure 7.31. In practice, however, when we encounter configurations with a GDP-body and a GTP-cap, i.e., proper dynamics simulations as discussed first in chapter 5, we will use restricted minimization as explained in section 3.3. In Figure 7.32(a), we see that the issue in the GTP-cap still exists for a relatively long cap of $N_{\mathrm{GTP}} = 20$ but we see no reflection back into the GDP-body as in Figure 7.31(b) because the majority of the GDP-body is static as it is not considered for minimization anymore due to the cutoff. If we, however, use a shorter cap resulting in a similar initial configuration used for our actual full simulations in chapter 5, we see no equivalent instabilities in Figure 7.32(b) as marked by arrows in Figure 7.32(a). We only see, compared to Figure 7.30(a), an asymmetry in the negative dips before and after the expected peaks at the GDP/GTP interface.

Previously, vibration modes of whole microtubules using near-atomic MD simulations have already been found[144] when researching the bending of microtubules. Kahraman et al.[219] modeled the microtubule lattice as a mesh with different bending potentials and using Langevin dynamics, they found individual tubulin dimers in a curved state, which they called either “partial confoplex” or “full confoplex” depending on whether only some or all tubulin dimers in a certain layer were curved. When considering whole microtubules, “confostacks” emerged

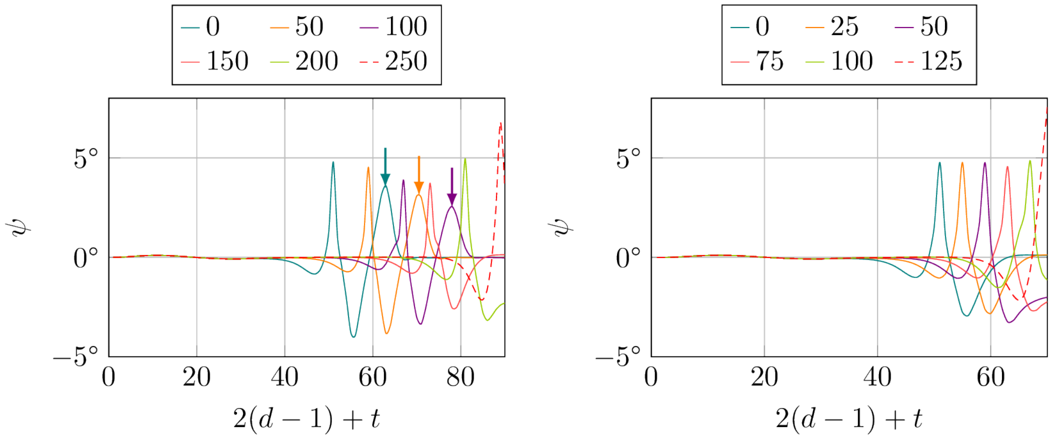

(a) $N_{\mathrm{GTP}} = 20$ **(b)** $N_{\mathrm{GTP}} = 10$

Figure 7.32: Bending angle ψ as a function of the tubulin monomer for protofilament $p = 7$ in an artificial simulation with $N_{\mathrm{GDP}} = 25$, $k_{\mathrm{lat}} = 100\,k_{\mathrm{B}}T/\mathrm{nm}^2$, and restricted minimization with $\Delta d_{\mathrm{cutoff}} = 10$.

where multiple confoplexes cooperated and resulted in a larger scale deflection similar to the previously mentioned vibration modes[144].

While the exact origin of the instability we observed here in our model is yet unknown, the results by Kahraman et al.[219] might give an indication that it could be due to the mechanical modeling. It is, however, important to note that in actual simulations, this phenomenon will not be very relevant. Firstly, there is no such systematic hydrolysis of tubulin dimers as in the manually controlled simulations here because we use random hydrolysis. Secondly, we start with configurations similar to the one used in Figure 7.32(b) without the instability and as the simulation progress, such artificially induced configurations will not occur. Nevertheless, in future research, the origin of this instability could be investigated further.

Analysis of Individual Microtubule Trajectories

8

An advantage of simulations over actual experiments is that existing simulations can be rerun to identify the point in the simulation where a catastrophe or a rescue is almost guaranteed to occur. To determine the probability of a certain event to occur, we will use configurations around the relevant events in the simulations as starting points for new simulations, similar to Margolin et al.[112] For each each starting point, 20 new simulations with a maximum simulation time of $t_{\text{max}} = 1\,\text{min}$ are run. Due to the stochastic nature of the microtubule simulation, each of the 20 “reruns” will result a in different growth trajectory.

We do this analysis for two simulations with a constant hydrolysis rate in section 8.1 and two simulations with mechanical hydrolysis in section 8.2. In addition to the analysis of the trajectories for simulations with a constant rate, we will also introduce the principles employed to analyze the trajectories in section 8.1 that will be reused in section 8.2 for mechanical hydrolysis.

8.1 Constant Hydrolysis Rate

In Figure 5.1, we have seen that our simulations are able to generate microtubule trajectories with catastrophes and rescues. Figure 8.1 shows two of these simulations in greater detail, where two catastrophes (C) and one rescue (R) occur. Additionally, in both simulations, there are dips (D) in which the growing phase is interrupted by a very short shrinkage phase (similar to the “stutters” found by Mahserejian et al.[206] and “transient pauses” found by Kim et al.[110]).

Figure 8.2 shows the trajectories of some of the rerun simulations around the catastrophe in Figure 8.1(a) together with the length trajectory of the original microtubule. To classify whether a rerun of a simulation follows the same path as the original simulation, different criteria could be used with varying levels of difficulty to implement them. For the relevant analysis here, we are only interested in whether the relevant event, for example a catastrophe, still occurred or whether the simulation followed a different path. For the events in the insets of Figure 8.1, we used the following criteria to determine whether the relevant event still happened:

- **Dips in Figure 8.1(a) and Figure 8.1(b)**

  For the dips, the relevant question is whether the dip persists, i.e., whether no actual catastrophe occurred. As a consequence, we demand that the microtubule is growing and should not be significantly shorter at the end of the rerun simulation than the microtubule in the original simulation at the same point in time. We chose 400 nm as the maximum length difference by which the microtubule in the reran simulation was allowed to be shorter than the microtubule in the original simulation. There is no cutoff criterion in case the microtubule in the reran simulation is longer because in such a case, there is also no catastrophe fulfilling our general criterion.

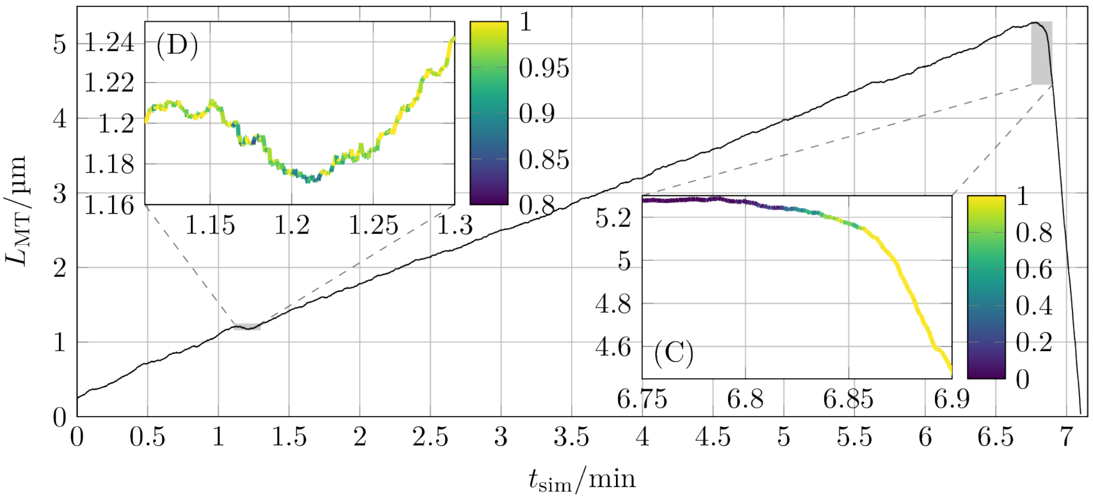

(a) $c_{\mathrm{tub}} = 8\,\mathrm{\mu M}$ and $k_{\mathrm{h}} = 0.1\,\mathrm{s}^{-1}$

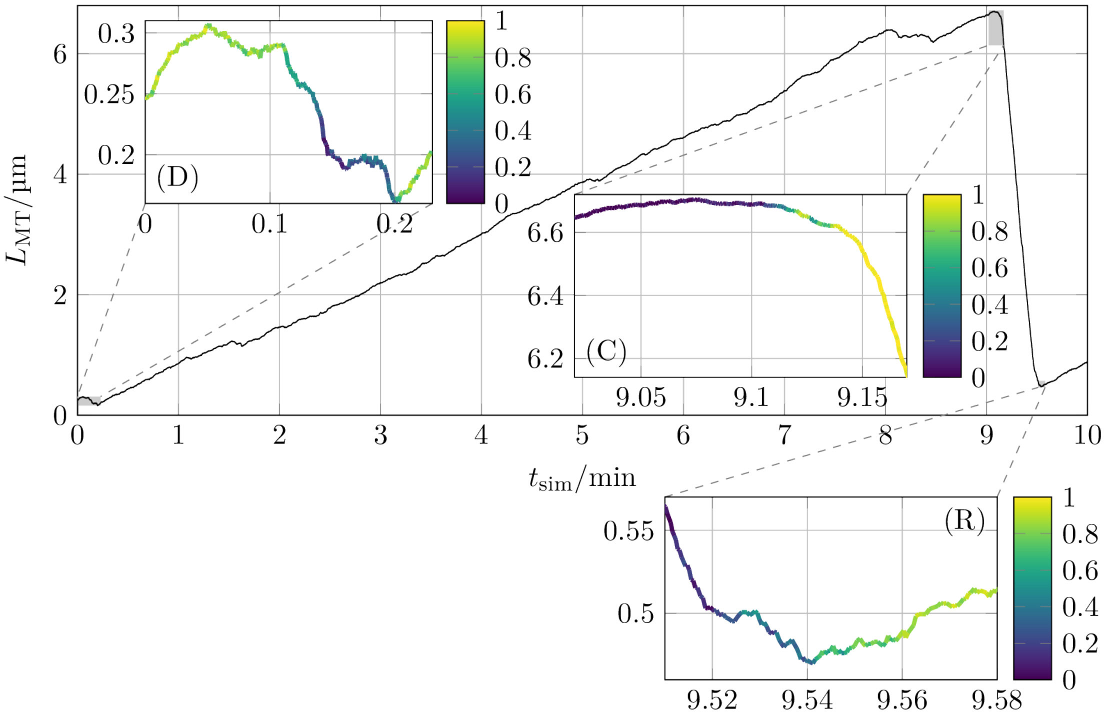

(b) $c_{\mathrm{tub}} = 9\,\mathrm{\mu M}$ and $k_{\mathrm{h}} = 0.2\,\mathrm{s}^{-1}$

Figure 8.1: Length L_{MT} of two exemplary microtubules as a function of the simulation time t_{sim}. The insets show three types of events of interest: dip (D), catastrophe (C), and rescue (R). The color coding of the curves in these insets is the probability that at the given point of the simulation, reruns of the simulation starting at this point are going to follow a similar path. (More details on this probability can be found in the main text.)

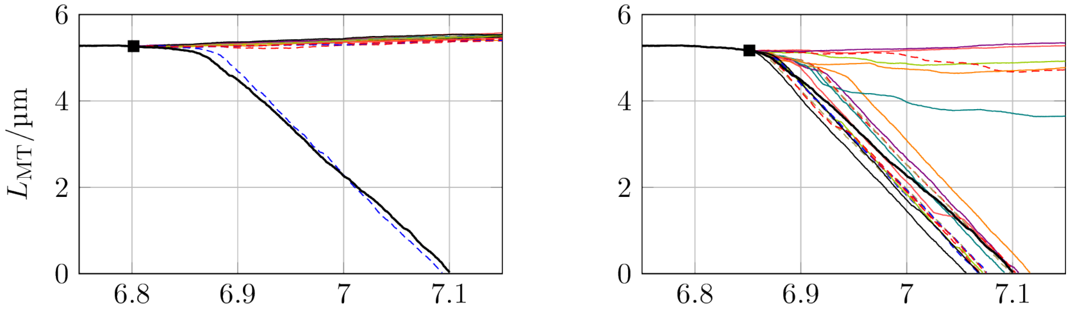

(a) Configuration 990 000.

(b) Configuration 1 000 000.

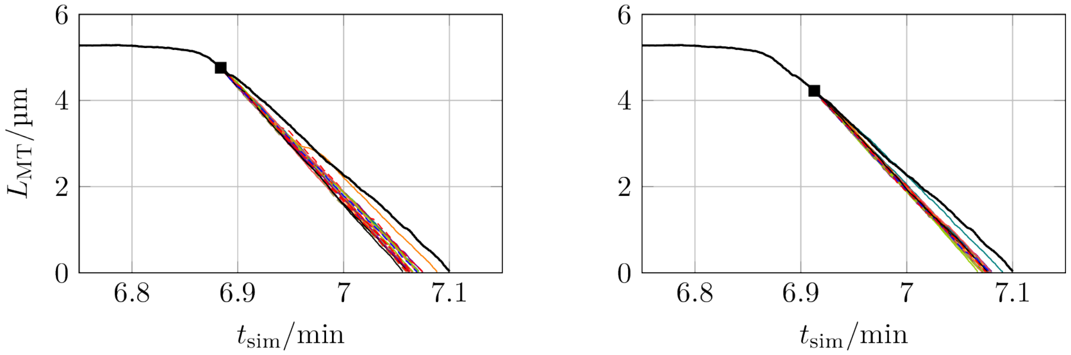

(c) Configuration 1 010 000.

(d) Configuration 1 020 000.

Figure 8.2: Trajectories of the reran simulations of the original simulation shown in Figure 8.1(a) using four different configurations around the catastrophe of the original simulation as starting points. The configuration number refers to the number of events that have been executed in the original simulation before the relevant configuration. The starting points of the rerun simulations are marked by black squares on the original trajectory.

- **Catastrophe in Figure 8.1(a)**

  For the catastrophe, the end time of the rerun simulation was only allowed to be 10 s later than the original simulation, and the final microtubule length must be less than 200 nm. These criteria ensure that the catastrophe actually happened around the same time as in the original simulation.

- **Catastrophe in Figure 8.1(b)**

  We cannot use the previous criterion for this catastrophe because there is a rescue in the original simulation afterwards. Instead, we demand that 15 s after the start of the rerun simulations (or 10 s if the reruns started after the catastrophe in the original simulation), the new microtubules are no more than 400 nm longer than the original microtubules.

- **Rescue in Figure 8.1(b)**

  For the rescue, the relevant question is whether the microtubule switched from shrinking to growing. The easiest way to check this case is to check whether the reruns terminated due to the microtubule depolymerizing or due to the time constraint. From Figure 8.1(b), it is obvious that if the microtubule simply continues depolymerizing completely, it would require much less than the maximum simulation time of the reruns of 1 min making the simulation time a viable quantity.

It must be noted that these criteria are not the most general criteria possible and do not cover every possible scenario (for example, a rescue could have happened after the catastrophe in Figure 8.1(b)), but these criteria proved sufficient for the results of the relevant reruns.

From the number of reruns that match the criteria above, we can calculate the fraction or probability that the relevant event is going to happen. This probability is used as color coding in the insets of Figure 8.1. For each event of interest, the configurations used as initial configuration for the reruns were chosen so that a sufficient number of configurations before and after the event are considered so that a total of 16 040 rerun simulations were performed for Figure 8.1(a) and 20 060 rerun simulations for Figure 8.1(b). In the insets in Figure 8.1 for the catastrophes and the rescue, we see that the probability to switch from growth to shrinkage and vice versa changes within seconds. Figure 8.3 and Figure 8.4 show some two-dimensional representations of the simulated microtubules during the catastrophes and rescues with enlarged versions of the relevant insets from Figure 8.2. Appendix H contains the matching three-dimensional representations for all of the two-dimensional configuration snapshots shown in this chapter.

To properly analyze catastrophes and rescues to deduce a microscopic mechanism for both, we would have to repeat this probability analysis for many more catastrophes and rescues to isolate the configurations for which catastrophes and rescues become unavoidable. Such an analysis, however, was out of scope for now, but we can still highlight similarities between the two catastrophes and the relevant configurations shown in Figure 8.3. We can see for both catastrophes that it is not simply sufficient for the microtubule to stop growing for a guaranteed catastrophe to happen, but it must also shrink by 50 nm to 100 nm initially before the catastrophe becomes unavoidable. This short period of shrinkage happens at a slower velocity that then becomes gradually faster until it reaches its final value with which the microtubule then shrinks. Such a "continuous transition" from growth to shrinkage was also found to be very common in vitro and was termed a "transitional catastrophe"[206] (as opposed to "abrupt catastrophes" with sharp transitions between growth and shrinkage). One common feature of the two exemplary catastrophes shown in Figure 8.1 is highlighted by the configuration snapshots numbered "7" shown in Figure 8.3 in the form of a "nucleus" of three to four neighboring protofilaments having lost their GTP-cap and starting to shrink.

Comparing the two dips in Figure 8.1(a) and Figure 8.1(b) reveals that the dip in Figure 8.1(b) would better be classified as a catastrophe with a subsequent rescue as the microtubule reaches a configuration from which it is very unlikely to be rescued. Compared to the dip in Figure 8.1(a), where a catastrophe remained unlikely throughout, the microtubule in Figure 8.1(a) did shrink the previously mentioned 50 nm to 100 nm until the catastrophe is almost ensured compared to the short shrinkage of less than 50 nm in Figure 8.1(a).

Lastly, the rescue and the sample configurations shown in Figure 8.4 hint that the general assumption of the reformation of a protective GTP-cap for a rescue to occur is correct. But it also shows that it is appears to be necessary that a "shrinkage front", i.e., neighboring protofilaments that have shrunken more than the other protofilaments (what we called a nucleus in the case of a catastrophe), must be "healed" by new stabilizing GTP-tubulin dimers

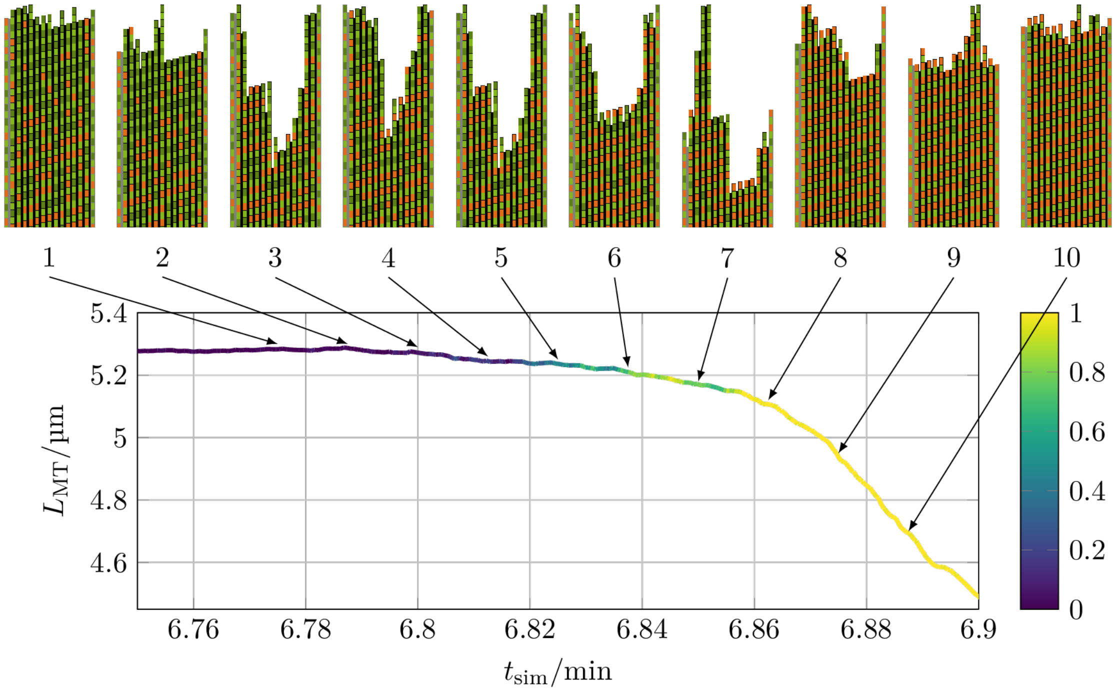

(a) Catastrophe from Figure 8.1(a).

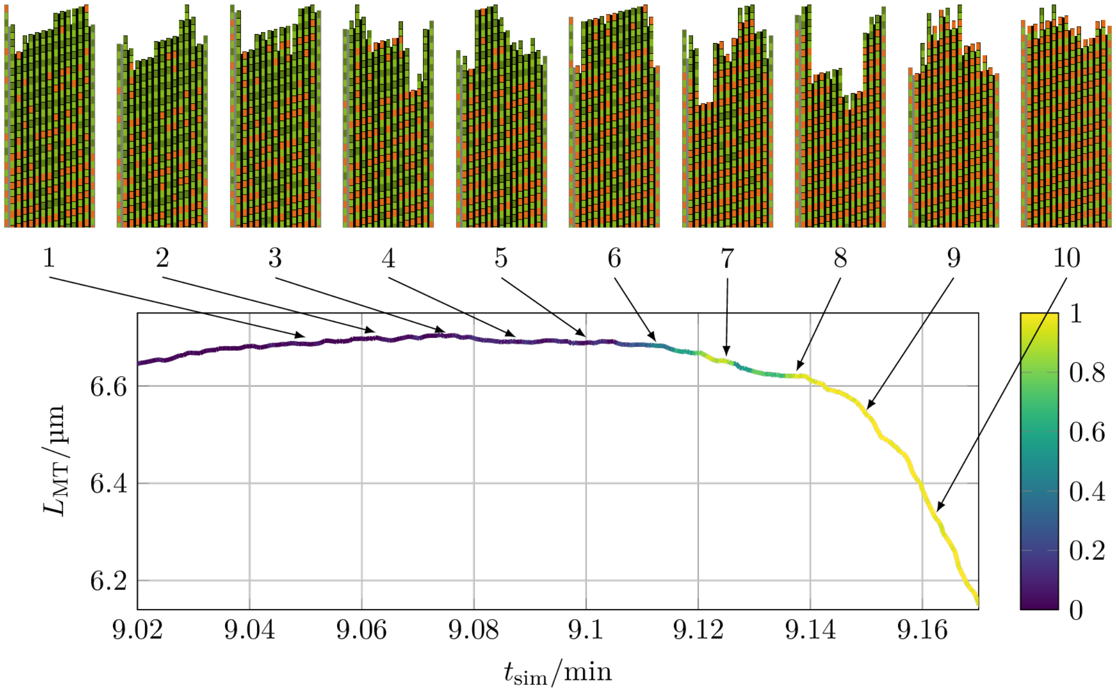

(b) Catastrophe from Figure 8.1(b).

Figure 8.3: Two-dimensional configuration snapshots around the catastrophes shown in Figure 8.1. Three-dimensional configuration snapshots can be found in Figure H.1.

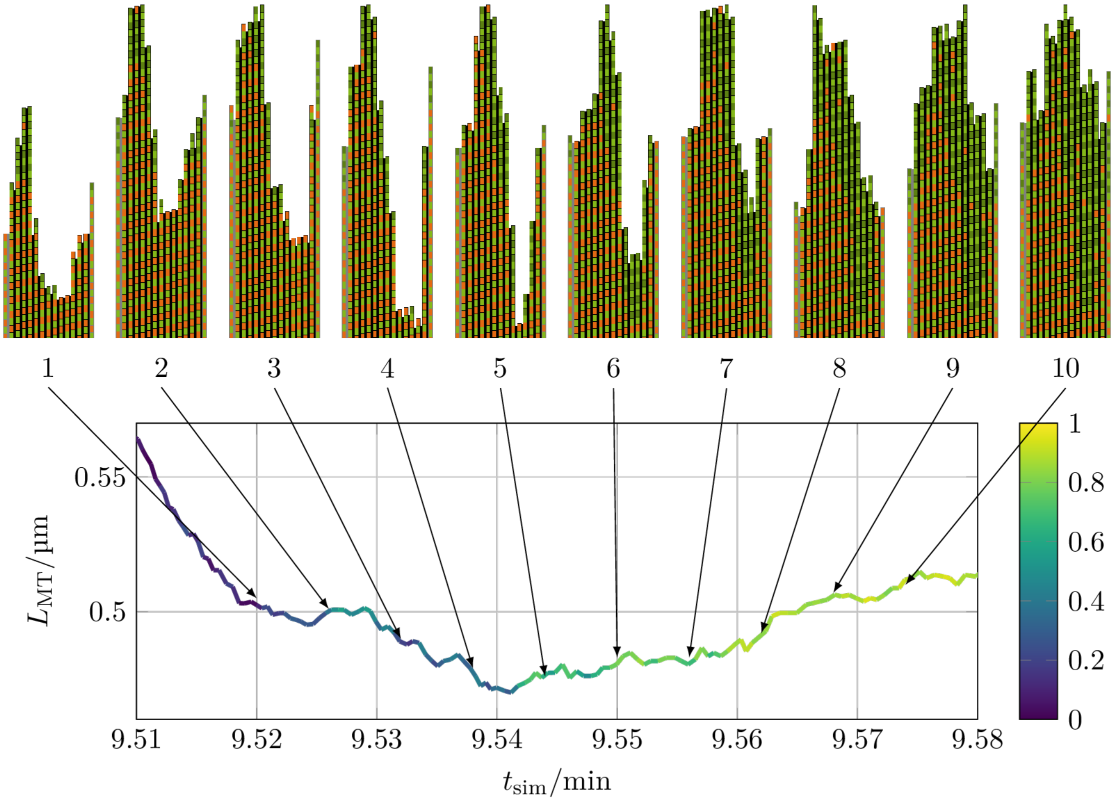

Figure 8.4: Two-dimensional configuration snapshots around the rescue shown in Figure 8.1(b). Three-dimensional configuration snapshots can be found in Figure H.2.

polymerizing onto the relevant protofilaments. The last point can be seen in the differences between configurations “5” and “7” in Figure 8.4.

To formalize these observations from the configuration snapshots, we considered different observables in Figure 8.5 around the catastrophes and rescue from Figure 8.1. The first observation is the confirmation, that catastrophes become unavoidable once the GTP-cap has almost completely vanished. The porous GTP-cap, on the other hand, still keeps on vanishing once the catastrophe has occurred showing that individual GTP-tubulin dimers at random positions in the GDP-body are insufficient to stop shrinkage. While we observe a slight increase in the crack length N_{crack} after the catastrophe, overall, however, cracks remain relatively short. The lack of deeper cracks prohibits protofilament tips from bending outward, see the three-dimensional configuration snapshots in Appendix H, in contrast to experimental results as previously shown in Figure 1.5. The absolute tip roughness $|\tau_{\mathrm{rough}}|$ does peak for the catastrophe in Figure 8.5(a), but for the catastrophe in Figure 8.5(b), there is no distinct peak.

To check for a nucleus, i.e., for neighboring protofilaments that have shrunken more than the rest of the protofilaments, we define ρ_{min} and ρ_{max} as the protofilament indices for which the

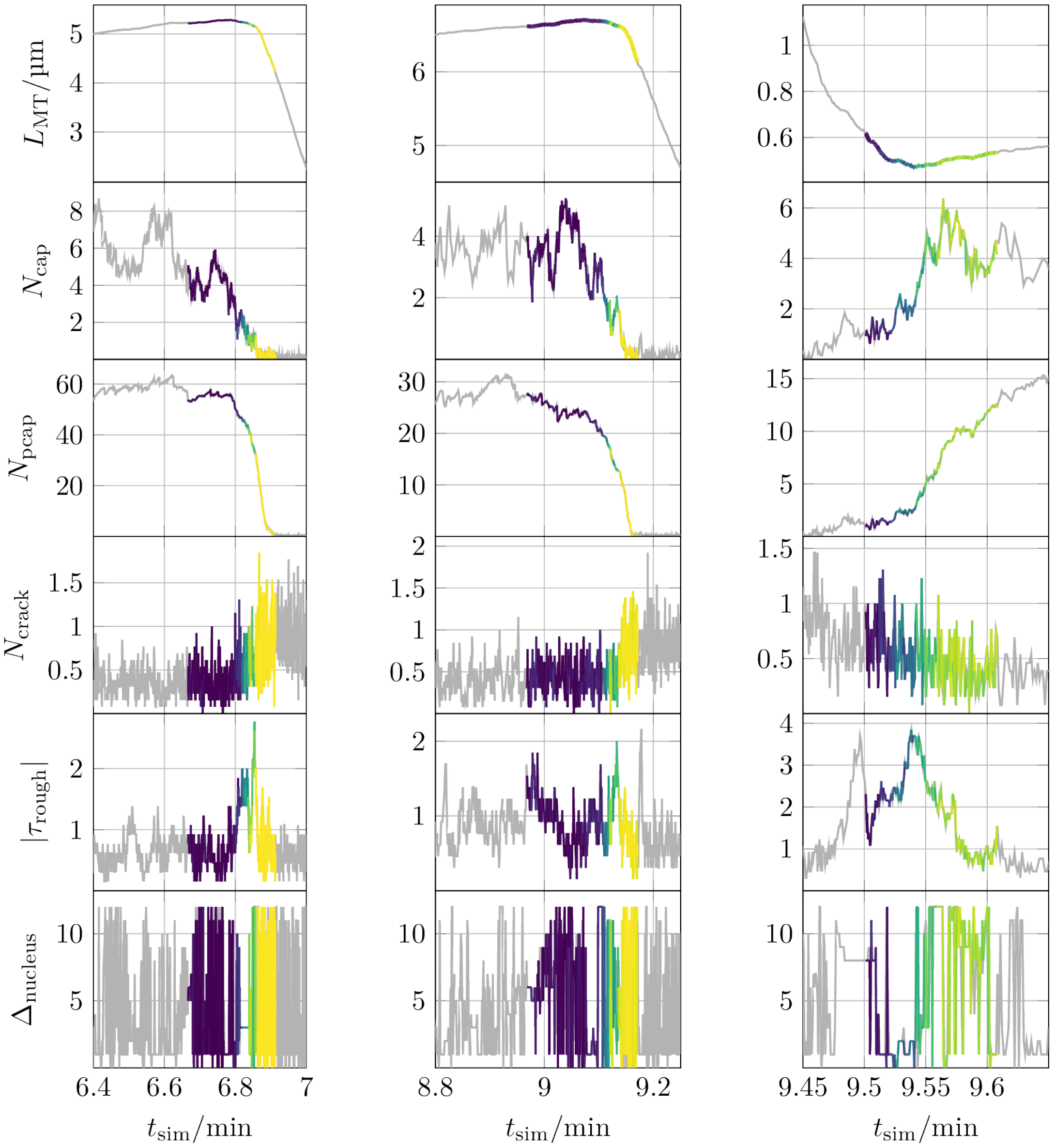

(a) Catastrophe from Figure 8.1(a).

(b) Catastrophe from Figure 8.1(b).

(c) Rescue from Figure 8.1(b).

Figure 8.5: The microtubule length L_{MT}, the average GTP-cap length per protofilament N_{cap}, the average porous GTP-cap length per protofilament N_{pcap}, the average crack length per protofilament N_{crack}, the average absolute tip roughness per protofilament $|\tau_{\mathrm{rough}}|$, and the width of the shrinking nucleus $\Delta_{\mathrm{nucleus}}$ for the catastrophes and the rescue from Figure 8.1 as a function of the simulation time t_{sim}. The same color coding as in the relevant insets of Figure 8.1 is used and additional data before and after the data shown in these insets is color-coded in gray.

tip roughness is the smallest and for which it is the largest:

$$\tau_{\text{rough}}(\rho_{\min}) = \min_{p} \tau_{\text{rough}}(p), \tag{8.1}$$

$$\tau_{\text{rough}}(\rho_{\max}) = \max_{p} \tau_{\text{rough}}(p). \tag{8.2}$$

From these indices, we can define the width of the (potential) nucleus as

$$\Delta_{\text{nucleus}} = (\rho_{\max} - \rho_{\min}) \bmod 13, \tag{8.3}$$

where the modulo operator accounts for the periodicity of the microtubule changing negative values of $\rho_{\max} - \rho_{\min}$ to the correct width. If a nucleus exists and persists for some time, we expect $\rho_{\min} = \text{const}$ and $\rho_{\max} = \text{const}$ resulting in $\Delta_{\text{nucleus}} = \text{const}$.

Before we can discuss the results for this observable, we have to come back to (8.1) and (8.2). While these formulas are conceptually correct, in practice, we will find multiple values of $\rho_{\min}$ and $\rho_{\max}$ that fulfill (8.1) and (8.2), respectively. The easiest configuration to illustrate this problem with is a configuration where all protofilaments contain the same number of tubulin dimers so that $\tau_{\text{rough}}(p) = 0$ for all protofilaments p. In all cases where $\rho_{\min}$ or $\rho_{\max}$ is not distinct, we calculate the nucleus widths (8.3) for all combinations of $\rho_{\min}$ or $\rho_{\max}$ and choose the pair of $\rho_{\min}$ and $\rho_{\max}$ values resulting in the nucleus with the smallest width because we expect the nucleus to be small[1]. If there are multiple pairs of $\rho_{\min}$ and $\rho_{\max}$ values with the smallest nucleus width (8.3), the first pair is selected, i.e., the pair with the smaller values of the protofilament indices $\rho_{\min}$ and $\rho_{\max}$ as they are iterated over from smallest to largest. In practice, however, this last special case of multiple pairs of $\rho_{\min}$ and $\rho_{\max}$ values resulting in the same smallest nucleus width Δ_{nucleus} was not relevant for our cases here.

While Figure 8.5(a) shows a persistent nucleus with $\Delta_{\text{nucleus}} = 3$ shortly before the catastrophe becomes unavoidable, overall, the Δ_{nucleus} data does not provide much further insight and might have to be replaced by a better observable in the future.

For the rescue observables shown in Figure 8.5(c), we see the increase in the GTP-cap length and it needs to pass $N_{\text{cap}} \simeq 2$ until a rescue becomes more likely. The tip roughness $|\tau_{\text{rough}}|$ also peaks for this rescue shortly before the rescue happens. The falling flank of this peak in the $|\tau_{\text{rough}}|$ data during which the rescue happens is a manifestation of the previously mentioned "healing of the shrinkage front".

---

[1] If the nucleus was not small, it would not make sense to discuss neighboring protofilaments being shorter than the other protofilaments but instead to discuss neighboring protofilaments that are longer than the rest.

8.2 Mechanical Hydrolysis

Like in Figure 8.1 for constant hydrolysis rates, Figure 8.6 shows two exemplary microtubule length trajectories with insets showing the probability for a certain event to happen (see section 8.1 for the basic explanation of how this probability is calculated). For the dip and catastrophe in Figure 8.6(a), we used the same criteria as for Figure 8.1(a). For catastrophes (C1) and (C3), we used the same criterion as for the catastrophe in Figure 8.1(b) (but always using 15 s), and for catastrophe (C4), we also used the same criterion but with a 10 s checkpoint for the length difference. For catastrophe (C2), we cannot use the same criterion as there is an immediate rescue, (R2), afterwards. Instead we use the point in time where rescue (R2) occurred in the original simulation as the reference point and demanded the microtubules in rerun simulations to be no more than 100 nm longer than the original microtubule at (R2). For the rescues in Figure 8.6(b), we simply checked whether the microtubule still existed after 15 s or whether it had depolymerized completely. As mentioned before in section 8.1, these criteria are not meant as general criteria to be used for any simulation, but they are simply criteria that work for the simulations that are relevant here.

Figure 8.7 shows some configurations before, during and after two catastrophes from Figure 8.6. While the second example in Figure 8.7(b) is inconclusive, the first example in Figure 8.7(a) again shows the formation of a “nucleus” of neighboring protofilaments having already shrunken further than the other protofilaments. This nucleus starts forming in configuration “6” and is present until configuration “9” and spans three protofilaments.

For a constant hydrolysis rate, we found in Figure 8.4 that any neighboring protofilaments that have shrunken more than the other protofilaments (which we called a “shrinkage front”) appear to require a GTP-cap for a rescue to occur. The two rescues shown in Figure 8.8 strengthen this point, see configurations “2” and “3” and configurations “8” and “9” in Figure 8.8(a) and configurations “7” and “9” in Figure 8.8(b).

Figure 8.9 shows the same observables for two catastrophes and one rescue from Figure 8.6 like we did for a constant hydrolysis rate in Figure 8.5. Overall, the results are qualitatively the same as for constant hydrolysis rates: Catastrophes become unavoidable once the GTP-cap has almost completely vanished and rescues happen once a GTP-cap has been rebuilt. The cracks between protofilaments become slightly longer during catastrophes and remain relatively short on average. Lastly, except for Figure 8.9(b), we again see peaks in the tip roughness $|\tau_{\text{rough}}|$ as expected by the visible nucleus for the catastrophe in Figure 8.7(a).

Overall, for the limited data analyzed here, there appears not to be a distinct difference between catastrophes and rescues in our models with constant hydrolysis rates and mechanical hydrolysis.

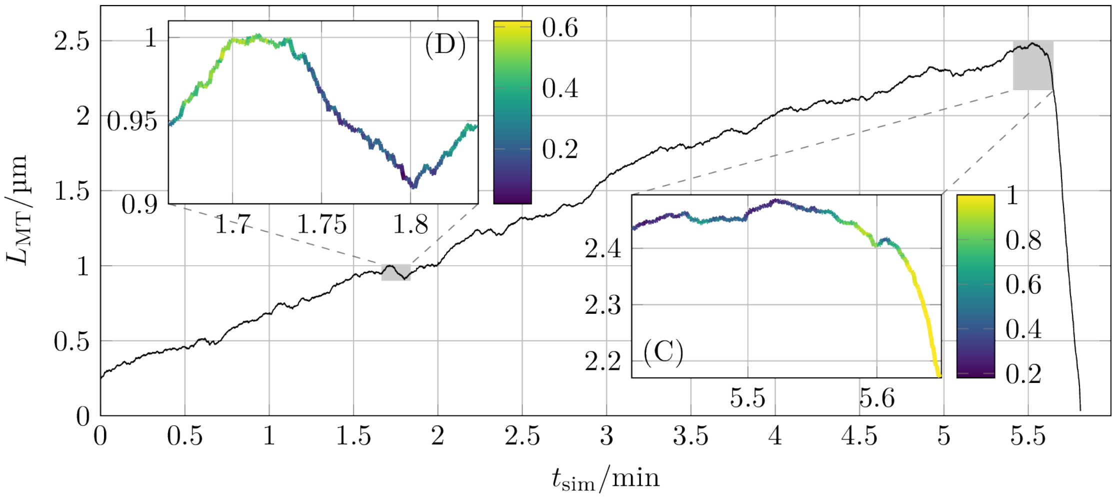

(a) $c_{\mathrm{tub}} = 9\,\mu\mathrm{M}$ and $k_{\mathrm{h}}^{0} = 1.5\,\mathrm{s}^{-1}$

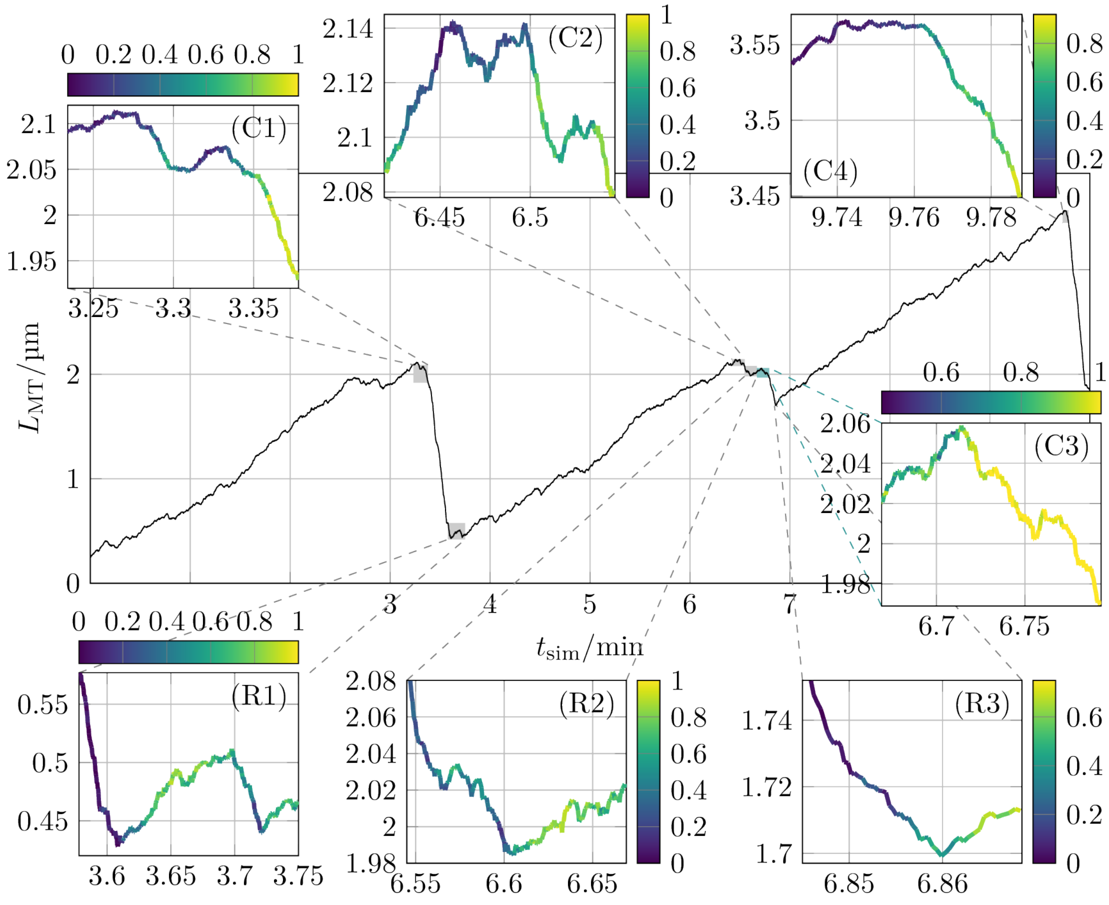

(b) $c_{\mathrm{tub}} = 11\,\mu\mathrm{M}$ and $k_{\mathrm{h}}^{0} = 3.0\,\mathrm{s}^{-1}$

Figure 8.6: Length L_{MT} of two exemplary microtubules as a function of the simulation time t_{sim} with dips, catastrophes, and rescues being highlighted in the insets like in Figure 8.1.

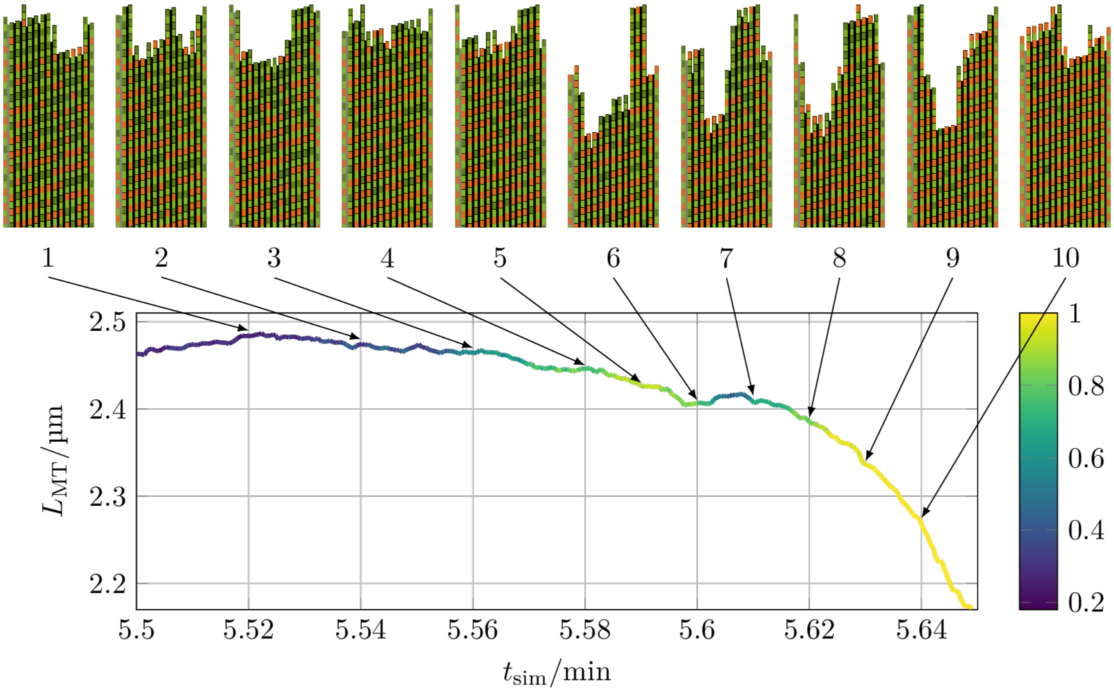

(a) Catastrophe from Figure 8.6(a).

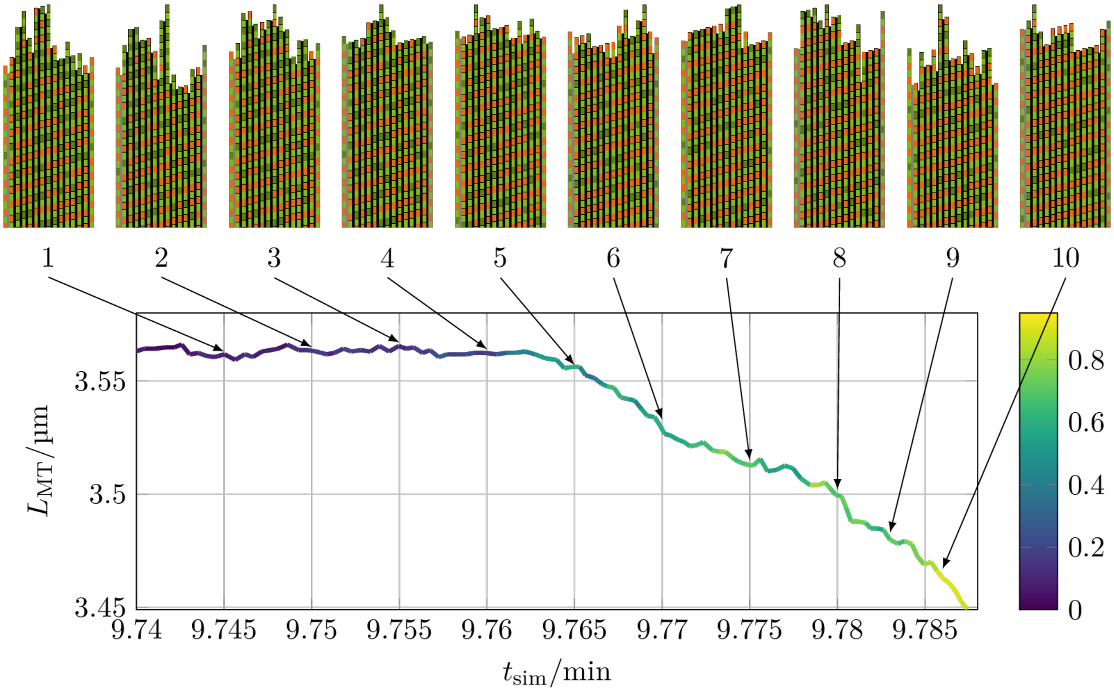

(b) Catastrophe (C4) from Figure 8.6(b).

Figure 8.7: Two-dimensional configuration snapshots around catastrophes shown in Figure 8.6. Three-dimensional configuration snapshots can be found in Figure H.3.

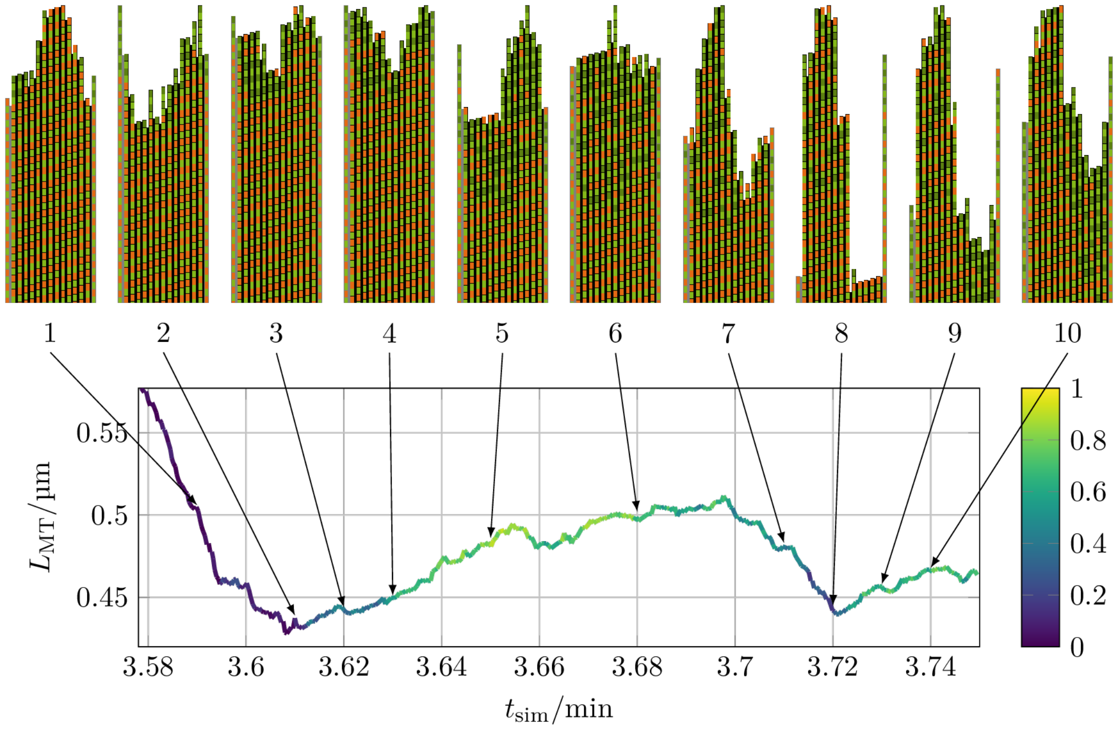

(a) Rescue (R1).

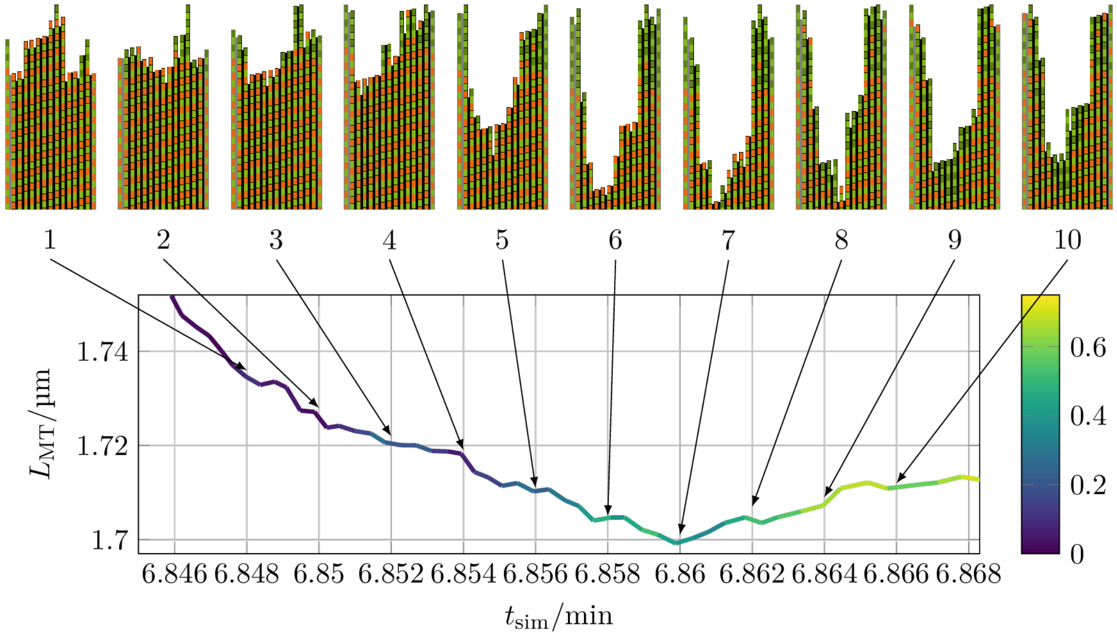

(b) Rescue (R3).

Figure 8.8: Two-dimensional configuration snapshots around rescues shown in Figure 8.6(b). Three-dimensional configuration snapshots can be found in Figure H.4 and Figure H.5.

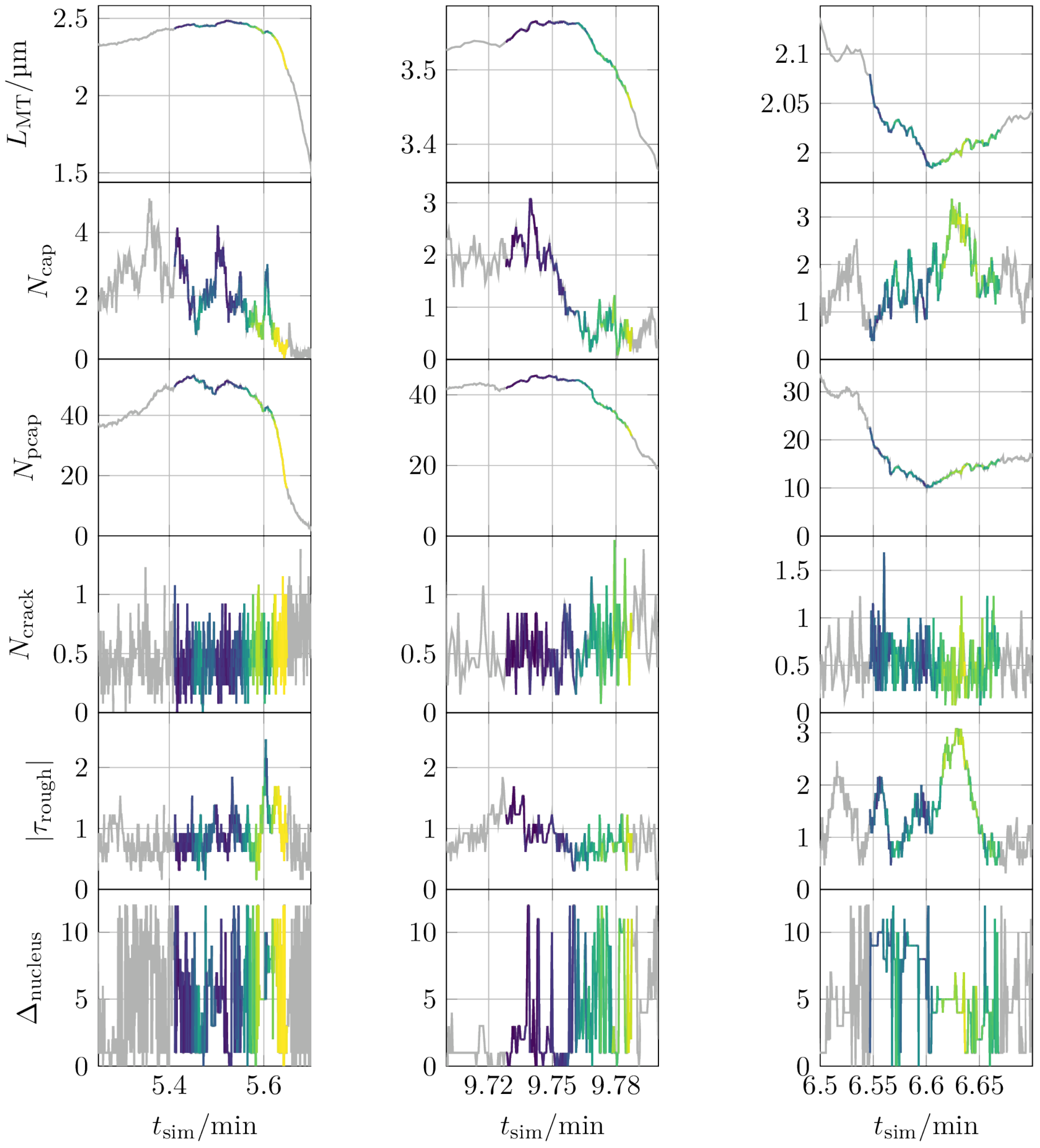

(a) Catastrophe from Figure 8.6(a).

(b) Catastrophe (C4) from Figure 8.6(b).

(c) Rescue (R2) from Figure 8.6(b).

Figure 8.9: The microtubule length L_{MT}, the average GTP-cap length per protofilament N_{cap}, the average porous GTP-cap length per protofilament N_{pcap}, the average crack length per protofilament N_{crack}, the average absolute tip roughness per protofilament $|\tau_{\mathrm{rough}}|$, and the width of the shrinking nucleus $\Delta_{\mathrm{nucleus}}$ for the catastrophes and the rescue from Figure 8.6 as a function of the simulation time t_{sim}. The same color coding as in the relevant insets of Figure 8.6 is used and additional data before and after the data shown in these insets is color-coded in gray.

Dilution

9

In dilution experiments[52,169,188,220–222], microtubules are grown at a concentration of free GTP-tubulin dimers c_{tub} that is quickly decreased to $c_{\mathrm{dil}} < c_{\mathrm{tub}}$ at a certain point in time during the experiment. Due to the change in the GTP-tubulin dimer concentration, the growth velocity of the microtubules changes. In experiments, c_{dil} is decreased below the critical concentration c_{crit} so that the microtubules undergo an "induced" catastrophe and shrink.

Walker et al.[223] found there to be a delay of several seconds between dilution and catastrophe during which they did not measure length changes in the observed microtubules. In the same year, Voter et al.[224], however, found no such delay in their experiments and attributed the different results by Walker et al.[223] to the higher post-dilution concentration c_{dil} in the experiments by Walker et al.[223] More recent studies[225,226], however, again found delays between dilution (or "tubulin wash out", as they call it) and catastrophe, as shown in Figure 9.1. Having better data resolution than the earlier dilution experiments, they were also able to show that during the delay, the microtubule dynamics do not actually pause, but the microtubules start to shrink with a slower speed compared to the speed after the "proper" catastrophe highlighted in Figure 9.1 with the blue arrow. They also found that the delay time increases with the pre-dilution growth speed (i.e., a higher free GTP-tubulin dimer concentration c_{tub}) indicating that such microtubules are more stable due to a longer GTP-cap. Their measured delay times range from a few seconds up to about 20 s.

In this chapter, we will focus on results for an initial free GTP-tubulin dimer concentration of $c_{\mathrm{tub}} = 16\,\mu\mathrm{M}$. Additional results for smaller values of c_{tub} can be found in Appendix I.

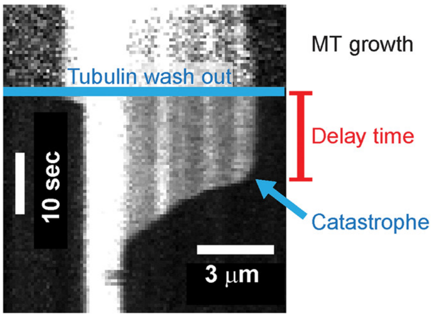

Figure 9.1: Kymograph illustrating the delay between dilution/wash out and the subsequent catastrophe[1].

---

[1] Used with permission of American Society for Cell Biology, from "Microtubule aging probed by microfluidics-assisted tubulin washout" by C. Duellberg, N. I. Cade, and T. Surrey, *Mol. Biol. Cell* **27** (22), 2016[225]; permission conveyed through Copyright Clearance Center, Inc.

9.1 Analysis of Dilution Simulations

To analyze the growth trajectories $(t_{\text{sim}}, L_{\text{MT}})$ of our dilution simulations, we split them into three parts: the initial growing phase until $t_{\text{sim}} = t_{\text{dil}}$ when c_{tub} is changed to c_{dil}, the second phase until the catastrophe at $t_{\text{sim}} = \tau_{\text{cat}}$ in which the microtubule lengths stay approximately the same $L_{\text{MT}}(t_{\text{dil}}) \simeq L_{\text{dil}}$, and the third and final phase in which the microtubule shrinks with the velocity v_{sh}. As a consequence, each actual trajectory is approximated by three lines:

1. growth phase for $t_{\text{sim}} \in [0, t_{\text{dil}}]$:

$$L_{\text{MT}}(t_{\text{sim}}) = v_{\text{gr}} t_{\text{sim}} + L_{\text{MT}}(0), \tag{9.1}$$

2. delay phase for $t_{\text{sim}} \in [t_{\text{dil}}, \tau_{\text{cat}}]$:

$$L_{\text{MT}}(t_{\text{sim}}) = L_{\text{dil}}, \tag{9.2}$$

3. shrinkage phase for $t_{\text{sim}} \geq \tau_{\text{cat}}$:

$$L_{\text{MT}}(t_{\text{sim}}) = v_{\text{sh}}(t_{\text{sim}} - \tau_{\text{cat}}) + L_{\text{dil}}. \tag{9.3}$$

During the analysis of the dilution simulation data, L_{dil} is given by the length in the first data sample with $t_{\text{sim}} \geq t_{\text{dil}}$. Additionally, τ_{cat} is the time at which the fit function of the shrinkage phase intersects $L_{\text{MT}}(t_{\text{sim}}) = L_{\text{dil}}$. The shrinkage velocity v_{sh} is determined from the last five seconds of data and simulations with non-negative v_{sh} determined from these last five seconds of data are ignored[2]. Thus, the delay time Δt_{delay} between dilution and when shrinkage starts is given by

$$\Delta t_{\text{delay}} = \tau_{\text{cat}} - t_{\text{dil}}. \tag{9.4}$$

Figure 9.2 shows two examples of how the actual microtubule growth trajectories in Figure 9.2(a) are simplified into the three phases in Figure 9.2(b). The example for $k_{\text{h}} = 0.5\,\text{s}^{-1}$ in particular shows that this procedure results in a coarse approximation as the real delay phase in which the microtubule does shrink but with a smaller shrinkage velocity is mapped onto a delay phase in which the microtubule length does not change. Nevertheless, Δt_{delay} gives us an indication of how long the actual delay phase is.

---

[2] Non-negative post-dilution velocities are relevant for high post-dilution concentrations c_{dil}. We, however, focus on sufficiently small values of c_{dil} for which this case is generally irrelevant.

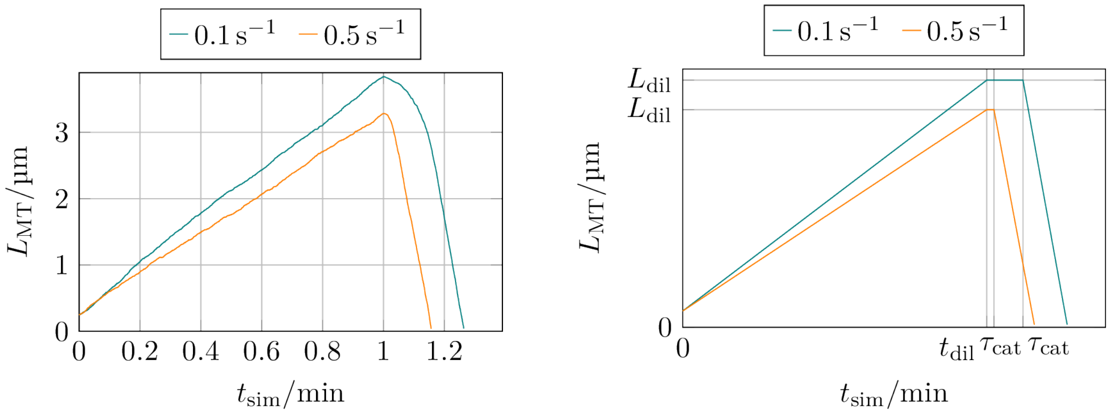

(a) Actual microtubule growth trajectories.

(b) Simplified microtubule growth trajectories split into a growth, delay, and shrinkage phase.

Figure 9.2: Example of how actual microtubule growth trajectories of dilution simulations with $c_{\mathrm{tub}} = 16\,\mu\mathrm{M}$, $c_{\mathrm{dil}} = 0\,\mu\mathrm{M}$, and two different values of k_{h} are simplified into a growth, delay, and shrinkage phase.

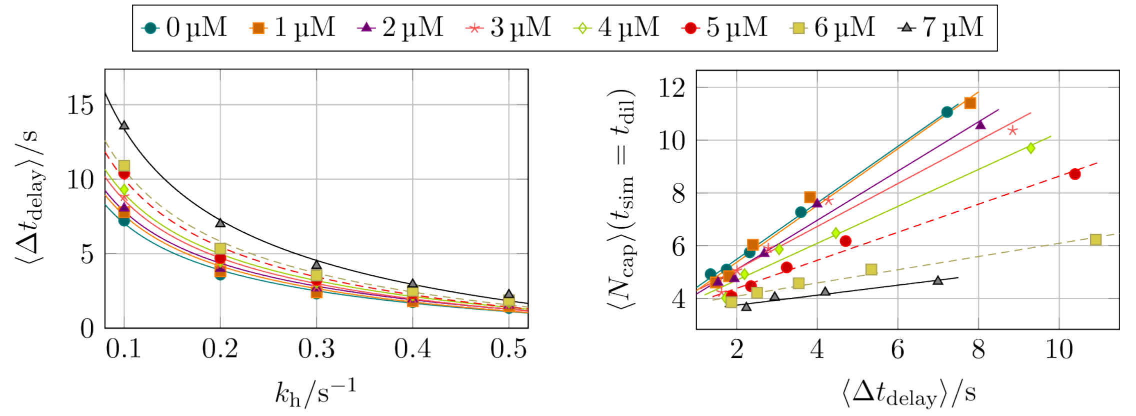

(a) Average post-dilution delay time $\langle \Delta t_{\mathrm{delay}} \rangle$ as a function of the hydrolysis rate k_{h}.

(b) Average GTP-cap length $\langle N_{\mathrm{cap}} \rangle$ at the time of dilution t_{dil} as a function of the average post-dilution delay time $\langle \Delta t_{\mathrm{delay}} \rangle$.

Figure 9.3: Average post-dilution delay time $\Delta t_{\mathrm{delay}}$ as a function of the hydrolysis rate k_{h} and the GTP-cap length N_{cap} at the time of dilution t_{dil} as a function of the average post-dilution delay time $\Delta t_{\mathrm{delay}}$ for $c_{\mathrm{tub}} = 16\,\mu\mathrm{M}$ and different post-dilution concentrations c_{dil}.

9.2 Dilution Simulations With Constant Hydrolysis Rate

There are two main parameters that are relevant for how the microtubule growth trajectories look in dilution experiments: the post-dilution concentration c_{dil} and the hydrolysis rate k_{h}. In Figure 9.2, we have already seen that for two exemplary simulations that a smaller hydrolysis rate increases the delay time $\Delta t_{\mathrm{delay}}$. For $c_{\mathrm{tub}} = 16\,\mu\mathrm{M}$ and different post-dilution concentrations c_{dil}, Figure 9.3(a) shows that the delay time $\Delta t_{\mathrm{delay}}$ does indeed increase for smaller hydrolysis rates. For each parameter set, 50 simulations were run and a script filtered out “irrelevant” simulations in which, for example, the microtubule already underwent a “normal” catastrophe before t_{dil} or if the calculated delay time is $\Delta t_{\mathrm{delay}} < 0$. Additionally, average values from each parameter set were only calculated if only at least 10 out of the 50 simulations are classified as “relevant”. Some of the growth trajectories, from which the delay times in Figure 9.3(a) are calculated, are shown in Figure I.1. The delay time-dependence on the hydrolysis rate for smaller concentrations can be found in Figure I.2.

To explain the dependence of $\langle \Delta t_{\mathrm{delay}} \rangle$ on k_{h}, we first consider the average GTP-cap length $\langle N_{\mathrm{cap}} \rangle$ at the time of dilution t_{dil}, as shown in Figure 9.3(b), which scales linearly with the average dilution delay time $\langle \Delta t_{\mathrm{delay}} \rangle$. Figure 9.4 shows the same two exemplary microtubule trajectories as in Figure 9.2(a), but now also together with the cap length N_{cap} and the porous GTP-cap length N_{pcap}. Regardless of whether a low or a high hydrolysis rate k_{h} is used, the cap length N_{cap} quickly decreases after the dilution at $t_{\mathrm{dil}} = 1\,\mathrm{min}$. While this decrease happens for the porous GTP-cap length N_{pcap} for $k_{\mathrm{h}} = 0.5\,\mathrm{s}^{-1}$ as well, which already reached its steady-state length at $t_{\mathrm{sim}} = 0.1\,\mathrm{min}$, for $k_{\mathrm{h}} = 0.1\,\mathrm{s}^{-1}$, the porous GTP-cap only vanished shortly before the microtubule had (almost) completely depolymerized. The results of the simulation with $k_{\mathrm{h}} = 0.1\,\mathrm{s}^{-1}$ are of interest in particular, as here, a significant delay phase exists in which the shrinkage velocity gradually increases to its final value. From this example, we

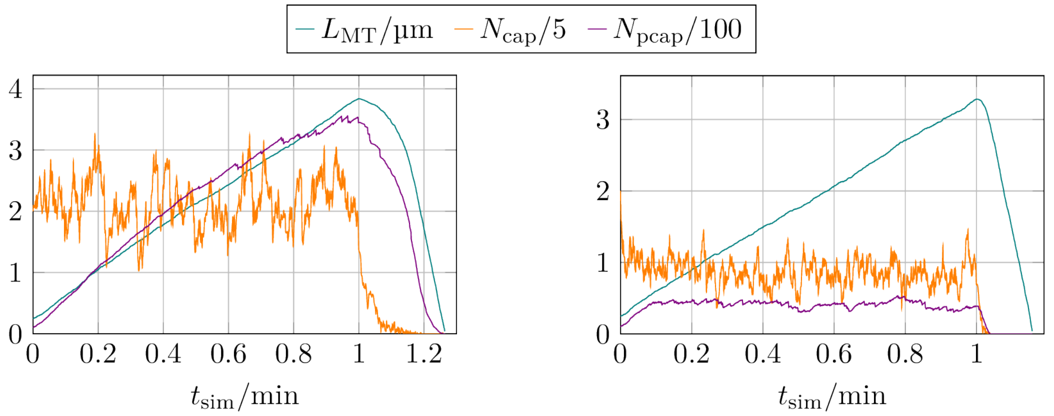

(a) $k_{\mathrm{h}} = 0.1\,\mathrm{s}^{-1}$ **(b)** $k_{\mathrm{h}} = 0.5\,\mathrm{s}^{-1}$

Figure 9.4: Microtubule growth trajectories and cap length trajectories of dilution simulations with $c_{\mathrm{tub}} = 16\,\mu\mathrm{M}$, $c_{\mathrm{dil}} = 0\,\mu\mathrm{M}$, and two different values of k_{h} indicate a correlation between the delay time $\Delta t_{\mathrm{delay}}$ and the cap length N_{cap} during dilution.

can postulate that there is a correlation between the length of the GTP-cap N_{cap} and the delay time $\Delta t_{\mathrm{delay}}$ as the point in time when the final shrinkage velocity is reached matches the point in time when the GTP-cap has vanished almost completely around $t_{\mathrm{sim}} = 1.5\,\mathrm{min}$. To explicitly check the relation between the dilution delay time $\langle \Delta t_{\mathrm{delay}} \rangle$ and the cap length N_{cap} at the time of dilution t_{dil}, we used the same simulation data as in Figure 9.3(a) and additionally determined $\langle N_{\mathrm{cap}} \rangle (t_{\mathrm{sim}} = t_{\mathrm{dil}})$. Figure 9.3(b) shows that there is linear relation between the $\langle N_{\mathrm{cap}} \rangle (t_{\mathrm{sim}} = t_{\mathrm{dil}})$ and $\langle \Delta t_{\mathrm{delay}} \rangle$ resulting in longer delay times for longer cap length at the time of dilution. The same linear relation can also be found for smaller initial GTP-tubulin dimer concentrations c_{tub}, see Figure I.3.

When analyzing the GTP-cap length in section 7.2, we haven shown that $\langle N_{\mathrm{cap}} \rangle \sim k_{\mathrm{h}}^{-0.5}$. Together with the linear dependence $\langle N_{\mathrm{cap}} \rangle (\langle \Delta t_{\mathrm{delay}} \rangle)$, we expect the following relation between the average delay time $\langle \Delta t_{\mathrm{delay}} \rangle$ and the hydrolysis rate:

$$\langle \Delta t_{\mathrm{delay}} \rangle (k_{\mathrm{h}}) = \frac{a_{\mathrm{delay}}}{\sqrt{k_{\mathrm{h}}}} + b_{\mathrm{delay}}. \tag{9.5}$$

The fits in Figure 9.3(a) show that the data points do follow (9.5).

Lastly, we want to compare the dependence of the average delay time $\langle \Delta t_{\mathrm{delay}} \rangle$ on the pre-dilution GTP-tubulin dimer concentration c_{tub} with the results by Duellberg et al.[226] that we mentioned at the beginning of this chapter. While a direct comparison is not possible due to different experimental conditions compared to Walker et al.[49], whose growth and shrinkage velocities were the basis for our parametrization, it gives us at least an insight on whether we get similar or completely different results. The data in Figure 9.5 for $c_{\mathrm{dil}} = 0\,\mu\mathrm{M}$ shows that the quantitative behavior of a slowly increasing delay time $\langle \Delta t_{\mathrm{delay}} \rangle$ potentially reaching a saturation value is similar. While the actual delay time values $\langle \Delta t_{\mathrm{delay}} \rangle$ are of the same order, only the data for $k_{\mathrm{h}} = 0.1\,\mathrm{s}^{-1}$ comes close to the actual values but appears to depend to steeply on c_{tub}.

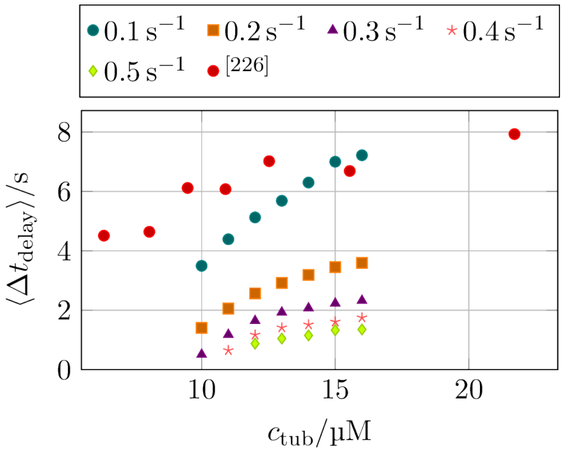

Figure 9.5: Average post-dilution delay time $\langle \Delta t_{\text{delay}} \rangle$ as a function of the pre-dilution GTP-tubulin dimer concentration c_{tub} for different hydrolysis rates k_{h} and $c_{\text{dil}} = 0\,\mu\text{M}$. The averaged data from Duellberg et al.[226] specified the pre-dilution growth velocity, which was converted to c_{tub} for this plot using (4.1).

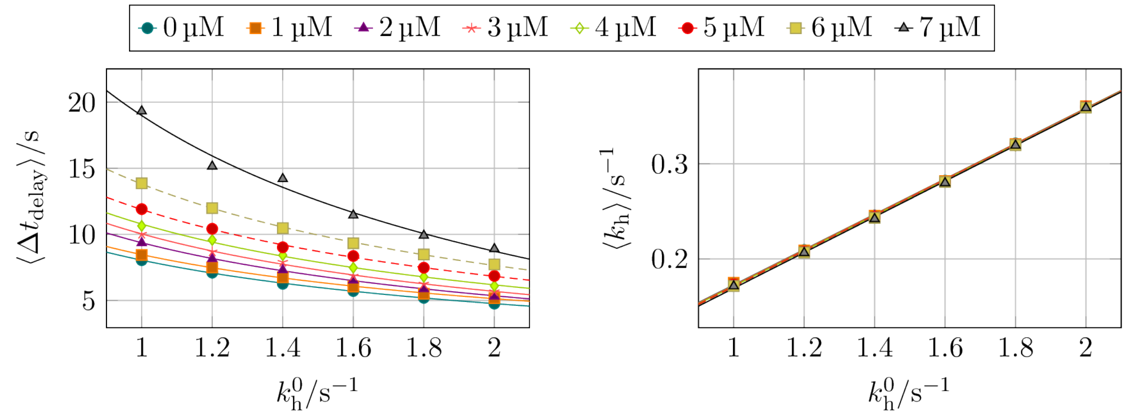

(a) Average post-dilution delay time $\langle \Delta t_{\mathrm{delay}} \rangle$ as a function of the base hydrolysis rate k_{h}^0.

(b) The average rate $\langle k_{\mathrm{h}} \rangle$ of executed hydrolysis events increases linearly with the base hydrolysis rate k_{h}^0.

Figure 9.6: Average post-dilution delay time $\langle \Delta t_{\mathrm{delay}} \rangle$ as a function of the base hydrolysis rate k_{h}^0 and average rate $\langle k_{\mathrm{h}} \rangle$ as a function of the base hydrolysis rate k_{h}^0 for $c_{\mathrm{tub}} = 16\,\mu\mathrm{M}$ and different post-dilution concentrations c_{dil}.

9.3 Dilution Simulations With Mechanical Hydrolysis

We repeated the previous analysis of simulations with constant hydrolysis rates with mechanical hydrolysis instead. We find the same dependence (9.5) of the average delay time $\langle \Delta t_{\mathrm{delay}} \rangle$ on the base hydrolysis rate k_{h}^0 as for a constant hydrolysis rate k_{h} as shown in Figure 9.6(a) (and in Figure I.4).

To compare these delay times in Figure 9.6(a) with the delay times for a constant hydrolysis rate in Figure 9.3(a), we determined the average rate $\langle k_{\mathrm{h}} \rangle$ of executed hydrolysis events as shown in Figure 9.6(b) (and Figure I.5) for different post-dilution concentrations c_{dil}. $\langle k_{\mathrm{h}} \rangle$ is independent of c_{dil} but increases linearly with k_{h}^0. We are now able to compare the delay times $\langle \Delta t_{\mathrm{delay}} \rangle$ as a function of the average actual hydrolysis rates for a constant hydrolysis rate (see Figure 9.7(a)) and mechanical hydrolysis (see Figure 9.7(b)). We find that $\langle \Delta t_{\mathrm{delay}} \rangle$ is significantly longer for mechanical hydrolysis than for a constant hydrolysis if $k_{\mathrm{h}} \approx \langle k_{\mathrm{h}} \rangle$ despite the GTP-cap being shorter (compare Figure 9.7(c) and Figure 9.7(d)). As compensation, however, Figure 9.7(e) and Figure 9.7(f) show that the average porous GTP-cap length $\langle N_{\mathrm{pcap}} \rangle$ is, as expected, significantly longer.

Compared to a constant hydrolysis rate (see Figure 9.5), we find an even steeper dependence of the average post-dilution delay time $\langle \Delta t_{\mathrm{delay}} \rangle$ on the pre-dilution GTP-tubulin dimer concentration c_{tub} without a flattening for higher values of c_{tub}.

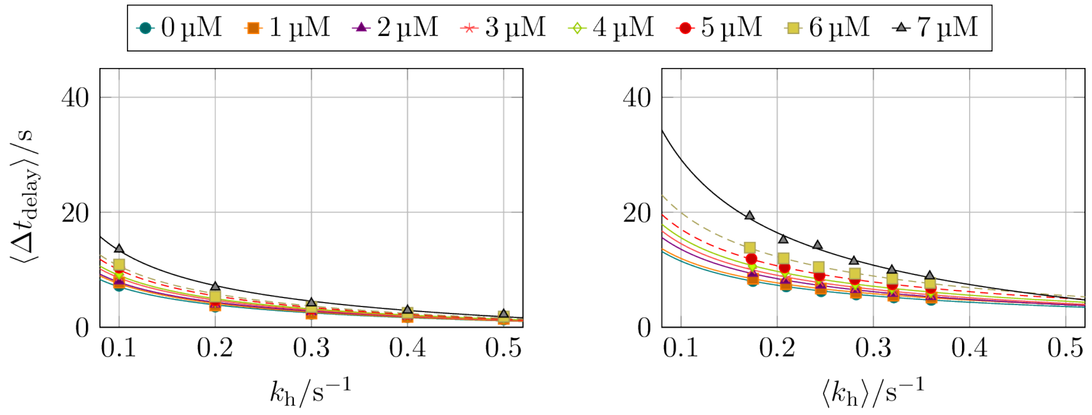

(a) Constant hydrolysis rate.

(b) Mechanical hydrolysis.

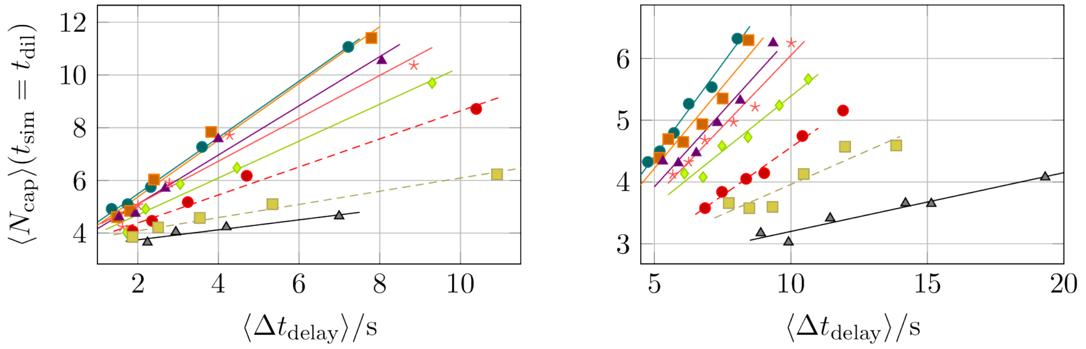

(c) Constant hydrolysis rate.

(d) Mechanical hydrolysis.

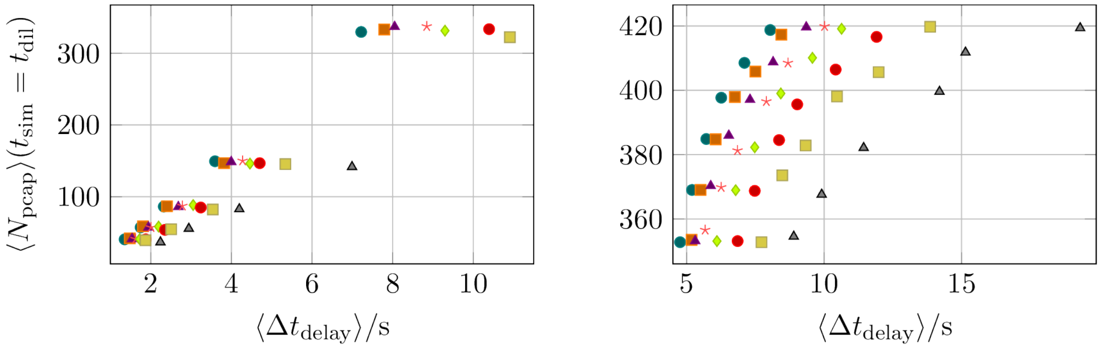

(e) Constant hydrolysis rate.

(f) Mechanical hydrolysis.

Figure 9.7: Comparison of the average post-dilution delay time $\langle \Delta t_{\mathrm{delay}} \rangle$ as a function of the hydrolysis rate k_{h} (or the average hydrolysis rate $\langle k_{\mathrm{h}} \rangle$ for mechanical hydrolysis) and the average cap length $\langle N_{\mathrm{cap}} \rangle$ and the average porous GTP-cap length $\langle N_{\mathrm{pcap}} \rangle$ at the time of dilution as a function of the following post-dilution delay time $\Delta t_{\mathrm{delay}}$ for $c_{\mathrm{tub}} = 16\,\mu\mathrm{M}$ and different post-dilution concentrations c_{dil}.

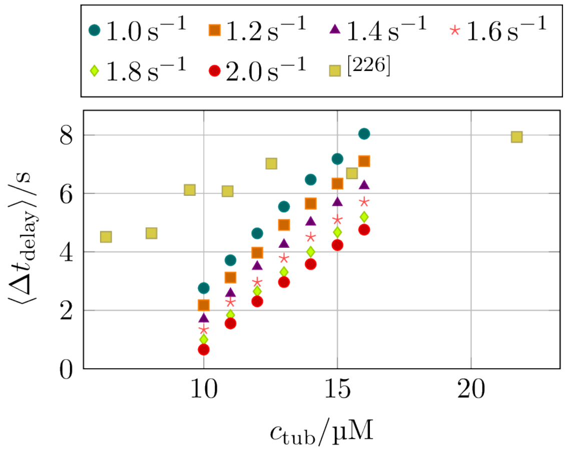

Figure 9.8: Average post-dilution delay time $\langle \Delta t_{\mathrm{delay}} \rangle$ as a function of the pre-dilution GTP-tubulin dimer concentration c_{tub} for different base hydrolysis rates k_{h}^{0} and $c_{\mathrm{dil}} = 0\,\mu\mathrm{M}$ and data from Duellberg et al.[226] for comparison.

Conclusions and Outlook

10

10.1 Conclusions

In the first chapters of this thesis, we explained how we modeled microtubules to simulate their growth dynamics and how we parameterized this chemomechanical model. The main features of the mechanical model are lateral springs connecting tubulin monomers in neighboring protofilaments and a bending energy favoring straight GTP-tubulin dimers and bent GDP-tubulin dimers. The chemical part of the model consists of polymerization and depolymerization of tubulin dimers, formation and rupture of lateral bonds, and hydrolysis of GTP-tubulin dimers. As the mechanical parts and chemical parts directly and indirectly influence each other, the overall model is chemomechanical.

To parameterize our model, we used growth and shrinkage velocity data from Walker et al.[49] First, we only considered growing microtubules to fix the longitudinal bond energy and the lateral bond energy. Using these values, we then determined the bending constant as a function of the lateral spring constant by simulating shrinking microtubules.

To combine these two growth dynamics into one proper simulation of microtubules, we had to focus on the energy minimization after each event so that the microtubule lattice assumes its equilibrium conformation. Using the bending angles of all tubulin monomers is infeasible as it causes the minimization time to scale up with the length of the microtubule resulting in a massive slowdown the longer the microtubules are. Such a slowdown makes it impossible to reach relevant growth times[126]. To avoid a length-dependent minimization time, we found the best way to improve minimization speed without a significant decrease in the minimization quality is to only consider the tubulin dimers above the tubulin dimer affected by the last event and the ten layers below it.

To enable switching between growth and shrinkage, hydrolysis has to be possible. With constant hydrolysis rates, we investigated the dynamics of microtubules and were able to generate catastrophes and rescues at realistic rates and to investigate the influence of dilution of the free GTP-tubulin dimers on microtubule growth. In both cases, however, we found the catastrophe and rescue rates on the one side and the delay time after dilution on the other side to depend too steeply on the concentration of free GTP-tubulin dimers c_{tub} compared to the experimental results by Walker et al.[49] and Duellberg et al.[226] As we have seen this steep dependence of the catastrophe and rescue rates for more than one set of mechanical parameters, it hints at a yet unknown issue with the microtubule model.

Once hydrolysis was enabled to simulate realistic microtubule growth dynamics, we also found that depending on the value of the hydrolysis rate, the growth velocities do not match the experimental values from Walker et al.[49] anymore but become lower. This finding shows a weakness of the "divide-and-conquer" approach employed here as simply merging the individual results together and then enabling hydrolysis is not possible. Instead, for future investigations, the parameter values obtained by separate growth-only and shrinkage-only simulations can be used as the base values, which are then gradually adjusted for a given hydrolysis rate until the experimental growth velocity is reproduced again.

We also considered mechanical feedback on the hydrolysis rate, which results in an increased hydrolysis rate at the microtubule tip. Additionally, hydrolysis of GTP-tubulin dimers deep in the GDP-body of the microtubule becomes more unlikely resulting in an increased porous GTP-cap length. We found the mechanical feedback to induce in an “anti-vectorial” bias so that GTP-islands are preferably hydrolyzed from the interior. Using mechanical hydrolysis also generates the same steep dependence of the catastrophe rate, rescue rate, and delay time after dilution on the free GTP-tubulin dimer concentration.

The analysis of different properties of the simulated microtubules showed that the distributions of GTP-island lengths and of GTP-cap lengths are consistent with predictions from a one-dimensional model[88,89]. We showed that in order to explain the distribution of the porous GTP-cap length, we have to consider separate distributions for different numbers of GTP-tubulin dimers in a protofilament, which then follow Gumbel-distributions. To analyze the structure of the tip, we considered the roughness of the tip and the length of cracks between protofilaments. From both of these quantities, we could conclude that the tips of our microtubules are generally quite blunt and do not exhibit bent ends as observed experimentally[63].

During the analysis of individual microtubule trajectories, we found “transitional catastrophes”[206] during which the microtubule switches from growth to slow shrinkage and then finally fast shrinkage, consistent with experimental data[206]. Additionally, we observed “dips”, i.e., short, intermediate phases of shrinkage that have also been observed in experiments[110,206]. The same analysis also gave insight into a potential requirement for catastrophes: the loss of the stabilizing GTP-cap of three to four neighboring protofilaments. For rescues, we observed that once neighboring protofilaments that have shrunken more than the other protofilaments have a GTP-cap again, a rescue is likely. Seeing that effects affecting neighboring protofilaments are important for catastrophes and rescues gives further confirmation that one-dimensional models or two-dimensional models with independent protofilaments are insufficient for explaining microtubule dynamics. Compared to constant hydrolysis rates, we find an increase in small dips when using mechanical hydrolysis.

10.2 Lattice Model

In section 1.2, as part of the introduction, we have mentioned two different models explaining how the curvature of tubulin dimers could influence dynamic instability. In the allosteric model, GTP-tubulin dimers are assumed to be straight and GDP-tubulin dimers to be bent resulting in mechanical strain in the microtubule lattice because the GDP-tubulin dimers in the lattice are held in an energetically unfavorable straight conformation. The lattice model, in contrast, assumes that both GTP- and GDP-tubulin dimers are bent and that lateral bonds are stronger for GTP-tubulin dimers than for GDP-tubulin dimers, resulting in the GTP-cap being more stable than the GDP-body. For the majority of previous three-dimensional modeling, the allosteric model was used[118,120–122,124,126]. Only McIntosh et al.[63], as part of an experimental study, discussed briefly adapting the model by Zakharov et al.[126] to the lattice model.

Recent extensive experimental data[63] found the ends of both growing and shrinking microtubules to be bent, which confirms earlier data[227–231]. Via the analysis of microtubule cryogenic electron microscopy (cryo-EM) structures with different nucleotide content[146,172] and by employing all-atom MD simulations of microtubules only consisting of GTP-tubulin dimers or GDP-tubulin dimers[232–234], it was revealed that the lateral bonds between GDP-tubulin dimers are weaker than between GTP-tubulin dimers and that the longitudinal bonds between GDP-tubulin dimers are stronger than between GTP-tubulin dimers. In order words, it was shown that lateral bonds are weakened and longitudinal bonds are strengthened by hydrolysis. Combined, these two findings support the lattice model instead of the allosteric model and show that for future microtubule modeling, the lattice model should be used (see the following discussion in section 10.3).

As changing from the allosteric model to the lattice model does not alter all but only some aspects of the microtubule model, there are still relevant aspects to be learned from this allosteric study that can then be also used in a lattice model:

1. In both models, hydrolysis weakens lateral interactions, which makes catastrophes possible. The difference in the models is how this weakening happens. In the allosteric model, more strain is put on lateral bonds after hydrolysis because GDP-tubulin dimers prefer to bent while GTP-tubulin dimers prefer to remain straight. In the lattice model, since both types of tubulin dimers are intrinsically bent, there is always a base amount of strain on the lateral bonds. Because of the lateral weakening after hydrolysis, however, the amount of strain that the lateral bonds can hold, is reduced. The result in both models is the same: The rate for these lateral bonds to rupture is increased, highlighting why it is important to consider the rupture of lateral bonds explicitly as in our model. Previously, lateral bond dynamics were only considered in the context of two-dimensional models without the crucial inclusion of mechanics[111–113] or as the result of computationally costly Brownian dynamics if the stretching energy exceeds an energy barrier[126].
2. Lateral bond rupture is essential for catastrophes as only the rupture of lateral bonds enables tubulin dimers to depolymerize from the microtubule. During catastrophes and during shrinkage, GDP-tubulin dimers at the microtubule tip are relevant due to the loss of the GTP-cap. In both models, GDP-tubulin dimers are bent and if they are directly exposed at the microtubule tip, they can start bending due to reduced lattice constraints compared to GDP-tubulin dimers embedded deep in the microtubule. This

bending at the tip stretches the lateral bonds of the relevant tubulin dimers. Due to this commonality in the models, we expect similar quantitative results for both models around catastrophes and during shrinkage. The only difference between the models relevant here is that the rupture rate (2.41) in the lattice model will also depend on the nucleotide type of the relevant tubulin dimers. As, however, the microtubules are mostly made up of GDP-tubulin dimers during and after catastrophe, there will be no significant influence of the nucleotide type on the rupture rate in this case. Consequently, parameterizing the lattice model using shrinkage velocity data should lead to similar results.

3. In section 3.3, we have discussed extensively the minimization part of our simulation and how it compares favorably to other approaches with respect to the actual mechanical relaxation[118] or the computational expense[126]. Re-using the same approach for a future simulation with the lattice model is perfectly viable.

4. A mechanical feedback mechanism for the hydrolysis rate cannot only be applied to the allosteric model via the equilibrium value of the bending angle (see (2.48)), but in the lattice model as well. An analogous approach in the lattice model would be to assume that due to hydrolysis weakening lateral bonds, mechanical strain weakening lateral bonds could also ease hydrolysis.

10.3 Outlook

As discussed in the previous section, probably the most important future change to the model is to change from the allosteric model to the lattice model by using the same equilibrium value of the bending angle for GTP- and GDP-tubulin dimers and having different longitudinal and lateral bond energies depending on the nucleotide content of the bonded tubulin monomers. If the lattice model is used, however, a parameter determination scheme first considering growing microtubules and then considering shrinking microtubules as described in chapter 4 will not be possible anymore because in the growing state, mechanics will now be relevant as well because of GTP-tubulin dimers also preferring to be bent. With regard to the different bond energies for GTP- and GDP-tubulin dimers, however, the divide-and-conquer approach might still be feasible because in a growing GTP-only simulation, we would only have to consider the bond energies for GTP-tubulin dimers.

Despite such a change from the allosteric model to the lattice model already introducing two new parameters (the two new bond energies), it might be useful to incorporate longitudinal stretching of tubulin monomers[118] as well so that if one tubulin monomer bends outward during minimization, it is only a local effect causing stretching of this tubulin monomer instead of having a global effect of all tubulin monomers above it also bending outward as a rigid segment. Having such an additional stretching energy, however, will result in another model parameter in form of a longitudinal spring constant and would introduce the tubulin monomer length as another parameter that has to be considered during minimization.

As recent studies have shed light on the intermediate hydrolysis state $\mathrm{GDP} \cdot \mathrm{P}_i$[110,172], splitting hydrolysis into two discrete steps of cleavage and release of the phosphate would be a natural addition. Such a more detailed hydrolysis model, however, would again be at the expense of having to replace one overall hydrolysis rate with two rates for both sub-processes and also a new longitudinal and a new lateral bond energy for this intermediate state. While in practice having additional parameters requires additional time to determine their values, on a practical level, we would need further experimental data with which we can determine their values then.

An important part of microtubule dynamics in cells are proteins called microtubule-associated proteins (MAPs) that interact with the microtubules and change their dynamics[235–237]. For us, as we focus on the plus end of microtubules, so called plus-end tracking proteins (+TIPs) would be relevant. Including such proteins would at least require the addition of attachment (and possibly detachment) events of such MAPs to the simulation and different possibilities of how they interact with the microtubule, for example by changing the mechanical parameters of the tubulin monomers to which the proteins are attached.

An additional aspect that has only been focused on in chemical models[93,114,158,238,239] is how external forces on growing microtubule end influence its dynamics[240,241], in particular catastrophes. External forces on the microtubule wall are also one way to damage the microtubule lattice, which has shown to be able to self-heal by incorporating new tubulin dimers[242–245].

There have been significant performance improvements in the simulation code during this research and using restricted minimization as explained in section 3.3 enabled us to run simulations for a longer time. To generate more statistics for catastrophe and rescue rates, making the code run even faster would require a major overhaul of the program relying on in-depth knowledge of C++ code optimization. After more catastrophe and rescue rates can be determined, they can also be used to fix the values of more model parameters. On a more practical level, in particular if longitudinal stretching is added to the model, it might make sense to investigate the introduction of an upper cutoff distance for energy minimization in addition to the present lower (i.e., directed to the minus-end) cutoff distance (see Figure 3.4). If a GTP-tubulin dimer relatively far from the microtubule tip is hydrolyzed, the effects of this hydrolysis event on neighboring tubulin dimers will diminish with their distance so that it might not be necessary to consider all tubulin dimers in the layers above it. By only considering "local" neighbors, we might be able to further speed up minimizations after hydrolysis, which, as we have discussed in section 6.4, slow down mechanical hydrolysis simulations.

Lastly, once sufficient statistics for catastrophe rates have been generated, an important aspect to investigate with regard to these catastrophe rates is whether they depend on the age of the microtubule. Experimental results have shown that the catastrophe rate increases with the microtubule age, which hints at catastrophes being multi-step processes[120,199,205].

Implementation

A

While the goal of this thesis was the implementation of a three-dimensional chemomechanical microtubule simulation, as a side-project that itself was not further utilized, a two-dimensional microtubule simulation similar to VanBuren et al.[104] and Margolin et al.[112] was implemented. Even though this implementation was not used to generate specific two-dimensional data, it was used to generate the growth-only parameters discussed in section 4.1 as they do not depend on mechanics. The parameter values were later validated by the three-dimensional implementation with mechanics and minimization enabled to ensure that there is no difference between the two implementations for this specific case. Coding the two-dimensional program after the three-dimensional program was already established allowed for some adjustments in the approach to the code structure. These adjustments improved the speed of the two-dimensional implementation compared to the three-dimensional implementation running the same type of simulation. Some of these changes (like compiling parameter values into the program instead of passing them around as variables) were later also added to the three-dimensional program if it did not result in major changes to the existing code base.

Both programs were written in C++ and the three-dimensional program also uses, as mentioned in section 3.3, the GNU Scientific Library (GSL)[183] for energy minimization and the Eigen library[246] for the vectors of the tubulin monomers discussed in section 2.1.

Gradient of the Microtubule Energy

B

To minimize the microtubule energy (2.30) as described in section 3.3, we must calculate the gradient of (2.30) with respect to the tubulin monomers' polar angle $\{\theta(p,d,t)\}$ as they are the tubulin monomers' only degree of freedom. Theoretically, it would be possible to calculate the gradient numerically, but as we are able to calculate it analytically and as the gradient is used to calculate an approximate inverse Hessian by the BFGS algorithm, we have also chosen to implement it analytically for better results. While this analytical calculation was already presented before in similar form[141], we present it here again for completeness and to discuss at the end of this chapter how calculating the gradient was sped up in the implementation.

The goal of this chapter it to calculate

$$\nabla E_{\mathrm{MT}} = \sum_{p=1}^{13} \sum_{d=1}^{d_{\max}(p)} \sum_{t=1}^{2} \frac{\partial E_{\mathrm{MT}}}{\partial \theta(p,d,t)} \, \boldsymbol{e}(p,d,t), \tag{B.1}$$

where $\boldsymbol{e}(p,d,t)$ is a unit vector with components

$$\big[\boldsymbol{e}(p,d,t)\big]_i = \begin{cases} 1, & \text{if } i = 2\displaystyle\sum_{p'=1}^{p-1} d_{\max}(p') + 2d - \delta_{t,1} \\ 0, & \text{else} \end{cases} \tag{B.2}$$

Consequently, we have to calculate partial derivative of the lateral energy (2.24), the repulsive energy (2.25), and the bending energy (2.26) with respect to one particular polar angle $\theta(p,d,t)$. To make calculating these derivatives easier, we first calculate the same derivative for the structural vectors introduced in section 2.1 as the lateral energy (2.24) and the repulsive energy (2.25) are only indirectly given in terms of the polar angles via these structural vectors:

$$\frac{\partial \boldsymbol{m}(p',1,1)}{\partial \theta(p,d,t)} = \frac{\partial}{\partial \theta(p,d,t)} \begin{pmatrix} R_{\mathrm{MT}} \cos\phi(p') \\ -R_{\mathrm{MT}} \sin\phi(p') \\ (p'-1)\Delta z_{\mathrm{h}} \end{pmatrix} \tag{B.3}$$

$$= \boldsymbol{0}, \tag{B.4}$$

$$\frac{\partial \boldsymbol{d}(p',d',t')}{\partial \theta(p,d,t)} = \frac{\partial}{\partial \theta(p,d,t)} \ell_{\mathrm{tub}} \begin{pmatrix} \cos\phi(p') \sin\theta(p',d',t') \\ -\sin\phi(p') \sin\theta(p',d',t') \\ \cos\theta(p',d',t') \end{pmatrix} \tag{B.5}$$

$$= \ell_{\mathrm{tub}} \begin{pmatrix} \cos\phi(p) \cos\theta(p,d,t) \\ -\sin\phi(p) \cos\theta(p,d,t) \\ -\sin\theta(p,d,t) \end{pmatrix} \delta_{p,p'} \delta_{d,d'} \delta_{t,t'} \tag{B.6}$$

$$= \frac{\partial \boldsymbol{d}(p,d,t)}{\partial \theta(p,d,t)} \, \delta_{p,p'} \delta_{d,d'} \delta_{t,t'}, \tag{B.7}$$

$$\frac{\partial \boldsymbol{p}(p', d', t')}{\partial \theta(p, d, t)} = \frac{\partial}{\partial \theta(p, d, t)} \left(\boldsymbol{m}(p', 1, 1) + \sum_{d''=1}^{d'} \sum_{t''=1}^{2} \boldsymbol{d}(p', d'', t'') - \delta_{t',1} \boldsymbol{d}(p', d', 2) \right) \tag{B.8}$$

$$= \sum_{d''=1}^{d'} \sum_{t''=1}^{2} \frac{\partial \boldsymbol{d}(p', d'', t'')}{\partial \theta(p, d, t)} - \delta_{t',1} \frac{\partial \boldsymbol{d}(p', d', 2)}{\partial \theta(p, d, t)} \tag{B.9}$$

$$= \frac{\partial \boldsymbol{d}(p, d, t)}{\partial \theta(p, d, t)} \left(\sum_{d''=1}^{d'} \sum_{t''=1}^{2} \delta_{p,p'} \delta_{d,d''} \delta_{t,t''} - \delta_{t',1} \delta_{p,p'} \delta_{d,d'} \delta_{t,2} \right) \tag{B.10}$$

$$= \frac{\partial \boldsymbol{d}(p, d, t)}{\partial \theta(p, d, t)} \delta_{p,p'} \left(\sum_{d''=1}^{d'} \delta_{d,d''} - \delta_{d,d'} \delta_{t,2} \delta_{t',1} \right) \tag{B.11}$$

$$= \frac{\partial \boldsymbol{d}(p, d, t)}{\partial \theta(p, d, t)} \delta_{p,p'} \left(\Theta(d' - d) - \delta_{d,d'} \delta_{t,2} \delta_{t',1} \right), \tag{B.12}$$

$$\frac{\partial \boldsymbol{c}(p', d', t')}{\partial \theta(p, d, t)} = -r_{\text{tub}} \frac{\partial}{\partial \theta(p, d, t)} \begin{pmatrix} \sin \phi(p') \\ \cos \phi(p') \\ 0 \end{pmatrix} \tag{B.13}$$

$$= \mathbf{0}, \tag{B.14}$$

$$\frac{\partial \boldsymbol{s}(p', d', t')}{\partial \theta(p, d, t)} = -\frac{\partial}{\partial \theta(p, d, t)} \left[\boldsymbol{p}(p', d', t') + \boldsymbol{c}(p', d', t') - \boldsymbol{p}(p' + 1, d', t') + \boldsymbol{c}(p' + 1, d', t') \right] \tag{B.15}$$

$$= -\frac{\partial \boldsymbol{p}(p', d', t')}{\partial \theta(p, d, t)} + \frac{\partial \boldsymbol{p}(p' + 1, d', t')}{\partial \theta(p, d, t)} \tag{B.16}$$

$$= \frac{\partial \boldsymbol{d}(p, d, t)}{\partial \theta(p, d, t)} \left(\delta_{p,p'+1} - \delta_{p,p'} \right) \left(\Theta(d' - d) - \delta_{d,d'} \delta_{t,2} \delta_{t',1} \right), \tag{B.17}$$

where $\Theta(x)$ is the Heaviside function. The term in the derivative of the tubulin plus end vector $\boldsymbol{p}(p', d', t')$ in (B.12) in which the Heaviside function occurs, $\Theta(d' - d)$, is an interesting term as it introduces long-ranging "interactions" in the microtubule with respect to the derivatives because the plus end vectors of all tubulin monomers on top of tubulin monomer (p, d, t) also depend on $\theta(p, d, t)$. A possibility to avoid such a long-ranging effect would be the introduction of longitudinal stretching of tubulin monomers (see section 10.3). Currently, if a tubulin monomer bends outward, the protofilament segment on top of it stays rigid, thus also changing the plus (and minus) end positions of every tubulin monomer above. If there was longitudinal stretching, however, the direct consequence of one tubulin monomer bending outward would be an increase in its length due to longitudinal stretching and the other tubulin monomers closer to the plus above it end staying in place.

We start with the derivative of the bending energy (2.26) with respect to polar angles:

$$\frac{\partial E_{\text{bend}}(p', d', t')}{\partial \theta(p, d, t)} = \frac{1}{2} \kappa \frac{\partial}{\partial \theta(p, d, t)} \Delta \psi^2(p', d', t') \tag{B.18}$$

$$= \kappa \Delta \psi(p', d', t') \frac{\partial \psi(p', d', t')}{\partial \theta(p, d, t)} \tag{B.19}$$

$$= \kappa \Delta \psi(p', d', t') \left[\frac{\partial \theta(p', d', t')}{\partial \theta(p, d, t)} - \frac{\partial \theta(p', d', t' - 1)}{\partial \theta(p, d, t)} \right] \tag{B.20}$$

$$= \kappa\Delta\psi(p',d',t')\left(\delta_{p,p'}\delta_{d,d'}\delta_{t,t'} - \delta_{p,p'}\delta_{d,d'}\delta_{t,t'-1}\right) \tag{B.21}$$

$$= \kappa\Delta\psi(p',d',t')\left(\delta_{t,t'} - \delta_{t,t'-1}\right)\delta_{p,p'}\delta_{d,d'}. \tag{B.22}$$

In (B.20), we have not considered the case of the first alpha-tubulin monomer in the protofilament, i.e., only $d' \neq 1$ and $t' \neq 1$, for the bending angle $\psi(p',d',t')$, see (2.27). The case $d' = 1$ and $t' = 1$, however, is still correctly covered by the final result, as the second term in (B.22) does not contribute in this case as it would require the derivative to be with respect to the polar angle of tubulin monomer $(p, 1, 0)$, which does not exist.

The derivative of the lateral energy (2.24) of tubulin monomer (p', d', t') with respect to the polar angle $\theta(p, d, t)$ is given by

$$\frac{\partial E_{\mathrm{lat}}(p',d',t')}{\partial\theta(p,d,t)} = \frac{1}{2}k_{\mathrm{lat}}\frac{\partial}{\partial\theta(p,d,t)}\left[|\boldsymbol{s}(p',d',t')| - s_0\right]^2 \tag{B.23}$$

$$= k_{\mathrm{lat}}\left[|\boldsymbol{s}(p',d',t')| - s_0\right]\frac{\boldsymbol{s}(p',d',t')}{|\boldsymbol{s}(p',d',t')|}\,\frac{\partial\boldsymbol{s}(p',d',t')}{\partial\theta(p,d,t)} \tag{B.24}$$

$$\begin{aligned}
&= k_{\mathrm{lat}}\left[|\boldsymbol{s}(p',d',t')| - s_0\right]\frac{\boldsymbol{s}(p',d',t')}{|\boldsymbol{s}(p',d',t')|}\,\frac{\partial\boldsymbol{d}(p,d,t)}{\partial\theta(p,d,t)}\left(\delta_{p,p'+1} - \delta_{p,p'}\right)\times\\
&\qquad\times\left[\Theta(d'-d) - \delta_{d,d'}\delta_{t,2}\delta_{t',1}\right]
\end{aligned} \tag{B.25}$$

in which

$$\frac{\partial|\boldsymbol{f}(x)|}{\partial x} = \frac{\boldsymbol{f}(x)}{|\boldsymbol{f}(x)|}\,\frac{\partial\boldsymbol{f}(x)}{\partial x} \tag{B.26}$$

was used.

Lastly, the derivative of the repulsive energy (2.25) of tubulin monomer (p', d', t') with respect to the polar angle $\theta(p, d, t)$ is given by

$$\frac{\partial E_{\mathrm{rep}}(p',d',t')}{\partial\theta(p,d,t)} \tag{B.27}$$

$$= k_{\mathrm{rep}}\frac{\partial}{\partial\theta(p,d,t)}\left[|\boldsymbol{p}(p',d',t') - \boldsymbol{p}(p'+1,d',t')| - 2r_{\mathrm{tub}}\right]^{-12} \tag{B.28}$$

$$\begin{aligned}
&= -12k_{\mathrm{rep}}\left[|\boldsymbol{p}(p',d',t') - \boldsymbol{p}(p'+1,d',t')| - 2r_{\mathrm{tub}}\right]^{-13}\times\\
&\qquad\times\frac{\boldsymbol{p}(p',d',t') - \boldsymbol{p}(p'+1,d',t')}{|\boldsymbol{p}(p',d',t') - \boldsymbol{p}(p'+1,d',t')|}\left[\frac{\partial\boldsymbol{p}(p',d',t')}{\partial\theta(p,d,t)} - \frac{\partial\boldsymbol{p}(p'+1,d',t')}{\partial\theta(p,d,t)}\right]
\end{aligned} \tag{B.29}$$

$$\begin{aligned}
&\overset{(B.17)}{=} 12k_{\mathrm{rep}}\left[|\boldsymbol{p}(p',d',t') - \boldsymbol{p}(p'+1,d',t')| - 2r_{\mathrm{tub}}\right]^{-13}\frac{\partial\boldsymbol{d}(p,d,t)}{\partial\theta(p,d,t)}\times\\
&\qquad\times\frac{\boldsymbol{p}(p',d',t') - \boldsymbol{p}(p'+1,d',t')}{|\boldsymbol{p}(p',d',t') - \boldsymbol{p}(p'+1,d',t')|}\left(\delta_{p,p'+1} - \delta_{p,p'}\right)\left(\Theta(d'-d) - \delta_{d,d'}\delta_{t,2}\delta_{t',1}\right).
\end{aligned} \tag{B.30}$$

Before we calculate the derivative of the sum of all energy contributions, it makes sense to calculate the derivatives of the total lateral energy, the total repulsive energy, and the bending energy separately. For the derivative of the total lateral energy, we get

$$\frac{\partial E_{\mathrm{bend}}}{\partial\theta(p,d,t)} = \sum_{p'=1}^{13}\sum_{d'=1}^{d_{\max}(p)}\sum_{t'=1}^{2}\frac{\partial E_{\mathrm{bend}}(p',d',t')}{\partial\theta(p,d,t)} \tag{B.31}$$

$$
\begin{aligned}
&= \kappa \sum_{p'=1}^{13} \sum_{d'=1}^{d_{\max}(p')} \sum_{t'=1}^{2} \Delta\psi(p',d',t') \left(\delta_{t,t'} - \delta_{t,t'-1}\right) \delta_{p,p'} \delta_{d,d'} && \text{(B.32)}\\
&= \kappa \sum_{t'=1}^{2} \Delta\psi(p,d,t') \left(\delta_{t,t'} - \delta_{t,t'-1}\right) && \text{(B.33)}\\
&= \kappa \left(\Delta\psi(p,d,t) - \Delta\psi(p,d,t+1)\right), && \text{(B.34)}
\end{aligned}
$$

for the repulsive energy, we get

$$
\begin{aligned}
&\frac{\partial E_{\mathrm{lat}}}{\partial \theta(p,d,t)} && \text{(B.35)}\\
&= \sum_{p'=1}^{13} \sum_{d'=1}^{d_{\max}(p')} \sum_{t'=1}^{2} \frac{\partial E_{\mathrm{lat}}(p',d',t')}{\partial \theta(p,d,t)} && \text{(B.36)}\\
&= k_{\mathrm{lat}} \sum_{p'=1}^{13} \sum_{d'=1}^{d_{\max}(p')} \sum_{t'=1}^{2} \left[|\boldsymbol{s}(p',d',t')| - s_0\right] \frac{\boldsymbol{s}(p',d',t')}{|\boldsymbol{s}(p',d',t')|} \frac{\partial \boldsymbol{d}(p,d,t)}{\partial \theta(p,d,t)} \left(\delta_{p,p'+1} - \delta_{p,p'}\right) \times\\
&\qquad \times \left(\Theta(d'-d) - \delta_{d,d'}\delta_{t,2}\delta_{t',1}\right) && \text{(B.37)}\\
&= k_{\mathrm{lat}} \frac{\partial \boldsymbol{d}(p,d,t)}{\partial \theta(p,d,t)} \Bigg(\\
&\qquad \sum_{d'=1}^{d_{\max}(p-1)} \sum_{t'=1}^{2} \left[|\boldsymbol{s}(p-1,d',t')| - s_0\right] \frac{\boldsymbol{s}(p-1,d',t')}{|\boldsymbol{s}(p-1,d',t')|} \left(\Theta(d'-d) - \delta_{d,d'}\delta_{t,2}\delta_{t',1}\right)\\
&\qquad - \sum_{d'=1}^{d_{\max}(p)} \sum_{t'=1}^{2} \left[|\boldsymbol{s}(p,d',t')| - s_0\right] \frac{\boldsymbol{s}(p,d',t')}{|\boldsymbol{s}(p,d',t')|} \left(\Theta(d'-d) - \delta_{d,d'}\delta_{t,2}\delta_{t',1}\right)\Bigg) && \text{(B.38)}\\
&= k_{\mathrm{lat}} \frac{\partial \boldsymbol{d}(p,d,t)}{\partial \theta(p,d,t)} \Bigg(\sum_{d'=d}^{d_{\max}(p-1)} \sum_{t'=1}^{2} \left[|\boldsymbol{s}(p-1,d',t')| - s_0\right] \frac{\boldsymbol{s}(p-1,d',t')}{|\boldsymbol{s}(p-1,d',t')|}\\
&\qquad - \left[|\boldsymbol{s}(p-1,d,1)| - s_0\right] \frac{\boldsymbol{s}(p-1,d,1)}{|\boldsymbol{s}(p-1,d,1)|} \delta_{t,2}\\
&\qquad - \sum_{d'=1d}^{d_{\max}(p)} \sum_{t'=1}^{2} \left[|\boldsymbol{s}(p,d',t')| - s_0\right] \frac{\boldsymbol{s}(p,d',t')}{|\boldsymbol{s}(p,d',t')|}\\
&\qquad + \left[|\boldsymbol{s}(p,d,1)| - s_0\right] \frac{\boldsymbol{s}(p,d,1)}{|\boldsymbol{s}(p,d,1)|} \delta_{t,2}\Bigg), && \text{(B.39)}
\end{aligned}
$$

and finally the derivative of the total bending energy with respect to the bending angle is

$$
\begin{aligned}
&\frac{\partial E_{\mathrm{rep}}}{\partial \theta(p,d,t)} && \text{(B.40)}\\
&= \sum_{p'=1}^{13} \sum_{d'=1}^{d_{\max}(p')} \sum_{t'=1}^{2} \frac{\partial E_{\mathrm{rep}}(p',d',t')}{\partial \theta(p,d,t)} && \text{(B.41)}\\
&= 12 k_{\mathrm{rep}} \sum_{p'=1}^{13} \sum_{d'=1}^{d_{\max}(p')} \sum_{t'=1}^{2} \left[|\boldsymbol{p}(p',d',t') - \boldsymbol{p}(p'+1,d',t')| - 2r_{\mathrm{tub}}\right]^{-13} \frac{\partial \boldsymbol{d}(p,d,t)}{\partial \theta(p,d,t)} \times
\end{aligned}
$$

$$\times \frac{\boldsymbol{p}(p',d',t') - \boldsymbol{p}(p'+1,d',t')}{|\boldsymbol{p}(p',d',t') - \boldsymbol{p}(p'+1,d',t')|} \left(\delta_{p,p'+1} - \delta_{p,p'}\right) \left(\Theta(d'-d) - \delta_{d,d'}\delta_{t,2}\delta_{t',1}\right) \tag{B.42}$$

$$\begin{aligned}
&= 12k_{\mathrm{rep}} \frac{\partial \boldsymbol{d}(p,d,t)}{\partial \theta(p,d,t)} \Bigg(\\
&\sum_{d'=1}^{d_{\max}(p-1)} \sum_{t'=1}^{2} \left[|\boldsymbol{p}(p-1,d',t') - \boldsymbol{p}(p,d',t')| - 2r_{\mathrm{tub}}\right]^{-13} \times \\
&\quad \times \frac{\boldsymbol{p}(p-1,d',t') - \boldsymbol{p}(p,d',t')}{|\boldsymbol{p}(p-1,d',t') - \boldsymbol{p}(p,d',t')|} \left(\Theta(d'-d) - \delta_{d,d'}\delta_{t,2}\delta_{t',1}\right) \\
&- \sum_{d'=1}^{d_{\max}(p)} \sum_{t'=1}^{2} \left[|\boldsymbol{p}(p,d',t') - \boldsymbol{p}(p+1,d',t')| - 2r_{\mathrm{tub}}\right]^{-13} \times \\
&\times \frac{\boldsymbol{p}(p,d',t') - \boldsymbol{p}(p+1,d',t')}{|\boldsymbol{p}(p,d',t') - \boldsymbol{p}(p+1,d',t')|} \left(\Theta(d'-d) - \delta_{d,d'}\delta_{t,2}\delta_{t',1}\right) \Bigg)
\end{aligned} \tag{B.43}$$

$$\begin{aligned}
&= 12k_{\mathrm{rep}} \frac{\partial \boldsymbol{d}(p,d,t)}{\partial \theta(p,d,t)} \Bigg(\\
&\sum_{d'=d}^{d_{\max}(p-1)} \sum_{t'=1}^{2} \left[|\boldsymbol{p}(p-1,d',t') - \boldsymbol{p}(p,d',t')| - 2r_{\mathrm{tub}}\right]^{-13} \frac{\boldsymbol{p}(p-1,d',t') - \boldsymbol{p}(p,d',t')}{|\boldsymbol{p}(p-1,d',t') - \boldsymbol{p}(p,d',t')|} \\
&- \left[|\boldsymbol{p}(p-1,d,1) - \boldsymbol{p}(p,d,1)| - 2r_{\mathrm{tub}}\right]^{-13} \frac{\boldsymbol{p}(p-1,d,1) - \boldsymbol{p}(p,d,1)}{|\boldsymbol{p}(p-1,d,1) - \boldsymbol{p}(p,d,1)|} \delta_{t,2} \\
&- \sum_{d'=d}^{d_{\max}(p)} \sum_{t'=1}^{2} \left[|\boldsymbol{p}(p,d',t') - \boldsymbol{p}(p+1,d',t')| - 2r_{\mathrm{tub}}\right]^{-13} \frac{\boldsymbol{p}(p,d',t') - \boldsymbol{p}(p+1,d',t')}{|\boldsymbol{p}(p,d',t') - \boldsymbol{p}(p+1,d',t')|} \Bigg) \\
&\qquad + \left[|\boldsymbol{p}(p,d,1) - \boldsymbol{p}(p+1,d,1)| - 2r_{\mathrm{tub}}\right]^{-13} \frac{\boldsymbol{p}(p,d,1) - \boldsymbol{p}(p+1,d,1)}{|\boldsymbol{p}(p,d,1) - \boldsymbol{p}(p+1,d,1)|} \delta_{t,2} \Bigg).
\end{aligned} \tag{B.44}$$

To keep the final result a bit clearer, we introduce the following abbreviations:

$$\bar{\boldsymbol{s}}(p,d,t) \equiv \left[|\boldsymbol{s}(p,d,t)| - s_0\right] \frac{\boldsymbol{s}(p,d,t)}{|\boldsymbol{s}(p,d,t)|}, \tag{B.45}$$

$$\bar{\boldsymbol{p}}(p,d,t) \equiv \left[|\boldsymbol{p}(p,d,t) - \boldsymbol{p}(p+1,d,t)| - 2r_{\mathrm{tub}}\right]^{-13} \frac{\boldsymbol{p}(p,d,t) - \boldsymbol{p}(p+1,d,t)}{|\boldsymbol{p}(p,d,t) - \boldsymbol{p}(p+1,d,t)|}, \tag{B.46}$$

$$\bar{\boldsymbol{v}}(p,d,t) \equiv k_{\mathrm{lat}} \bar{\boldsymbol{s}}(p,d,t) + 12k_{\mathrm{rep}} \bar{\boldsymbol{p}}(p,d,t). \tag{B.47}$$

Additionally, we introduce the following new summation operator:

$$\sum_{d',t'>(d,t)}^{p} f(p,d',t') \equiv \sum_{d'=d}^{d_{\max}(p)} \sum_{t'=1}^{2} f(p,d',t') - f(p,d',1)\delta_{t,2}, \tag{B.48}$$

which sums over all tubulin monomers starting with (p,d,t) and ending with $(p, d_{\max}(p), 2)$.

With these abbreviations, the components of the energy gradient (B.1) are

$$\frac{\partial E_{\mathrm{MT}}}{\partial \theta(p,d,t)} \tag{B.49}$$

$$= \sum_{p'=1}^{13} \sum_{d'=1}^{d_{\max}(p')} \sum_{t'=1}^{2} \frac{\partial}{\partial \theta(p,d,t)} \left(E_{\text{bend}}(p',d',t') + E_{\text{lat}}(p',d',t') + E_{\text{rep}}(p',d',t')\right) \tag{B.50}$$

$$\begin{aligned}
&= \kappa \left[\Delta\psi(p,d,t) - \Delta\psi(p,d,t+1)\right] \\
&\quad + k_{\text{lat}} \frac{\partial \boldsymbol{d}(p,d,t)}{\partial \theta(p,d,t)} \left(\sum_{d',t'>(d,t)}^{p-1} \bar{\boldsymbol{s}}(p-1,d',t') - \sum_{d',t'>(d,t)}^{p} \bar{\boldsymbol{s}}(p,d',t') \right) \\
&\quad + 12 k_{\text{rep}} \frac{\partial \boldsymbol{d}(p,d,t)}{\partial \theta(p,d,t)} \left(\sum_{d',t'>(d,t)}^{p-1} \bar{\boldsymbol{p}}(p-1,d',t') - \sum_{d',t'>(d,t)}^{p} \bar{\boldsymbol{p}}(p,d',t') \right)
\end{aligned}$$

$$\begin{aligned}
&= \kappa \left[\Delta\psi(p,d,t) - \Delta\psi(p,d,t+1)\right] \\
&\quad + \frac{\partial \boldsymbol{d}(p,d,t)}{\partial \theta(p,d,t)} \left(\sum_{d',t'>(d,t)}^{p-1} \left[k_{\text{lat}} \bar{\boldsymbol{s}}(p-1,d',t') + 12 k_{\text{rep}} \bar{\boldsymbol{p}}(p-1,d',t')\right] \right. \\
&\qquad \left. - \sum_{d',t'>(d,t)}^{p} \left[k_{\text{lat}} \bar{\boldsymbol{s}}(p,d',t') + 12 k_{\text{rep}} \bar{\boldsymbol{p}}(p,d',t')\right] \right)
\end{aligned} \tag{B.51}$$

$$\begin{aligned}
&= \kappa \left[\Delta\psi(p,d,t) - \Delta\psi(p,d,t+1)\right] \\
&\quad + \frac{\partial \boldsymbol{d}(p,d,t)}{\partial \theta(p,d,t)} \left(\sum_{d',t'>(d,t)}^{p-1} \bar{\boldsymbol{v}}(p-1,d',t') - \sum_{d',t'>(d,t)}^{p} \bar{\boldsymbol{v}}(p,d',t') \right).
\end{aligned} \tag{B.52}$$

When the gradient of the microtubule energy (B.1) is calculated in the simulation, the whole microtubule structure[1] is iterated, and each tubulin calculates the derivative of the microtubule energy with respect to its own polar angle $\theta(p,d,t)$. Simply calculating the gradient component (B.52) as is would result in a complexity of $\mathcal{O}(N^2)$ for the calculation of the gradient (with N being the number of tubulin monomers here) because of the two sums in (B.52) that consider all tubulin monomers starting with tubulin monomer (p,d,t) in the same protofilament and all tubulin monomers in the previous protofilament starting with the lateral neighbor of tubulin monomer (p,d,t). It is, however, possible to calculate all of these sums immediately before the actual gradient is calculated by only iterating over the microtubule once because the only influence the tubulin monomer (p,d,t) has on these sums is the starting point of the sum but *not* the function values that are summed (i.e., there is no explicit dependence of the summed terms on p, d, or t). In practice, to calculate these sums along each protofilament, an iteration over all tubulin monomers in the considered protofilament is started from the plus end. The value of the sum for tubulin monomer (p,d,t) is simply the sum of the summed up value for the tubulin monomer on top of it, tubulin monomer $(p,d,t+1)$, and the relevant value $\bar{\boldsymbol{v}}(p,d,t)$ for the current tubulin monomer (p,d,t). In summary, by intelligently calculating the gradient, it can be done in two iterations over the whole microtubule with a complexity of $\mathcal{O}(N)$ instead of a complexity of $\mathcal{O}(N^2)$.

---

[1] We only consider full minimizations here. Restricted minimizations work the same way except that the starting value of d for the iteration is generally greater than one.

C

Model Parameter Values

$\Delta G^{0*}_{\text{long}}/k_\text{B}\,T$	$\Delta G^{0}_{\text{lat}}/k_\text{B}\,T$	$k_{\text{att}}/\text{s}^{-1}$
−14.0	−0.127	282
−13.8	−0.143	256
−13.6	−0.161	235
−13.4	−0.181	216
−13.2	−0.204	198
−13.0	−0.231	183
−12.8	−0.260	170
−12.6	−0.294	159
−12.4	−0.332	150
−12.2	−0.374	143
−12.0	−0.42	136
−11.8	−0.47	130
−11.6	−0.53	128
−11.4	−0.60	128
−11.2	−0.67	129
−11.0	−0.75	133
−10.8	−0.83	139
−10.6	−0.92	150
−10.4	−1.02	165
−10.2	−1.11	185
−10.0	−1.22	215
−9.8	−1.33	255
−9.7	−1.38	281
−9.6	−1.44	311
−9.5	−1.49	345
−9.4	−1.55	389
−9.3	−1.60	413
−9.2	−1.66	495
−9.0	−1.77	647
−8.8	−1.89	871
−8.6	−2.01	1205
−8.4	−2.12	1736
−8.2	−2.23	2568
−8.0	−2.34	4119
−7.8	−2.454	7365
−7.6	−2.565	16 361

(a) $k_+ = 2\,\text{s}^{-1}\,\mu\text{M}^{-1}$

$\Delta G^{0*}_{\text{long}}/k_\text{B}\,T$	$\Delta G^{0}_{\text{lat}}/k_\text{B}\,T$	$k_{\text{att}}/\text{s}^{-1}$
−14.0	−0.105	270
−13.8	−0.119	248
−13.6	−0.136	221
−13.4	−0.155	201
−13.2	−0.177	182
−13.0	−0.202	165
−12.8	−0.230	151
−12.6	−0.262	139
−12.4	−0.30	129
−12.2	−0.34	121
−12.0	−0.39	115
−11.8	−0.44	109
−11.6	−0.50	105
−11.4	−0.56	102
−11.2	−0.64	102
−11.0	−0.72	103
−10.8	−0.80	105
−10.6	−0.89	110
−10.4	−0.99	118
−10.2	−1.09	130
−10.0	−1.19	145
−9.8	−1.30	167
−9.7	−1.36	181
−9.6	−1.41	196
−9.5	−1.47	214
−9.4	−1.53	234
−9.3	−1.58	258
−9.2	−1.64	286
−9.0	−1.76	355
−8.8	−1.88	447
−8.6	−1.99	571
−8.4	−2.11	736
−8.2	−2.22	964
−8.0	−2.33	1280
−7.8	−2.447	1713
−7.6	−2.555	2328
−7.4	−2.660	3202
−7.2	−2.764	4494
−7.0	−2.862	6398
−6.8	−2.960	9274
−6.6	−3.055	13 939

(b) $k_+ = 4\,\text{s}^{-1}\,\mu\text{M}^{-1}$

Table C.1: Model parameter values from growth-only simulations for our two values of k_+ as shown in Figure 4.2. The highlighted parameter sets in each table are the values resulting the most linear $v_{\text{gr}}(c_{\text{tub}})$ relation (see Table 4.1).

$\Delta G^{0*}_{\text{long}}/k_{\text{B}}\,T$	1	5	10	20	50	100	150	200	250	300	350	400	450	500	600	700	800	900	1000
−14.0	61	88	107	131	178	227	266	294	324	346	370	389	410	428	464	496	525	551	577
−13.8	62	90	109	133	180	232	268	298	325	349	371	394	413	433	467	498	529	556	581
−13.6	63	91	109	135	182	232	270	298	325	350	372	396	412	433	467	499	527	555	579
−13.4	64	92	111	137	183	232	270	300	327	351	375	394	413	433	469	500	529	556	582
−13.2	65	93	112	138	185	234	270	302	327	351	374	394	414	431	470	502	531	556	581
−13.0	66	93	112	138	185	234	270	299	327	349	372	393	412	431	466	499	526	557	580
−12.8	67	94	113	137	184	233	269	297	325	348	370	392	409	428	465	493	526	551	576
−12.6	67	94	113	138	183	231	268	295	322	347	367	387	407	425	461	492	520	545	572
−12.4	67	95	112	137	182	229	264	293	318	341	362	383	402	422	455	487	514	539	565
−12.2	67	93	111	136	179	226	262	288	314	337	358	378	396	414	450	480	505	533	557
−12.0	67	93	110	135	178	224	258	285	310	332	353	374	390	409	446	474	500	524	550
−11.8	67	92	110	134	176	221	256	283	306	329	349	368	389	406	439	468	495	519	544
−11.6	66	90	108	130	173	216	249	276	300	320	340	360	380	395	429	457	483	507	530
−11.4	64	88	105	128	168	211	242	268	292	312	333	351	369	386	418	446	472	495	515
−11.2	62	86	102	124	163	205	235	260	285	305	325	343	361	377	408	434	459	481	501
−11.0	61	83	99	120	158	199	228	253	276	296	315	332	350	367	395	421	447	465	488
−10.8	59	80	96	116	154	193	220	246	267	288	306	323	340	356	383	408	431	449	474
−10.6	56	77	92	112	148	186	211	235	257	276	295	312	328	343	370	395	415	436	457
−10.4	54	74	89	107	142	178	204	227	247	266	284	301	315	330	355	380	399	419	437
−10.2	51	71	85	103	136	171	196	218	237	254	273	290	303	317	342	363	383	403	418
−10.0	49	67	80	98	130	163	187	208	227	244	262	277	291	303	326	346	368	384	399
−9.8	46	64	77	94	124	155	179	199	217	235	251	265	278	291	312	332	352	364	381
−9.7	45	63	75	91	121	151	175	195	212	230	246	259	271	284	304	324	342	356	373
−9.6	44	61	73	89	118	148	170	191	208	225	240	253	266	278	297	317	333	349	366
−9.5	42	59	72	87	115	144	166	186	203	221	234	248	260	271	291	310	325	341	358
−9.4	41	58	70	85	113	141	163	182	199	216	230	242	254	264	285	303	317	334	349
−9.3	41	57	70	84	111	139	161	180	197	213	227	240	251	262	282	298	313	330	346
−9.2	39	55	67	82	108	135	156	175	191	208	220	233	242	253	273	289	303	320	335
−9.0	37	53	64	78	103	129	150	168	184	199	211	222	232	242	259	276	292	307	322
−8.8	36	51	63	75	100	125	145	163	178	191	204	214	224	234	250	265	281	296	310
−8.6	35	50	61	73	97	121	140	158	173	186	197	207	216	226	240	257	272	286	300
−8.4	34	48	59	71	94	118	136	153	168	180	191	200	210	218	232	249	263	276	290
−8.2	33	47	58	70	91	114	132	149	163	175	185	194	203	211	226	242	255	268	280
−8.0	32	46	58	68	90	112	130	146	158	170	181	190	198	205	221	235	248	261	272
−7.8	31	46	58	67	89	110	128	143	155	167	177	185	193	200	216	230	242	255	267
−7.6	31	45	55	66	87	108	125	141	153	164	173	182	189	196	212	226	237	250	263

Table C.2: κ values (in units of $k_{\text{B}}\,T/\text{rad}^2$) for different values of $\Delta G^{0*}_{\text{long}}$, k_{lat} (which are given in the column headings in units of $k_{\text{B}}\,T/\text{nm}^2$), and $k_+ = 2\,\text{s}^{-1}\,\mu\text{M}^{-1}$ as shown in Figure 4.5(a). The highlighted parameter sets use the best growth parameter set (see Table 4.1).

$\Delta G^{0*}_{\text{long}}/k_{\text{B}}\,T$	1	5	10	20	50	100	150	200	250	300	350	400	450	500	600	700	800	900	1000
−14.0	67	96	117	144	193	248	288	321	352	375	399	421	446	464	500	535	567	597	624
−13.8	68	97	117	144	195	248	288	321	351	372	400	422	442	459	498	531	567	594	619
−13.6	70	100	120	148	199	253	292	325	353	379	403	426	446	465	502	540	572	599	630
−13.4	71	102	122	148	199	252	293	327	353	380	404	425	447	466	503	538	570	599	625
−13.2	73	102	123	150	202	254	295	325	354	377	405	425	446	466	500	539	568	598	628
−13.0	74	104	124	151	201	255	295	325	356	379	404	424	446	467	503	537	568	602	623
−12.8	74	104	124	152	202	256	294	325	356	378	403	423	444	462	498	535	568	595	622
−12.6	75	105	124	152	202	254	290	324	351	374	398	419	442	459	495	533	562	591	620
−12.4	75	105	124	150	200	251	289	319	346	370	396	413	434	454	488	524	553	583	610
−12.2	75	104	123	150	198	249	286	314	341	364	389	409	428	447	480	518	548	577	601
−12.0	75	102	121	147	195	242	280	307	333	357	380	399	418	437	472	507	536	563	590
−11.8	74	101	120	146	192	239	275	303	330	352	374	393	413	432	469	501	530	556	582
−11.6	73	100	118	143	188	234	270	296	322	344	365	387	405	422	459	489	518	543	568
−11.4	72	98	116	141	185	230	265	291	314	338	360	379	397	413	451	481	508	533	558
−11.2	70	95	112	137	179	224	256	280	305	328	348	367	386	402	435	465	492	515	540
−11.0	68	92	109	133	173	217	247	274	296	317	338	356	375	392	424	451	478	503	523
−10.8	66	90	106	129	169	210	240	266	289	309	328	348	365	382	413	439	465	487	505
−10.6	64	86	103	124	162	203	231	256	278	299	318	336	353	372	399	425	450	467	488
−10.4	61	83	99	120	156	196	222	246	267	287	307	324	340	357	385	409	431	449	471
−10.2	58	79	94	114	148	187	212	235	257	276	294	311	328	343	369	393	410	434	453
−10.0	55	75	89	108	143	178	203	226	245	264	282	300	314	328	354	378	395	416	433
−9.8	52	71	85	103	136	170	194	215	235	251	270	287	301	313	338	358	377	396	411
−9.7	51	69	83	101	132	165	189	210	229	247	265	280	294	306	330	348	368	387	401
−9.6	49	68	80	98	129	161	185	205	224	240	258	273	287	299	322	340	361	377	392
−9.5	48	66	79	96	126	158	181	201	219	236	253	268	280	292	312	333	353	366	384
−9.4	47	64	76	94	123	154	177	196	214	231	248	261	275	287	305	326	344	359	376
−9.3	45	62	75	91	120	149	172	192	209	227	242	255	268	280	299	318	335	350	368
−9.2	44	61	74	89	117	146	168	188	205	222	237	250	262	273	291	311	327	342	359
−9.0	42	58	70	85	112	139	161	179	197	214	226	239	250	259	279	296	311	328	344
−8.8	39	56	67	81	108	134	155	173	190	205	218	229	239	249	267	284	301	317	331
−8.6	38	53	65	78	103	128	148	166	183	197	209	221	228	238	256	271	289	303	319
−8.4	36	51	63	76	100	124	144	161	177	190	202	212	220	231	247	263	279	293	307
−8.2	35	49	61	73	97	120	139	157	172	184	196	204	214	223	239	255	270	283	296
−8.0	33	48	59	71	94	116	135	152	167	179	189	198	207	216	231	248	261	274	288
−7.8	33	47	57	70	92	114	132	149	163	175	185	193	202	210	226	242	254	268	278
−7.6	32	46	56	68	90	112	129	146	159	170	180	188	196	205	220	235	247	259	272
−7.4	31	45	55	67	88	109	127	143	156	166	176	185	192	199	215	229	242	253	267
−7.2	30	44	54	67	86	108	125	140	153	164	173	181	188	194	212	224	236	249	262
−7.0	29	43	53	65	85	106	123	138	150	160	169	178	183	191	208	218	231	244	260
−6.8	29	43	52	64	84	105	121	136	148	158	167	175	179	187	205	215	228	242	256
−6.6	28	43	51	63	83	103	119	134	146	155	164	172	176	186	201	211	223	237	254

Table C.3: κ values (in units of $k_{\text{B}}\,T/\text{rad}^2$) for different values of $\Delta G^{0*}_{\text{long}}$, k_{lat} (which are given in the column headings in units of $k_{\text{B}}\,T/\text{nm}^2$), and $k_+ = 4\,\text{s}^{-1}\,\mu\text{M}^{-1}$ in Figure 4.5(b). The highlighted parameter sets use the best growth parameter set (see Table 4.1).

$\Delta G^{0*}_{\mathrm{long}}/k_{\mathrm{B}}T$	$a_{\mathrm{rup}}/\sqrt{k_{\mathrm{B}}T}$	$b_{\mathrm{rup}}/(k_{\mathrm{B}}T/\mathrm{nm})$
−14.0	1.24	−0.25
−13.0	1.36	−0.13
−12.0	1.40	0.08
−11.0	1.36	0.10
−10.0	1.22	0.17
−9.0	1.07	0.30
−8.0	1.05	0.21

(a) $k_+ = 2\,\mathrm{s}^{-1}\,\mu\mathrm{M}^{-1}$

$\Delta G^{0*}_{\mathrm{long}}/k_{\mathrm{B}}T$	$a_{\mathrm{rup}}/\sqrt{k_{\mathrm{B}}T}$	$b_{\mathrm{rup}}/(k_{\mathrm{B}}T/\mathrm{nm})$
−14.0	1.32	−0.34
−13.0	1.46	−0.19
−12.0	1.52	−0.15
−11.0	1.49	−0.13
−10.0	1.34	−0.01
−9.0	1.17	0.35
−8.0	1.09	0.19

(b) $k_+ = 4\,\mathrm{s}^{-1}\,\mu\mathrm{M}^{-1}$

Table C.4: Values of the parameters a_{rup} and b_{rup} from (4.12) of the fits shown in Figure 4.6(a) and Figure 4.6(b).

Additional Microtubule Dynamics Figures and Tables

D

In this appendix, we present microtubule trajectories and figures and data tables for sets of mechanical parameters in addition to the standard set in Table 4.2.

D.1 Microtubule Trajectories

Some of the simulations whose trajectories are shown in this section, in particular those with higher free GTP-tubulin dimer concentrations c_{tub} and/or smaller hydrolysis rates k_{h}, were aborted due to runtime restrictions and thus did not reach $t_{\mathrm{sim}} = 10\,\mathrm{min}$.

While the results in Figure D.1, Figure D.2, and Figure D.3 are qualitatively similar to the results in Table 4.2, the trajectories for the extremely high $k_{\mathrm{lat}} = 20\,000\,k_{\mathrm{B}}\,T/\mathrm{nm}^2$ are different in that they are “rougher”, i.e., there is a greater number of “micro-dips” and that for $k_{\mathrm{h}} = 0.5\,\mathrm{s}^{-1}$ and high values of c_{tub}, the microtubules are still growing, but tend to slow down their growth.

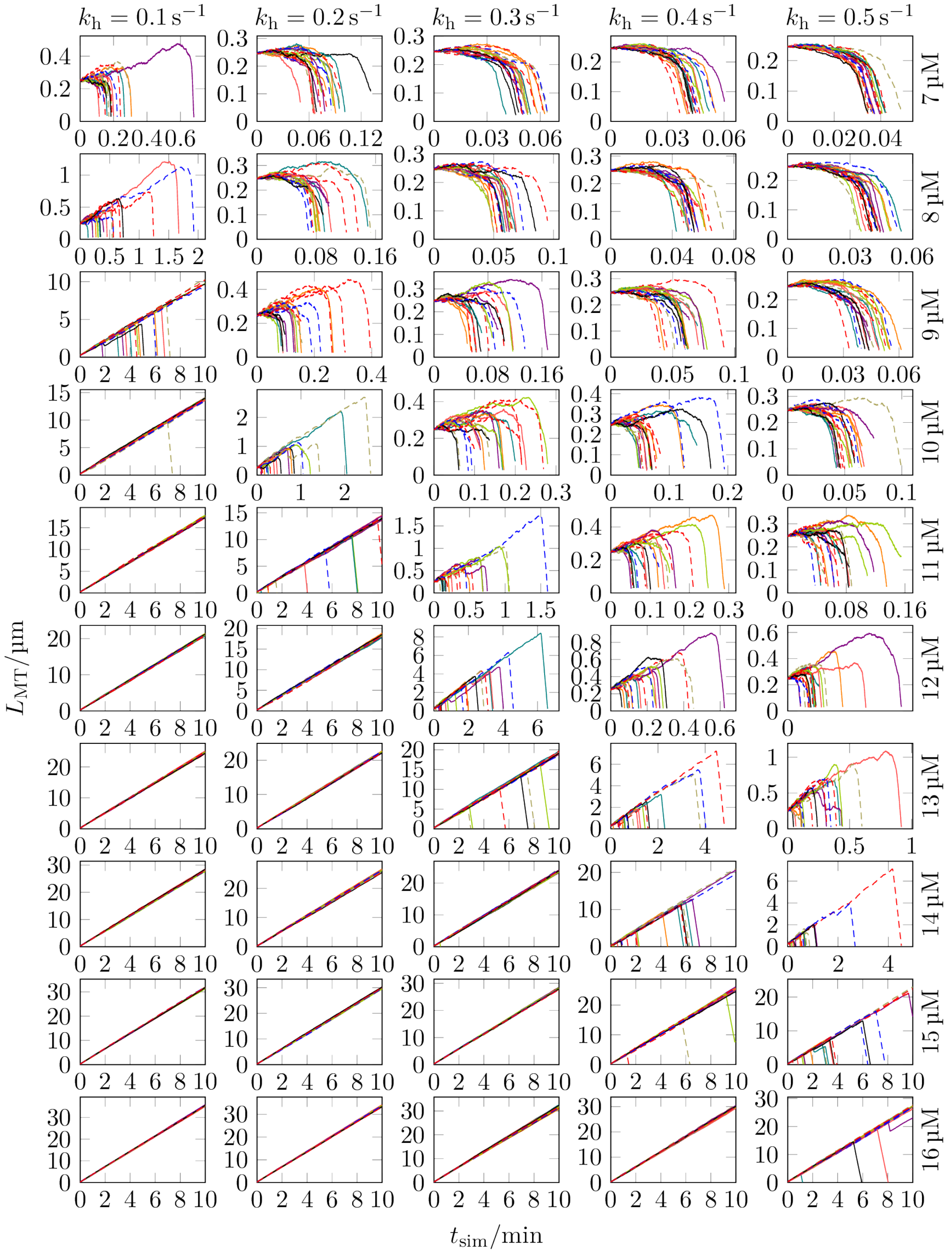

Figure D.1: Microtubule growth trajectories of 20 different simulations for each of the considered values of the free GTP-tubulin dimer concentration c_tub and the hydrolysis rate k_h with $k_+ = 4\,\mathrm{s}^{-1}\,\mathrm{\mu M}^{-1}$, $\Delta G^{0*}_\mathrm{long} = -9.3\,k_\mathrm{B}\,T$, and $k_\mathrm{lat} = 1\,k_\mathrm{B}\,T/\mathrm{nm}^2$.

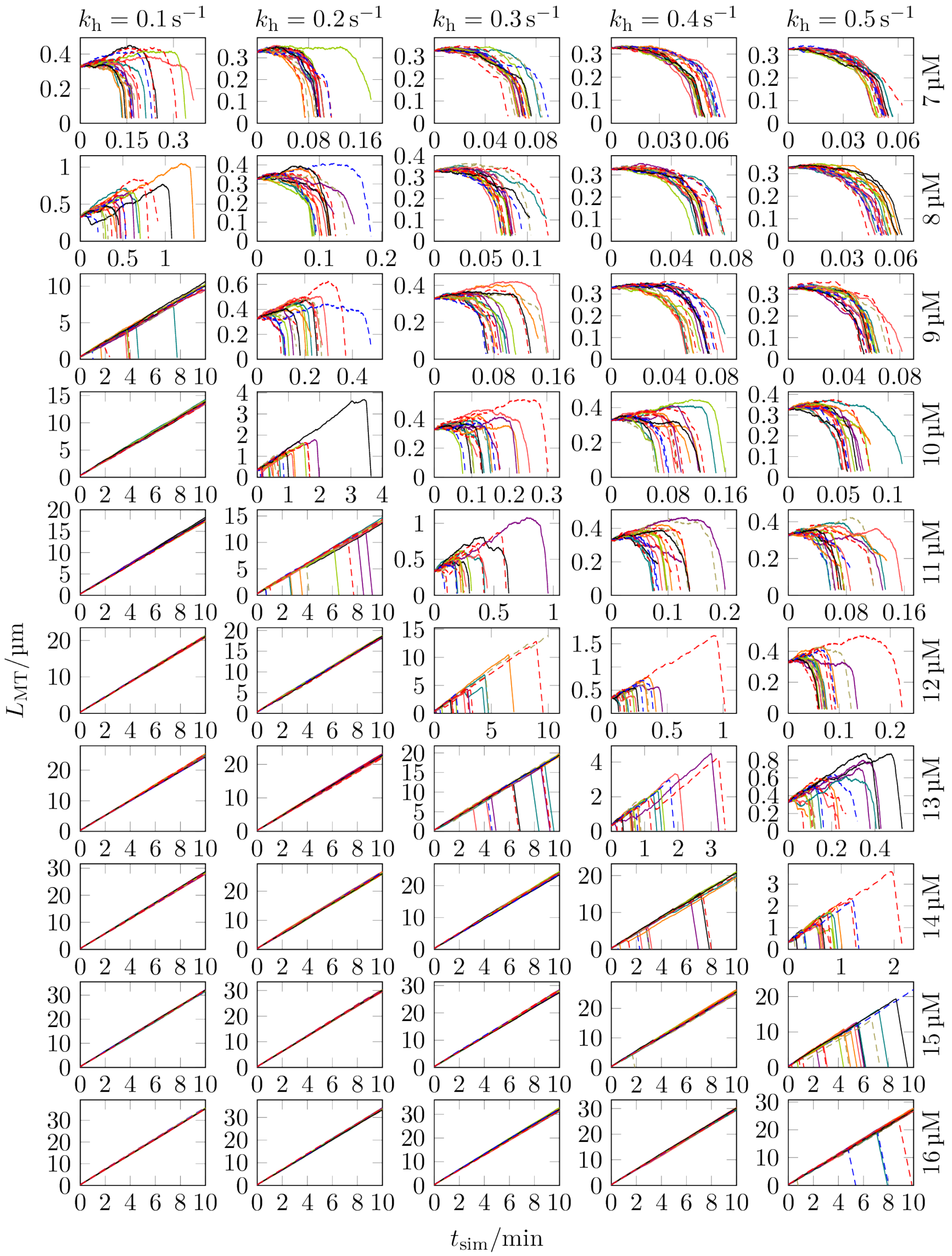

Figure D.2: Microtubule growth trajectories of 20 different simulations for each of the considered values of the free GTP-tubulin dimer concentration c_tub and the hydrolysis rate k_h with $k_+ = 4\,\mathrm{s}^{-1}\,\mathrm{\mu M}^{-1}$, $\Delta G^{0*}_\mathrm{long} = -9.3\,k_\mathrm{B}\,T$, $k_\mathrm{lat} = 1\,k_\mathrm{B}\,T/\mathrm{nm}^2$ and an initial cap length of $N_\mathrm{GTP} = 20$ per protofilament.

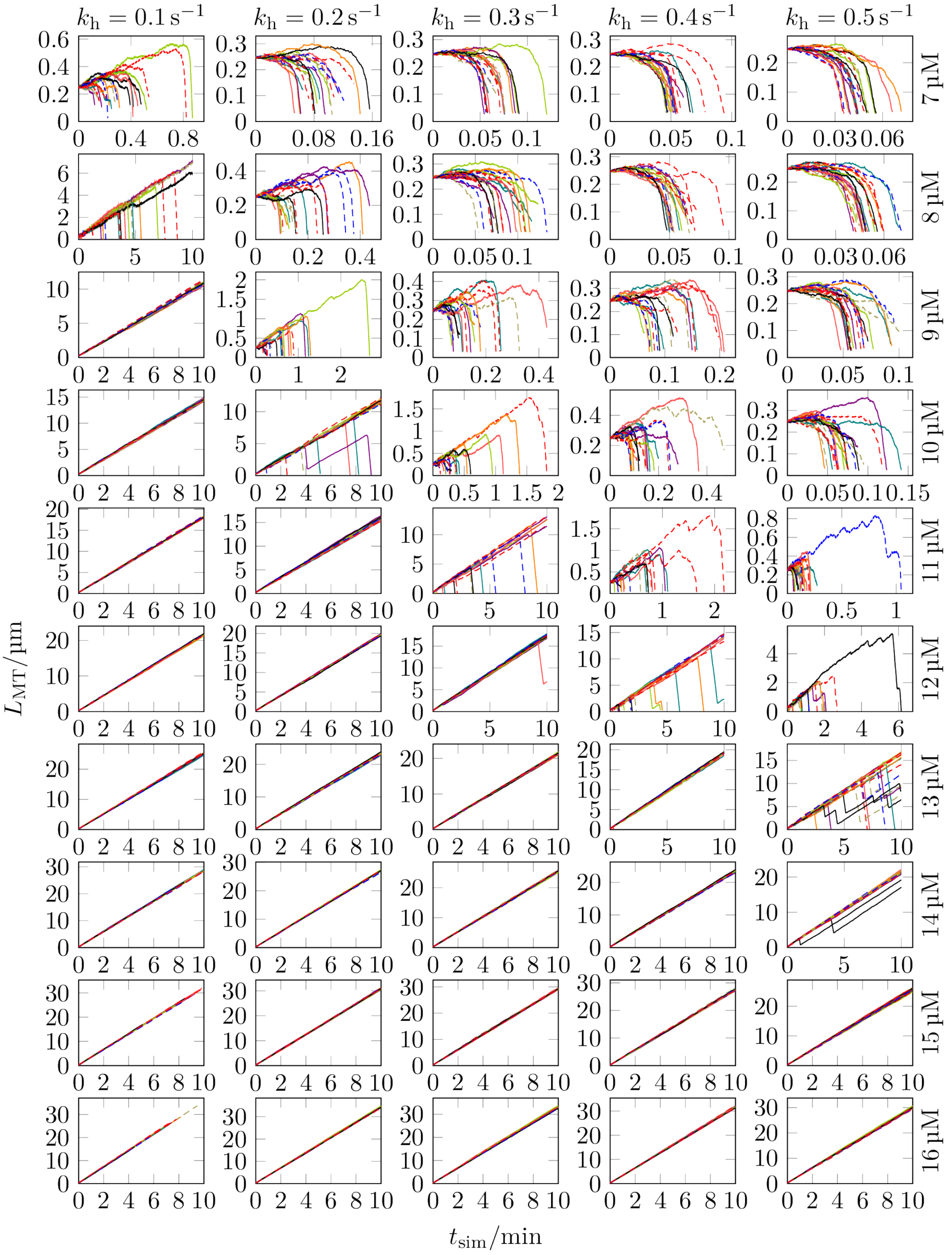

Figure D.3: Microtubule growth trajectories of 20 different simulations for each of the considered values of the free GTP-tubulin dimer concentration c_{tub} and the hydrolysis rate k_h with $k_+ = 4\,\mathrm{s}^{-1}\,\mathrm{\mu M}^{-1}$, $\Delta G^{0*}_{\mathrm{long}} = -9.3\,k_B T$, and $k_{\mathrm{lat}} = 10\,k_B T/\mathrm{nm}^2$.

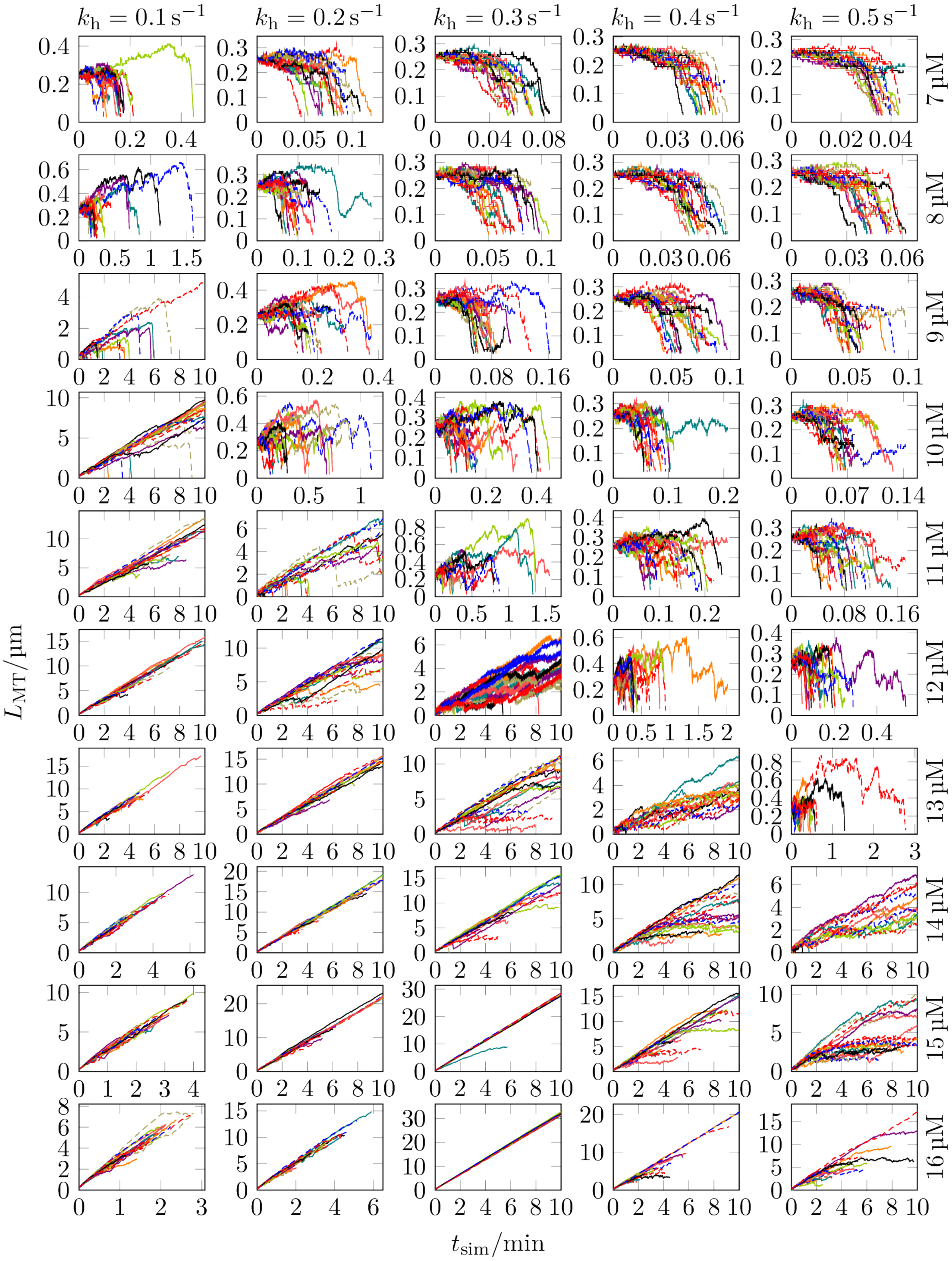

Figure D.4: Microtubule growth trajectories of 20 different simulations for each of the considered values of the free GTP-tubulin dimer concentration c_{tub} and the hydrolysis rate k_{h} with $k_+ = 4\,\text{s}^{-1}\,\mu\text{M}^{-1}$, $\Delta G^{0*}_{\text{long}} = -9.3\,k_{\text{B}}\,T$, and $k_{\text{lat}} = 20\,000\,k_{\text{B}}\,T/\text{nm}^2$.

D.2 Catastrophe and Rescue Rate Values

k_{h} \ c_{tub}	$0.1\,\mathrm{s}^{-1}$	$0.2\,\mathrm{s}^{-1}$	$0.3\,\mathrm{s}^{-1}$	$0.4\,\mathrm{s}^{-1}$	$0.5\,\mathrm{s}^{-1}$
$7\,\mu\mathrm{M}$	—	—	—	—	—
$8\,\mu\mathrm{M}$	$0.89\,\mathrm{min}^{-1}$	—	—	—	—
$9\,\mu\mathrm{M}$	$0.11\,\mathrm{min}^{-1}$	—	—	—	—
$10\,\mu\mathrm{M}$	~ 0	$1.14\,\mathrm{min}^{-1}$	—	—	—
$11\,\mu\mathrm{M}$	~ 0	$0.06\,\mathrm{min}^{-1}$	$1.38\,\mathrm{min}^{-1}$	—	$(1.25\,\mathrm{min}^{-1})$
$12\,\mu\mathrm{M}$	~ 0	~ 0	$0.46\,\mathrm{min}^{-1}$	$2.67\,\mathrm{min}^{-1}$	$(3.50\,\mathrm{min}^{-1})$
$13\,\mu\mathrm{M}$	~ 0	~ 0	$0.04\,\mathrm{min}^{-1}$	$0.75\,\mathrm{min}^{-1}$	$2.67\,\mathrm{min}^{-1}$
$14\,\mu\mathrm{M}$	~ 0	~ 0	~ 0	$0.22\,\mathrm{min}^{-1}$	$1.17\,\mathrm{min}^{-1}$
$15\,\mu\mathrm{M}$	~ 0	~ 0	~ 0	$0.02\,\mathrm{min}^{-1}$	$0.21\,\mathrm{min}^{-1}$
$16\,\mu\mathrm{M}$	~ 0	~ 0	~ 0	~ 0	$0.02\,\mathrm{min}^{-1}$

(a) Catastrophe rates ω_{cat} for different free GTP-tubulin dimer concentrations c_{tub} and different hydrolysis rates k_{h}. For parameter combinations with "—" as catastrophe rate, no proper growth phase was observed, so no catastrophe rates could be calculated. "~ 0" is used to denote cases in which microtubules grew during the whole simulation without any catastrophe resulting in catastrophe rates close to zero (at least $\omega_{\mathrm{cat}} \ll 0.01\,\mathrm{min}^{-1}$). For values in parentheses, only one or two catastrophe happened.

k_{h} \ c_{tub}	$0.1\,\mathrm{s}^{-1}$	$0.2\,\mathrm{s}^{-1}$	$0.3\,\mathrm{s}^{-1}$	$0.4\,\mathrm{s}^{-1}$	$0.5\,\mathrm{s}^{-1}$
$7\,\mu\mathrm{M}$	—	—	—	—	—
$8\,\mu\mathrm{M}$	—	—	—	—	—
$9\,\mu\mathrm{M}$	$(0.27\,\mathrm{min}^{-1})$	—	—	—	—
$10\,\mu\mathrm{M}$	—	$(0.64\,\mathrm{min}^{-1})$	—	—	—
$11\,\mu\mathrm{M}$	—	—	—	—	—
$12\,\mu\mathrm{M}$	—	—	—	—	—
$13\,\mu\mathrm{M}$	—	—	—	—	—
$14\,\mu\mathrm{M}$	—	—	—	—	$(0.52\,\mathrm{min}^{-1})$
$15\,\mu\mathrm{M}$	—	—	—	—	$(0.17\,\mathrm{min}^{-1})$
$16\,\mu\mathrm{M}$	—	—	—	—	$(0.52\,\mathrm{min}^{-1})$

(b) Rescue rates ω_{res} for different free GTP-tubulin dimer concentrations c_{tub} and different hydrolysis rates k_{h}. For parameter combinations with "—" as rescue rate, no rescues were observed and for values in parentheses only one or two rescues happened.

Table D.1: Catastrophe rates ω_{cat} and rescue rates ω_{res} for $k_{\mathrm{lat}} = 1\,k_{\mathrm{B}}\,T/\mathrm{nm}^2$, different free GTP-tubulin dimer concentrations c_{tub}, and different hydrolysis rates k_{h}.

k_h c_tub	$0.1\,\mathrm{s}^{-1}$	$0.2\,\mathrm{s}^{-1}$	$0.3\,\mathrm{s}^{-1}$	$0.4\,\mathrm{s}^{-1}$	$0.5\,\mathrm{s}^{-1}$
$7\,\mu\mathrm{M}$	$(1.43\,\mathrm{min}^{-1})$	—	—	—	—
$8\,\mu\mathrm{M}$	$0.17\,\mathrm{min}^{-1}$	—	—	—	—
$9\,\mu\mathrm{M}$	~ 0	$1.09\,\mathrm{min}^{-1}$	—	—	—
$10\,\mu\mathrm{M}$	~ 0	$0.05\,\mathrm{min}^{-1}$	$1.19\,\mathrm{min}^{-1}$	—	—
$11\,\mu\mathrm{M}$	~ 0	~ 0	$0.31\,\mathrm{min}^{-1}$	$1.21\,\mathrm{min}^{-1}$	$(1.25\,\mathrm{min}^{-1})$
$12\,\mu\mathrm{M}$	~ 0	~ 0	~ 0	$0.13\,\mathrm{min}^{-1}$	$0.79\,\mathrm{min}^{-1}$
$13\,\mu\mathrm{M}$	~ 0	~ 0	~ 0	~ 0	$0.12\,\mathrm{min}^{-1}$
$14\,\mu\mathrm{M}$	~ 0	~ 0	~ 0	~ 0	$(0.01\,\mathrm{min}^{-1})$
$15\,\mu\mathrm{M}$	~ 0	~ 0	~ 0	~ 0	~ 0
$16\,\mu\mathrm{M}$	~ 0	~ 0	~ 0	~ 0	~ 0

(a) Catastrophe rates ω_cat for different free GTP-tubulin dimer concentrations c_tub and different hydrolysis rates k_h. For parameter combinations with "—" as catastrophe rate, no proper growth phase was observed, so no catastrophe rates could be calculated. "~ 0" is used to denote cases in which microtubules grew during the whole simulation without any catastrophe resulting in catastrophe rates close to zero (at least $\omega_\mathrm{cat} \ll 0.01\,\mathrm{min}^{-1}$). For values in parentheses, only one or two catastrophe happened.

k_h c_tub	$0.1\,\mathrm{s}^{-1}$	$0.2\,\mathrm{s}^{-1}$	$0.3\,\mathrm{s}^{-1}$	$0.4\,\mathrm{s}^{-1}$	$0.5\,\mathrm{s}^{-1}$
$7\,\mu\mathrm{M}$	—	—	—	—	—
$8\,\mu\mathrm{M}$	—	—	—	—	—
$9\,\mu\mathrm{M}$	—	—	—	—	—
$10\,\mu\mathrm{M}$	—	$(0.36\,\mathrm{min}^{-1})$	—	—	—
$11\,\mu\mathrm{M}$	—	—	$(0.31\,\mathrm{min}^{-1})$	—	—
$12\,\mu\mathrm{M}$	—	—	$(1.84\,\mathrm{min}^{-1})$	$1.38\,\mathrm{min}^{-1}$	$(0.80\,\mathrm{min}^{-1})$
$13\,\mu\mathrm{M}$	—	—	—	—	$1.96\,\mathrm{min}^{-1}$
$14\,\mu\mathrm{M}$	—	—	—	—	$(4.78\,\mathrm{min}^{-1})$
$15\,\mu\mathrm{M}$	—	—	—	—	—
$16\,\mu\mathrm{M}$	—	—	—	—	—

(b) Rescue rates ω_res for different free GTP-tubulin dimer concentrations c_tub and different hydrolysis rates k_h. For parameter combinations with "—" as rescue rate, no rescues were observed and for values in parentheses only one or two rescues happened.

Table D.2: Catastrophe rates ω_cat and rescue rates ω_res for $k_\mathrm{lat} = 10\,k_\mathrm{B}\,T/\mathrm{nm}^2$, different free GTP-tubulin dimer concentrations c_tub, and different hydrolysis rates k_h.

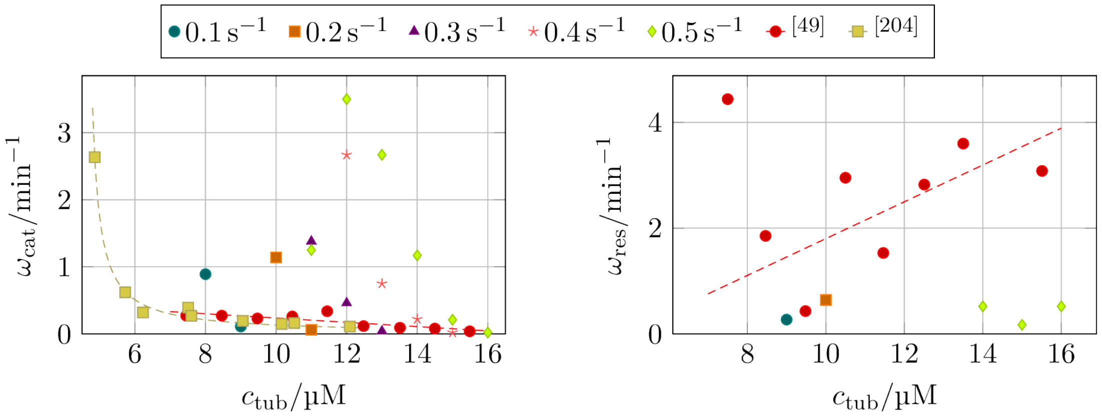

(a) Catastrophe rate ω_{cat} as a function of the free GTP-tubulin dimer concentration c_{tub} for $k_{\mathrm{lat}} = 1\,k_{\mathrm{B}}\,T/\mathrm{nm}^2$.

(b) Rescue rate ω_{res} as a function of the free GTP-tubulin dimer concentration c_{tub} for $k_{\mathrm{lat}} = 1\,k_{\mathrm{B}}\,T/\mathrm{nm}^2$.

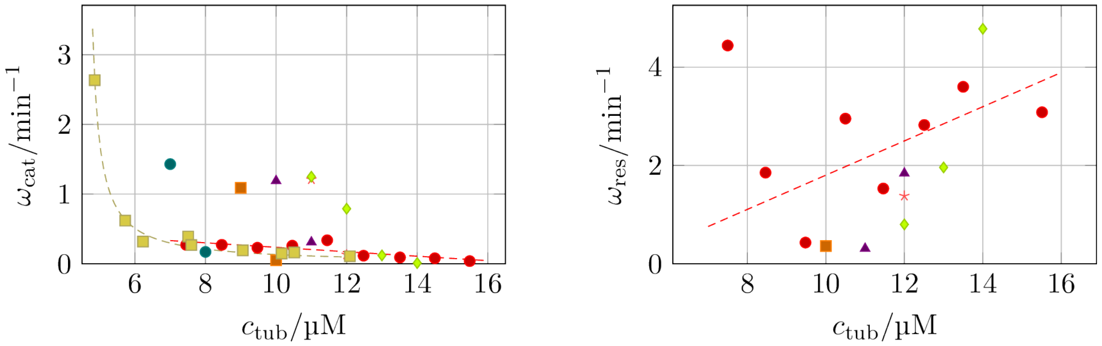

(c) Catastrophe rate ω_{cat} as a function of the free GTP-tubulin dimer concentration c_{tub} for $k_{\mathrm{lat}} = 10\,k_{\mathrm{B}}\,T/\mathrm{nm}^2$.

(d) Rescue rate ω_{res} as a function of the free GTP-tubulin dimer concentration c_{tub} for $k_{\mathrm{lat}} = 10\,k_{\mathrm{B}}\,T/\mathrm{nm}^2$.

Figure D.5: Comparison between our values for the catastrophe and rescue rates from Table D.1 and Table D.2 and the values measured by Walker et al.[49] and Janson et al.[204]

Additional Mechanical Hydrolysis Figures

E

All data presented in this chapter are for our standard set of parameters with $k_{\mathrm{lat}} = 10\,k_{\mathrm{B}}\,T/\mathrm{nm}^2$ and $\kappa = 75\,k_{\mathrm{B}}\,T/\mathrm{rad}^2$.

E.1 Hydrolysis Rates

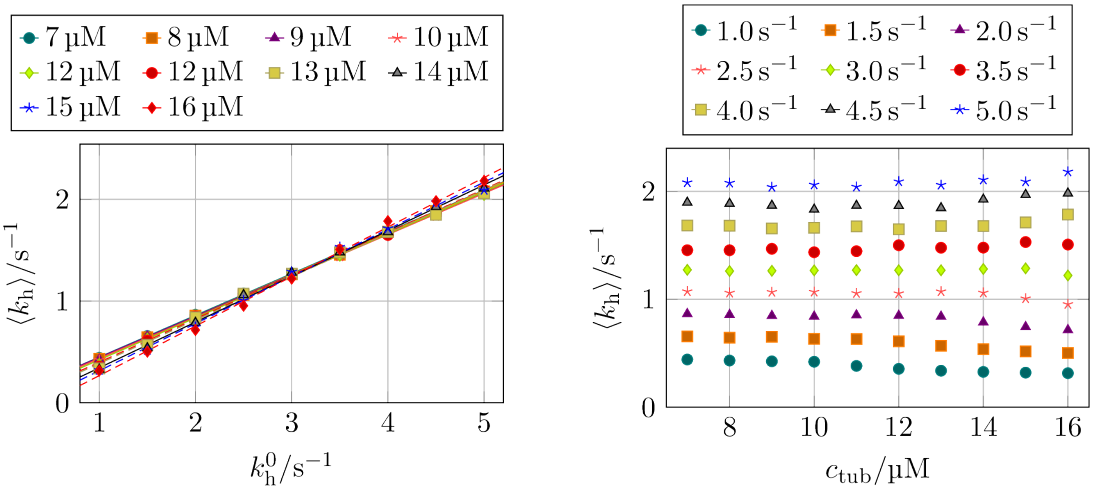

(a) Average hydrolysis rate $\langle k_{\mathrm{h}} \rangle$ as a function of the base hydrolysis rate k_{h}^0 for different free GTP-tubulin dimer concentrations c_{tub}.

(b) Average hydrolysis rate $\langle k_{\mathrm{h}} \rangle$ as a function of the free GTP-tubulin dimer concentration c_{tub} for different base hydrolysis rates k_{h}^0.

Figure E.1: Average hydrolysis rate $\langle k_{\mathrm{h}} \rangle$ calculated from the hydrolysis events executed in the relevant simulations.

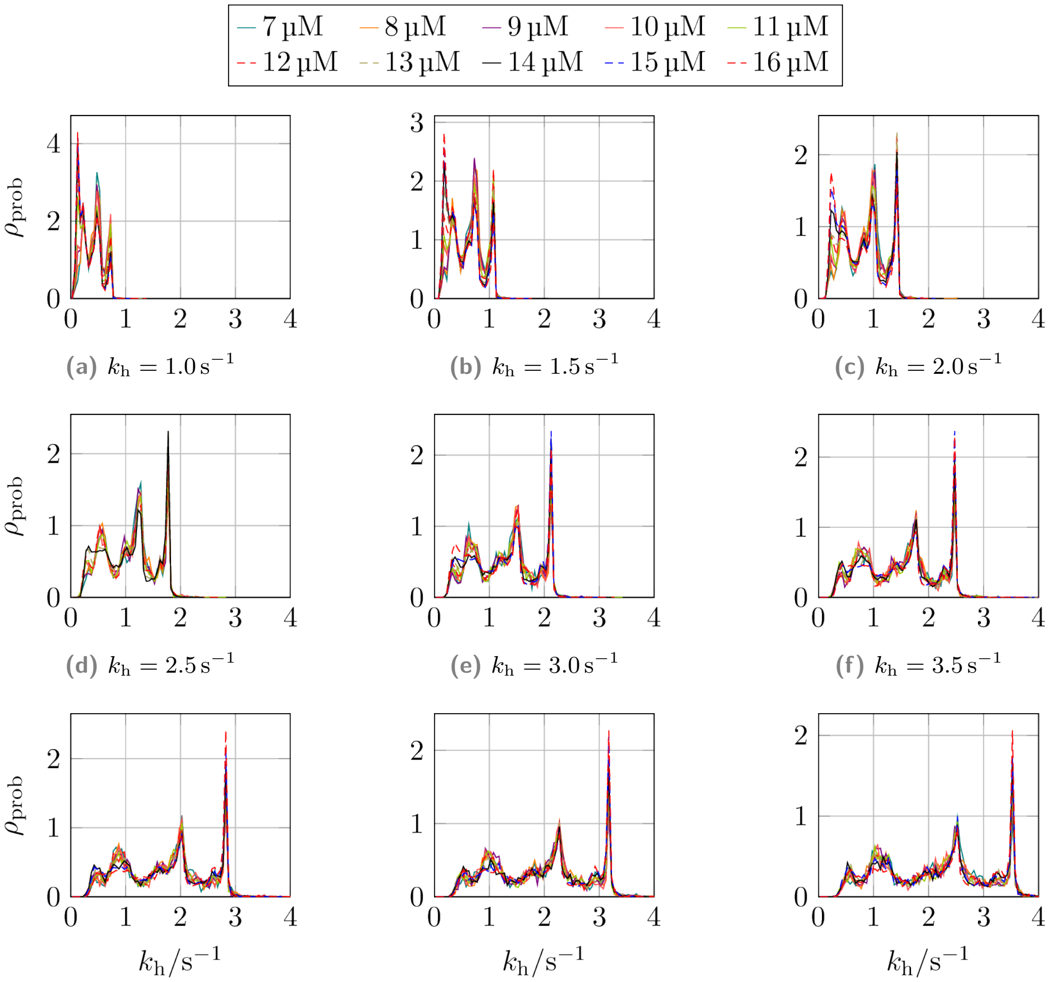

(a) $k_{\mathrm{h}} = 1.0\,\mathrm{s}^{-1}$ (b) $k_{\mathrm{h}} = 1.5\,\mathrm{s}^{-1}$ (c) $k_{\mathrm{h}} = 2.0\,\mathrm{s}^{-1}$

(d) $k_{\mathrm{h}} = 2.5\,\mathrm{s}^{-1}$ (e) $k_{\mathrm{h}} = 3.0\,\mathrm{s}^{-1}$ (f) $k_{\mathrm{h}} = 3.5\,\mathrm{s}^{-1}$

(g) $k_{\mathrm{h}} = 4.0\,\mathrm{s}^{-1}$ (h) $k_{\mathrm{h}} = 4.5\,\mathrm{s}^{-1}$ (i) $k_{\mathrm{h}} = 5.0\,\mathrm{s}^{-1}$

Figure E.2: Probability density ρ_{prob} of the actual hydrolysis rates k_{h} for different base hydrolysis rates k_{h}^{0} and free GTP-tubulin dimer concentrations c_{tub}. ρ_{prob} was generated as a histogram with a histogram bar width of $\Delta k_{\mathrm{h}} = 0.05\,\mathrm{s}^{-1}$. The cutoff $k_{\mathrm{h}}^{0} = 4\,\mathrm{s}^{-1}$ for the plots has been chosen as beyond $k_{\mathrm{h}}^{0} = 4\,\mathrm{s}^{-1}$, ρ_{prob} is negligible.

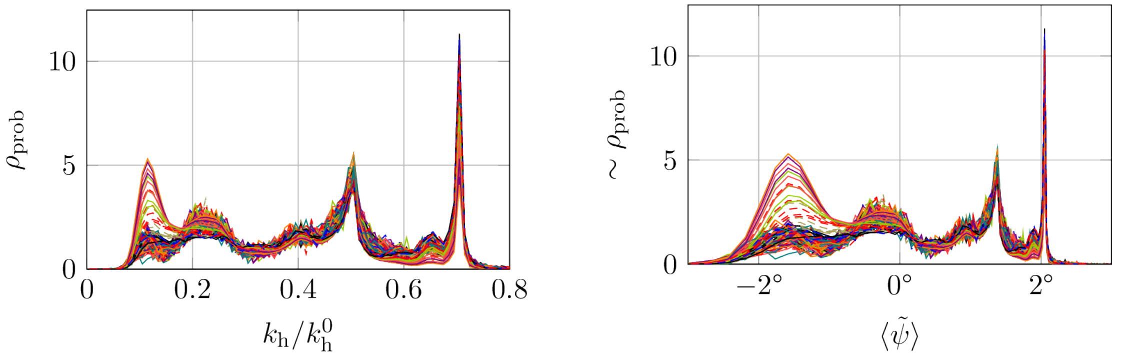

(a) Probability density ρ_{prob} of the actual hydrolysis rates k_{h} normalized by the base hydrolysis rate k_{h}^0 for different base hydrolysis rates k_{h}^0 and free GTP-tubulin dimer concentrations c_{tub}. ρ_{prob} was generated as a histogram with a histogram bar width of $\Delta(k_{\mathrm{h}}/k_{\mathrm{h}}^0) = 0.01$.

(b) Relative occurrence probability of the average bending angle $\langle\tilde{\psi}\rangle$ calculated via (6.6) using the k_{h} values from the left plot for the average bending angles on the x-axis, while keeping the y-data the same (and thus not making it probability *density* anymore).

Figure E.3: Further analysis of the hydrolysis rate distribution and the resulting bending angle distribution using the data in Figure E.2. The cutoffs on the x-axis for the plots have been chosen so that beyond it, ρ_{prob} is negligible. Due to the large amount of indistinguishable individual lines in the plots, no legend is given.

E.2 Microtubule Trajectories and Catastrophe and Rescue Rates

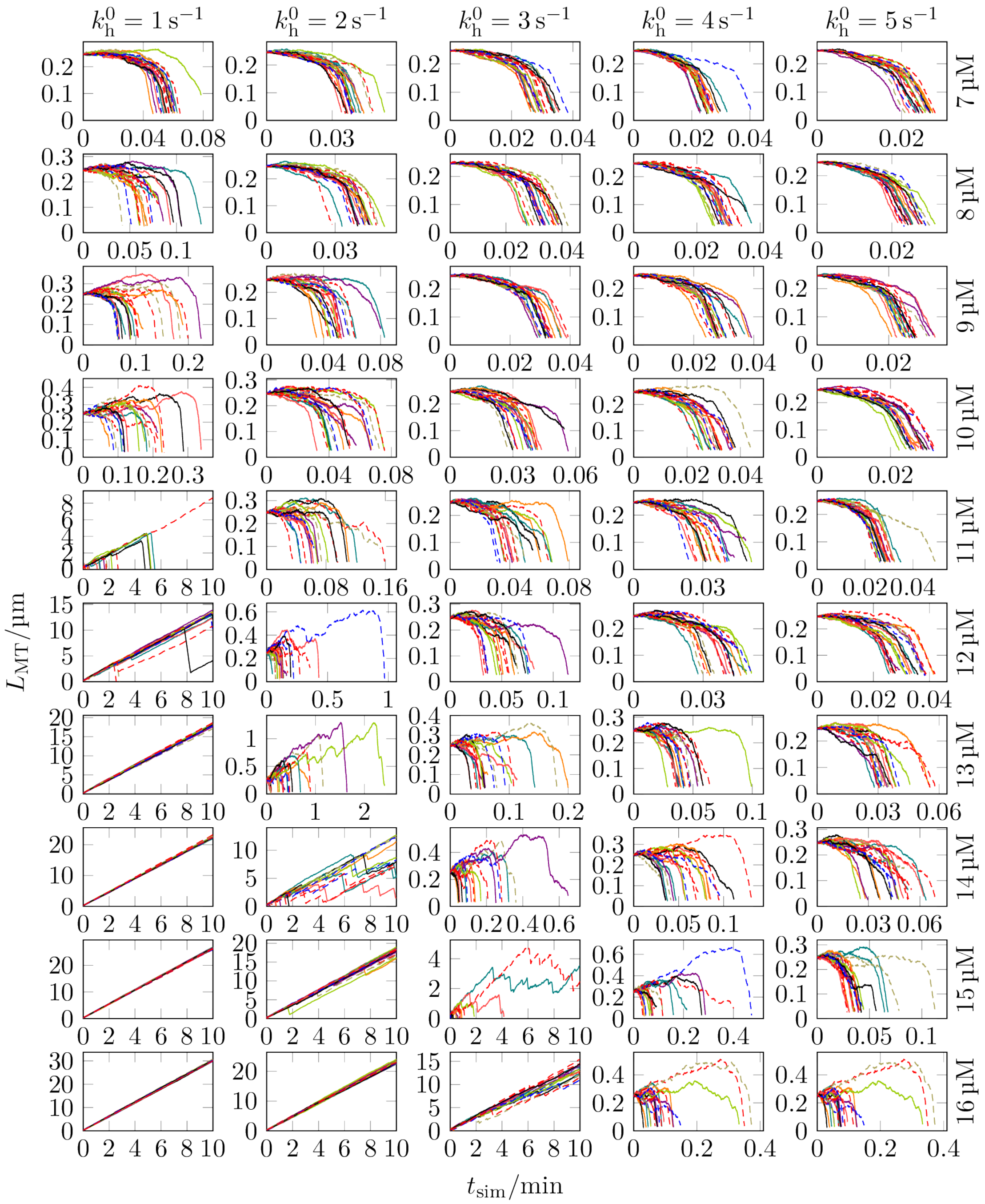

Figure E.4: Microtubule growth trajectories of 20 different simulations for each of the considered values of the free GTP-tubulin dimer concentration c_tub and the base hydrolysis rate k_h^0.

k_h^0 c_tub	$1\,\mathrm{s}^{-1}$	$2\,\mathrm{s}^{-1}$	$3\,\mathrm{s}^{-1}$	$4\,\mathrm{s}^{-1}$	$5\,\mathrm{s}^{-1}$
7 µM	—	—	—	—	—
8 µM	—	—	—	—	—
9 µM	—	—	—	—	—
10 µM	—	—	—	—	—
11 µM	$0.34\,\mathrm{min}^{-1}$	—	—	—	—
12 µM	$0.04\,\mathrm{min}^{-1}$	($0.27\,\mathrm{min}^{-1}$)	—	—	—
13 µM	~ 0	$0.80\,\mathrm{min}^{-1}$	—	—	—
14 µM	~ 0	$0.26\,\mathrm{min}^{-1}$	($0.34\,\mathrm{min}^{-1}$)	—	—
15 µM	~ 0	$0.03\,\mathrm{min}^{-1}$	$0.86\,\mathrm{min}^{-1}$	($0.39\,\mathrm{min}^{-1}$)	—
16 µM	~ 0	~ 0	$0.15\,\mathrm{min}^{-1}$	$0.52\,\mathrm{min}^{-1}$	—

(a) Catastrophe rates ω_cat for different free GTP-tubulin dimer concentrations c_tub and different base hydrolysis rates k_h^0. For parameter combinations with "—" as catastrophe rate, no proper growth phase was observed, so no catastrophe rates could be calculated. "~ 0" is used to denote cases in which microtubules grew during the whole simulation without any catastrophe resulting in catastrophe rates close to zero (at least $\omega_\mathrm{cat} \ll 0.01\,\mathrm{min}^{-1}$). For values in parentheses, only one or two catastrophe happened.

k_h^0 c_tub	$1\,\mathrm{s}^{-1}$	$2\,\mathrm{s}^{-1}$	$3\,\mathrm{s}^{-1}$	$4\,\mathrm{s}^{-1}$	$5\,\mathrm{s}^{-1}$
7 µM	—	—	—	—	—
8 µM	—	—	—	—	—
9 µM	—	—	—	—	—
10 µM	—	—	—	—	—
11 µM	—	—	—	—	—
12 µM	$2.20\,\mathrm{min}^{-1}$	—	—	—	—
13 µM	—	—	—	—	—
14 µM	—	$4.36\,\mathrm{min}^{-1}$	—	—	—
15 µM	—	$8.34\,\mathrm{min}^{-1}$	$2.17\,\mathrm{min}^{-1}$	—	—
16 µM	—	—	$7.68\,\mathrm{min}^{-1}$	$1.47\,\mathrm{min}^{-1}$	—

(b) Rescue rates ω_res for different free GTP-tubulin dimer concentrations c_tub and different base hydrolysis rates k_h^0. For parameter combinations with "—" as rescue rate, no rescues were observed and for values in parentheses only one or two rescues happened.

Table E.1: Catastrophe rates ω_cat and rescue rates ω_res for different free GTP-tubulin dimer concentrations c_tub and different base hydrolysis rates k_h^0.

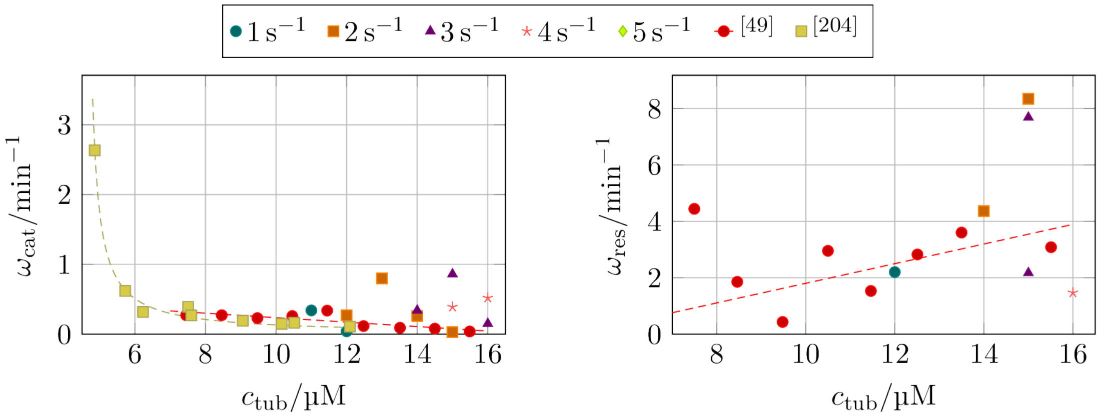

(a) Catastrophe rate ω_{cat} as a function of the free GTP-tubulin dimer concentration c_{tub}.

(b) Rescue rate ω_{res} as a function of the free GTP-tubulin dimer concentration c_{tub}.

Figure E.5: Comparison between our values for the catastrophe and rescue rates from Table E.1 and the values measured by Walker et al.[49] and Janson et al.[204]

GTP-Probability Distribution in One-Dimensional Model

F

Let us consider a one-dimensional microtubule model[1] in which GTP-tubulin dimers can attach with rate k_{on}, the terminal dimer can detach with rate k_{off}, and any GTP-tubulin dimer can hydrolyze with rate k_{h}. Tubulin dimers are indexed via their position i in the microtubule counted from the plus end with $i = 1$ being the terminal tubulin dimer at the plus end. A consequence of this choice of the starting point for the indices is that the index changes for all tubulin dimers whenever a tubulin dimer attaches or detaches. In the following discussion, we will only consider growing microtubules.

Let $p_{\text{GTP}}(i,t)$ be the probability of the tubulin dimer at position i and time t to be a GTP-tubulin dimer. As a consequence, $1 - p_{\text{GTP}}(i,t)$ is the probability of the tubulin dimer at position i and time t to be a GDP-tubulin dimer. The time evolution of $p_{\text{GTP}}(i,t)$ for $i > 1$ is given by[94]:

$$\begin{aligned}\partial_t p_{\text{GTP}}(i,t) = &- k_{\text{h}} p_{\text{GTP}}(i,t)\\ &+ k_{\text{on}}\left[1 - p_{\text{GTP}}(i,t)\right] p_{\text{GTP}}(i-1,t)\\ &- k_{\text{on}} p_{\text{GTP}}(i,t)\left[1 - p_{\text{GTP}}(i-1,t)\right]\\ &+ k_{\text{off}}\left[1 - p_{\text{GTP}}(i,t)\right] p_{\text{GTP}}(i+1,t)\\ &- k_{\text{off}} p_{\text{GTP}}(i,t)\left[1 - p_{\text{GTP}}(i+1,t)\right]. \end{aligned} \tag{F.1}$$

The origin of the different terms of (F.1) are described in Figure F.1. Equation (F.1) can be simplified to:

$$\begin{aligned}\partial_t p_{\text{GTP}}(i,t) = &- k_{\text{h}} p_{\text{GTP}}(i,t) + k_{\text{on}}\left[p_{\text{GTP}}(i-1,t) - p_{\text{GTP}}(i,t)\right]\\ &+ k_{\text{off}}\left[p_{\text{GTP}}(i+1,t) - p_{\text{GTP}}(i,t)\right]. \end{aligned} \tag{F.2}$$

For the terminal tubulin dimer at the plus end, we get the following boundary condition:

$$\begin{aligned}\partial_t p_{\text{GTP}}(1,t) = &- k_{\text{h}} p_{\text{GTP}}(1,t) + k_{\text{on}}\left[1 - p_{\text{GTP}}(1,t)\right]\\ &+ k_{\text{off}}\left[1 - p_{\text{GTP}}(1,t)\right] p_{\text{GTP}}(2,t) - k_{\text{off}} p_{\text{GTP}}(1,t)\left[1 - p_{\text{GTP}}(2)(t)\right] \qquad \text{(F.3)}\\ = &- k_{\text{h}} p_{\text{GTP}}(1,t) + k_{\text{on}}\left[1 - p_{\text{GTP}}(1,t)\right]\\ &+ k_{\text{off}}\left[p_{\text{GTP}}(2,t) - p_{\text{GTP}}(1,t)\right]. \qquad \text{(F.4)}\end{aligned}$$

In the steady state $\partial_t p_{\text{GTP}}(i,t) = 0$, $p_{\text{GTP}}(i,t)$ does not change with t, thus $p_{\text{GTP}}(i,t) = p_{\text{GTP}}(i)$ so that the master equation (F.2) simplify to:

$$0 = -k_{\text{h}} p_{\text{GTP}}(i) + k_{\text{on}}\left[p_{\text{GTP}}(i-1) - p_{\text{GTP}}(i)\right] + k_{\text{off}}\left[p_{\text{GTP}}(i+1) - p_{\text{GTP}}(i)\right] \tag{F.5}$$

resulting in the following recursion equation for $p_{\text{GTP}}(i)$:

$$p_{\text{GTP}}(i+1) = p_{\text{GTP}}(i) + \frac{k_{\text{h}}}{k_{\text{off}}} p_{\text{GTP}}(i) + \frac{k_{\text{on}}}{k_{\text{off}}}\left[p_{\text{GTP}}(i-1) - p_{\text{GTP}}(i)\right] \tag{F.6}$$

---

[1] An equivalent name would be “single protofilament microtubule model”.

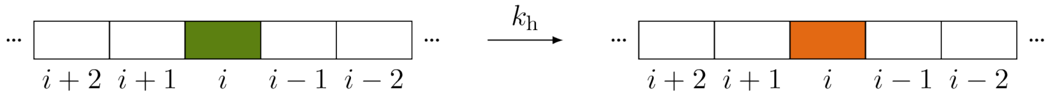

(a) Illustration of the first term describing the decrease of $p_\mathrm{GTP}(i,t)$ due to the hydrolysis of the GTP-tubulin dimer at position i.

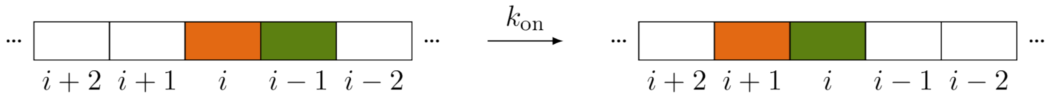

(b) Illustration of the second term describing the increase of $p_\mathrm{GTP}(i,t)$ due to the polymerization of a new GTP-tubulin dimer resulting in a shift of the tubulin dimers towards the minus end so that the GTP-tubulin dimer at position $i-1$ moves to position i, which was previously occupied by a GDP-tubulin dimer.

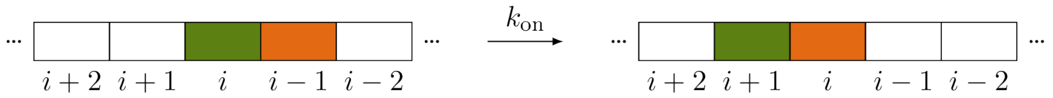

(c) Illustration of the third term describing the decrease of $p_\mathrm{GTP}(i,t)$ due to the polymerization of a new GTP-tubulin dimer resulting in a shift of the tubulin dimers towards the minus end so that the GDP-tubulin dimer at position $i-1$ moves to position i, which was previously occupied by a GTP-tubulin dimer.

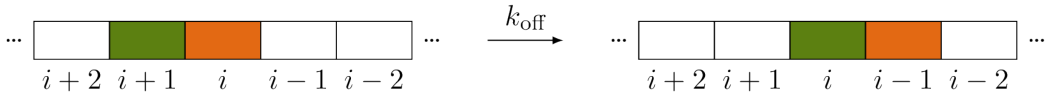

(d) Illustration of the fourth term describing the increase of $p_\mathrm{GTP}(i,t)$ due to the depolymerization of a tubulin dimer resulting in a shift of the tubulin dimers towards the plus end so that the GTP-tubulin dimer at position $i+1$ moves to position i, which was previously occupied by a GDP-tubulin dimer.

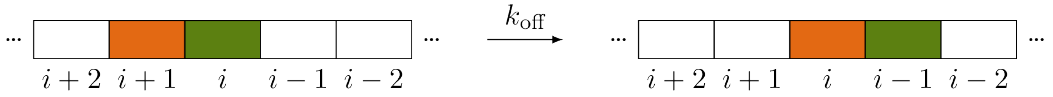

(e) Illustration of fifth term describing the decrease of $p_\mathrm{GTP}(i,t)$ due to the depolymerization of a tubulin dimer resulting in a shift of the tubulin dimers towards the plus end so that the GDP-tubulin dimer at position $i+1$ moves to position i, which was previously occupied by a GTP-tubulin dimer.

Figure F.1: Illustrations of the individual terms (line by line) of the master equation (F.1) for $p_\mathrm{GTP}(i,t)$. The microtubule's plus end position is on the right-hand side of the microtubules and their minus end on the left-hand side.

$$\begin{aligned} &= \frac{k_\mathrm{on}+k_\mathrm{off}+k_\mathrm{h}}{k_\mathrm{off}} p_\mathrm{GTP}(i) - \frac{k_\mathrm{on}}{k_\mathrm{off}} p_\mathrm{GTP}(i-1) && \text{(F.7)} \\ &\equiv \alpha p_\mathrm{GTP}(i) + \beta p_\mathrm{GTP}(i-1) && \text{(F.8)} \end{aligned}$$

with

$$\alpha = \frac{k_\mathrm{on}+k_\mathrm{off}+k_\mathrm{h}}{k_\mathrm{off}}, \tag{F.9}$$

$$\beta = -\frac{k_{\text{on}}}{k_{\text{off}}}. \tag{F.10}$$

In the steady state, the boundary condition (F.4) simplifies to:

$$\begin{aligned}
0 &= -k_{\text{h}} p_{\text{GTP}}(1) + k_{\text{on}}(1 - p_{\text{GTP}}(1)) + k_{\text{off}} \left[p_{\text{GTP}}(2) - p_{\text{GTP}}(1) \right] && \text{(F.11)} \\
p_{\text{GTP}}(2) &= p_{\text{GTP}}(1) + \frac{k_{\text{h}}}{k_{\text{off}}} p_{\text{GTP}}(1) + \frac{k_{\text{on}}}{k_{\text{off}}} \left[1 - p_{\text{GTP}}(1) \right] && \text{(F.12)} \\
&= \frac{k_{\text{on}} + k_{\text{off}} + k_{\text{h}}}{k_{\text{off}}} p_{\text{GTP}}(1) - \frac{k_{\text{on}}}{k_{\text{off}}} && \text{(F.13)} \\
&= \alpha p_{\text{GTP}}(1) + \beta. && \text{(F.14)}
\end{aligned}$$

Equation (F.8) is a homogeneous linear recurrence equation for which an ansatz

$$p_{\text{GTP}}(i) = q^i \tag{F.15}$$

with $q \in [0, 1]$ (as $p_{\text{GTP}}(i)$ is a probability) can be used to solve it:

$$\begin{aligned}
q^{i+1} &= \alpha q^i + \beta q^{i-1} && \text{(F.16)} \\
q^2 - \alpha q &= \beta && \text{(F.17)} \\
q_\pm &= \frac{1}{2} \left(\alpha \pm \sqrt{\alpha^2 + 4\beta} \right) && \text{(F.18)} \\
&= \frac{1}{2} \left(\frac{k_{\text{on}} + k_{\text{off}} + k_{\text{h}}}{k_{\text{off}}} \pm \sqrt{\left(\frac{k_{\text{on}} + k_{\text{off}} + k_{\text{h}}}{k_{\text{off}}} \right)^2 - 4 \frac{k_{\text{on}}}{k_{\text{off}}}} \right) && \text{(F.19)} \\
&= \frac{k_{\text{on}} + k_{\text{off}} + k_{\text{h}}}{2k_{\text{off}}} \left(1 \pm \sqrt{1 - \frac{4k_{\text{on}}k_{\text{off}}}{(k_{\text{on}} + k_{\text{off}} + k_{\text{h}})^2}} \right). && \text{(F.20)}
\end{aligned}$$

To simplify the right-hand side of (F.20) further to check which solution satisfies $q_\pm \leq 1$, we have to show that we can use Taylor expansion of the square root:

$$\begin{aligned}
(k_{\text{on}} + k_{\text{off}} + k_{\text{h}})^2 &> 4k_{\text{on}}k_{\text{off}} && \text{(F.21)} \\
k_{\text{on}}^2 + k_{\text{off}}^2 + k_{\text{h}}^2 + 2k_{\text{on}}k_{\text{off}} + 2k_{\text{on}}k_{\text{h}} + 2k_{\text{off}}k_{\text{h}} &> 4k_{\text{on}}k_{\text{off}} && \text{(F.22)} \\
k_{\text{on}}^2 - 2k_{\text{on}}k_{\text{off}} + k_{\text{off}}^2 + k_{\text{h}}^2 + 2k_{\text{on}}k_{\text{h}} + 2k_{\text{off}}k_{\text{h}} &> 0 && \text{(F.23)} \\
(k_{\text{on}} - k_{\text{off}})^2 + k_{\text{h}}^2 + 2k_{\text{h}}(k_{\text{on}} + k_{\text{off}}) &> 0. && \text{(F.24)}
\end{aligned}$$

As all rates are positive and we only consider growing microtubules, thus $k_{\text{on}} > k_{\text{off}}$, the inequality is satisfied. With that shown, the right-hand side can be approximated as

$$q_\pm \simeq \frac{k_{\text{on}} + k_{\text{off}} + k_{\text{h}}}{2k_{\text{off}}} \left(1 \pm 1 \mp \frac{2k_{\text{on}}k_{\text{off}}}{(k_{\text{on}} + k_{\text{off}} + k_{\text{h}})^2} \right) \tag{F.25}$$

and the two solutions are

$$q_+ \simeq \frac{k_{\text{on}} + k_{\text{off}} + k_{\text{h}}}{2k_{\text{off}}} \left(2 - \frac{2k_{\text{on}}k_{\text{off}}}{(k_{\text{on}} + k_{\text{off}} + k_{\text{h}})^2} \right) \tag{F.26}$$

$$= \frac{k_{\text{on}} + k_{\text{off}} + k_{\text{h}}}{k_{\text{off}}} - \frac{k_{\text{on}}}{k_{\text{on}} + k_{\text{off}} + k_{\text{h}}} \tag{F.27}$$

$$q_- \simeq \frac{k_{\text{on}} + k_{\text{off}} + k_{\text{h}}}{2k_{\text{off}}} \frac{2k_{\text{on}}k_{\text{off}}}{(k_{\text{on}} + k_{\text{off}} + k_{\text{h}})^2} \tag{F.28}$$

$$= \frac{k_{\text{on}}}{k_{\text{on}} + k_{\text{off}} + k_{\text{h}}} \tag{F.29}$$

The general solution is

$$p_{\text{GTP}}(i) = Aq_+^i + Bq_-^i. \tag{F.30}$$

As $k_{\text{on}} > k_{\text{off}}$ and $k_{\text{on}} > k_{\text{h}}$ for steady-state growth, it follows that $q_+ > 1$ and $q_- \in [0,1]$ for the approximations above so that $A = 0$:

$$p_{\text{GTP}}(i) = Bq_-^i. \tag{F.31}$$

To determine B, the boundary condition (F.14) has to be satisfied:

$$p_{\text{GTP}}(1) = Bq_- = \frac{B}{2}\left(\alpha - \sqrt{\alpha^2 + 4\beta}\right) \tag{F.32}$$

$$p_{\text{GTP}}(2) = Bq_-^2 = \frac{B}{4}\left(\alpha^2 - 2\sqrt{\alpha^2 + 4\beta} + \alpha^2 + 4\beta\right) \tag{F.33}$$

$$= \frac{B}{2}\left(\alpha^2 - \alpha\sqrt{\alpha^2 + 4\beta}\right) + B\beta \tag{F.34}$$

$$\overset{!}{=} \alpha p_{\text{GTP}}(1) + \beta \tag{F.35}$$

$$= \frac{B}{2}\left(\alpha^2 - \alpha\sqrt{\alpha^2 + 4\beta}\right) + \beta. \tag{F.36}$$

Hence, it follows that

$$B = 1 \tag{F.37}$$

and the solution is given by

$$p_{\text{GTP}}(i) = q_-^i = \left[\frac{k_{\text{on}} + k_{\text{off}} + k_{\text{h}}}{2k_{\text{off}}}\left(1 - \sqrt{1 - \frac{4k_{\text{on}}k_{\text{off}}}{(k_{\text{on}} + k_{\text{off}} + k_{\text{h}})^2}}\right)\right]^i. \tag{F.38}$$

From the simulation data, we do not calculate p_i but create a histogram of how often the i-th tubulin dimer is a GTP-tubulin dimer. To compare results between different simulations with different numbers of measurements, we will calculate the probability density:

$$\rho_{\text{prob}}(i) = Cp_{\text{GTP}}(i) \tag{F.39}$$

with

$$1 \overset{!}{=} \sum_{i=1}^{\infty} \rho_{\text{prob}}(i) = \sum_{i=0}^{\infty} \rho_{\text{prob}}(i+1) = C\sum_{i=0}^{\infty} q_-^{i+1} = \frac{Cq_-}{1 - q_-} \tag{F.40}$$

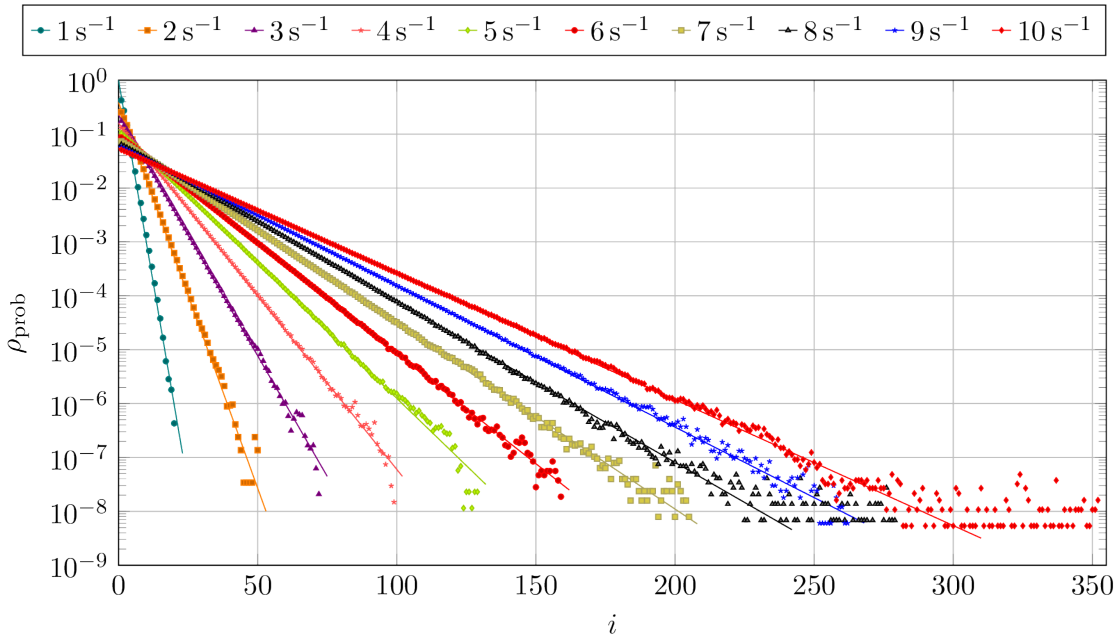

Figure F.2: Probability density ρ_{prob} to find a GTP-tubulin dimer at position i (from the microtubule's plus end) for $k_{\mathrm{off}} = 1\,\mathrm{s}^{-1}$, $k_{\mathrm{h}} = 0.5\,\mathrm{s}^{-1}$, and different values of k_{on}. The data points are the results of one-dimensional microtubule simulations and the lines are the expected results according to (F.42). Deviations from the expected result for very small values of ρ_{prob}, in particular for $k_{\mathrm{on}} = 10\,\mathrm{s}^{-1}$ are due to small samples sizes for the corresponding high values of i.

from which C follows as

$$C = \frac{1 - q_-}{q_-} \tag{F.41}$$

and the relevant probability density as

$$\rho_{\mathrm{prob}}(i) = (1 - q_-)q_-^{i-1}. \tag{F.42}$$

To validate (F.42), we have implemented a simple one-dimensional microtubule simulation and calculated $\rho_{\mathrm{prob}}(i)$ from the simulation data. Figure F.2 shows that the simulation data perfectly reproduces the expected result given in (F.42).

An alternative approach is to start with the steady-state equation (F.5), and consider the difference in the GTP-tubulin dimer probability p_{GTP} at neighboring positions as the derivative of p_{GTP} with respect to the position i:

$$p_{\mathrm{GTP}}(i-1) - p_{\mathrm{GTP}}(i) = -\frac{p_{\mathrm{GTP}}(i) - p_{\mathrm{GTP}}(i-1)}{i - (i-1)} \simeq -\frac{\partial p_{\mathrm{GTP}}(i)}{\partial i}\,, \tag{F.43}$$

$$p_{\mathrm{GTP}}(i+1) - p_{\mathrm{GTP}}(i) = \frac{p_{\mathrm{GTP}}(i+1) - p_{\mathrm{GTP}}(i)}{(i+1) - i} \simeq \frac{\partial p_{\mathrm{GTP}}(i)}{\partial i}\,. \tag{F.44}$$

Using i as a continuous variable with $i \in [1, \infty)$, (F.5) becomes a differential equation for the GTP-tubulin dimer probability p_{GTP}:

$$\frac{\partial p_{\mathrm{GTP}}(i)}{\partial i} = -\frac{k_{\mathrm{h}}}{k_{\mathrm{on}} - k_{\mathrm{off}}} p_{\mathrm{GTP}}(i) \tag{F.45}$$

with the solution

$$\begin{aligned} p_{\mathrm{GTP}}(i) &= p_{\mathrm{GTP}}(1) \exp\left(-\int_1^i \mathrm{d}j \, \frac{k_{\mathrm{h}}}{k_{\mathrm{on}} - k_{\mathrm{off}}} \right) && \text{(F.46)} \\ &= p_{\mathrm{GTP}}(1) \exp\left(-\frac{k_{\mathrm{h}}}{k_{\mathrm{on}} - k_{\mathrm{off}}} (i-1) \right). && \text{(F.47)} \end{aligned}$$

As we are again considering a probability density (F.39), it must also hold that

$$\int_1^\infty \mathrm{d}i \, \rho_{\mathrm{prob}}(i) = 1 \tag{F.48}$$

resulting in

$$\rho_{\mathrm{prob}}(i) = \frac{k_{\mathrm{h}}}{k_{\mathrm{on}} - k_{\mathrm{off}}} \exp\left(-\frac{k_{\mathrm{h}}}{k_{\mathrm{on}} - k_{\mathrm{off}}} (i-1) \right). \tag{F.49}$$

Normally, approximating a difference quotient with a derivative only works for small differences between neighboring positions. As in our model this difference is, by definition, always $\Delta i = 1$, the approximation can alternatively be viewed as valid if i spans a large interval of values so that $\Delta i = 1$ is comparably small to the overall length of the interval and changes between neighboring ρ_{prob} become smaller. Figure F.3 shows that indeed, the approximation is insufficient for small values of k_{on}, which also in turn results in a smaller maximum value of i, thus a smaller interval of i values. However, the larger the value of k_{on} becomes, the better the exponential version (F.49) of $\rho_{\mathrm{prob}}(i)$ fits the simulation data.

From (F.49), we can define a characteristic cap length L_{cap} as the denominator in the exponential function

$$\rho_{\mathrm{prob}}(i) = \frac{1}{L_{\mathrm{cap}}} \exp\left(-\frac{i-1}{L_{\mathrm{cap}}} \right) \tag{F.50}$$

with

$$L_{\mathrm{cap}} = \frac{k_{\mathrm{on}} - k_{\mathrm{off}}}{k_{\mathrm{h}}}. \tag{F.51}$$

To get a better understanding of the characteristic cap length (F.51), we consider the GTP-tubulin dimer current j_{on} into the microtubule from the polymerization and depolymerization dynamics given by

$$j_{\mathrm{on}} = k_{\mathrm{on}} - k_{\mathrm{off}} = \frac{v_{\mathrm{gr}}}{\ell_{\mathrm{dim}}}. \tag{F.52}$$

It should be noted that (F.52) is only the best possible simple approximation to this current because it assumes that the off-part of the current (k_{off}) is entirely made up of GTP-tubulin

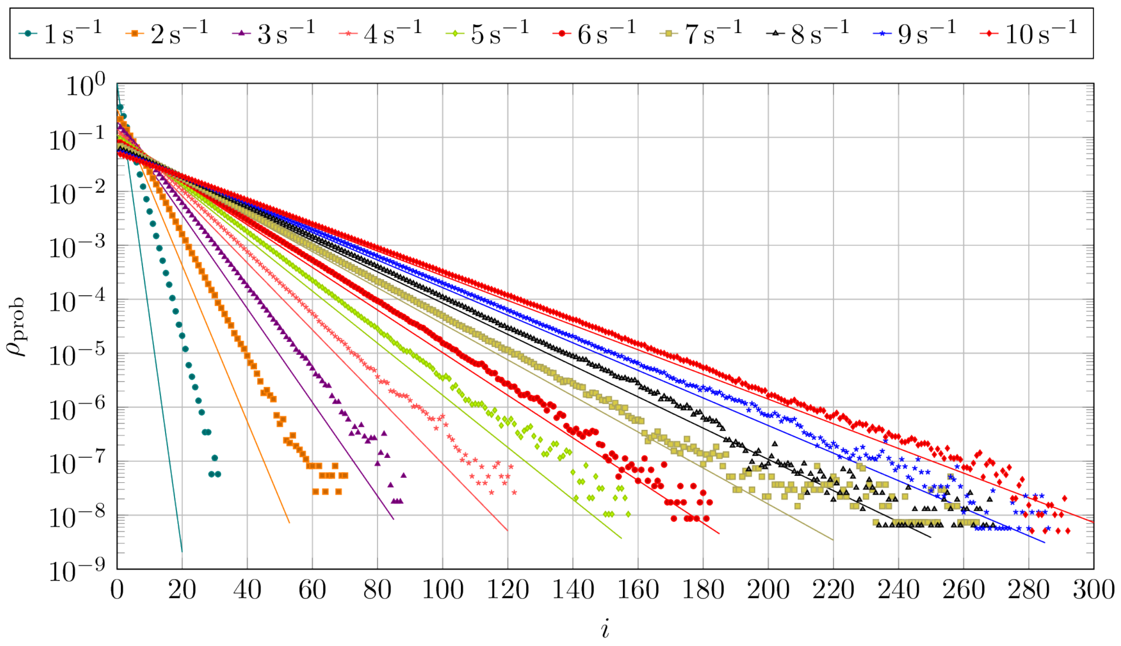

Figure F.3: Probability density ρ_{prob} to find a GTP-tubulin dimer at position i (from the microtubule's plus end) for $k_{\text{off}} = 0.5\,\text{s}^{-1}$, $k_{\text{h}} = 0.5\,\text{s}^{-1}$, and different values of k_{on}. The data points are results from one-dimensional microtubule simulations and the lines are the expected results according to (F.49).

dimers, while in reality, it also contains GDP-tubulin dimers. As depolymerization is only possible for the terminal tubulin dimer in this one-dimensional model and because this terminal tubulin dimer has the highest probability of being a GTP-tubulin dimer, see Figure F.2, this approximation is acceptable.

The second current related to GTP-tubulin dimers is the hydrolysis current j_{h} that describes the conversion of GTP-tubulin dimers due to hydrolysis into GDP-tubulin dimers and is given by

$$j_{\text{h}} = N_{\text{GTP}} k_{\text{h}}. \tag{F.53}$$

In the steady state, both currents (F.52) and (F.53) balance each other out resulting in:

$$j_{\text{on}} = j_{\text{h}} \qquad \Longleftrightarrow \qquad N_{\text{GTP}} = \frac{k_{\text{on}} - k_{\text{off}}}{k_{\text{h}}}. \tag{F.54}$$

Thus, the characteristic cap length (F.51) from the spatial GTP-tubulin dimer distribution (F.49) is simply the total number of GTP-tubulin dimers. From all three "types" of GTP-caps, we have considered, the continuous GTP-cap (N_{cap}) is the shortest, followed by the characteristic cap length ($L_{\text{cap}} = N_{\text{GTP}}$), and the porous GTP-cap (N_{pcap}) being the longest.

Additional Microtubule Properties Figures and Data

G

G.1 GTP-Cap Length

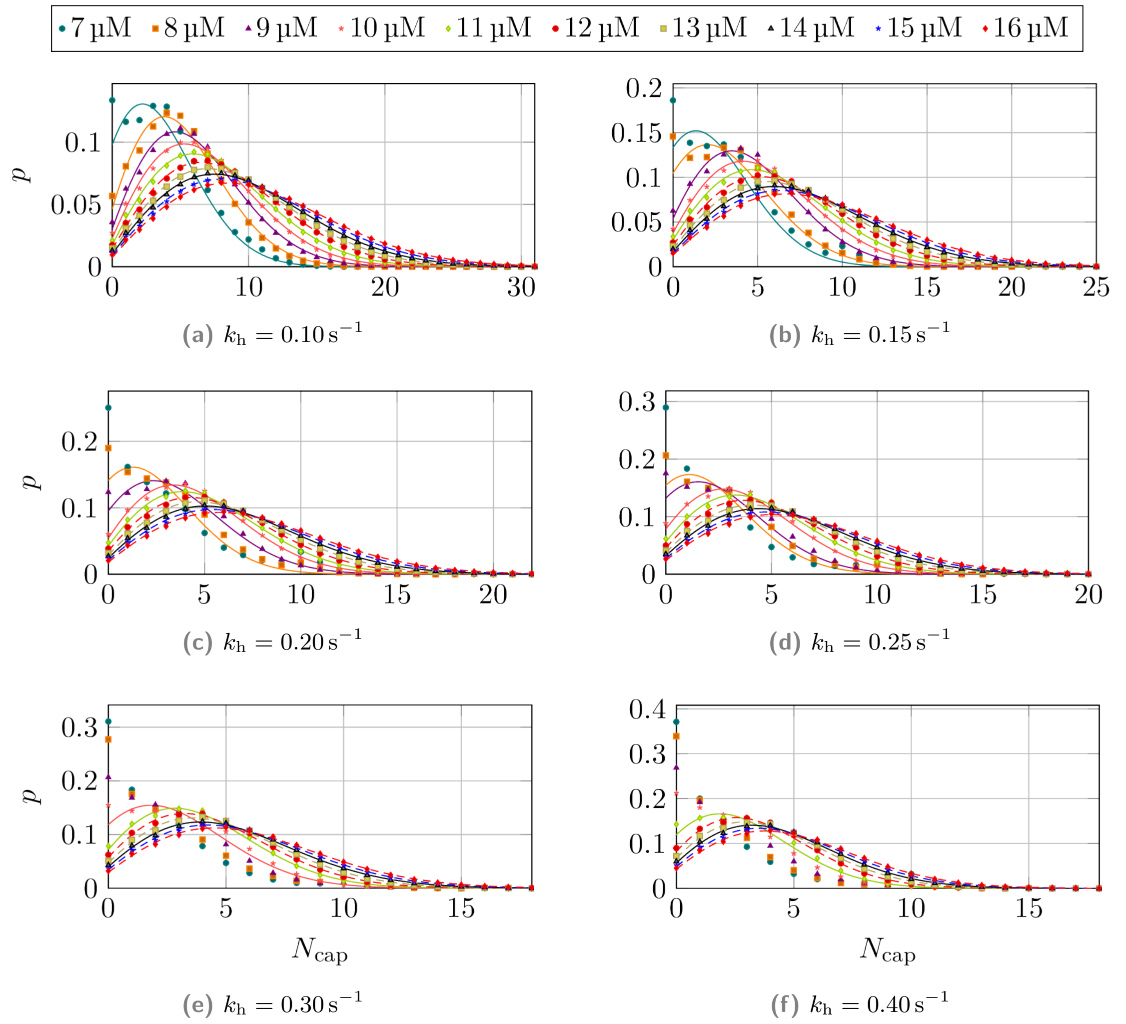

(a) $k_{\text{h}} = 0.10\,\text{s}^{-1}$

(b) $k_{\text{h}} = 0.15\,\text{s}^{-1}$

(c) $k_{\text{h}} = 0.20\,\text{s}^{-1}$

(d) $k_{\text{h}} = 0.25\,\text{s}^{-1}$

(e) $k_{\text{h}} = 0.30\,\text{s}^{-1}$

(f) $k_{\text{h}} = 0.40\,\text{s}^{-1}$

Figure G.1: The GTP-cap length distribution $p(N_{\text{cap}})$ for different constant hydrolysis rates k_{h} and different free GTP-tubulin dimer concentrations c_{tub}. The lines are fits using the fit function $a(N_{\text{cap}} + b)\exp\left[-0.5a(N_{\text{cap}} + b)^2\right]$.

G.2 Porous GTP-Cap Length

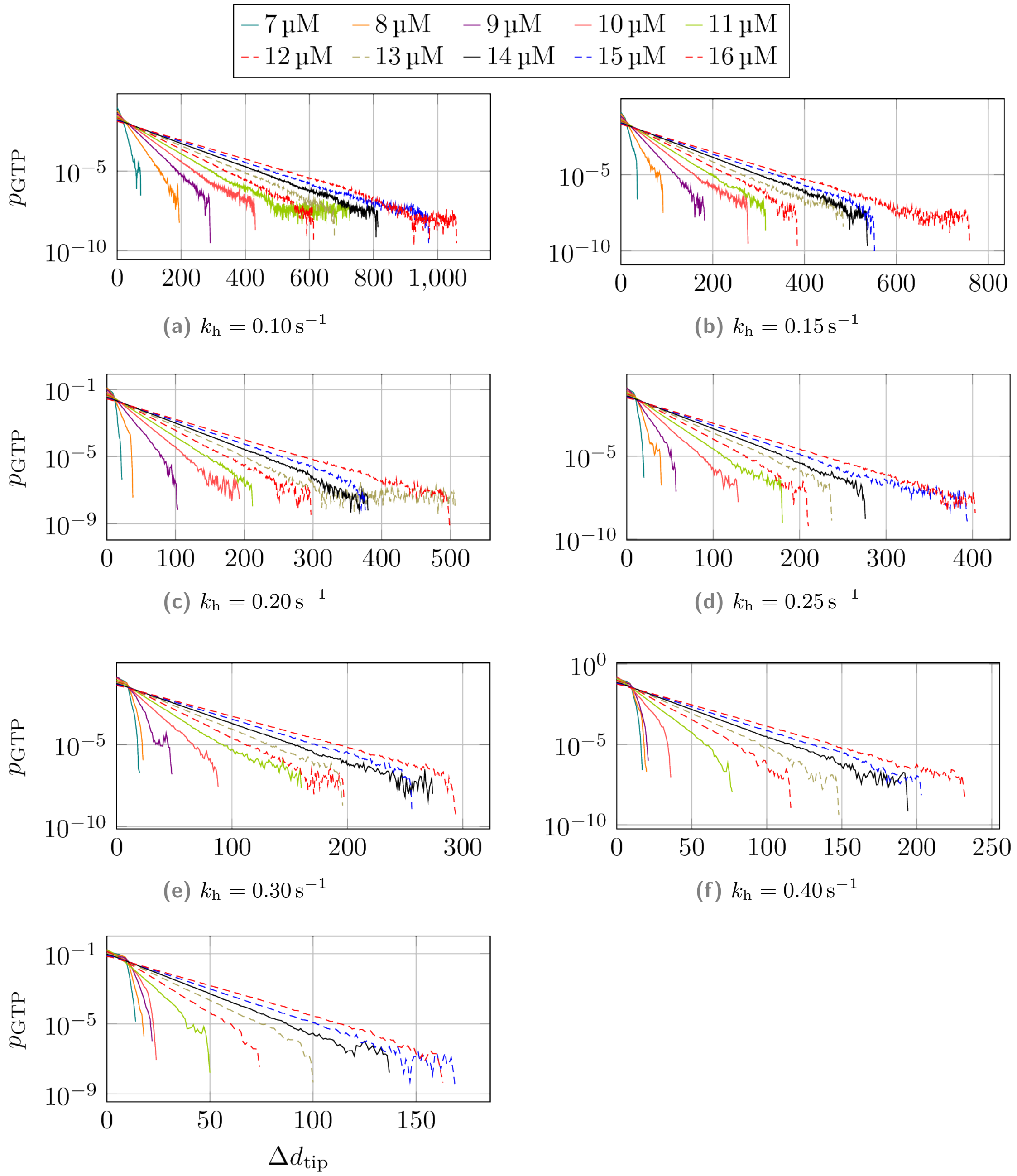

(a) $k_{\mathrm{h}} = 0.10\,\mathrm{s}^{-1}$

(b) $k_{\mathrm{h}} = 0.15\,\mathrm{s}^{-1}$

(c) $k_{\mathrm{h}} = 0.20\,\mathrm{s}^{-1}$

(d) $k_{\mathrm{h}} = 0.25\,\mathrm{s}^{-1}$

(e) $k_{\mathrm{h}} = 0.30\,\mathrm{s}^{-1}$

(f) $k_{\mathrm{h}} = 0.40\,\mathrm{s}^{-1}$

(g) $k_{\mathrm{h}} = 0.50\,\mathrm{s}^{-1}$

Figure G.2: Probability p_{GTP} to find a GTP-tubulin dimer at the distance Δd_{tip} from the tip of its protofilament for different hydrolysis rates k_{h} and free GTP-tubulin dimer concentrations c_{tub}. (Due to the large amount of data, it is plotted as lines instead of individual data points.)

k_h c_tub	$0.10\,\mathrm{s}^{-1}$	$0.15\,\mathrm{s}^{-1}$	$0.20\,\mathrm{s}^{-1}$	$0.25\,\mathrm{s}^{-1}$	$0.30\,\mathrm{s}^{-1}$	$0.40\,\mathrm{s}^{-1}$	$0.50\,\mathrm{s}^{-1}$
7 µM	(0.106)	(0.132)	(0.138)	(0.148)	(0.154)	(0.148)	(0.155)
8 µM	0.061	0.104	(0.134)	(0.143)	(0.146)	(0.153)	(0.148)
9 µM	0.043	0.070	0.101	0.135	(0.145)	(0.153)	(0.152)
10 µM	0.033	0.051	0.072	0.097	0.123	(0.170)	(0.165)
11 µM	0.027	0.041	0.057	0.074	0.092	0.134	(0.175)
12 µM	0.022	0.034	0.047	0.060	0.074	0.104	0.137
13 µM	0.019	0.030	0.040	0.051	0.063	0.086	0.112
14 µM	0.017	0.026	0.035	0.044	0.054	0.074	0.095
15 µM	0.015	0.023	0.031	0.039	0.047	0.065	0.083
16 µM	0.014	0.021	0.028	0.035	0.042	0.058	0.073

Table G.1: Exponential distribution parameter λ (see (7.23)) for the GTP-tubulin dimer distributions in Figure G.2. The values in parentheses are for parameter sets for which the exponential fit only matches the first few data points due to $c_\mathrm{tub} < c_\mathrm{crit}$, see the relevant lines in Figure G.2.

Additional Individual Microtubule Trajectory Figures

H

In this appendix, we present the three-dimensional configuration snapshots of the same configurations shown in two dimensions in chapter 8.

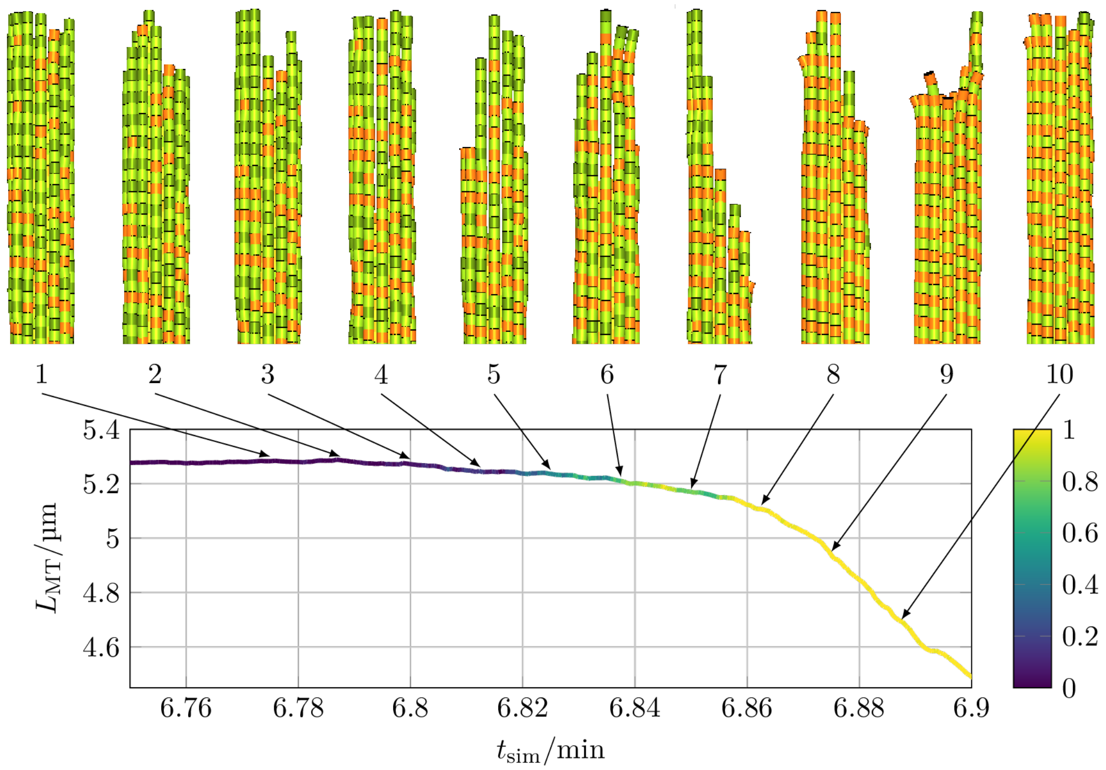

(a) Catastrophe from Figure 8.1(a).

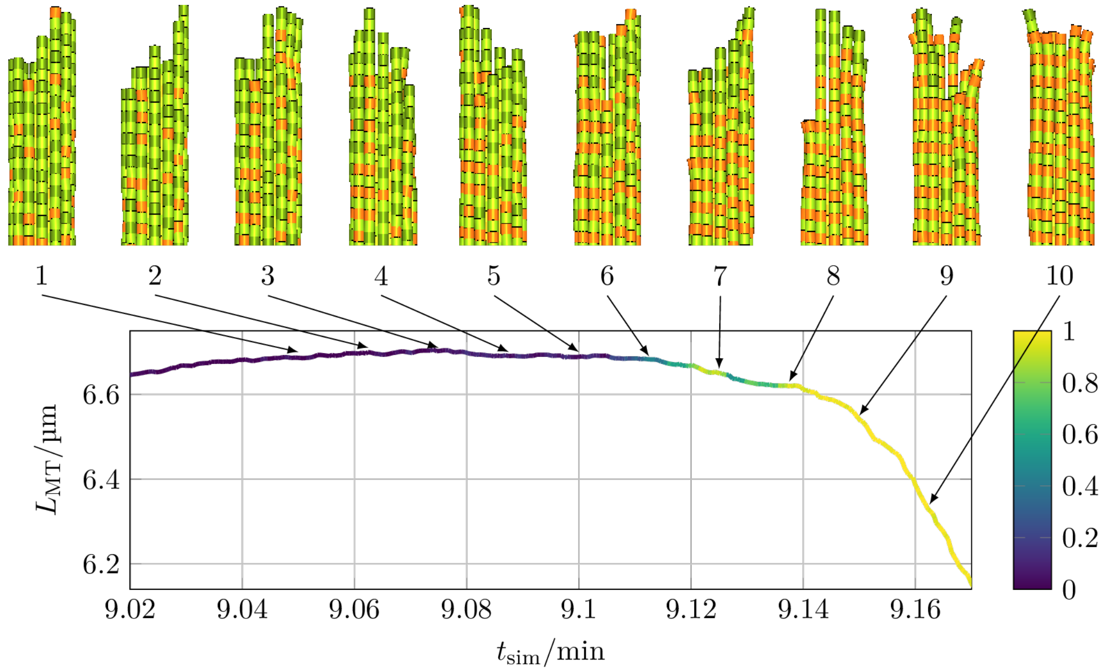

(b) Catastrophe from Figure 8.1(b).

Figure H.1: Three-dimensional configuration snapshots around the catastrophes shown in Figure 8.1.

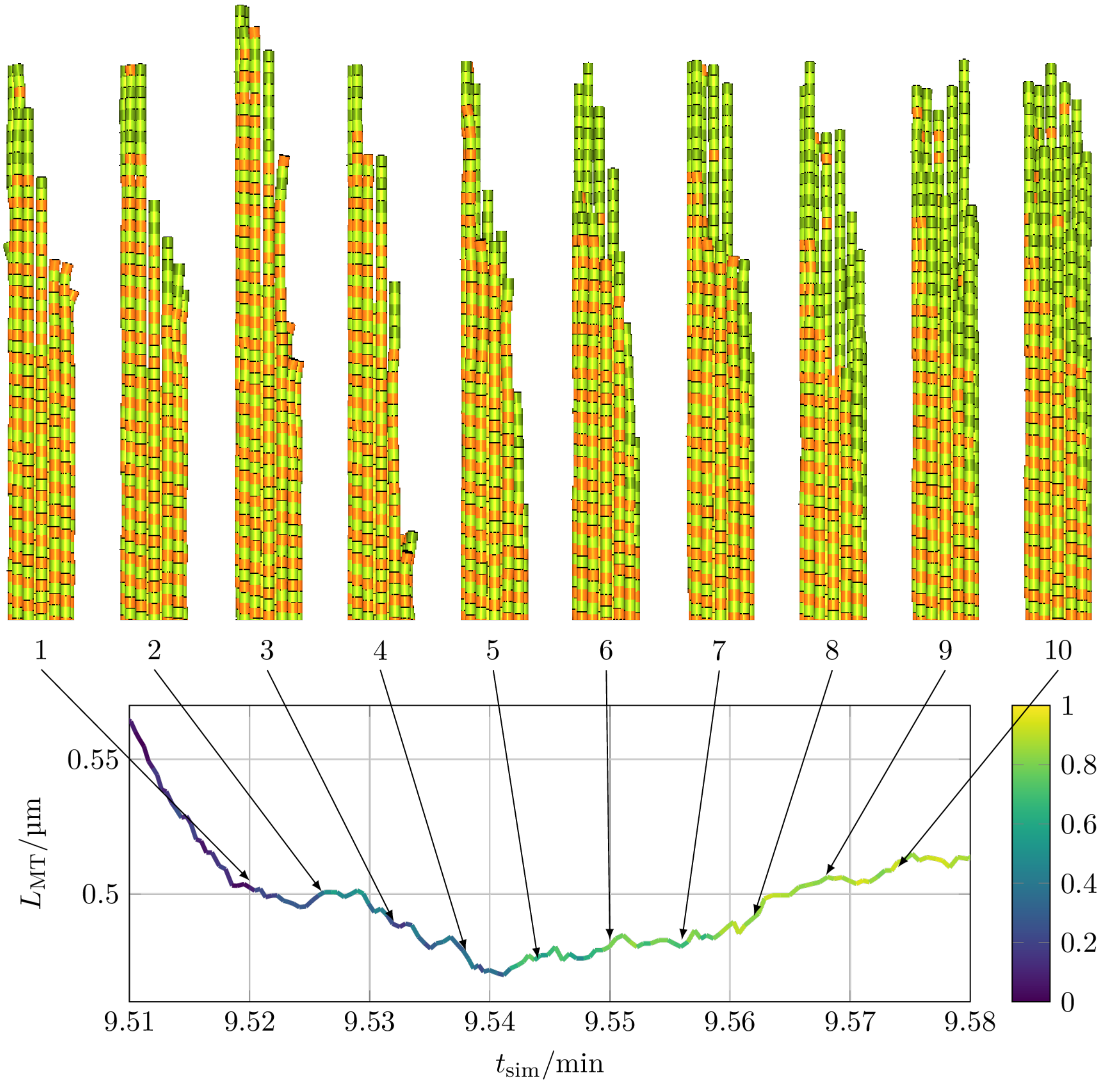

Figure H.2: Three-dimensional configuration snapshots around the rescue shown in Figure 8.1(b).

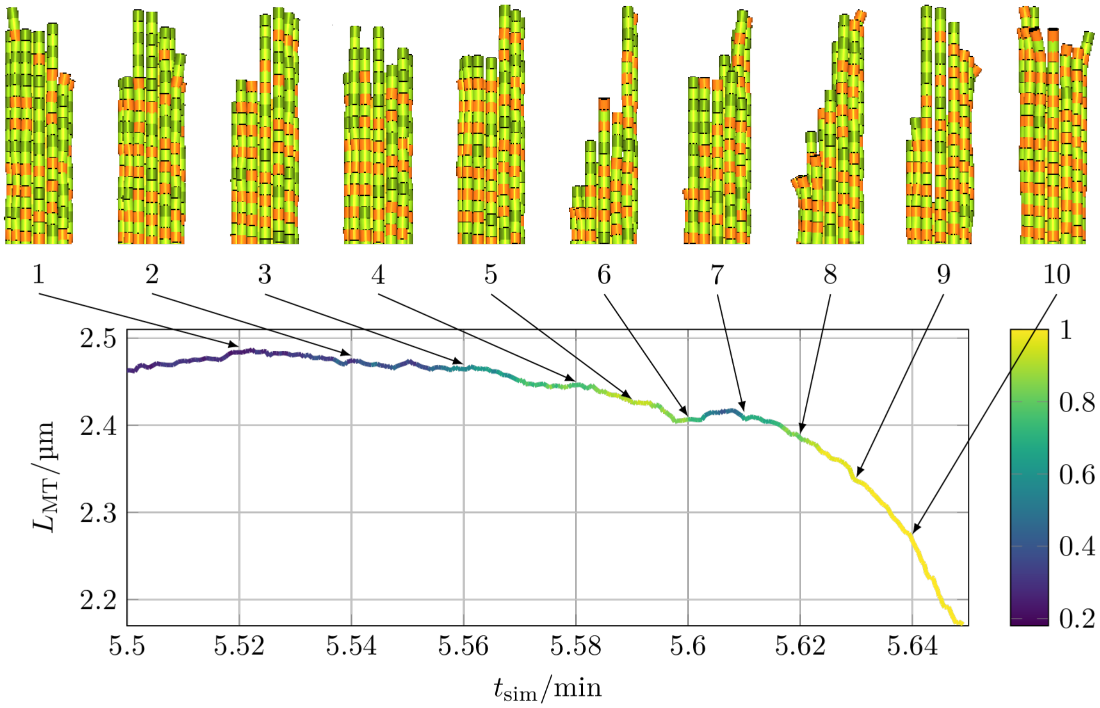

(a) Catastrophe from Figure 8.6(a).

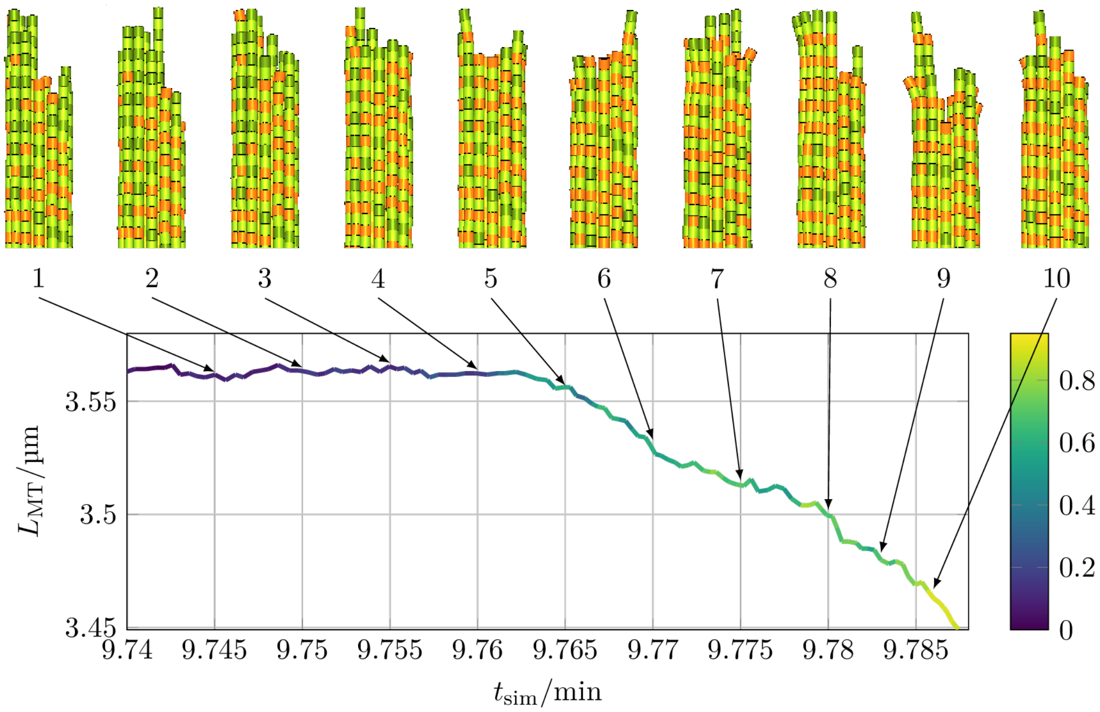

(b) Catastrophe (C4) from Figure 8.6(b).

Figure H.3: Three-dimensional configuration snapshots around catastrophes shown in Figure 8.6.

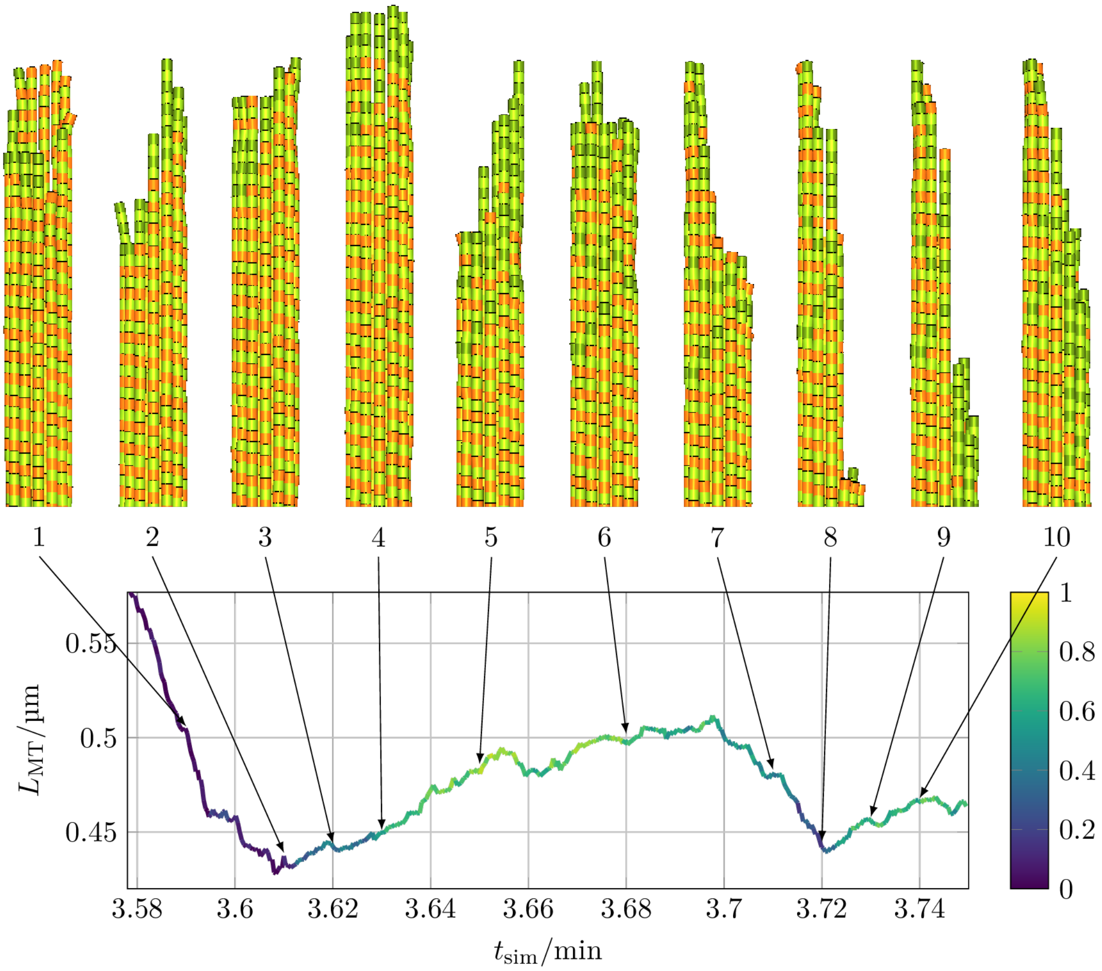

Figure H.4: Three-dimensional configuration snapshots around rescue (R1) shown in Figure 8.6(b).

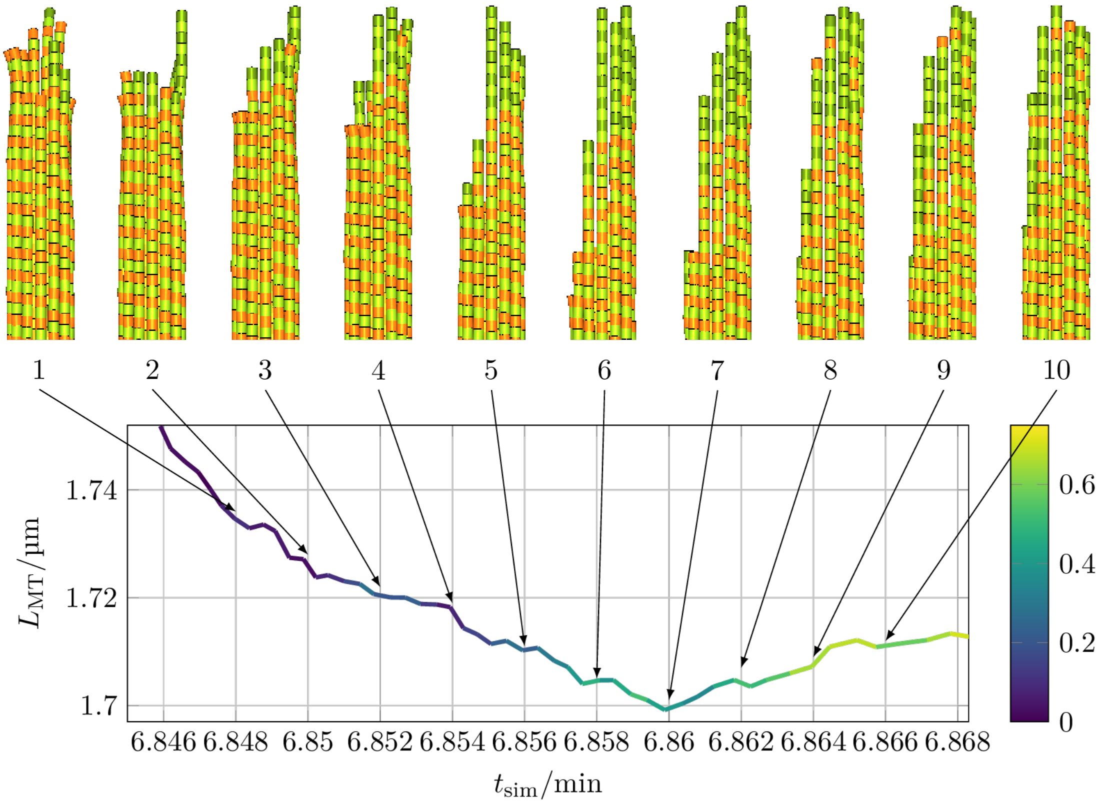

Figure H.5: Three-dimensional configuration snapshots around rescue (R3) shown in Figure 8.6(b).

Additional Dilution Figures

In the main chapter on dilution, chapter 9, we only presented the results for a pre-dilution free GTP-tubulin dimer concentration of $c_{\mathrm{tub}} = 16\,\mu\mathrm{M}$. Here, we show additional results for smaller values of c_{tub}, which are qualitatively similar to the previously shown results for $c_{\mathrm{tub}} = 16\,\mu\mathrm{M}$.

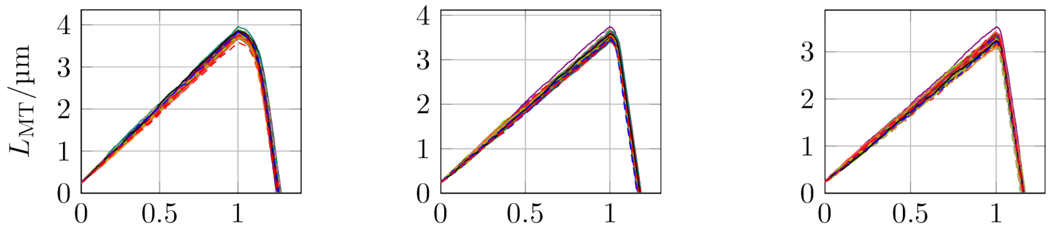

(a) $c_{\mathrm{dil}} = 0\,\mu\mathrm{M}$, $k_{\mathrm{h}} = 0.1\,\mathrm{s}^{-1}$ **(b)** $c_{\mathrm{dil}} = 0\,\mu\mathrm{M}$, $k_{\mathrm{h}} = 0.3\,\mathrm{s}^{-1}$ **(c)** $c_{\mathrm{dil}} = 0\,\mu\mathrm{M}$, $k_{\mathrm{h}} = 0.5\,\mathrm{s}^{-1}$

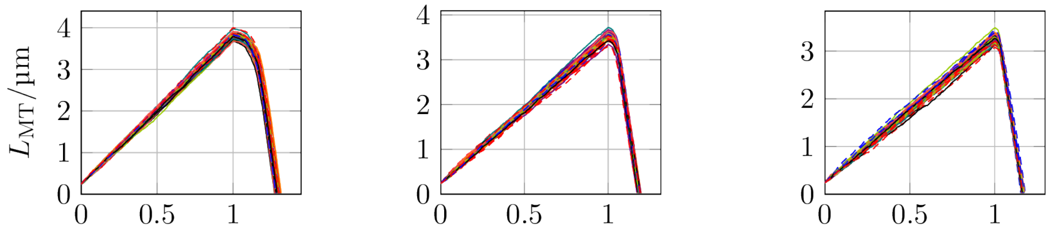

(d) $c_{\mathrm{dil}} = 3\,\mu\mathrm{M}$, $k_{\mathrm{h}} = 0.1\,\mathrm{s}^{-1}$ **(e)** $c_{\mathrm{dil}} = 3\,\mu\mathrm{M}$, $k_{\mathrm{h}} = 0.3\,\mathrm{s}^{-1}$ **(f)** $c_{\mathrm{dil}} = 3\,\mu\mathrm{M}$, $k_{\mathrm{h}} = 0.5\,\mathrm{s}^{-1}$

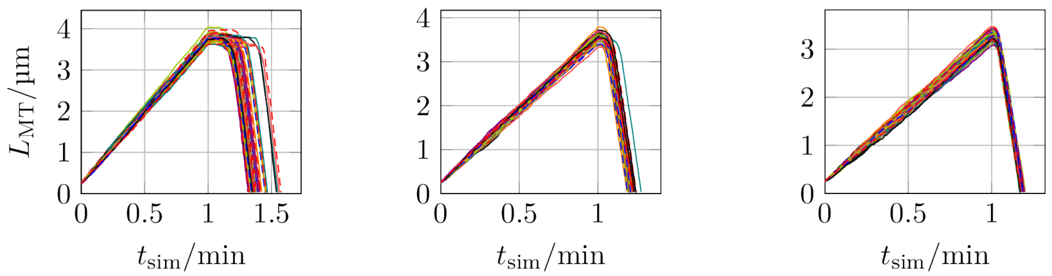

(g) $c_{\mathrm{dil}} = 6\,\mu\mathrm{M}$, $k_{\mathrm{h}} = 0.1\,\mathrm{s}^{-1}$ **(h)** $c_{\mathrm{dil}} = 6\,\mu\mathrm{M}$, $k_{\mathrm{h}} = 0.3\,\mathrm{s}^{-1}$ **(i)** $c_{\mathrm{dil}} = 6\,\mu\mathrm{M}$, $k_{\mathrm{h}} = 0.5\,\mathrm{s}^{-1}$

Figure I.1: Microtubule trajectories of dilution simulations for $c_{\mathrm{tub}} = 16\,\mu\mathrm{M}$, $t_{\mathrm{dil}} = 1\,\mathrm{min}$, different post-dilution concentrations c_{dil}, and different hydrolysis rates k_{h}. The associated average delay times $\langle \Delta t_{\mathrm{delay}} \rangle$ are shown in Figure 9.3(a).

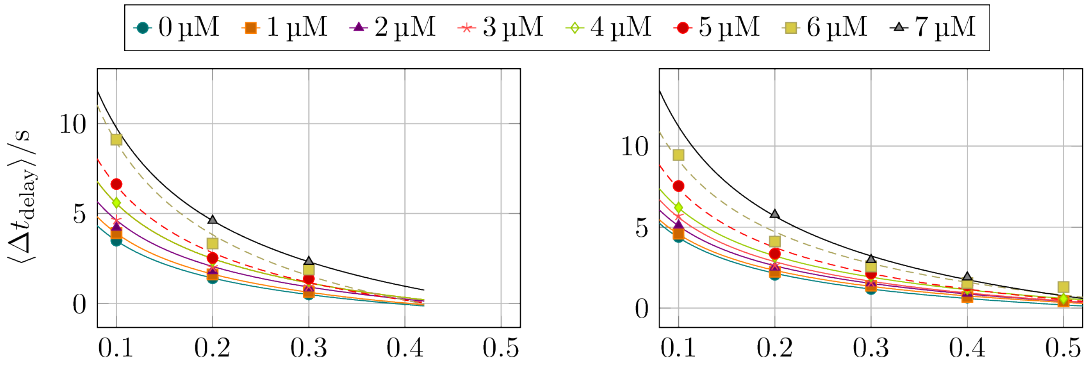

(a) $c_{\mathrm{tub}} = 10\,\mu\mathrm{M}$

(b) $c_{\mathrm{tub}} = 11\,\mu\mathrm{M}$

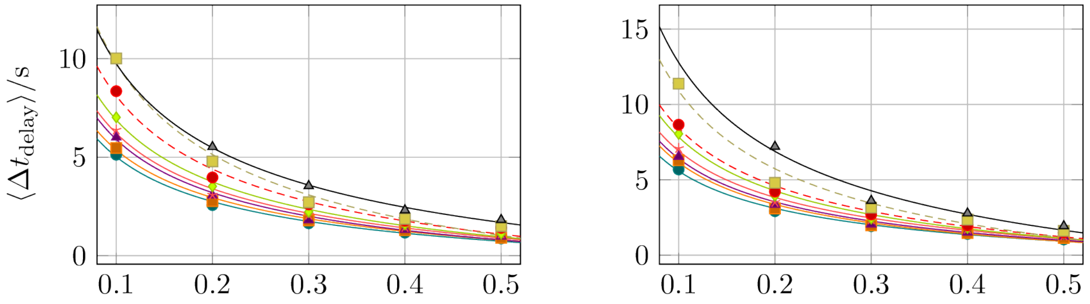

(c) $c_{\mathrm{tub}} = 12\,\mu\mathrm{M}$

(d) $c_{\mathrm{tub}} = 13\,\mu\mathrm{M}$

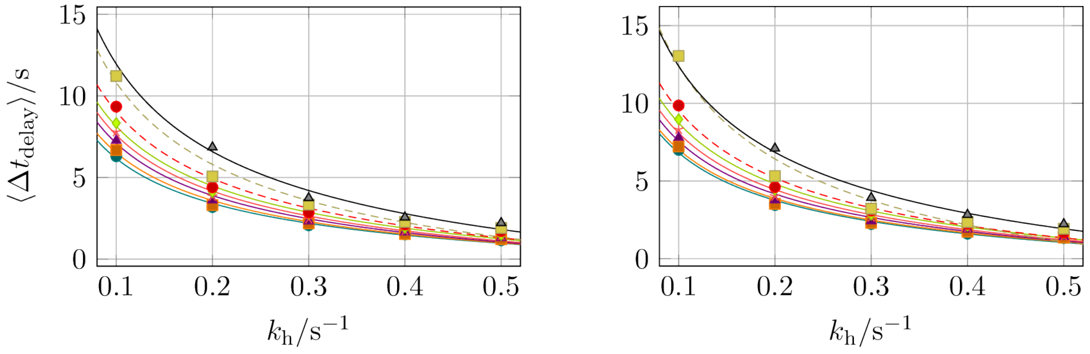

(e) $c_{\mathrm{tub}} = 14\,\mu\mathrm{M}$

(f) $c_{\mathrm{tub}} = 15\,\mu\mathrm{M}$

Figure I.2: The average post-dilution delay time $\langle \Delta t_{\mathrm{delay}} \rangle$ as a function of the hydrolysis rate k_{h} for different pre-dilution concentrations c_{tub} and post-dilution concentrations c_{dil}.

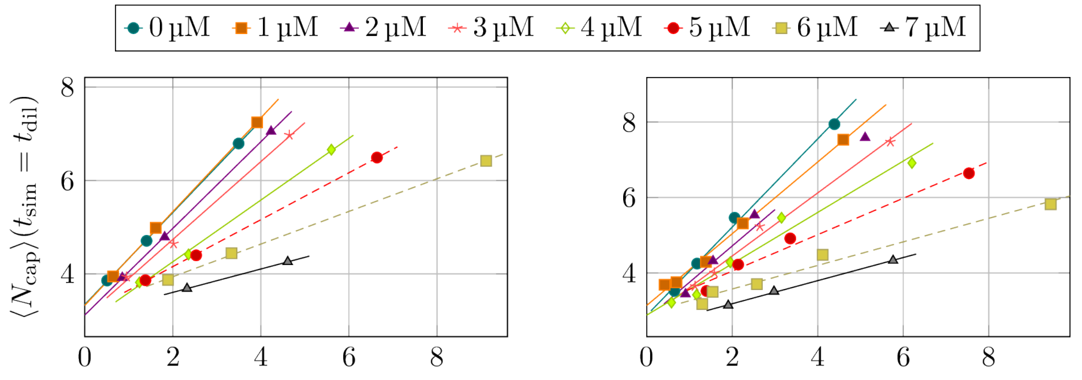

(a) $c_{\mathrm{tub}} = 10\,\mu\mathrm{M}$ **(b)** $c_{\mathrm{tub}} = 11\,\mu\mathrm{M}$

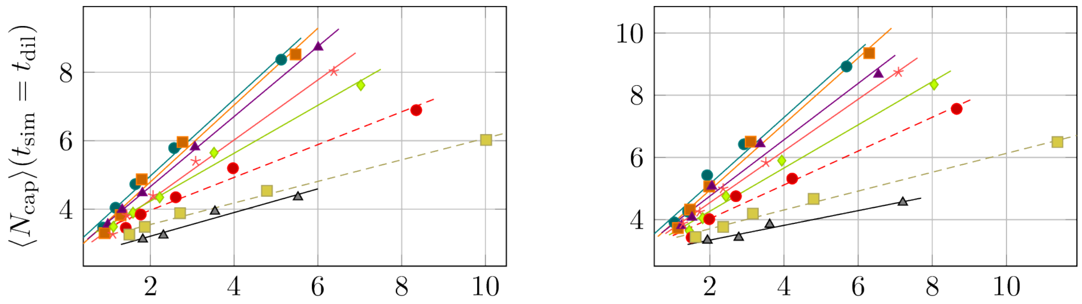

(c) $c_{\mathrm{tub}} = 12\,\mu\mathrm{M}$ **(d)** $c_{\mathrm{tub}} = 13\,\mu\mathrm{M}$

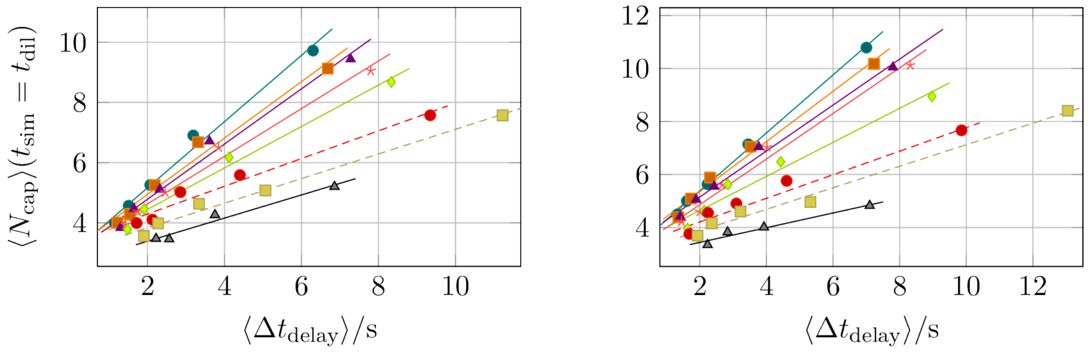

(e) $c_{\mathrm{tub}} = 14\,\mu\mathrm{M}$ **(f)** $c_{\mathrm{tub}} = 15\,\mu\mathrm{M}$

Figure I.3: The average GTP-cap length $\langle N_{\mathrm{cap}} \rangle$ at the time of dilution t_{dil} as a function of the average post-dilution delay time $\langle \Delta t_{\mathrm{delay}} \rangle$ for different pre-dilution concentrations c_{tub} and post-dilution concentrations c_{dil}.

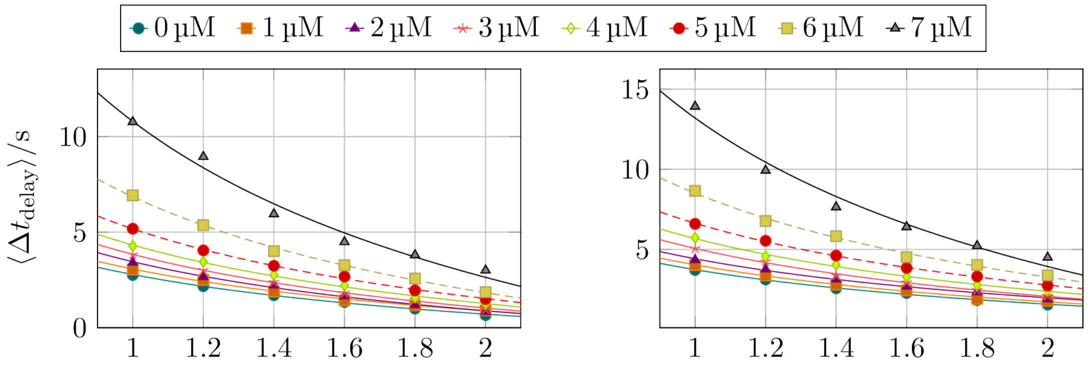

(a) $c_{\mathrm{tub}} = 10\,\mu\mathrm{M}$

(b) $c_{\mathrm{tub}} = 11\,\mu\mathrm{M}$

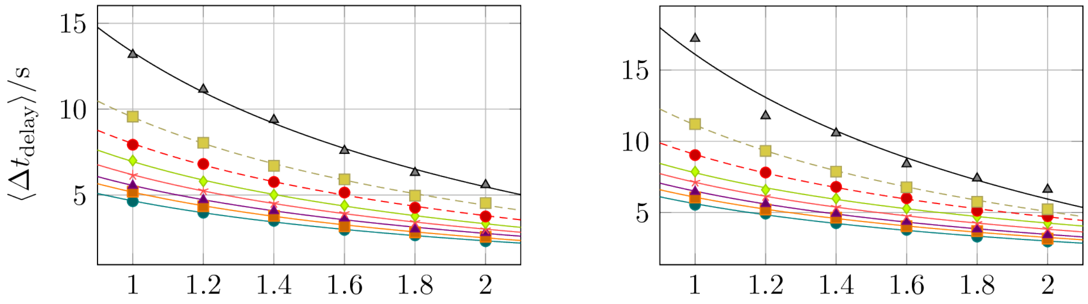

(c) $c_{\mathrm{tub}} = 12\,\mu\mathrm{M}$

(d) $c_{\mathrm{tub}} = 13\,\mu\mathrm{M}$

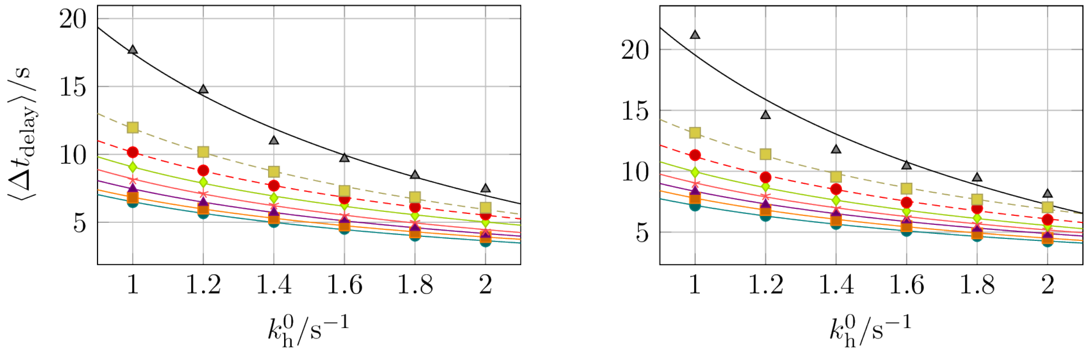

(e) $c_{\mathrm{tub}} = 14\,\mu\mathrm{M}$

(f) $c_{\mathrm{tub}} = 15\,\mu\mathrm{M}$

Figure I.4: The average post-dilution delay time $\langle \Delta t_{\mathrm{delay}} \rangle$ as a function of the base hydrolysis rate k_{h}^{0} for different pre-dilution concentrations c_{tub} and post-dilution concentrations c_{dil}.

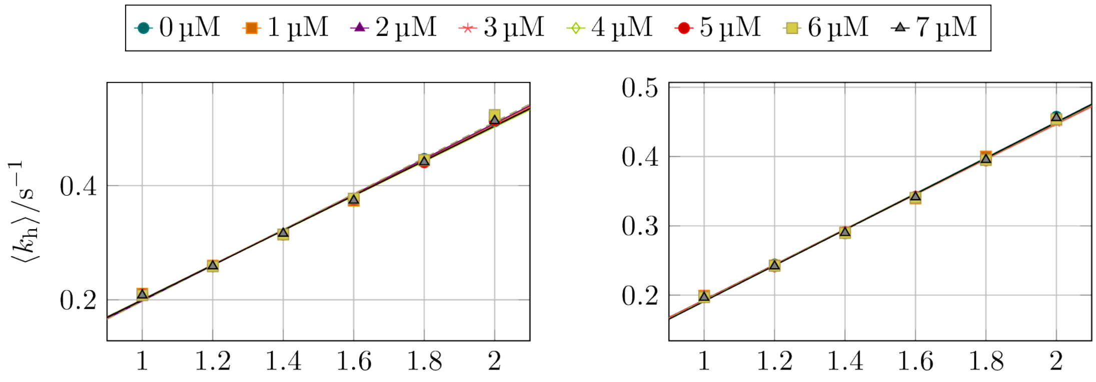

(a) $c_{\text{tub}} = 10\,\mu\text{M}$ (b) $c_{\text{tub}} = 11\,\mu\text{M}$

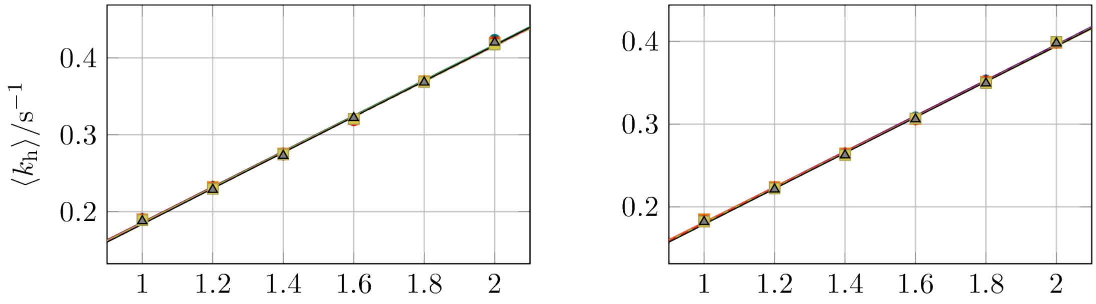

(c) $c_{\text{tub}} = 12\,\mu\text{M}$ (d) $c_{\text{tub}} = 13\,\mu\text{M}$

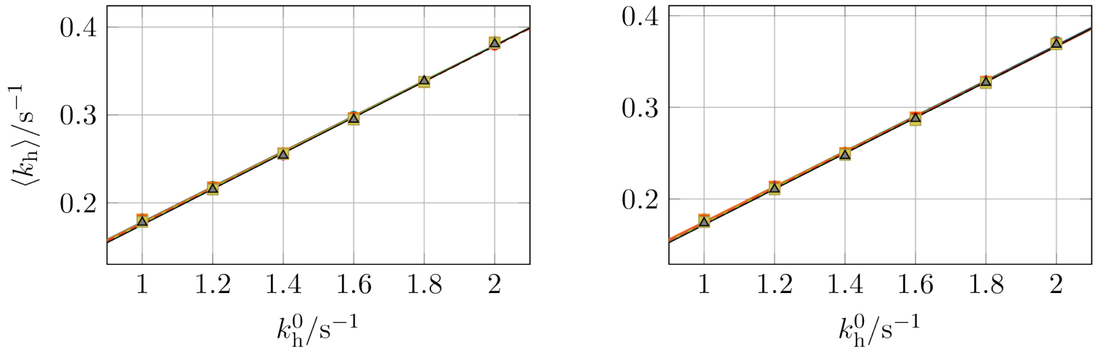

(e) $c_{\text{tub}} = 14\,\mu\text{M}$ (f) $c_{\text{tub}} = 15\,\mu\text{M}$

Figure I.5: The average rate $\langle k_h \rangle$ of executed hydrolysis events increases with the base hydrolysis rate k_h^0 for different pre-dilution concentrations c_{tub} and is independent of the different post-dilution concentrations c_{dil}.

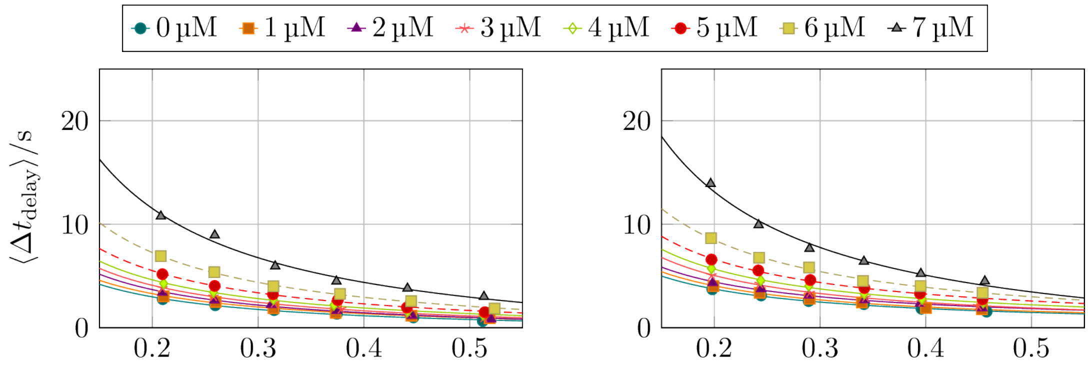

(a) $c_{\mathrm{tub}} = 10\,\mu\mathrm{M}$ (b) $c_{\mathrm{tub}} = 11\,\mu\mathrm{M}$

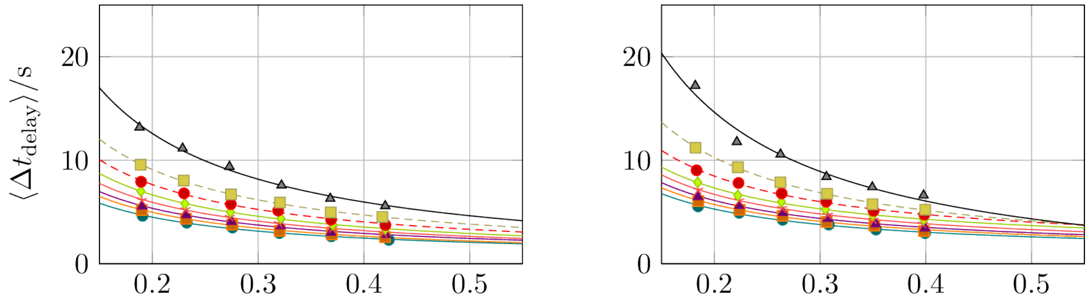

(c) $c_{\mathrm{tub}} = 12\,\mu\mathrm{M}$ (d) $c_{\mathrm{tub}} = 13\,\mu\mathrm{M}$

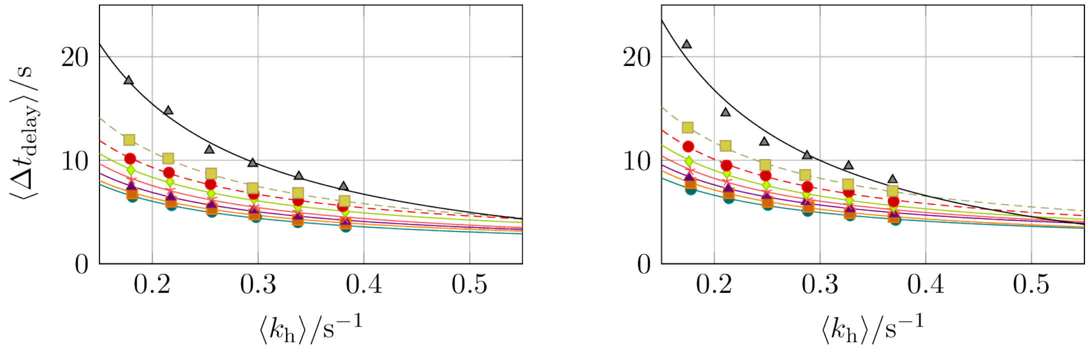

(e) $c_{\mathrm{tub}} = 14\,\mu\mathrm{M}$ (f) $c_{\mathrm{tub}} = 15\,\mu\mathrm{M}$

Figure I.6: The average post-dilution delay time $\langle \Delta t_{\mathrm{delay}} \rangle$ as a function of the average hydrolysis rate $\langle k_{\mathrm{h}} \rangle$ for different pre-dilution concentrations c_{tub} and different post-dilution concentrations c_{dil}.

Symbols

L_p	persistence length [µm]
L_MT	microtubule length [µm]
v_gr	velocity with which a microtubule grows [$\mu\mathrm{m}\,\mathrm{min}^{-1}$]
v_sh	velocity with which a microtubule shrinkage [$\mu\mathrm{m}\,\mathrm{min}^{-1}$]
k_on	polymerization rate [s^{-1}]
k_off	depolymerization rate [s^{-1}]
r_tub	radius of tubulin monomers in our model, value: 2 nm
ℓ_tub	length of tubulin monomers in our model, value: 4 nm
p	protofilament index, values: $\{1, \ldots, 13\}$
$d_\mathrm{max}(p)$	number of tubulin dimers in protofilament p
d	tubulin dimer index within a protofilament, values: $\{1, \ldots, d_\mathrm{max}\}$
t	tubulin monomer index within a tubulin dimer, values: $\{1, 2\}$
$\phi(p)$	azimuthal angle of all tubulin monomers in protofilament p [rad]
$\theta(p, d, t)$	polar angle of tubulin monomers (p, d, t) [rad]
$\boldsymbol{m}(p, d, t)$	vector pointing to minus end of tubulin monomer (p, d, t)
$\boldsymbol{p}(p, d, t)$	vector pointing to plus end of tubulin monomer (p, d, t)
$\boldsymbol{d}(p, d, t)$	direction vector of tubulin monomer (p, d, t)
R_MT	average microtubule radius, value: 10.5 nm
Δz_h	helical shift between protofilaments, value: 0.92 nm
$L_\mathrm{proto}(p)$	length of protofilament p
$\boldsymbol{c}(p, d, t)$	vector connecting $\boldsymbol{p}(p, d, t)$ with the point on the surface of tubulin monomer (p, d, t) at which the lateral bond to tubulin monomer $(p + 1, d, t)$ starts
$\boldsymbol{s}(p, d, t)$	spring vector representing lateral bond from monomer (p, d, t) to monomer $(p + 1, d, t)$
s_0	rest length of spring vector representing lateral bonds [nm]
$s_{0,\parallel}$	length of the projection of a lateral spring at its rest length into the x-y-plane
$s_{0,\perp}$	length of the projection of a lateral spring at its rest length onto the z-axis
$\Delta G^{0*}_\mathrm{long}$	longitudinal bond energy between tubulin dimers [$k_\mathrm{B}T$]
$E_\mathrm{lat}(p, d, t)$	energy of the lateral bond between laterally neighboring tubulin monomers (p, d, t) and $(p + 1, d, t)$ [$k_\mathrm{B}T$]
$\Delta G^{0}_\mathrm{lat}$	lateral bond energy between tubulin monomers at equilibrium [$k_\mathrm{B}T$]
k_lat	spring constant of lateral bonds [$k_\mathrm{B}T/\mathrm{nm}^2$]
k_rep	lateral repulsion constant [$k_\mathrm{B}T\mathrm{nm}^{-12}$]
$E_\mathrm{bend}(p, d, t)$	bending energy of tubulin monomer (p, d, t) [$k_\mathrm{B}T$]
κ	bending constant [$k_\mathrm{B}T/\mathrm{rad}^2$]
$\psi(p, d, t)$	bending angle of tubulin monomer (p, d, t) [rad]
$\psi_0(p, d, t)$	equilibrium bending angle of tubulin monomer (p, d, t) [rad]
$\Delta\psi(p, d, t)$	deviation of the bending angle of tubulin monomer (p, d, t) from its equilibrium value [rad]
E_MT	total microtubule energy [$k_\mathrm{B}T$]
P_n	polymer consisting of n monomers
M	monomer of a polymer
K_diss	dissociation constant

ΔG^0	general bond energy $[k_\mathrm{B}\,T]$
c	concentration [µM]
c^0	standard concentration, value: 1 M
β	thermodynamic beta: $\beta = (k_\mathrm{B}\,T)^{-1}$
k_+	pseudo-first order polymerization rate $[\mathrm{s}^{-1}\,\mu\mathrm{M}^{-1}]$
c_tub	GTP-tubulin dimer concentration [µM]
k_rup	lateral bond formation rate $[\mathrm{s}^{-1}]$
k_form	lateral bond rupture rate $[\mathrm{s}^{-1}]$
k_att	lateral bond formation/rupture attempt rate $[\mathrm{s}^{-1}]$
F_lat	force acting on a lateral bond $[k_\mathrm{B}\,T/\mathrm{nm}]$
ℓ_rup	characteristic lateral bond rupture length [nm]
k_h	hydrolysis rate $[\mathrm{s}^{-1}]$
k_h^0	constant base hydrolysis rate if hydrolysis is coupled to mechanics $[\mathrm{s}^{-1}]$
$\Delta E_\mathrm{h}(p,d)$	change in hydrolysis energy barrier if hydrolysis is coupled to mechanics $[k_\mathrm{B}\,T]$
$\psi_{0,\mathrm{b}}$	position of the energy barrier on the ψ_0-axis that limits the hydrolysis rate [°]
$\Delta E_\mathrm{h,b}$	height of unaltered energy barrier that limits the hydrolysis rate $[k_\mathrm{B}\,T]$
ω_cat	rate with which a microtubule undergoes a catastrophe $[\mathrm{min}^{-1}]$
ω_res	rate with which a microtubule undergoes a rescue $[\mathrm{min}^{-1}]$
N_GDP	(initial) number of GDP-tubulin dimers per protofilament
N_GTP	(initial) number of GTP-tubulin dimers per protofilament
t_sim	time passed within the microtubule simulation [s]
t_max	maximum time than can pass within the microtubule simulation [s]
Δd_cutoff	number of additional layer below a layer affected by an event that are also considered during restricted minimization
N_iter	maximum number of minimization iterations during restricted minimization
a_gr	slope of the linear $v_\mathrm{gr}(c_\mathrm{tub})$ relation
b_gr	intercept of the linear $v_\mathrm{gr}(c_\mathrm{tub})$ relation
$k_\mathrm{on}^\mathrm{eff}$	effective polymerization rate
$k_\mathrm{form}^\mathrm{eff}$	effective lateral bond formation rate
c_crit	critical free GTP-tubulin dimer concentration at which $v_\mathrm{gr} = 0$ [µM]
a_sh	constant factor of the $\sqrt{k_\mathrm{lat}}$ term in the $\kappa(k_\mathrm{lat})$ relation $[\sqrt{k_\mathrm{B}\,T}\mathrm{nm}\,\mathrm{rad}^{-2}]$
b_sh	constant term in the $\kappa(k_\mathrm{lat})$ relation $[k_\mathrm{B}\,T/\mathrm{rad}^2]$
F_bend	bending force $[k_\mathrm{B}\,T/\mathrm{rad}]$
F_rup	lateral bond force during bond rupture $[k_\mathrm{B}\,T/\mathrm{nm}]$
a_rup	constant factor of the $\sqrt{k_\mathrm{lat}}$ term in the $F_\mathrm{rup}(k_\mathrm{lat})$ relation $[\sqrt{k_\mathrm{B}\,T}]$
b_rup	constant term in the $F_\mathrm{rup}(k_\mathrm{lat})$ relation $[k_\mathrm{B}\,T/\mathrm{nm}]$
c_rup	constant factor of the $\sqrt{k_\mathrm{lat}}^{-1}$ term in the $F_\mathrm{rup}(k_\mathrm{lat})\ell_\mathrm{rup}(k_\mathrm{lat})$ relation $[\sqrt{k_\mathrm{B}\,T}/\mathrm{nm}]$
d_rup	constant term in the $F_\mathrm{rup}(k_\mathrm{lat})\ell_\mathrm{rup}(k_\mathrm{lat})$ relation $[k_\mathrm{B}\,T/\mathrm{nm}^2]$
N_poly	number of polymerization events
N_depoly	number of depolymerization events
N_form	number of lateral bond formation events
N_rup	number of lateral bond rupture events
K_b	bending rigidity $[k_\mathrm{B}\,T\mathrm{nm}]$
$\hat{\boldsymbol{t}}$	unit tangent vector
s	position along the contour of a polymer [nm]

t_{cat}	average time a microtubule grows until it undergoes a catastrophe [min]
t_{run}	runtime of a simulation [h]
N_{cap}	average number of GTP-tubulin dimers in the GTP-cap of a microtubule per protofilament or number of GTP-tubulin dimers in the GTP-cap of an individual protofilament
p	probability
τ_{cat}	time at which a microtubule undergoes a catastrophe [min]
τ_{resc}	time at which a microtubule undergoes a rescue [min]
N_{cat}	number of catastrophes
N_{resc}	number of rescues
a_{Jan}	parameter in the $\omega_{\mathrm{cat}}(c_{\mathrm{tub}})$ relation according to data by Janson et al.[204] [min µM^{-1}]
b_{Jan}	parameter in the $\omega_{\mathrm{cat}}(c_{\mathrm{tub}})$ relation according to data by Janson et al.[204] [min]
N_{pcap}	counted from the plus end of the microtubule, the average position of the last GTP-tubulin dimer per protofilament or the position of the last GTP-tubulin dimer of an individual protofilament
Δd_{tip}	distance of a tubulin dimer from the tip of the protofilament (with $\Delta d_{\mathrm{tip}} = 0$ for the tubulin dimer directly at the plus end)
$k_{\mathrm{off}}^{\mathrm{eff}}$	effective depolymerization rate when mapping our three-dimensional model to a one-dimensional model [s^{-1}]
ρ_{prob}	probability density
L_{isl}	number of GTP-tubulin dimers in a GTP-island
N_{isl}	number of GTP-islands in a protofilament
k_{gr}	growth rate [s^{-1}]
τ_{rough}	tip roughness, i.e., the difference in the number of tubulin dimers in neighboring protofilaments
N_{crack}	number of laterally neighboring tubulin monomers at the plus end, which do not have a bond connecting them, resulting in a crack
$\Delta_{\mathrm{nucleus}}$	width a shrinking nucleus, i.e., neighboring protofilaments that have shrunken more than the other protofilaments
c_{dil}	GTP-tubulin dimer concentration after dilution [µM]
t_{dil}	time at which the GTP-tubulin dimer concentration is changed from c_{tub} to c_{dil} in dilution experiments/simulations [min]
L_{dil}	length of a microtubule at the time of dilution that it can also approximately keep in the following delay phase [µm]
a_{delay}	constant factor of the $k_{\mathrm{h}}^{-0.5}$ term in the $\langle \Delta t_{\mathrm{delay}} \rangle (k_{\mathrm{h}})$ relation, [$\sqrt{\mathrm{s}}$]
b_{delay}	constant term in the $\langle \Delta t_{\mathrm{delay}} \rangle (k_{\mathrm{h}})$ relation [s]
L_{cap}	characteristic cap length
j_{on}	GTP-tubulin dimer current into the microtubule from polymerization and depolymerization [s^{-1}]
ℓ_{dim}	length of a tubulin dimer, value: 8 nm
j_{h}	GTP-tubulin dimer current out of the microtubule due to hydrolysis [s^{-1}]

Bibliography

[1] B. Alberts et al. 5th ed. Garland Science.
Molecular Biology of the Cell

[2] F. Gittes et al. (1993), *J. Cell Biol.* **120** (4), 923–934.
Flexural Rigidity of Microtubules and Actin Filaments Measured from Thermal Fluctuations in Shape

[3] B. J. Harris, J. L. Ross, and T. L. Hawkins (2018), *Phys. Rev. E* **97** (6), 062408.
Microtubule seams are not mechanically weak defects

[4] E. M. De La Cruz et al. (2010), *Biophys. J.* **99** (6), 1852–1860.
Origin of Twist-Bend Coupling in Actin Filaments

[5] J. Block et al. (2015), *Biochim. Biophys. Acta Mol. Cell Res.* **1853** (11, Part B), 3053–3064.
Physical properties of cytoplasmic intermediate filaments

[6] B. R. Brinkley (1985), *Annu. Rev. Cell Biol.* **1** (1), 145–172.
Microtubule Organizing Centers

[7] J. Wu and A. Akhmanova (2017), *Annu. Rev. Cell Dev. Biol.* **33** (1), 51–75.
Microtubule-Organizing Centers

[8] A. J. Matamoros and P. W. Baas (2016), *Brain Res. Bull.* **126** (3), 217–225.
Microtubules in health and degenerative disease of the nervous system

[9] M. A. Jordan and L. Wilson (2004), *Nat. Rev. Cancer* **4** (4), 253–265.
Microtubules as a target for anticancer drugs

[10] A. L. Parker, M. Kavallaris, and J. A. McCarroll (2014), *Front. Oncol.* **4**, 153.
Microtubules and Their Role in Cellular Stress in Cancer

[11] S. L. Palay (1956), *J. Cell Biol.* **2** (4), 193–202.
Synapses in the central nervous system

[12] D. B. Slautterback (1963), *J. Cell Biol.* **18** (2), 367–388.
Cytoplasmic Microtubules

[13] M. C. Ledbetter and K. R. Porter (1963), *J. Cell Biol.* **19** (1), 239–250.
A “microtubule” in plant cell fine structure

[14] M. C. Ledbetter and K. R. Porter (1964), *Science* **144** (3620), 872–874.
Morphology of Microtubules of Plant Cells

[15] B. Kiefer et al. (1966), *J. Mol. Biol.* **20** (1), 75–79.
The Molecular Unit of the Microtubules of the Mitotic Apparatus

[16] P. R. Burton, R. E. Hinkley, and G. B. Pierson (1975), *J. Cell Biol.* **65** (1), 227–233.
Tannic acid-stained microtubules with 12, 13, and 15 protofilaments

[17] T. Nagano and F. Suzuki (1975), *J. Cell Biol.* **64** (1), 242–245.
Microtubules with 15 subunits in cockroach epidermal cells

[18] G. B. Pierson, P. R. Burton, and R. H. Himes (1978), *J. Cell Biol.* **76** (1), 223–228.
Alterations in number of protofilaments in microtubules assembled in vitro

[19] E. J. Aamodt and J. G. Culotti (1986), *J. Cell Biol.* **103** (1), 23–31.
Microtubules and Microtubule-associated Proteins from the Nematode Caenorhabditis elegans: Periodic Cross-links Connect Microtubules In Vitro

[20] R. H. Wade, D. Chrétien, and D. Job (1990), *J. Mol. Biol.* **212** (4), 775–786.
Characterization of Microtubule Protofilament Numbers

[21] D. Chrétien and R. H. Wade (1991), *Biol. Cell* **71** (1), 161–174.
New data on the microtubule surface lattice

[22] D. Chrétien and S. D. Fuller (2000), *J. Mol. Biol.* **298** (4), 663–676.
Microtubules Switch Occasionally into Unfavorable Configurations During Elongation

[23] H. Sui and K. H. Downing (2010), *Structure* **18** (8), 1022–1031.
Structural Basis of Interprotofilament Interaction and Lateral Deformation of Microtubules

[24] S. Chaaban and G. J. Brouhard (2017), *Mol. Biol. Cell* **28** (22), 2924–2931.
A microtubule bestiary: structural diversity in tubulin polymers

[25] D. Chrétien et al. (1992), *J. Cell Biol.* **117** (5), 1031–1040.
Lattice Defects in Microtubules: Protofilament Numbers Vary Within Individual Microtubules

[26] D. L. Ringo (1967), *J. Ultrastruct. Res.* **17** (3), 266–277.
The arrangement of subunits in flagellar fibers

[27] M. W. Kirschner et al. (1974), *Proc. Natl. Acad. Sci. USA* **71** (4), 1159–1163.
Microtubules from Mammalian Brain: Some Properties of Their Depolymerization Products and a Proposed Mechanism of Assembly and Disassembly

[28] R. Melki et al. (1989), *Biochemistry* **28** (23), 9143–9152.
Cold Depolymerization of Microtubules to Double Rings: Geometric Stabilization of Assemblies

[29] E. M. Mandelkow, E. Mandelkow, and R. A. Milligan (1991), *J. Cell Biol.* **114** (5), 977–991.
Microtubule Dynamics and Microtubule Caps: A Time-resolved Cryo-Electron Microscopy Study

[30] W. A. Wells (2005), *J. Cell Biol.* **169** (4), 552.
The discovery of tubulin

[31] H. Mohri (1968), *Nature* **217** (5133), 1053–1054.
Amino-acid Composition of "Tubulin" constituting Microtubules of Sperm Flagella

[32] A. V. Grimstone and A. Klug (1966), *J. Cell Sci.* **1** (3), 351–362.
Observations on the Substructure of Flagellar Fibres

[33] D. C. Pease (1963), *J. Cell Biol.* **18** (2), 313–326.
The Ultrastructure of Flagellar Fibrils

[34] R. C. Weisenberg, G. G. Broisy, and E. W. Taylor (1968), *Biochemistry* **7** (12), 4466–4479.
Colchicine-Binding Protein of Mammalian Brain and Its Relation to Microtubules

[35] J. Bryan and L. Wilson (1971), *Proc. Natl. Acad. Sci. USA* **68** (8), 1762–1766.
Are Cytoplasmic Microtubules Heteropolymers?

[36] T. Kobayashi (1974), *J. Biochem.* **76** (1), 201–204.
Nucleotides Bound to Brain Tubulin and Reconstituted Microtubules

[37] E. Nogales, S. G. Wolf, and K. H. Downing (1998), *Nature* **391** (6663), 199–203.
Structure of the $\alpha\beta$ tubulin dimer by electron crystallography

[38] T. J. Mitchison (1993), *Science* **261** (5124), 1044–1047.
Localization of an exchangeable GTP binding site at the plus end of microtubules

[39] G. G. Borisy, J. B. Olmsted, and R. A. Klugman (1972), *Proc. Natl. Acad. Sci. USA* **69** (10), 2890–2894.
In Vitro Aggregation of Cytoplasmic Microtubule Subunits

[40] R. C. Weisenberg (1972), *Science* **177** (4054), 1104–1105.
Microtubule Formation in vitro in Solutions Containing Low Calcium Concentrations

[41] J. B. Olmsted and G. G. Borisy (1975), *Biochemistry* **14** (13), 2996–3005.
Ionic and Nucleotide Requirements for Microtubule Polymerization in Vitro

[42] M. Caplow et al. (1989), *Biochemistry* **28** (20), 8136–8141.
Stabilization of Microtubules by Tubulin-GDP-P_i Subunits

[43] J. Wolff, D. L. Sackett, and L. Knipling (1996), *Protein Sci.* **5** (10), 2020–2028.
Cation selective promotion of tubulin polymerization by alkali metal chlorides

[44] C. J. Bode et al. (2003), *EMBO Rep.* **4** (1), 94–99.
The two α-tubulin isotypes in budding yeast have opposing effects on microtubule dynamics in vitro

[45] R. F. Ludueña and A. Banerjee (2008), *The Role of Microtubules in Cell Biology, Neurobiology, and Oncology*, ed. by T. Fojo, Humana Press, 123–175.
The Isotypes of Tubulin

[46] T. Mitchison and M. Kirschner (1984), *Nature* **312** (5991), 232–237.
Microtubule assembly nucleated by isolated centrosomes

[47] T. Mitchison and M. Kirschner (1984), *Nature* **312** (5991), 237–242.
Dynamic instability of microtubule growth

[48] T. Horio and H. Hotani (1986), *Nature* **321** (6070), 605–607.
Visualization of the dynamic instability of individual microtubules by dark-field microscopy

[49] R. A. Walker et al. (1988), *J. Cell Biol.* **107** (4), 1437–1448.
Dynamic instability of individual microtubules analyzed by video light microscopy: rate constants and transition frequencies

[50] A. Wegner (1976), *J. Mol. Biol.* **108** (1), 139–150.
Head to tail polymerization of actin

[51] M. W. Kirschner (1980), *J. Cell Biol.* **86** (1), 330–334.
Implications of Treadmilling for the Stability and Polarity of Actin and Tubulin Polymers in Vivo

[52] M.-F. Carlier, T. L. Hill, and Y.-d. Chen (1984), *Proc. Natl. Acad. Sci. USA* **81** (3), 771–775.
Interference of GTP hydrolysis in the mechanism of microtubule assembly: An experimental study

[53] A. Dimitrov et al. (2008), *Science* **322** (5906), 1353–1356.
Detection of GTP-Tubulin Conformation in Vivo Reveals a Role for GTP Remnants in Microtubule Rescues

[54] M. Zanic et al. (2009), *PLOS ONE* **4** (10), e7585.
EB1 Recognizes the Nucleotide State of Tubulin in the Microtubule Lattice

[55] A. Guesdon et al. (2016), *Nat. Cell Biol.* **18** (10), 1102–1108.
EB1 interacts with outwardly curved and straight regions of the microtubule lattice

[56] T. A. Reid et al. (2019), *Elife* **8**, e48117.
Structural state recognition facilitates tip tracking of EB1 at growing microtubule ends

[57] C. Tropini et al. (2012), *PLoS ONE* **7** (1), e30103.
Islands Containing Slowly Hydrolyzable GTP Analogs Promote Microtubule Rescues

[58] E. Nogales et al. (1999), *Cell* **96** (1), 79–88.
High-Resolution Model of the Microtubule

[59] L. A. Amos and A. Klug (1974), *J. Cell Sci.* **14** (3), 523–549.
Arrangement of Subunits in Flagellar Microtubules

[60] R. L. Margolis and L. Wilson (1981), *Nature* **293** (5835), 705–711.
Microtubule treadmills — possible molecular machinery

[61] V. I. Rodionov and G. G. Borisy (1997), *Science* **275** (5297), 215–218.
Microtubule Treadmilling in Vivo

[62] J. R. McIntosh et al. (2008), *Cell* **135** (2), 322–333.
Fibrils Connect Microtubule Tips with Kinetochores: A Mechanism to Couple Tubulin Dynamics to Chromosome Motion

[63] J. R. McIntosh et al. (2018), *J. Cell Biol.* **217** (8), 2691–2708.
Microtubules grow by the addition of bent guanosine triphosphate tubulin to the tips of curved protofilaments

[64] R. M. Buey, J. F. Díaz, and J. M. Andreu (2006), *Biochemistry* **45** (19), 5933–5938.
The Nucleotide Switch of Tubulin and Microtubule Assembly: A Polymerization-Driven Structural Change

[65] L. M. Rice, E. A. Montabana, and D. A. Agard (2008), *Proc. Natl. Acad. Sci. USA* **105** (14), 5378–5383.
The lattice as allosteric effector: Structural studies of $\alpha\beta$- and γ-tubulin clarify the role of GTP in microtubule assembly

[66] K. H. Downing and E. Nogales (1998), *Curr. Opin. Cell Biol.* **10** (1), 16–22.
Tubulin and microtubule structure

[67] T. Müller-Reichert et al. (1998), *Proc. Natl. Acad. Sci. USA* **95** (7), 3661–3666.
Structural changes at microtubule ends accompanying GTP hydrolysis: Information from a slowly hydrolyzable analogue of GTP, guanylyl (α,β)methylenediphosphonate

[68] J. B. Olmsted and G. G. Borisy (1973), *Annu. Rev. Biochem.* **42** (1), 507–540.
Microtubules

[69] H. P. Erickson and E. T. O'Brien (1992), *Annu. Rev. Biophys. Biomol. Struct.* **21** (1), 145–166.
Microtubule Dynamic Instability and GTP Hydrolysis

[70] A. Desai and T. J. Mitchison (1997), *Annu. Rev. Cell Dev. Biol.* **13** (1), 83–117.
Microtubule Polymerization Dynamics

[71] E. Nogales (2000), *Annu. Rev. Biochem.* **69** (1), 277–302.
Structural Insights into Microtubule Function

[72] J. Howard and A. A. Hyman (2009), *Nat. Rev. Mol. Cell Biol.* **10** (8), 569–574.
Growth, fluctuation and switching at microtubule plus ends

[73] R. H. Wade (2009), *Mol. Biotechnol.* **43** (2), 177–191.
On and Around Microtubules: An Overview

[74] A. Akhmanova and M. O. Steinmetz (2015), *Nat. Rev. Mol. Cell Biol.* **16** (12), 711–726.
Control of microtubule organization and dynamics: two ends in the limelight

[75] J. Roostalu and T. Surrey (2017), *Nat. Rev. Mol. Cell Biol.* **18** (11), 702–710.
Microtubule nucleation: beyond the template

[76] V. Barsegov, J. L. Ross, and R. I. Dima (2017), *J. Phys. Condens. Matter* **29** (43), 433003.
Dynamics of microtubules: highlights of recent computational and experimental investigations

[77] G. J. Brouhard and L. M. Rice (2018), *Nat. Rev. Mol. Cell Biol.* **19** (7), 451–463.
Microtubule dynamics: an interplay of biochemistry and mechanics

[78] J. van Haren and T. Wittmann (2019), *Bioessays* **41** (3), 1800194.
Microtubule Plus End Dynamics — Do We Know How Microtubules Grow?

[79] H. Bowne-Anderson et al. (2013), *Bioessays* **35** (5), 452–461.
Microtubule dynamic instability: A new model with coupled GTP hydrolysis and multistep catastrophe

[80] P. N. Zakharov et al. (2016), *Physics-Uspekhi* **59** (8), 773–786.
Microtubules: dynamically unstable stochastic phase-switching polymers

[81] Y.-d. Chen and T. L. Hill (1983), *Proc. Natl. Acad. Sci. USA* **80** (24), 7520–7523.
Use of Monte Carlo calculations in the study of microtubule subunit kinetics

[82] T. L. Hill and M.-F. Carlier (1983), *Proc. Natl. Acad. Sci. USA* **80** (23), 7234–7238.
Steady-state theory of the interference of GTP hydrolysis in the mechanism of microtubule assembly

[83] T. L. Hill and Y.-d. Chen (1984), *Proc. Natl. Acad. Sci. USA* **81** (18), 5772–5776.
Phase changes at the end of a microtubule with a GTP cap

[84] T. L. Hill (1984), *Proc. Natl. Acad. Sci. USA* **81** (21), 6728–6732.
Introductory analysis of the GTP-cap phase-change kinetics at the end of a microtubule

[85] M. Caplow and R. Reid (1985), *Proc. Natl. Acad. Sci. USA* **82** (10), 3267–3271.
Directed elongation model for microtubule GTP hydrolysis

[86] H. Flyvbjerg, T. E. Holy, and S. Leibler (1994), *Phys. Rev. Lett.* **73** (17), 2372–2375.
Stochastic Dynamics of Microtubules: A Model for Caps and Catastrophes

[87] H. Flyvbjerg, T. E. Holy, and S. Leibler (1996), *Phys. Rev. E* **54** (5), 5538–5560.
Microtubule dynamics: Caps, catastrophes, and coupled hydrolysis

[88] T. Antal, P. L. Krapivsky, and S. Redner (2007), *J. Stat. Mech.* **2007** (05), L05004.
Dynamics of microtubule instabilities

[89] T. Antal et al. (2007), *Phys. Rev. E* **76** (4), 041907.
Dynamics of an idealized model of microtubule growth and catastrophe

[90] Sumedha, M. F. Hagan, and B. Chakraborty (2011), *Phys. Rev. E* **83** (5), 051904.
Prolonging assembly through dissociation: A self-assembly paradigm in microtubules

[91] A. Janulevicius, J. van Pelt, and A. van Ooyen (2006), *Biophys. J.* **90** (3), 788–798.
Compartment Volume Influences Microtubule Dynamic Instability: A Model Study

[92] G. Margolin et al. (2006), *Phys. Rev. E* **74** (4), 041920.
Analysis of a mesoscopic stochastic model of microtubule dynamic instability

[93] P. Ranjith et al. (2009), *Biophys. J.* **96** (6), 2146–2159.
Nonequilibrium Self-Assembly of a Filament Coupled to ATP/GTP Hydrolysis

[94] R. Padinhateeri, A. B. Kolomeisky, and D. Lacoste (2012), *Biophys. J.* **102** (6), 1274–1283.
Random Hydrolysis Controls the Dynamic Instability of Microtubules

[95] X. Li and A. B. Kolomeisky (2013), *J. Phys. Chem. B* **117** (31), 9217–9223.
Theoretical Analysis of Microtubules Dynamics Using a Physical–Chemical Description of Hydrolysis

[96] X. Li and A. B. Kolomeisky (2014), *J. Phys. Chem. B* **118** (11), 2966–2972.
A New Theoretical Approach to Analyze Complex Processes in Cytoskeleton Proteins

[97] X. Li and A. B. Kolomeisky (2014), *J. Phys. Chem. B* **118** (48), 13777–13784.
Theoretical Analysis of Microtubule Dynamics at All Times

[98] H. Bolterauer, H.-J. Limbach, and J. A. Tuszyński (1999), *J. Biol. Phys.* **25** (1), 1–22.
Models of Assembly and Disassembly of Individual Microtubules: Stochastic and Averaged Equations

[99] J. S. Aparna, R. Padinhateeri, and D. Das (2017), *Sci. Rep.* **7**, 45747.
Signatures of a macroscopic switching transition for a dynamic microtubule

[100] Y.-d. Chen and T. L. Hill (1985), *Proc. Natl. Acad. Sci. USA* **82** (4), 1131–1135.
Monte Carlo study of the GTP cap in a five-start helix model of a microtubule

[101] P. Bayley, M. Schilstra, and S. Martin (1989), *FEBS Lett.* **259** (1), 181–184.
A Lateral Cap model of microtubule dynamic instability

[102] P. M. Bayley, M. J. Schilstra, and S. R. Martin (1990), *J. Cell Sci.* **95** (1), 33–48.
Microtubule dynamic instability: numerical simulation of microtubule transition properties using a Lateral Cap model

[103] S. R. Martin, M. J. Schilstra, and P. M. Bayley (1993), *Biophys. J.* **65** (2), 578–596.
Dynamic Instability of Microtubules: Monte Carlo Simulation and Application to Different Types of Microtubule Lattice

[104] V. VanBuren, D. J. Odde, and L. Cassimeris (2002), *Proc. Natl. Acad. Sci. USA* **99** (9), 6035–6040.
Estimates of lateral and longitudinal bond energies within the microtubule lattice

[105] V. VanBuren, D. J. Odde, and L. Cassimeris (2004), *Proc. Natl. Acad. Sci. USA* **101** (41), 14989.
errata for VanBuren et al., Estimates of lateral and longitudinal bond energies within the microtubule lattice, PNAS 2002 99:6035-6040

[106] B. M. A. G. Piette et al. (2009), *PLoS ONE* **4** (8), e6378.
A Thermodynamic Model of Microtubule Assembly and Disassembly

[107] Z. Wu et al. (2009), *PLoS ONE* **4** (10), e7291.
Simulations of Tubulin Sheet Polymers as Possible Structural Intermediates in Microtubule Assembly

[108] M. K. Gardner et al. (2011), *Cell* **146** (4), 582–592.
Rapid Microtubule Self-Assembly Kinetics

[109] F.-A. Piedra et al. (2016), *Mol. Biol. Cell* **27** (22), 3515–3525.
GDP-to-GTP exchange on the microtubule end can contribute to the frequency of catastrophe

[110] T. Kim and L. M. Rice (2019), *Mol. Biol. Cell* **30** (12), 1451–1462.
Long-range, through-lattice coupling improves predictions of microtubule catastrophe

[111] G. Margolin, H. V. Goodson, and M. S. Alber (2011), *Phys. Rev. E* **83** (4), 041905.
Mean-field study of the role of lateral cracks in microtubule dynamics

[112] G. Margolin et al. (2012), *Mol. Biol. Cell* **23** (4), 642–656.
The mechanisms of microtubule catastrophe and rescue: implications from analysis of a dimer-scale computational model

[113] C. Li et al. (2014), *Soft Matter* **10** (12), 2069–2080.
Microtubule dynamic instability: the role of cracks between protofilaments

[114] E. B. Stukalin and A. B. Kolomeisky (2004), *J. Chem. Phys.* **121** (2), 1097–1104.
Simple growth models of rigid multifilament biopolymers

[115] J. Son, G. Orkoulas, and A. B. Kolomeisky (2005), *J. Chem. Phys.* **123** (12), 124902.
Monte Carlo simulations of rigid biopolymer growth processes

[116] V. Jemseena and M. Gopalakrishnan (2013), *Phys. Rev. E* **88** (3), 032717.
Microtubule catastrophe from protofilament dynamics

[117] X. Li and A. B. Kolomeisky (2015), *J. Phys. Chem. B* **119** (13), 4653–4661.
The Role of Multifilament Structures and Lateral Interactions in Dynamics of Cytoskeleton Proteins and Assemblies

[118] V. VanBuren, L. Cassimeris, and D. J. Odde (2005), *Biophys. J.* **89** (5), 2911–2926.
Mechanochemical Model of Microtubule Structure and Self-Assembly Kinetics

[119] Z. Wu, E. Nogales, and J. Xing (2012), *Biophys. J.* **102** (12), 2687–2696.
Comparative Studies of Microtubule Mechanics with Two Competing Models Suggest Functional Roles of Alternative Tubulin Lateral Interactions

[120] C. E. Coombes et al. (2013), *Curr. Biol.* **23** (14), 1342–1348.
Evolving Tip Structures Can Explain Age-Dependent Microtubule Catastrophe

[121] N. Müller and J. Kierfeld (2014), *Phys. Biol.* **11** (4), 046001.
Effects of microtubule mechanics on hydrolysis and catastrophes

[122] M. I. Molodtsov et al. (2005), *Biophys. J.* **88** (5), 3167–3179.
A Molecular-Mechanical Model of the Microtubule

[123] X.-Y. Ji and X.-Q. Feng (2011), *PLoS ONE* **6** (12), e29049.
Mechanochemical Modeling of Dynamic Microtubule Growth Involving Sheet-to-Tube Transition

[124] I. Jain, M. M. Inamdar, and R. Padinhateeri (2015), *PLoS Comput. Biol.* **11** (2), e1004099.
Statistical Mechanics Provides Novel Insights into Microtubule Stability and Mechanism of Shrinkage

[125] B. T. Castle and D. J. Odde (2013), *Biophys. J.* **105** (11), 2528–2540.
Brownian Dynamics of Subunit Addition-Loss Kinetics and Thermodynamics in Linear Polymer Self-Assembly

[126] P. Zakharov et al. (2015), *Biophys. J.* **109** (12), 2574–2591.
Molecular and Mechanical Causes of Microtubule Catastrophe and Aging

[127] I. M. Jánosi, D. Chrétien, and H. Flyvbjerg (1998), *Eur. Biophys. J.* **27** (5), 501–513.
Modeling elastic properties of microtubule tips and walls

[128] M. Arslan and M. C. Boyce (2012), *J. Appl. Mech.* **79** (2), 021002.
A Micromechanically Based Anisotropic Constitutive Model for the Microtubule Wall

[129] Y. Ding and Z. Xu (2011), *BioNanoSci.* **1** (4), 173–182.
Mechanics of Microtubules from a Coarse-Grained Model

[130] X.-Y. Ji and X.-Q. Feng (2011), *Phys. Rev. E* **84** (3), 031933.
Coarse-grained mechanochemical model for simulating the dynamic behavior of microtubules

[131] J. Zhang and C. Wang (2014), *Biomech. Model. Mechanobiol.* **13** (6), 1175–1184.
Molecular structural mechanics model for the mechanical properties of microtubules

[132] N. A. Baker et al. (2001), *Proc. Natl. Acad. Sci. USA* **98** (18), 10037–10041.
Electrostatics of nanosystems: Application to microtubules and the ribosome

[133] P. Drabik, S. Gusarov, and A. Kovalenko (2007), *Biophys. J.* **92** (2), 394–403.
Microtubule Stability Studied by Three-Dimensional Molecular Theory of Solvation

[134] D. Sept, N. A. Baker, and J. A. McCammon (2003), *Protein Sci.* **12** (10), 2257–2261.
The physical basis of microtubule structure and stability

[135] S. Enemark et al. (2008), *J. Biomech. Eng.* **130** (4), 041008.
Mechanical Model of the Tubulin Dimer Based on Molecular Dynamics Simulations

[136] M. A. Deriu et al. (2010), *Biophys. J.* **99** (7), 2190–2199.
Anisotropic Elastic Network Modeling of Entire Microtubules

[137] D. B. Wells and A. Aksimentiev (2010), *Biophys. J.* **99** (2), 629–637.
Mechanical Properties of a Complete Microtubule Revealed through Molecular Dynamics Simulation

[138] K. E. Theisen et al. (2012), *J. Phys. Chem. B* **116** (29), 8545–8555.
Multiscale Modeling of the Nanomechanics of Microtubule Protofilaments

[139] Y. Feng and S. Mitran (2018), *Cytoskeleton* **75** (2), 45–60.
Data-driven reduced-order model of microtubule mechanics

[140] J. A. Bollinger and M. J. Stevens (2018), *Soft Matter* **14** (10), 1748–1752.
Catastrophic depolymerization of microtubules driven by subunit shape change

[141] M. Schmidt (2014), MA thesis. TU Dortmund University.
Implementing a Mechanochemical Model to Simulate Microtubule Dynamics

[142] M. A. Deriu et al. (2007), *J. Mater. Sci.* **42** (21), 8864–8872.
Tubulin: from atomistic structure to supramolecular mechanical properties

[143] O. Kononova et al. (2014), *J. Am. Chem. Soc.* **136** (49), 17036–17045.
Tubulin Bond Energies and Microtubule Biomechanics Determined from Nanoindentation in Silico

[144] D. Havelka et al. (2017), *Sci. Rep.* **7** (1), 4227.
Deformation pattern in vibrating microtubule: Structural mechanics study based on an atomistic approach

[145] E.-M. Mandelkow et al. (1986), *J. Cell Biol.* **102** (3), 1067–1073.
On the Surface Lattice of Microtubules: Helix Starts, Protofilament Number, Seam, and Handedness

[146] G. M. Alushin et al. (2014), *Cell* **157** (5), 1117–1129.
High-Resolution Microtubule Structures Reveal the Structural Transitions in $\alpha\beta$-Tubulin upon GTP Hydrolysis

[147] M. Katsuki, D. R. Drummond, and R. A. Cross (2014), *Nat. Commun.* **5**, 3094.
Ectopic A-lattice seams destabilize microtubules

[148] R. Zhang et al. (2015), *Cell* **162** (4), 849–859.
Mechanistic Origin of Microtubule Dynamic Instability and Its Modulation by EB Proteins

[149] R. Zhang and E. Nogales (2015), *J. Struct. Biol.* **192** (2), 245–254.
A new protocol to accurately determine microtubule lattice seam location

[150] R. Zhang, B. LaFrance, and E. Nogales (2018), *Proc. Natl. Acad. Sci. USA* **115** (27), E6191–E6200.
Separating the effects of nucleotide and EB binding on microtubule structure

[151] J. G. Gall (1966), *Journal of Cell Biology* **31** (3), 639–643.
Microtubule Fine Structure

[152] H. Li et al. (2002), *Structure* **10** (10), 1317–1328.
Microtubule Structure at 8 Å Resolution

[153] C. Elie-Caille et al. (2007), *Curr. Biol.* **17** (20), 1765–1770.
Straight GDP-Tubulin Protofilaments Form in the Presence of Taxol

[154] B. Gigant et al. (2000), *Cell* **102** (6), 809–816.
The 4 Å X-Ray Structure of a Tubulin:Stathmin-like Domain Complex

[155] H.-W. Wang and E. Nogales (2005), *Nature* **435** (7044), 911–915.
Nucleotide-dependent bending flexibility of tubulin regulates microtubule assembly

[156] H. Sawada. Marcel Dekker, Inc.
Thermodynamics of Polymerization

[157] H. P. Erickson (1989), *J. Mol. Biol.* **206** (3), 465–474.
Co-operativity in Protein-Protein Association: The Structure and Stability of the Actin Filament

[158] A. B. Kolomeisky and M. E. Fisher (2001), *Biophys. J.* **80** (1), 149–154.
Force-Velocity Relation for Growing Microtubules

[159] G. I. Bell (1978), *Science* **200** (4342), 618–627.
Models for the specific adhesion of cells to cells

[160] E. Evans and K. Ritchie (1997), *Biophys. J.* **72** (4), 1541–1555.
Dynamic Strength of Molecular Adhesion Bonds

[161] R. W. Berry and M. L. Shelanski (1972), *J. Mol. Biol.* **71** (1), 71–80.
Interactions of tubulin with vinblastine and guanosine triphosphate

[162] M. Jacobs, H. Smith, and E. W. Taylor (1974), *J. Mol. Biol.* **89** (3), 455–468.
Tubulin: Nucleotide Binding and Enzymic Activity

[163] A. Levi et al. (1974), *Biochim. Biophys. Acta Protein Struct.* **365** (2), 450–453.
Studies on binding of GTP to the microtubule protein

[164] T. Kobayashi (1975), *J. Biochem.* **77** (6), 1193–1197.
Dephosphorylation of Tubulin-bound Guanosine Triphosphate during Microtubule Assembly

[165] R. L. Geahlen and B. E. Haley (1979), *J. Biol. Chem.* **254** (23), 11982–11987.
Use of a GTP Photoaffinity Probe to Resolve Aspects of the Mechanism of Tubulin Polymerization

[166] R. L. Geahlen and B. E. Haley (1977), *Proc. Natl. Acad. Sci. USA* **74** (10), 4375–4377.
Interactions of a photoaffinity analog of GTP with the proteins of microtubules

[167] M.-F. Carlier and D. Pantaloni (1981), *Biochemistry* **20** (7), 1918–1924.
Kinetic analysis of guanosine 5'-triphosphate hydrolysis associated with tubulin polymerization

[168] M.-F. Carlier (1988), *Cell Biophys.* **12** (1), 105.
Role of Nucleotide Hydrolysis in the Polymerization of Actin and Tubulin

[169] M. F. Carlier et al. (1988), *Biochemistry* **27** (10), 3555–3559.
Stabilization of Microtubules by Inorganic Phosphate and Its Structural Analogs, the Fluoride Complexes of Aluminum and Beryllium

[170] M.-F. Carlier (1989), *Int. Rev. Cytol.* **115**, Academic Press, 139–170.
Role of Nucleotide Hydrolysis in the Dynamics of Actin Filaments and Microtubules

[171] R. Melki, S. Fievez, and M.-F. Carlier (1996), *Biochemistry* **35** (37), 12038–12045.
Continuous Monitoring of P_i Release Following Nucleotide Hydrolysis in Actin or Tubulin Assembly Using 2-Amino-6-mercapto-7-methylpurine Ribonucleoside and Purine-Nucleoside Phosphorylase as an Enzyme-Linked Assay

[172] S. W. Manka and C. A. Moores (2018), *Nat. Struct. Mol. Biol.* **25** (7), 607–615.
The role of tubulin–tubulin lattice contacts in the mechanism of microtubule dynamic instability

[173] M. Caplow, R. L. Ruhlen, and J. Shanks (1994), *J. Cell Biol.* **127** (3), 779–788.
The Free Energy for Hydrolysis of a Microtubule-Bound Nucleotide Tripllosphate Is Near Zero: All of the Free Energy for Hydrolysis Is Stored in the Microtubule Lattice

[174] E. L. Grishchuk et al. (2005), *Nature* **438** (7066), 384–388.
Force production by disassembling microtubules

[175] J. W. Driver et al. (2017), *Elife* **6**, e28433.
Direct measurement of conformational strain energy in protofilaments curling outward from disassembling microtubule tips

[176] A. Efremov et al. (2007), *Proc. Natl. Acad. Sci. USA* **104** (48), 19017–19022.
In search of an optimal ring to couple microtubule depolymerization to processive chromosome motions

[177] E. T. O'Brien, W. A. Voter, and H. P. Erickson (1987), *Biochemistry* **26** (13), 4148–4156.
GTP hydrolysis during microtubule assembly

[178] J. Löwe et al. (2001), *J. Mol. Biol.* **313** (5), 1045–1057.
Refined Structure of $\alpha\beta$-Tubulin at 3.5 Å Resolution

[179] D. T. Gillespie (1976), *J. Comput. Phys.* **22** (4), 403–434.
A general method for numerically simulating the stochastic time evolution of coupled chemical reactions

[180] D. T. Gillespie (1977), *J. Phys. Chem.* **81** (25), 2340–2361.
Exact stochastic simulation of coupled chemical reactions

[181] A. Chatterjee and D. G. Vlachos (2007), *J. Computer-Aided. Mater. Des.* **14** (2), 253–308.
An overview of spatial microscopic and accelerated kinetic Monte Carlo methods

[182] D. Job, O. Valiron, and B. Oakley (2003), *Curr. Opin. Cell Biol.* **15** (1), 111–117.
Microtubule nucleation

[183] M. Galassi et al.
GNU Scientific Library Reference Manual
`https://www.gnu.org/software/gsl/`

[184] W. H. Press et al. 3rd ed. Cambridge University Press.
Numerical Recipes: The Art of Scientific Computing

[185] S. H. Northrup and H. P. Erickson (1992), *Proc. Natl. Acad. Sci. USA* **89** (8), 3338–3342.
Kinetics of protein-protein association explained by Brownian dynamics computer simulation

[186] P. Ayaz et al. (2014), *Elife* **3**, e03069.
A tethered delivery mechanism explains the catalytic action of a microtubule polymerase

[187] K. J. Mickolajczyk et al. (2019), *Proc. Natl. Acad. Sci. USA* **116** (15), 7314–7322.
Direct observation of individual tubulin dimers binding to growing microtubules

[188] M.-F. Carlier, D. Didry, and D. Pantaloni (1987), *Biochemistry* **26** (14), 4428–4437.
Microtubule Elongation and Guanosine 5'-Triphosphate Hydrolysis. Role of Guanine Nucleotides in Microtubule Dynamics

[189] E. T. O'Brien et al. (1990), *Biochemistry* **29** (28), 6648–6656.
Effects of magnesium on the dynamic instability of individual microtubules

[190] D. N. Drechsel et al. (1992), *Mol. Biol. Cell* **3** (10), 1141–1154.
Modulation of the dynamic instability of tubulin assembly by the microtubule-associated protein tau

[191] B. Trinczek et al. (1993), *Mol. Biol. Cell* **4** (3), 323–335.
Dynamics of microtubules from erythrocyte marginal bands

[192] D. Chrétien, S. D. Fuller, and E. Karsenti (1995), *J. Cell Biol.* **129** (5), 1311–1328.
Structure of Growing Microtubule Ends: Two-Dimensional Sheets Close Into Tubes at Variable Rates

[193] S. Pedigo and R. C. Williams Jr. (2002), *Biophys. J.* **83** (4), 1809–1819.
Concentration Dependence of Variability in Growth Rates of Microtubules

[194] H. Sim and D. Sept (2013), *Cell Mol. Bioeng.* **6** (4), 361–368.
Properties of Microtubules with Isotropic and Anisotropic Mechanics

[195] A. Grafmüller and G. A. Voth (2011), *Structure* **19** (3), 409–417.
Intrinsic Bending of Microtubule Protofilaments

[196] D. Boal. 2nd ed. Cambridge University Press.
Mechanics of the Cell

[197] R. Melki, M. F. Carlier, and D. Pantaloni (1990), *Biochemistry* **29** (38), 8921–8932.
Direct Evidence for GTP and GDP-P_i Intermediates in Microtubule Assembly

[198] A. Vandecandelaere, S. R. Martin, and P. M. Bayley (1995), *Biochemistry* **34** (4), 1332–1343.
Regulation of Microtubule Dynamic Instability by Tubulin-GDP

[199] M. K. Gardner et al. (2011), *Cell* **147** (5), 1092–1103.
Depolymerizing Kinesins Kip3 and MCAK Shape Cellular Microtubule Architecture by Differential Control of Catastrophe

[200] L. Cassimeris, N. K. Pryer, and E. D. Salmon (1988), *J. Cell Biol.* **107** (6), 2223–2231.
Real-Time Observations of Microtubule Dynamic Instability in Living Cells

[201] J. R. Simon, S. F. Parsons, and E. D. Salmon (1992), *Cell Motil. Cytoskeleton* **21** (1), 1–14.
Buffer Conditions and Non-Tubulin Factors Critically Affect the Microtubule Dynamic Instability of Sea Urchin Egg Tubulin

[202] F. Verde et al. (1992), *J. Cell Biol.* **118** (5), 1097–1108.
Control of microtubule dynamics and length by cyclin A- and cyclin B-dependent kinases in Xenopus egg extracts

[203] D. K. Fygenson, E. Braun, and A. Libchaber (1994), *Phys. Rev. E* **50** (2), 1579–1588.
Phase diagram of microtubules

[204] M. E. Janson, M. E. de Dood, and M. Dogterom (2003), *J. Cell Biol.* **161** (6), 1029–1034.
Dynamic instability of microtubules is regulated by force

[205] D. J. Odde, L. Cassimeris, and H. M. Buettner (1995), *Biophys. J.* **69** (3), 796–802.
Kinetics of Microtubule Catastrophe Assessed by Probabilistic Analysis

[206] S. M. Mahserejian et al. (2019), *bioRxiv.*
Stutter: a Transient Dynamic Instability Phase that is Strongly Associated with Catastrophe

[207] R. J. Patel et al. (2020), *Methods Cell Biol.* **158**, Academic Press, 117–143.
Chapter 7 - Using STADIA to quantify dynamic instability in microtubules

[208] B. Zelinski and J. Kierfeld (2013), *Phys. Rev. E* **87** (1), 012703.
Cooperative dynamics of microtubule ensembles: Polymerization forces and rescue-induced oscillations

[209] D. Seetapun et al. (2012), *Curr. Biol.* **22** (18), 1681–1687.
Estimating the Microtubule GTP Cap Size In Vivo

[210] Intel.
Intel® Xeon® Processor E5-2650
`https://ark.intel.com/content/www/us/en/ark/products/64590/intel-xeon-processor-e5-2650-20m-cache-2-00-ghz-8-00-gt-s-intel-qpi.html`

[211] Intel.
Intel® Xeon® Processor E5-2630 v3
`https://ark.intel.com/content/www/us/en/ark/products/83356/intel-xeon-processor-e5-2630-v3-20m-cache-2-40-ghz.html`

[212] X. Li, R. Lipowsky, and J. Kierfeld (2010), *Europhys. Lett.* **89** (3), 38010.
Coupling of actin hydrolysis and polymerization: Reduced description with two nucleotide states

[213] E. J. Gumbel. Columbia University Press.
Statistics of Extremes

[214] S. Kotz and S. Nadarajah. Imperical College Press.
Extreme Value Distributions

[215] B. Schmittmann and R. K. P. Zia (1999), *Am. J. Phys.* **67** (12), 1269–1276.
"Weather" records: Musings on cold days after a long hot Indian summer

[216] J. R. Kuhn and T. D. Pollard (2005), *Biophys. J.* **88** (2), 1387–1402.
Real-Time Measurements of Actin Filament Polymerization by Total Internal Reflection Fluorescence Microscopy

[217] D. Vavylonis, Q. Yang, and B. O'Shaughnessy (2005), *Proc. Natl. Acad. Sci. USA* **102** (24), 8543–8548.
Actin polymerization kinetics, cap structure, and fluctuations

[218] E. B. Stukalin and A. B. Kolomeisky (2006), *Biophys. J.* **90** (8), 2673–2685.
ATP Hydrolysis Stimulates Large Length Fluctuations in Single Actin Filaments

[219] O. Kahraman et al. (2014), *Soft Matter* **10** (16), 2836–2847.
Confotronic dynamics of tubular filaments

[220] T. L. Karr and D. L. Purich (1979), *J. Biol. Chem.* **254** (21), 10885–10888.
A Microtubule Assembly/Disassembly Model Based on Drug Effects and Depolymerization Kinetics after Rapid Dilution

[221] T. L. Karr, D. Kristofferson, and D. L. Purich (1980), *J. Biol. Chem.* **255** (18), 8560–8566.
Mechanism of Microtubule Depolymerization: Correlation of Rapid Induced Disassembly Experiments with a Kinetic Model for Endwise Depolymerization

[222] D. Pantaloni and M.-F. Carlier (1986), *Ann. N. Y. Acad. Sci.* **466** (1), 496–509.
Involvement of Guanosine Triphosphate (GTP) Hydrolysis in the Mechanism of Tubulin Polymerization: Regulation of Microtubule Dynamics at Steady State by a GTP Cap

[223] R. A. Walker, N. K. Pryer, and E. D. Salmon (1991), *J. Cell Biol.* **114** (1), 73–81.
Dilution of individual microtubules observed in real time in vitro: evidence that cap size is small and independent of elongation rate.

[224] W. A. Voter, E. T. O'Brien, and H. P. Erickson (1991), *Cell Motil. Cytoskeleton* **18** (1), 55–62.
Dilution-Induced Disassembly of Microtubules: Relation to Dynamic Instability and the GTP Cap

[225] C. Duellberg, N. I. Cade, and T. Surrey (2016), *Mol. Biol. Cell* **27** (22), 3563–3573.
Microtubule aging probed by microfluidics-assisted tubulin washout

[226] C. Duellberg et al. (2016), *Elife* **5**, e13470.
The size of the EB cap determines instantaneous microtubule stability

[227] J. L. Höög et al. (2011), *J. Cell Sci.* **124** (5), 693–698.
Electron tomography reveals a flared morphology on growing microtubule ends

[228] W. Kukulski et al. (2011), *J. Cell Biol.* **192** (1), 111–119.
Correlated fluorescence and 3D electron microscopy with high sensitivity and spatial precision

[229] A. Nawrotek, M. Knossow, and B. Gigant (2011), *J. Mol. Biol.* **412** (1), 35–42.
The Determinants That Govern Microtubule Assembly from the Atomic Structure of GTP-Tubulin

[230] P. Ayaz et al. (2012), *Science* **337** (6096), 857–860.
A TOG:$\alpha\beta$-tubulin Complex Structure Reveals Conformation-Based Mechanisms for a Microtubule Polymerase

[231] L. Pecqueur et al. (2012), *Proc. Natl. Acad. Sci. USA* **109** (30), 12011–12016.
A designed ankyrin repeat protein selected to bind to tubulin caps the microtubule plus end

[232] A. Grafmüller, E. G. Noya, and G. A. Voth (2013), *J. Mol. Biol.* **425** (12), 2232–2246.
Nucleotide-Dependent Lateral and Longitudinal Interactions in Microtubules

[233] A. T. Ayoub, M. Klobukowski, and J. A. Tuszynski (2015), *PLoS Comput. Biol.* **11** (6), e1004313.
Detailed Per-residue Energetic Analysis Explains the Driving Force for Microtubule Disassembly

[234] V. A. Fedorov et al. (2019), *PLOS Computational Biology* **15** (8), 1–25.
Mechanical properties of tubulin intra- and inter-dimer interfaces and their implications for microtubule dynamic instability

[235] E. Mandelkow and E.-M. Mandelkow (1995), *Curr. Opin. Cell Biol.* **7** (1), 72–81.
Microtubules and microtubule-associated proteins

[236] A. Akhmanova and M. O. Steinmetz (2008), *Nat. Rev. Mol. Cell Biol.* **9** (4), 309–322.
Tracking the ends: a dynamic protein network controls the fate of microtubule tips

[237] G. J. Brouhard and L. M. Rice (2014), *J. Cell Biol.* **207** (3), 323–334.
The contribution of $\alpha\beta$-tubulin curvature to microtubule dynamics

[238] G. S. van Doorn et al. (2000), *Eur. Biophys. J.* **29** (1), 2–6.
On the stall force for growing microtubules

[239] J. Krawczyk and J. Kierfeld (2011), *Europhys. Lett.* **93** (2), 28006.
Stall force of polymerizing microtubules and filament bundles

[240] M. Dogterom and B. Yurke (1997), *Science* **278** (5339), 856–860.
Measurement of the Force-Velocity Relation for Growing Microtubules

[241] M. Dogterom et al. (2005), *Curr. Opin. Cell Biol.* **17** (1), 67–74.
Force generation by dynamic microtubules

[242] L. Schaedel et al. (2015), *Nat. Mater.* **14** (11), 1156–1163.
Microtubules self-repair in response to mechanical stress

[243] N. Jiang et al. (2017), *Cytoskeleton* **74** (1), 3–17.
Modeling the Effects of Lattice Defects on Microtubule Breaking and Healing

[244] T. A. Reid, C. Coombes, and M. K. Gardner (2017), *Biol. Open* **6** (8), 1245–1256.
Manipulation and quantification of microtubule lattice integrity

[245] L. Schaedel et al. (2019), *Nature Physics* **15** (8), 830–838.
Lattice defects induce microtubule self-renewal

[246] G. Guennebaud, B. Jacob, et al.
Eigen v3
`https://eigen.tuxfamily.org`